Polymer Electrolytes for Magnesium Batteries

Zur Erlangung des akademischen Grades eines

DOKTORS DER NATURWISSENSCHAFTEN

(Dr. rer. nat.)

von der KIT-Fakultät für Chemie und Biowissenschaften
des Karlsruher Instituts für Technologie (KIT)

genehmigte

DISSERTATION

von

David Antonius Sundermann

Tag der mündlichen Prüfung: 14.07.2023
Erster Gutachter: Prof. Dr. Patrick Théato
Zweiter Gutachter: Prof. Dr. Maximilian Fichtner

Declaration of Authorship

Die vorliegende Arbeit wurde im Zeitraum von Februar 2019 bis Januar 2022 am Institut für Technische Chemie und Polymerchemie (ITCP) am Karlsruher Institut für Technologie (KIT) unter der wissenschaftlichen Betreuung von Prof. Dr. Patrick Théato angefertigt.

Ich erkläre hiermit, dass ich die vorliegende Arbeit im Rahmen der Betreuung durch Prof. Dr. Patrick Théato selbstständig verfasst und keine anderen als die angegebenen Quellen und Hilfsmittel verwendet habe. Wörtlich oder inhaltlich übernommene Stellen sind als solche kenntlich gemacht und die Satzung des Karlsruher Instituts für Technologie (KIT) zur Sicherung guter wissenschaftlicher Praxis wurde beachtet. Des Weiteren erkläre ich, dass ich mich derzeit in keinem laufenden Promotionsverfahren befinde, und auch keine vorausgegangenen Promotionsversuche unternommen habe. Die elektronische Version der Arbeit stimmt mit der schriftlichen Version überein und die Primärdaten sind gemäß Abs. A (6) der Regeln zur Sicherung guter wissenschaftlicher Praxis des KIT beim Institut abgegeben und archiviert.

Karlsruhe, den 08.08.2023

David Antonius Sundermann

List of Publications

1.1 Publications within this Dissertation

[1] Magnesium polymer electrolytes based on polycarbonate poly(2-butyl-2-ethyltrimethylene-carbonate), *ACS Omega*, **2023**, in press, 10.1021/acsomega.3c00761.

1.2 Conference Contributions

[1] 4th international symposium on magnesium batteries (MagBattIV), 6 – 8 September 2022

Poster: Crosslinked single-ion conductors with borate anions for magnesium battery applications

Abstract

Batteries are of crucial importance with regard to the electrification of our society with a multitude of mobile electrical devices. Lithium batteries in particular have been of focus in research due to their high performance and long life. However, the comparatively high raw material costs of lithium are a major disadvantage, especially in the ongoing electrification of our society, which is why the development of alternative and potentially, cheaper batteries is required. One possible alternative are magnesium batteries, due to the significantly higher availability of inexpensive magnesium compared to lithium. Nevertheless, rechargeable magnesium batteries often contain corrosive, toxic, liquid and volatile electrolytes, which are a safety concern.

One solution involves the utilization of polymer electrolytes instead of commercial small molecule liquid electrolytes, a strategy that has already been successfully applied to lithium batteries. However, the low-cost availability, excellent mechanical properties and good mechanical processability are still opposed by low cycling stability, moderate magnesium ion conductivities and high deposition potentials. Significant solutions are already known for lithium batteries and include plasticizers, additives in addition to polymer blends as well as single-ion conductors and polymer-in-salt electrolytes, however, have not been adopted in all cases to magnesium batteries.

Therefore, this dissertation deals with different design approaches and synthesis of self-standing polymer electrolytes along their characterizations with respect to ion coordination, ion conductivity and magnesium metal electrode compatibility.

In the first chapter, a library of self-standing, crosslinked single-ion electrolytes based on borates and a poly(ethylene oxide)-based (PEO-based) copolymer was prepared. Parameters were optimized to high ionic conductivity with respect to monomer ratio, molecular architecture, plasticizer and PEO chain length. Based on the best system, different magnesium-lithium hybrid electrolytes were prepared, in which magnesium ions were partially exchanged for lithium ions. A complex, current-dependent, magnesium deposition and uptake behavior was observed. These observations were interpreted in the context of ion dissociation, crystallinity and ion conductivity and provided reduced plating and stripping potentials for hybrid electrolytes in magnesium batteries.

In the second chapter, a library of polymer electrolytes with anion receptors, as an alternative to single-ion electrolytes were prepared. For this purpose, two new borate-based monomers with mono- and difluoro aromatics were developed and copolymerized with poly(ethylene glycol) methacrylate (M_n = 500 g mol^{-1}). The architecture, monomer ratio and salt concentration were

optimized for ionic conductivity and mechanical stability. The interaction of the newly degranulated anion receptors was then considered by varying the cations, Mg^{2+} and Li^{+}, as well as the anions, bis(trifluoromethanesulfonyl)imide anion ($TFSI^{-}$) and perchlorate anion (ClO_4^{-}). The salt especially the anion interactions and consequently the electrochemical properties are mainly determined by the electrical properties of the receptor. Therefore, an increasing interaction for the monofluorinated polymer electrolyte was observed as successful anion receptor.

In the third chapter, electrochemical and mechanical properties were investigated as a function of two opposing magnesium salts in an aliphatic polycarbonate. In addition to the commercial and established $Mg(TFSI)_2$, $Mg(B(HFIP)_4)_2$, which has already been used in the literature in cyclic stable magnesium batteries, was also explored. A transformation from a salt-in-polymer electrolyte to a polymer-in-salt electrolyte was demonstrated by rheological and spectroscopic measurements for $Mg(B(HFIP)_4)_2$ at high salt concentrations up to 40 mol%. The polymer-in-salt electrolyte was characterized by a significantly increased ionic conductivity and high mechanical elasticity. It was shown that the concentration of the salt at which the transition to the polymer-in-salt electrolyte occurs is clearly dependent on the properties of the salt and its polymer coordination.

In summary, trends and interrelationships of polymer electrolytes, single ion electrolytes and magnesium-lithium hybrid electrolytes for magnesium accumulators were discussed and classified. This is of special interest, as the development of lithium-free energy storage systems is necessary due to the limited amounts of raw materials and increasing demand.

Zusammenfassung

Akkumulatroren sind von entscheidender Bedeutung hinsichtlich der Elektrifizierung unserer Gesellschaft mit einer Vielzahl an beweglichen elektrischen Geräten. Insbesondere Lithiumakkumulatoren standen im Fokus der Forschung, da diese über eine hohe Leistung und Lebensdauer verfügen. Die vergleichsweisen hohen Rohstoffkosten für Lithium sind jedoch von großem Nachteil, insbesondere im Bereich der fortschreitenden Elektrifizierung unserer Gesellschaft, weshalb die Entwicklung von anderen, günstigeren Akkumulatoren im Vordergrund steht. Eine mögliche Alternative sind Magnesiumakkumulatoren, aufgrund der deutlich höheren Verfügbarkeit von kostengünstigem Magnesium im Vergleich zu Lithium. Wiederaufladbare Magnesiumakkumulatoren beinhalten des Weiteren in vielen Fällen korrosive, giftige, flüssige und flüchtige Elektrolyte, welche dem Sicherheitsaspekt gegenüberstehen.

Ein Lösungsansatz, beinhaltet Polymerelektrolyte anstelle der kommerziellen Flüssigelektrolyten, eine Strategie, die bereits erfolgreich in Lithiumakkumulatoren angewandt worden ist. Die kostengünstige Verfügbarkeit, herausragenden mechanischen Eigenschaften und gute Verarbeitbarkeit stehen jedoch weiterhin einer geringen Zyklenstabilität als auch moderaten Magnesium-Ionen Ionenleitfähigkeiten und hohen Abscheidungspotentialen gegenüber. Dazu gehörige Lösungsansätze sind bereits für Lithiumakkumulatoren bekannt und umfassen neben Weichmachern, Zusätzen und Polymer-Mischungen auch Einzel-Ionen Leiter und Polymer-in-salz Elektrolyte.

Daher beschäftigt sich diese Dissertation mit verschiedenen Ansätzen und Synthese von selbststehenden Polymerelektrolyten und deren Charakterisierungen hinsichtlich Ionenkoordination, Ionenleitfähigkeit und Magnesium Elektroden Kompatibilität.

Im ersten Ansatz wurde eine Bibliothek selbststehender, quervernetzer Einzel-Ionen Elektrolyte, basierend auf Boraten und einem PEO-basiertem Copolymer hergestellt. Hierbei wurden die Parameter hinsichtlich des Monomer Verhältnisses, der Architektur, Weichmacher und PEO-Kettenlänge optimiert. Basierend auf dem besten System wurden unterschiedliche Magnesium-Lithium Hybrid Elektrolyte hergestellt, in denen teilweise Magnesium Ionen gegen Lithium-Ionen ausgetauscht wurde. Dabei deutete sich ein komplexes, Stromstärken abhängiges, Magnesium Abscheidungs- und Aufnahme verhalten ab. Diese Beobachtungen wurden in Zusammenhang mit der Ionendissoziation, Kristallinität und Ionenleitfähigkeit interpretiert und liefern wichtige Erkenntnisse zu Einzelionenleitern und Hybridelektrolyten für Magnesiumakkumulatoren.

Im zweiten Ansatz wurde eine Bibliothek feststehende Polymerelektrolyte mit Anionrezeptoren, als Alternative zu Einzel Ionen Elektrolyten hergestellt. Dazu wurden zwei neue auf Boraten-basierte Monomer mit mono- und difluorierten Aromaten entwickelt und mit PEGMA zu Kamm-polymeren polymerisiert. Die Architektur, Monomer Verhältnisses und Salzkonzentration wurde hinsichtlich ihrer Ionenleitfähigkeit und mechanischen Stabilität hin optimiert. Die Wechselwirkung der neu designten Anionrezeptoren wurde daraufhin betrachtet, indem die Kationen, Mg^{2+} und Li^{+}, als auch die Anionen, $TFSI^{-}$ und ClO_4^{-}, variiert wurden. Die Salz- und insbesondere Anionen-Wechselwirkungen und damit einhergehend die elektrochemischen Eigenschaften sind hauptsächlich bedingt durch die elektrischen Eigenschaften des Rezeptors. Daher wurden wichtige Erkenntnisse bezüglich Anionenrezeptoren in Magnesiumakkumulatoren und deren Design geleistet.

Im dritten Ansatz wurden elektrochemische und mechanische Eigenschaften in Abhängigkeit von zwei gegensätzlichen Magnesiumsalzen in einem aliphatischen Polycarbonat untersucht. Hierzu wurden neben dem kommerziellen und etablierten $Mg(TFSI)_2$ auch $Mg(B(HFIP)_4)_2$ verwendet, das in der Literatur bereits in zyklenstabilen Magnesiumakkumulatoren Anwendung fand. Dabei wurde eine Transformation von einem Salz-in-Polymer Elektrolyten zu einem Polymer-in-Salz Elektrolyten mittels rheologischer und spektroskopischen Messungen für $Mg(B(HFIP)_4)_2$ bei hohen Konzentrationen nachgewiesen. Das Polymer-in-Salz Elektrolyte zeichnete sich dabei durch eine deutlich erhöhte Ionenleitfähigkeit und hoher mechanischer Elastizität aus. Hierbei wurde gezeigt, dass die Konzentration des Salzes, an dem der Übergang zum Polymer-in-Salz Elektrolyten stattfindet, deutlich von den Eigenschaften des Salzes und dessen Polymer Koordination abhängig ist.

Zusammenfassend wurden Trends und Zusammenhänge von Polymer Elektrolyten, Einzel-Ionen Elektrolyten und Magnesium-Lithium Hybrid Elektrolyten für Magnesiumakkumulatoren diskutiert und eingeordnet. Dies ist von gesondertem Interesse, da die Entwicklung von Lithium-freien energiespeichern auf Grund der begrenzten Rohstoffmengen und steigendem Bedarf notwendig ist.

Table of Content

Introduction

1.1 Lithium-Ion batteries

The increasing demand for electrical energy as power source for portable electronics, such as phones, electric vehicles (EVs), requires power storage in small, portable units.[1,2] Because of their high energy density, batteries based on "Galvanic cells" remain a key technique compared to other more pioneer approaches like solar panels or hydrogen fuels.[3,4] Lithium-ion batteries (LIBs) are the most common batteries since Sony corporation introduced their LIBs in the 1990.[3,5]

LIBs distinguish through a high cycle stability, high gravimetric capacity of about 300 Wh kg^{-1} and high potential.[6] Thus, the demand for LIBs in particular for EVs is increasing substantially since 2000s. In 2017 the number of sold EVs in the world increased about 50% to about 1.1 million and is expected to further increase to 2030.[7,8] The working principle of LIBs initially described by Allessandro Volta in the eighteenth century.[9] LIBs are constructed by three main components anodes, cathodes and electrolyte in between those but could also include separators (Figure 1).

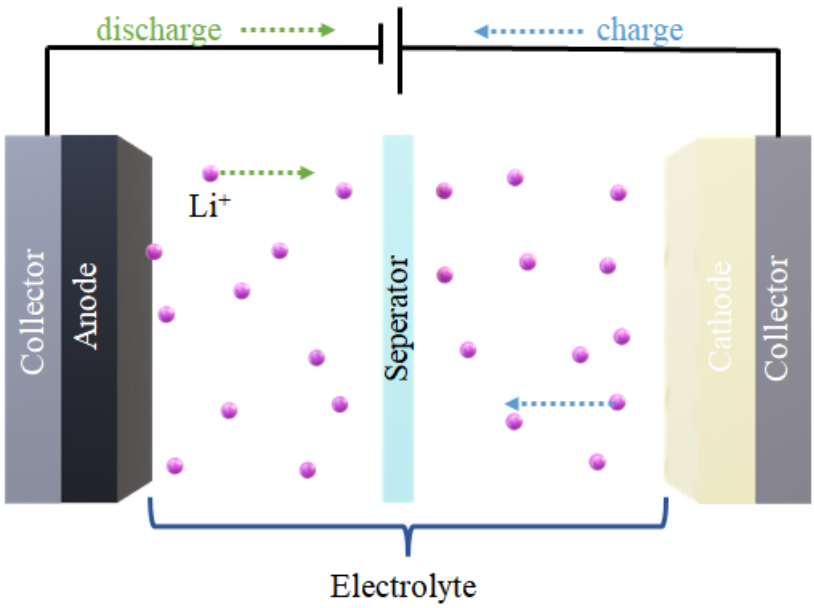

Figure 1:Schematic illustration of the working principle of LIBs.

During the discharge process lithium cations are shuttling from the anode through the electrolyte and separator to the cathode, whereas in the charging process the lithium cation moves from the

cathode to the anode. To maintain electrical neutrality, electrons move contrary to the lithium cations through an external circuit at the same time. Therefore, the electrolyte has to be only an ionic conductor but not an electrical conductor. The driving force of a battery is related to the potential differences between the anode and cathode.[10]

Today´s most common anodes are graphite and $Li_4Ti_5O_{12}$ (LTO), whereas for cathode materials $LiCoO_2$ (LCO), $LiMn_2O_4$ (LMO), $LiFePO_4$ (LFP), $Li(Ni_xMn_yCo_{1-x-y}O_2)$ ($0 \leq x \leq 1$, $0 \leq y \leq 1$ and $x + y \leq 1$) (NMC) and lithium metal oxides (LMO_2) and (LMO) were established.[11,12] Theoretically, the anode material with the highest theoretical capacity (3860 mAh g^{-1}) is metallic lithium, expressing an increased energy density compared to graphite.[13] Another benefit would be the kinetic stability of lithium in aprotic electrolytes by the formation of a solid electrolyte interphase (SEI) on the surface. The SEI is a degradation product of lithium and the electrolyte with ideally permeable Li^+ properties.[14] Nevertheless, the formation of random dendritic growth throughout the cycling process is a major drawback because the dendritic growth can connect anode and cathode when penetrating the separator, which leads to short curcuits.[15] This dendrite growth can be supressed by either surface modifications or solid electrolytes by its mechanical stability (SEs).[16–18]

Established electrolytes generally consist off an aprotic organic solvent, for example ethers, carbonates or esters and a lithium source.[19] While they perform with high ionic conductivities, disadvantages include poor capacity efficiency, dendritic morphology, toxicity and low boiling point.[20] On one hand, the limited safety of LIBs are major drawbacks. On the other hand, the limited abundance of lithium limits LIBs future applications, due to the increasing demand of low-cost batteries. In order to achieve wide scale vehicle electrification, post-lithium materials get in focus of researchers including potassium, sodium or magnesium batteries.[21–23]

1.2 Magnesium-Ion batteries

After Gregory *et al.* constructed a Mg||Cu battery, ongoing research activities focus on magnesium-ion batteries (MIBs) as an alternative to their lithium-based counterparts.[24] The higher abundancy of magnesium compared to lithium in the earth´s crust (approximately 2.1%, which is 104 times higher than of lithium metal) makes magnesium easier accessible at lower costs.[25] Furthermore, the redox process of Mg to Mg^{2+} provides two electrons instead one compared to lithium. This increases the theoretical capacity to 3866 mAh cm^{-3} calculated equation Eq. 1, where *n* is the numbers of electrons, *F* is the Faraday´s constant and *M* the molecular weight.

$$Q = \frac{nF}{M}\frac{1}{3600} \qquad \text{Eq. 1}$$

Moreover, magnesium metal anodes provide less dendrite growth compared to lithium metal anodes, due to lower magnesium diffusion barriers.[26] The potential of Mg vs. SHE is with -2.4 V (lithium is -3 V vs. SHE) higher than for other divalent metals as Zn or Al.[27] Nevertheless, MIBs drawbacks are the formation of passivation layers on the magnesium metal anodes and cathodes surface by its reductive nature. The high potential for cathode de/-intercalation, and lower ionic conductivity in electrolytes was mainly traced back to the small cation size and high charge density.[28]

Magnesium anodes provides, similar to LIBs, the highest capacities and thus are the holy grail in MIBs but are limited by the formation of a magnesium non-conductive passivation layer for many solvent-magnesium salt systems.[29] As for lithium metal anodes, magnesium metal anodes can react with the salt-containing aprotic electrolytes, leading to decomposition products on the electrode surface, which hinders a reversible magnesium plating and stripping.[30] In particular, the formation of organic decomposition products seems to reduce the cycle abilities as indicated by Dou and coworkers in 2021.[31] They prepared an organic and inorganic rich magnesium surface and tested them by constant current deposition experiments. To overcome the formation of passivation layer without pre-treatment Connor *et al*. investigated in 1957 Grignard-based electrolytes, which showed deposition of metallic magnesium with limited thickness.[32] Since then, Grignard reagents were known not to passivate magnesium electrodes, but to enable reversible cycling.[33] In 2000, Aurbach *et al.* published a reversible plating stripping behaviour for a 2 M BuMgCl in tetrahydrofuran (THF). In addition, a superior stripping plating behaviour for a 0.25 M $Mg(Al_2BuEt)$ in THF was found, constructing a reversible MIB with $Mg||Mg_xMo_3S_4$ ($0 < x < 1$) electrodes with a maximum capacity of 122 mAh g^{-1}. Since then, various reversible MIBs based

on Grignards and aluminiumorganyls have been reported.[28,34] In 2008, reversible intercalation of Mg^{2+} into a Chevrel phase cathode ($Mg_xMo_6S_8$) was reported for an $PhMgCl)_2$-$AlCl_3$ electrolyte in THF expressing 80% of the theoretical capacity.[35] Although those systems enable reversible magnesium de-/position, Grignard reagents and Lewis acids are less compatible with metallic cases, which leads to corrosion.[36] Further drawbacks are their high toxicity and reduced safety, which limits their applications especially in mobile electrical devices.

Other approaches include $MgCl_2$ and/or other chlorine containing additives to enable reversible cyclizations.[37,38,39] Doe *et al.* reported on a studied $MgCl_2$-$AlCl_3$ (2:1 ratio) electrolyte in dimethyl ether (DME) coulombic efficiencies of 99% and deposition overpotentials of < 200 mV.[40] Furthermore, Lia *et al.* reported $Mg_xMo_6S_8$ cells with high reversible capacities and rate capabilities with a $MgCl_2$:$Mg(HMDS)_2$:THF electrolyte.[41] The addition of tetrabutylammonium chloride (TBAC) was also found to improve the cycle stability to over 200 cycles at 0.5 mA cm^{-2}.[42] The enhanced cycle stability was explained by the adsorption of Cl^- on the anode surface, reducing decomposition side reactions on the surface and within the growth of a passivation layer.[43] Furthermore, Cl^- anions support the intercalation of Mg^{2+} into Chevrel phase cathodes by reducing the activation barrier of the charge-transfer process.[44]

Although $MgCl_2$ is less corrosive than $AlCl_3$-derivatives, chlorine-containing electrolytes still suffer from safety aspects due to corrosion.[45] Therefore, Cl^--free electrolytes were investigated.[46–48] Borohydrides as additives or salts prevented surface passivation by their strong reductive nature.[27,43] As for the Grignard-based electrolytes, Connor *et al.* pioneered with $Mg(BH_4)_2$ in magnesium electrolytes, where the deposited magnesium contained traces of boron (about 9 wt.%).[32] An additional benefit is the overall weak interaction between Mg^{2+} and BH_4^- combined with a high ion dissociation.[32] Instead of THF, the ion interaction was suppressed with DME to enhance the electrochemical performance.[49] In 2022, Kristensen *et al.* reported ionic conductivities of 2.7 10^{-4} S cm^{-1} at 45 °C for $Mg(BH_4)_2$-1.5$(CH_3)_2CHNH_2$ electrolytes with activation energies of E_a = 122 eV.[50] Further boron-based electrolytes are organoborane and fluorinated organoborates ($Mg(B(HFIP_4)_2$.[48] $Mg(B(HFIP)_4)_2$ was in focus due to its high ion dissociation but also high stability of $B(HFIP)_4^-$ counter anion against metallic magnesium, indicated by theoretical calculations.[51] In particular, $Mg(B(HFIP)_4)_2$ was tested extensively against sulfur cathodes in magnesium-sulfur (Mg-S) batteries were high coulombic efficiencies and cycle stability were shown.[46,52] Depending on the starting material such as $Mg(BH_4)_2$ or $MgBu_2$, the synthetic process also seems to have also an significant effect on the overall performance and reproducibility.[48] For the aluminium homologous $Mg(Al(HFIP)_4)_2$ a reversible Mg decomposition for over 50 cycles with high

coulombic efficiencies were reported. Herein, its higher compatibility with water (1000 ppm) were shown, although $Mg(Al(HFIP)_4)_2$ was reported to be more water instable than $Mg(B(HFIP)_4)_2$.[53,54]

Other concepts for reversible magnesium plating/stripping are magnesium dual-salt or magnesium hybrid ion batteries (MHBs), where in addition to a magnesium source Li^+ or Na^+ were incorporated. Next to the magnesium deposition on the anode side, mainly lithium or sodium deposition takes place on the cathode side (Figure 2).[55] Hereby, the advancements of magnesium metal electrodes, reduced dendrite growth and increased safety as well as lithium cathodes benefits, such as fast reversible lithium re-/intercalation cathodes, were combined.[56] Magnesium-lithium hybrid batteries (MLHBs) were tested with several cathode materials e.g. $LiFePO_4$ by Yagi *et al.* or TiS_2 by Yao *et al.*.[57,58] Furthermore, Du and coworkers reported a Mg||Cu cell setup with $Li(B(HFIP)_4)_2$/DME electrolyte that exhibited Li-species containing SEI on the magnesium anode surface, enabling reversible stripping/plating.[59] Further reports incorporated sodium for magnesium-sodium hybrid batteries (MSHBs).[60] Disadvantages of magnesium hybrid batteries are the large quantities of electrolyte that are needed to provide enough Li^+ and Mg^{2+} during the redox reactions.[56] In addition the anodic stability of the magnesium electrolyte was reduced as reported for $LiBH_4$ in all-phenyl complex.[58]

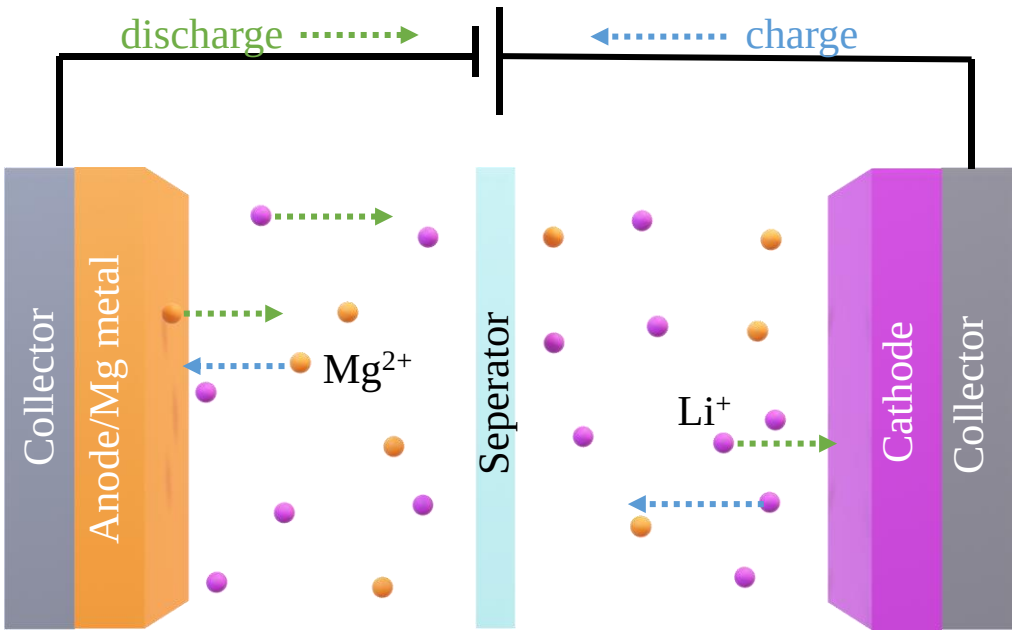

Figure 2: Schematic illustration of the working principle of a Mg-Li hybrid battery.

However, many employed electrolytes are liquid electrolytes, which typically are highly flammable organic aprotic solvents such as cyclic/aliphatic carbonates, short chain glycol ethers or

aliphatic esters. This could lead, in case of battery demolition, to leaks and inherent dangers of (bio)safety. To overcome those issues, alternative battery systems without flammable liquids e.g., solid electrolytes (SE) have been investigated and will be discussed in the following.

The first class of SE are ceramic oxides ($A_xM_y(XO_4)_3$), chalcogenides or metal-organic frameworks (MOFs) and polymer electrolytes (PEs).[25] Sulaiman *et al.* reported for $Mg(NO_4)_2$-$x$$Al_2O_3$ and $Mg(NO_3)_2$-xMgO composites Mg^{2+} ionic conductivities of 4 10^{-4} and 10^{-6} S cm^{-1}.[61,62] For a NASICON-type conductor $(Mg_xFH_{1-x})_{4/(4-2)}Nb(PO_4)_2$ ($0.05 \leq x \leq 0.3$) ionic conductivities of 2.1 10^{-6} S cm^{-1} at 400 °C were reported.[63] Although some improvements could be achieved in the last years, only moderate ionic conductivities at room temperature were determined, which limits the application of such oxides. Replacement of oxygen with sulfur led to chalcogenides with a weaker bonding strength between sulfur and magnesium and the larger atomic radius providing wider migration tunnels compared to oxides.[25] While lithium-based chalgocinates exhibit an extreme increase in ionic conductivity, only a moderate enhancement was detected for magnesium-based materials. For example, $MgSc_2Se_4$ was reported having an ionic conductivity of 10^{-4} S cm^{-1} at room temperature while having a migration barrier of about 370 mV.[64]

The second class, MOFs, are assembled materials formed by metal ion clusters coordinated to organic compounds in one, two or three dimensions. The porous structure of MOFs may provide high ionic conductivity for various ions.[65] Dinca *et al.* investigated Cu(II)-azolate MOFs coordinated to halides or pseudohalide salts and reported a moderate Mg-ion mobility of 8.8 10^{-7} S cm^{-1}.[66] Furthermore, the isolation of stoichiometric amounts of mobile Mg^{2+} ions in one-dimensional mesopores enabled a single-ion conducting approach. Nevertheless, MOFs show only low electrochemical stability and strong ion pairing, which is still considered a major challenge to overcome.

The third class of SE are polymer-based electrolytes. Here, usually magnesium salts are incorporated into a polymer matrix, which resulted in a good contact with the electrode surface due to its high flexibility and an easy processability compared to liquid electrolytes.[27,67] Their comparably low costs and large electrochemical window makes polymer-based electrolytes an attractive alternative to liquid electrolytes, ceramics and MOFs and will be further discussed in the following chapter.[68]

1.3 Polymer electrolytes

Polymer electrolytes (PEs) are a well-established class of materials for LIBs and are of interest for researchers over decades.[69] Due to the limitations of LIBs, such as low abundance, dendrite growth and reduced safety, PEs represents a potential alternative for MIBs because of their increased safety.[67] Polymer-based electrolytes for MIBs are classic salt-in polymer electrolytes consisting of an uncharged polymer matrix with incorporated magnesium salts and feasible additives. If the magnesium salt content is dominant in the polymer-based electrolyte (above 50 wt.%), it is often called polymer-in-salt electrolyte (PISE) and differs in its ion conductivity mechanism.[69] Another class are single-ion conductors (SICs), which are based on negatively-charged polymer matrixes with Mg^{2+} as cations. A schematic illustration of PEs, PISE and SICs is given in Figure 3 and will be discussed below.

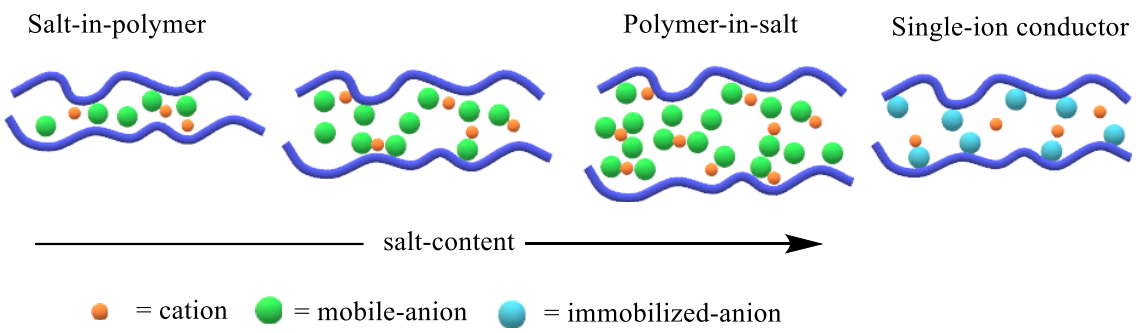

Figure 3: Schematic illustration of salt-in-polymer electrolytes, single-ion conductors and polymer-in-salt electrolytes. Reproduced with permission from ACS Omega, in press. Unpublished work copyright 2023 American Chemical Society.

1.3.1 Salt-in-polymer electrolytes

Salt-in-polymer electrolytes or (PEs), consists in most cases of an uncharged polymer matrix with incorporated magnesium source and can contain various additional additives, including plasticizers, ionic liquids (ILs) or fillers. Depending on the type of additives PEs can be classified by solid-polymer electrolytes (SPEs), gel-polymer electrolytes (GPEs), gel-composite polymer electrolytes (GCPEs) or gel-gel-polymer electrolytes (GGPEs).[69,70] Classification beyond physical state are additive or polymer structure related as schematically shown in Figure 4.

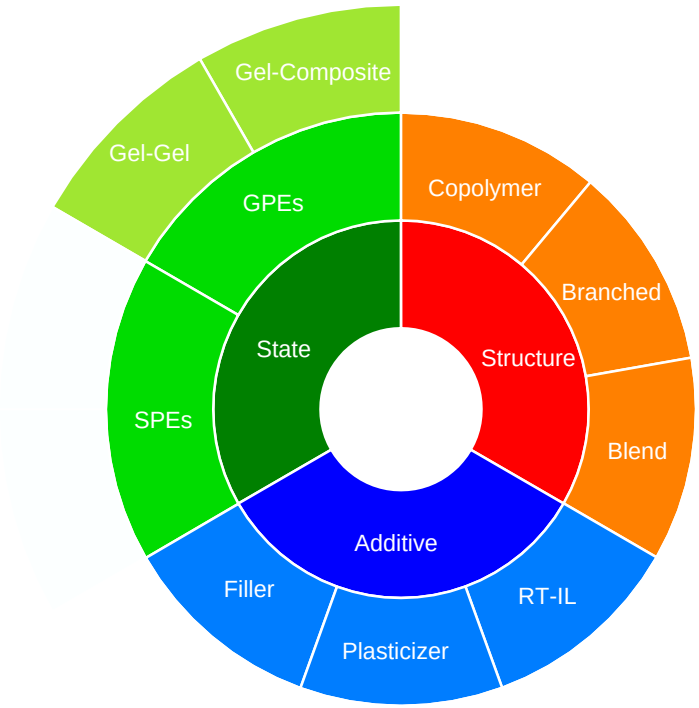

Figure 4: Schematic representation of the classification of polymer electrolytes.

SPEs summarize typically additive-free PEs or PEs containing inorganic fillers, whereas GPEs contains mostly IL, plasticizers or solvents. A comprehensive overview about their advantages and disadvantages compared to liquid organic electrolytes (LOE) are given in Table 1.

Table 1: List of SPEs and GPEs properties compared to organic liquid electrolytes.

	LOE	**GPEs**	**SPEs**
Ionic conductivity	High	Medium	low
Electrochemical stability	Low	Low	High
Thermal stability	Low	Low	High
Dimensional stability	Low	Medium	High
Electrode surface contact	High	Medium	Low

SPEs exhibit large electrochemical stability, thermal stability and safety, but are limited in regards to ionic conductivity and electrode contact.[25] GPEs have moderate ionic conductivities, dimensional stability and interfacial contact but show insufficient thermal and electrochemical stability. Lastly, organic liquid-based electrolytes (LOE) show comparable high ionic conductivity and good electrode contact but are limited in safety aspects and thermal/dimensional stability.

Therefore, the choice of electrolytes demands on the battery applications, but improved SPEs have the potential for future applications.

Solid polymer electrolytes

Reports on additive-free SPEs include various synthetic polymers as PEG, polyvinyl alcohol (PVA) and polyvinylpyrrolidone (PVP), respectively (Scheme 1).[71,72]

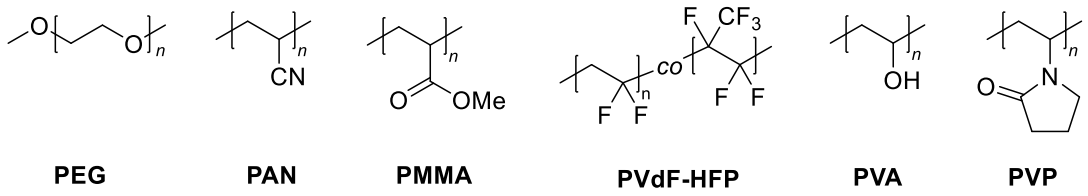

Scheme 1: Polymer structure of selected synthetic polymers used as PEs in MIBs.

Natural biopolymers further extend the scope and were tested for MIBs, for example I-carrageenan, tamarind seed polysaccharide (TSP), pectin, cellulose acetate, methyl cellulose, chitosan and agar.[72–81] In contrast to PEG, pectin was reported to have high ionic conductivities and moderate t^{+}_{Li}. Kiruthika *et al.* reported for pectin with $Mg(NO_3)_2$ and $MgCl_2$ ionic conductivities of about 10^{-3} to 10^{-4} S cm^{-1} at RT and t^{+}_{Li} of about 0.3, respectively.[72,73] Alves and coworkers reported a reversible magnesium de-/solvation, constructing a WO_3||agar||CeO_2-TiO_2 cell.[81] independent on synthetic or natural polymers. Therefore, the polymer matrix is not limited to a single polymer but could also include polymer blends as well as copolymers. The polymers matrix ratios are used to balance the ratio of ionic conductive and functional segments or to design dynamic inter-molecular forces, which enhance the electrolytes ionic conductivity.[70] Polymer blends can be prepared from polyacrylonitrile (PAN), poly(3,4-etylenedioxythiophene) (PEDOT), corn silk extract or poly(styrenesulfonate) (PSS).[82,83,84] Anilkumar and coworkers reported a reversible behavior by incorporating $Mg(NO_3)_2$ in PVP and PEG, when using V_2O_5 or MnO_2 cathodes.[85] The most prominent copolymers is PVDF-HFP, due to its high ionic conductivity, which was reported to be about 10^{-3} S cm^{-1} at 80 °C.[86] The high ionic conductivity was traced back to its high dielectric constant, low crystallinity and glass-transition temperature.[87]. An overview of publications, which deals with additive-free SPEs and their reported ionic conductivity, transference numbers and cell characteristics are given in Table 2.

Table 2: Summary of additive-free SPEs in MIBs. Room temperature = RT, - = no parameters mentioned.

Polymer host	Mg salt	Ionic Conductivity [Scm^{-1}]	t^{+}_{Mg}	Cell characteristics	References
PEO	$Mg(ClO_4)_2$	$1.42\ 10^{-6}$	-	-	71
PEO	$MgCl_2$	$\approx 10^{-9}$ (RT)	-	-	88
PEO	$Mg(NO_3)_2$	$1.34\ 10^{-5}$	-	Discharge characteristics Mg‖C	89
PEO	$Mg(ClO_4)_2$	$1.42\ 10^{-6}$ (25°C)	-	-	90
PEO	$Mg(ClO_4)_2$	$10^{-5} – 10^{-6}$ (30°C)	-	-	91
PEO	$MgTf_2$	$\approx 10^{-6}$ (RT)	-	-	92
PVA	$Mg(AcO)_2$	$1.34\ 10^{-7}$ (30°C)	-	Discharge characteristics Mg‖(I_2+C)	93
PVA	$MgTf_2$	$5.41\ 10^{-4}$	-	-	94
PVA	$Mg(NO_3)_2$	$7.36\ 10^{-7}$ (30°C)	-	Discharge characteristics Mg‖(I_2+C)	95
PVP	$MgSO_4$	$1.05\ 10^{-5}$ (RT)	-	Discharge characteristics Mg‖(I_2+C)	96
PEC	$Mg(TFSI)_2$ $Mg(ClO_4)_2$	$5.2\ 10^{-5}$ (90°C) $6.0\ 10^{-6}$ (90°C)	-	-	97
I-carrageenan	$Mg(ClO_4)_2$	$2.18\ 10^{-3}$ (30°C)	0.31	Discharge characteristics Mg‖MnO_2	78
TSP	$Mg(ClO_4)_2$	$5.66\ 10^{-4}$ (RT)	-	-	98
Pectin	$Mg(NO_3)_2$	10^{-4} (RT)	0.29	Discharge characteristics Mg‖MnO_2	73
Pectin	$MgCl_2$	$1.4\ 10^{-3}$ (RT)	0.31	Discharge characteristics Mg‖MnO_2	72
Cellulose acetate	$Mg(ClO_4)_2$	$4.05\ 10^{-4}$ (RT)	0.31	Discharge characteristics Mg‖MnO_2	75
Cellulose acetate	$Mg(NO_3)_2$	$9.19\ 10^{-4}$ (RT)	0.35	Discharge characteristics Mg‖MnO_2	74
Cellulose acetate	$Mg(ClO_4)_2$	$7.79\ 10^{-4}$ (RT)	-	-	99
Methyl cellulose	$Mg(NO_3)_2$	$1.02\ 10^{-4}$ (RT)	-	-	77
Chitosan	$MgTf_2$	$\approx 10^{-4}$ (RT)	-	-	79
Agar	$MgTf_2$	$1\ 10^{-6}$ (30°C)	-	Reversibility of WO_3‖CeO_2-TiO_2	81
PVdF-HFP/PVAc	$Mg(ClO_4)_2$	$1.6\ 10^{-5}$ (30°C)	-	-	87
PVdF/PEO	$Mg(TFSI)_2$	$1.2\ 10^{-5}$ (25°C)	-	-	100
PMMA:PVdF	$Mg(ClO_4)_2$	$1.89\ 10^{-4}$	-	-	101

Polymer host	Mg salt	Ionic Conductivity [Scm^{-1}]	t^{+}_{Mg}	Cell characteristics	References
PVA:PVP	$MgCl_2$	9.358 10^{-4} (70°C)	-	-	102
PVA:PAN	$Mg(NO_3)_2$	1.71 10^{-3} (RT)	0.30	Discharge characteristics Mg‖MnO_2	82
PVA:PEO	$Mg(OAc)_2$	7.44 10^{-8} (30°C)	-	Discharge characteristics Mg‖(C+I_2)	103
PVA:PEO	$Mg(NO_3)_2$	9.63 10^{-5} (30°C)	-	-	104
PVA:PAN	$Mg(ClO_4)_2$	2.94 10^{-4} (30°C)	-	Discharge characteristics Mg‖MnO_2	105
PVA:PAN	$MgCl_2$	1.01 10^{-3} (30°C)	-	Discharge characteristics Mg‖MnO_2	106
PVA:PVP	$Mg(ClO_4)_2$	1.1 10^{-4} (30°C)	-	-	107
PVA:Corn Silk Extracte	$MgCl_2$	1.28 10^{-3} (30°C)	0.32	Discharge characteristics Mg‖MnO_2	84
PVA:PE-DOT:PSS	$MgBr_2$	9.8 10^{-6} (RT)	-	-	83
PVP:PEO	$Mg(NO_3)_2$	5.8 10^{-4} (RT)	0.33	Reversibility of Mg‖$MgMn_2O_4$	85
PVdF-HFP	$MgTf_2$	≈ 10^{-3} (80°C)	-	-	86
P(VdCl-co-AN-co-MMA)	$Mg(NO_3)_2$	1.6 10^{-4} (RT)	0.36	Discharge characteristics V_2O_5‖Mg and MnO_2‖Mg	108
P(VdCl-co-AN-co-MMA)	$MgCl_2$	1.89 10^{-5} (RT)	-	-	109
PEGDE-(PEO-PMA)	$Mg(TFSI)_2$, $MgTf_2$, $Mg(ClO_4)_2$	≈ 10^{-4}	-	-	110
PPEGMAm-b-SPB	$Mg(TFSI)_2$	≈ 10^{-4} (60°C)	-	-	111

Due to the overall low ionic conductivity, additive-free SPEs were further improved by the addition of nanosized fillers, also called nanosized-composite polymer electrolytes (NCPEs). The enhanced ionic conductivity of NCPEs was explained by the Lewis acid-base interaction between the surface and the migrating ions, resulting in additional jumping sites and favorable ion motion pathways.[112] In addition, a decrease in crystallinity and therefore glass-transition temperature (T_g) was found, which decreased the activation energy for ion transport by segmental motion.[113] Thus, nanosized particles are more efficient than macroscopic particles.[114] Reported NCPEs for MIB applications are CeO_2, TiO_2, MgO, Al_2O_3, SiO_2, B_2O_3, V_2O_3, $MgAl_2O_4$ and $MgTiO_3$.[113–123] Fillers

can further be subdivided into active (e.g. TiO_2) and passive fillers (e.g. MgO).[114,115] Hashmi and coworkers reported an improvement of mechanical strength for both, active and passive filler, but only a significant effect on t^+_{Mg} for the active filler.[115] Reversible charge and discharge experiments were reported by Ponmani and colleague in 2020 for a PVdF-HFP:PVAc:$Mg(ClO_4)_2$:$MgTiO_3$ (69:23:8:6 wt.%) NCPE a transference numbers of 0.34.[124] The corresponding Mg||Mo_6S_8 cell performed with a high discharge coulombic efficiency of 98% after 40 cycles and with a first discharge capacity of 116 mA h g^{-1} at 0.5 C. Further NCPEs and their performance in MIB applications is collected in Table 3.

Table 3: Summery of SPEs containing fillers in MIBs. Room temperature = RT, - = no parameters mentioned.

Filler	**Polymer host**	**Salt**	**σ [Scm^{-1}]**	**t^+_{Mg}**	**Cell characteristics**	**Refs**
CeO_2	PEO	$Mg(OAc)_2$	3.4 10^{-6} (30°C)	-	Discharge characteristics Mg||(I_2+C+electrolyte)	125
TiO_2	PEO	$Mg(OAc)_2$	5.01 10^{-5} (30°C)	-	Discharge characteristics Mg||(I_2+C+electrolyte)	126
MgO	PEO	$MgSO_4$	3.63 10^{-3} (RT)	-	-	119
MgO	PVdF	$Mg(NO_3)_2$	1.04 10^{-4}	-	-	127
MgO	PEO	$Mg(BH_4)_2$	-	-	Intercalation/deintercalation characteristics Mg||Mo_6S_8	128
MgO TiO_2 SiO_2	PEO	$Mg(TFSI)_2$	1.67 10^{-5} 1.53 10^{-5} 5.86 10^{-6}	0.38 0.37 0.31	-	114
Al_2O_3	PVP	$MgCl_2$	1.22 10^{-6} (30°C)	-	Discharge characteristics Mg||(I_2+C+electrolyte)	117
Al_2O_3	PEO	$Mg(ClO_4)_2$	≈ 10^{-5} (30°C)	-	-	112

Filler	Polymer host	Salt	σ [Scm^{-1}]	t^{+}_{Mg}	Cell characteristics	Refs
B_2O_3	PEO	$MgCl_2$	7.16 10^{-6} (30°C)	-	Reversibility of Mg||MnO_2	113
V_2O_3	Chitosan	$MgCl_2$	1.4 10^{-3}	-	Discharge characteristics Mg||MnO_2	123
$MgTiO_3$	PVdF-HFP:PVAc	$Mg(ClO_4)_2$	5.8 10^{-3} (30°C)	0.34	Charge/discharge characteristics Mg||Mo_6S_8	124

Gel-polymer electrolytes

Due to their liquid character, GPEs exhibit higher ionic conductivities compared to SPEs. Liquid non-charged organic compounds, known as plasticizers, or alternatively charged organic compounds as IL, have been successfully incorporated (Scheme 2A). IL are characterized by strongly delocalized cations and anions, which lead to a melting temperature (T_m) below room temperature. Their advantages are the low flammability, negligible vapor pressure and wide electrochemical window.[129] The most frequently used cation in IL is 1-ethyl-3-methylimidazol (EMI). Other ILs as 1-butyl-3-methylimidazolium chloride (BmImCl),[130] BmImBr,[131] choline nitrate,[132] tetrabutylammonium chloride (TBACl),[133,134] *N*-butyl-*N*-methylpyrrolidinium bis(trifluoromethyl)sulfonylamide (MBPyrTFSI)[135–137] and PEGlated *N*-methylpyrrolidinium bis(trifluoromethyl)sulfonylamide (MPEG$_x$PyrTFSI)[135] have also been studied. Other established anions are bis(trifluoromethane sulfonyl)imide (TFSI$^-$) and bistrifluromethanesulfonate (Tf$^-$).

IL increases the PEs performance, by increasing the ion dissociation, on one hand and on the other hand by reduceing the crystallinity.[138] In 2009 Pandey and Hashmi reported a reversibly plating and stripping process by cyclovoltammetry (CV) for a PVdF-HFP matrix with 0.3 M $MgTf_2$ solution in EMITf.[139] On the contrary, Vila and coworkers examined no correlation between the anion size and ionic conductivity of EMI-X (X=Cl$^-$, Br$^-$, BF_4^-, PF_6^-, ethylsulfate and tosylate) by opposite size effects of surface electrical charge density and dynamical movement, reporting a maximum for BF_4^-.[140] Herein, they observed an increase in ionic conductivity with increasing alkyl chain length of the imidazole. The difference between MBPyrTFSI and MPEG$_x$PyrTFSI with x = 3 and 7 were in focus of Watkins and coworkers, employing $Mg(BH_4)_2$ salt.[135]

$MPEG_xPyrTFSI$ with x = 7 superior electrochemical performance compared to MBPyrTFSI (x = 3) was explained by the high ion dissociation of $TFSI^-$ and Mg^{2+} and by free BH_4^- ions.

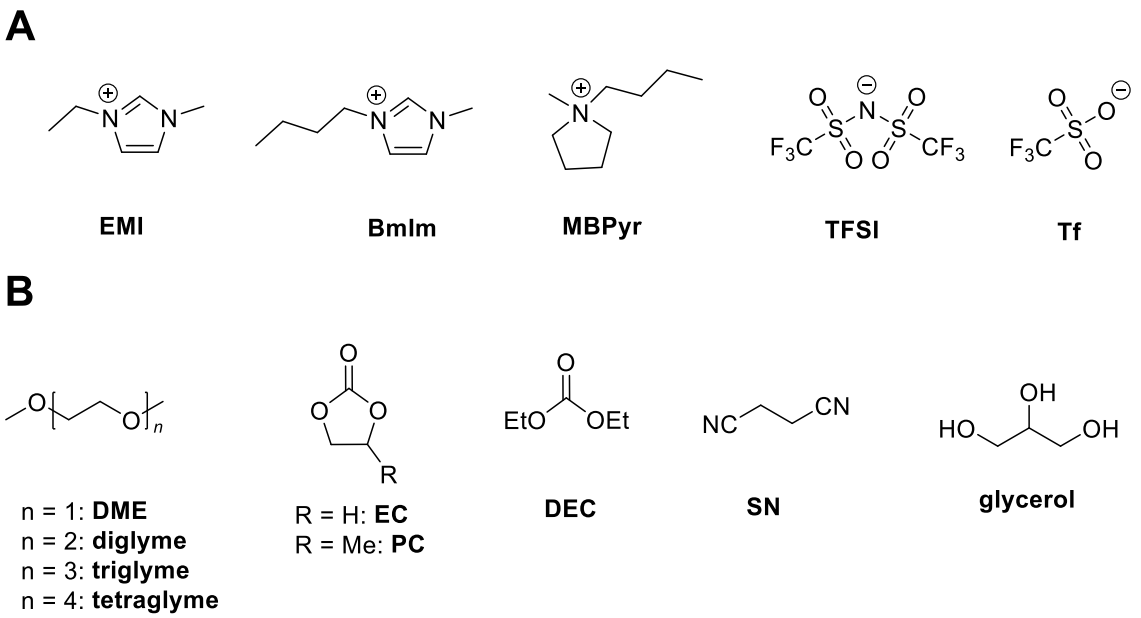

Scheme 2: Chemical structure of A) IL cations and anions and B) plasticizers.

In contrast to IL, plasticizers are uncharged organic compounds expressing high dielectric constants.[84] Plasticizers increase the ion dissociation and reduce the polymer crystallinity similar to IL, which enhance overall the ionic conductivity.[141] Common plasticizers are EC,[115,118,120,142–154] PC,[115,118,120,142–149,153,154] succinonitrile (SN),[150,155–157] tetraglyme,[133,134,157–160] triglyme,[161] 1,2-dimethoxyethan (DME),[162] diethyl carbonate (DEC),[151] glycerol,[130,163] tetrahydrofuran (THF)[164] and urea[165] (Scheme 2B). Carbonates can be further subdivided into cyclic (e.g., PC) and linear carbonates (e.g., EC). For example, PC and EC were tested within a PVdF:$MgTf_2$ matrix and reversible charge/discharge experiments revealed a cyclability of 30 cycles against metal magnesium and MnO_2 electrodes, where discharge capacities of 160, 80 and 50 mA h g^{-1} (for C/8, C/6 and C/4, respectively) were reported.[149] The work of Zainol and coworkers focused on the comparison of $MgTf_2$ and $Mg(TFSI)_2$ in a PVdC-AN copolymer with EC and SN.[150] $Mg(TFSI)_2$ was found to exhibit higher ionic conductivity up to two magnitudes (10^{-7} to 10^{-6} vs. 10^{-8} to 10^{-7}) but lower t^+_{Mg} (0.59 over 0.56) compared to $Mg(ClO_4)_2$. Moreover, measured discharge capacity of 51 to 223 mA h g^{-1} were higher for $Mg(TFSI)_2$, when using Mg and $MgMn_2O_4$ electrodes. Another dominant class of plasticizer are short chain glycol ethers, like tetraglyme or DME. Mesallam and coworkers focused on the performance of a PVDF host, including DME and $MgBr_2$ as plasticizer and magnesium salt.[162] They reported reversible stripping and plating for 20 cycles at 20 µA for an Mg||Mg cell setup, with a gradual increase in overpotential by the formation of a

passivation layer. Further, larger glycol ethers were in focus of Morita *et al.* with polyethylene glycol dimethyl ether (PEGDME) with M_n = 400 g mol^{-1}.[166,167] They employed PEGDME with a crosslinked brush polymer poly(ethylene glycol) monomethyl ether methacrylate (PEGMA), due to a reduced crystallinity compared to linear PEG with increased ionic conductivity. Additional GPEs containing IL or plasticizers are listed in Table 4. Fichtner *et al.* prepared a GPE with $Mg(B(HFIP)_4)_2$ and PTHF with high coulombic efficiencies (99%, 1000 cycles) and ionic conductivities (10^{-3} S cm^{-1}) by implementing THF.[168]

Table 4: Summary of GPEs containing IL or plasticizers in MIBs. Room temperature = RT, - = no parameters mentioned.

Plasticizer/ IL	**Polymer host**	**Salt**	**σ [Scm^{-1}]**	**t^+_{Mg}**	**Cell characteristics**	**Refs**
EC:PC	PAN	$MgTf_2$	2 10^{-3} (20°C)	-	Reversibility of Mg||MnO_2	142
EC:PC	PAN	$MgTf_2$	1.8 10^{-3}	-	-	143
EC:PC	PAN	$MgTf_2$	2 10^{-3} (20°C)	-	-	144
EC:PC	PEO	$MgTf_2$	≈ 10^{-5}	-	-	145
EC:PC	PMMA	$MgTf_2$	4.2 10^{-4} (20°C)	0.55	Reversibility of Mg||MnO_2	146
EC:PC	PMMA	$MgTf_2$ $Mg(ClO_4)_2$	1.27 10^{-3} (RT) 3.13 10^{-3} (RT)	0.4 0.4	-	147
EC:PC	PMMA	$MgTf_2$	1.27 10^{-3} (RT)	-	-	148
EC:PC	PVdF	$MgTf_2$	1.67 10^{-3}	-	-	149
EC:PC	PVdF	MgTf2	3 10^{-3} (26°C)	0.26	-	115

Plasticizer/ IL	Polymer host	Salt	σ [Scm^{-1}]	t^{+}_{Mg}	Cell characteristics	Refs
EC:SN	PVdC	$MgTf_2$ $Mg(TFSI)_2$	$\approx 10^{-8} – 10^{-7}$ $\approx 10^{-7}$ - 10^{-6}	0.56 0.59	Discharge characteristics $Mg\|\|MgMn_2O_4$	150
EC:DEC	PMMA	$Mg(TFSI)_2$	6 10^{-5} (25°C)	0.37	-	151
EC:DMC	PEO-PMMA	$Mg(TFSI)_2$	3 10^{-3} (20°C)	-	Charge/discharge characteristics $MgV_2O_5\|\|V_2O_5$	152
SN	PEO	$MgTf_2$	6 10^{-4} (RT)	-	-	155
SN:tetraglyme	PVdF	$MgTf_2$	$\approx 10^{-5}$	0.4	Charge/discharge characteristic Mg||S	169
Urea	PEO	$MgTf_2$	6 10^{-5}	-	-	165
Glycerol	chitosan	$MgCl_2$	1.03 10^{-3}	-	-	163
THF	PTHF	$Mg(B(HFIP)_4)_2$	10^{-3}	-	Charge/discharge characteristics	168
DME	PVdF	$MgBr_2$	1.2 10^{-6} (RT)	0.55	Galvanostatic measurement	162
PEGDME	P(PEGMA)	$Mg(TFSI)_2$	About 10^{-4}	0.5	-	167
PEGDME	P(PEGMA)	$Mg(TFSI)_2$	0.4 10^{-3} (60°C)	-	Dis-/Charge characteristics MgV_2O_5/ $Mg\|\|V_2O_5$	166

Plasticizer/ IL	Polymer host	Salt	σ [Scm^{-1}]	t^{+}_{Mg}	Cell characteristics	Refs
Tetraglyme	PVA	$MgBr_2$	5 10^{-4} (30°C)	0.34	Discharge for Mg‖V_2O_5 and Mg‖TiO_2	158
Tetraglyme	PVA	$MgBr_2$	1.3 10^{-6} (RT)	-	-	159
Tetraglyme	PVdF-HFP	$Mg(ClO_4)_2$	1.2 10^{-3} (RT)	-	-	160
Triglyme	c-PTHF	$Mg(TFSI)_2$	≈ 10^{-4} (80°C)	-	-	161
EMITf	PVdF-HFP	$MgTf_2$	5 10^{-3} (20°C)	0.26	-	139
EMITf	PVdF-HFP	$MgTf_2$	4.6 10^{-3} (RT)	-	-	170
EMITf	PVA	$MgTf_2$	1.2 10^{-3} (RT)	-	EDLC fabrication	171
EMITf	PVA	$MgTf_2$	2.36 10^{-6} (RT)	-	-	172
EMITf	PEO	$MgTf_2$	≈ 10^{-4} (RT)	-	EDLC fabrication	173
EMITf	PEO	$MgTf_2$	5.6 10^{-4} (RT)	0.45	-	174
EMITFSI	PEO-PMA-PEGDMA	$Mg(TFSI)_2$	1 10^{-4} (20°C)	-	-	175
EMITFSI	PEO-PMA	$Mg(TFSI)_2$	4 10^{-3} (60°C)	-	-	176
BmImBr	PVdF-PAN	$Mg(ClO_4)_2$	3.71 10^{-3}	-	-	131
MBPyrTFSI $MPEG_xPyrTFSI$	-	$Mg(BH_4)_2$	0.38 10^{-3} 0.24 10^{-3}	-	-	135

Plasticizer/ IL	Polymer host	Salt	σ [Scm^{-1}]	t^{+}_{Mg}	Cell characteristics	Refs
MBPyrTFSI	PEO	$MgTf_2$	3.66 10^{-4} (RT)	0.4	Charge/discharge characteristics Mg||TiO_2	[136]
Choline nitrate	chitosane	-	8.9 10^{-3}	-	Mg-air battery	[132]

Gel-composite and gel-gel polymer electrolytes

GCPEs and GGPEs are occasionally employed subclassifications of GPEs and CNPEs. Their characteristics are the implementation of at least two different additives either filler, plasticizer or IL. Combinations of plasticizer and IL are collected as GGPEs and filled with plasticizer/ILs as GCPEs. In both approaches the benefits of fillers, plasticizers and IL, respectively, are combined to further improve the mechanical and electrochemical performance. Deivanayagam and coworkers synthesized a GCPEs based on $MBPyr_{14}$-TFSI, TiO_2, $Mg(ClO_4)_2$ and PVDF-HFP.[137] Cycling tests at 0.05, 0.1 and 0.2 mA cm^{-2} were performed over 100 cycles and at 0.05 mA cm^{-2} for even 400 cycles, which is significant longer compared to other PEs. In 2018 GGPEs, combining SN as plasticizer with EMITf as RTIL, were investigated by Sharma and Hashmi, using PVdF-HFP and $MgTf_2$.[156] This resulted in ionic conductivities up to 4 10^{-3} S cm^{-1} and a discharge capacity of 40 mA h g^{-1} for the first cycle in a MnO_2||Mg cell. A summary of further GCPEs and GGPEs is given in Table 5.

Table 5: Summary of GCPEs and GGPEs in MIBs. Room temperature = RT, - = no parameters mentioned.

Additive	**Polymer host**	**Salt**	**σ [Scm^{-1}]**	**t^{+}_{Mg}**	**Cell characteristics**	**References**
SiO_2:EC:PC	PVdF-HFP	$Mg(ClO_4)_2$	1.1 10^{-2} (RT)	0.3	Charge/discharge characteristics Mg||MoO_3	[153]
SiO_2:EC:PC	PVdF-HFP	$Mg(ClO_4)_2$	3.2 10^{-3}	-	Charge/discharge characteristics Mg||V_2O_5	[120]
MgO:EC:PC	PVdF-HFP	$Mg(ClO_4)_2$	8 10^{-3} (25°C)	0.44	-	[154]
MgO:EC:PC	TPU-PVdF	$Mg(ClO_4)_2$	4.6 10^{-3}	-	-	[118]
Al_2O_3:EC:PC $MgAl_2O_4$:EC:PC	PVdF-HFP	$MgTf_2$	3 10^{-3} (26°C) 4 10^{-3} (26°C)	0.52 0.66	-	[115]
TBACl:tetraglyme	PVdF	$Mg(ClO_4)_2$	4.32 10^{-4}	-	-	[134]
TBACl:tetraglyme	PVdF	$Mg(TFSI)_2$	0.44 10^{-3}	-	-	[133]
Pyr_{14}-TFSI:TiO_2	PVdF-HFP	$Mg(ClO_4)_2$	1.6 10^{-4} (30°C)	0.23	Galvanostatic measurements	[137]
EMITf:SN	PVdF-HFP	$MgTf_2$	4 10^{-3} (RT)	-	Charge/discharge characteristics Mg||MnO_2	[156]
BmImCl:glycerol	Potato starch	$Mg(OAc)_2$	1.12 10^{-5} (RT)	-	-	[130]

1.3.2 Polymer-in-salt electrolytes

PISE differs from PEs by its higher salt content (> 50 wt.%), which lead to a change in ion conductivity mechanism.[69] In PEs the ion conductivity is mainly caused by segmental motion of the polymer host, whereas for PISE several authors have proposed mechanism such as ion transport through percolated ion aggregates (Mishra *et al.*) or by infinite cluster formation of aggregates (Bushkova *et al.*).[177,178] This overall change in mechanism leads to an improved ionic conductivity compared to PEs.[179] As polymer hosts, polymers with low T_gs such as PEC or PAN-based materials have been reported for lithium ion batteries.[179–181] To the best of my knowledge PISE were not mentioned in MIB related literature but are still of high interest for the present work.

1.3.3 Single-ion conductors

Single-ion conductors (SICs) are mostly designed by polymer matrixes with covalent bonded anions and mobile Mg^{2+} as counter ions. Similar to PEs, additives such as fillers, plasticizers or IL were established to improve the overall electrochemical performance. Due to the immobilized anion, Mg^{2+} mobility is mainly responsible for the ion conductivity, which leads to high t^+.[182] In addition, the anion mobility triggers a concentration gradient, causing a concentration polarization. For example, in LIBs the, depletion of Li^+ on the back of the cathode and salt precipitation at the LIBs anode were shown.[183] Moreover, the polarization gradient was considered to be a potential reason for lithium dendrite formation in LIBs but can be suppressed by high t^+_{Li}.[184] Therefore, SICs reduces the formation of dendrites, by immobilized anions.

In 1991, Chen and coworkers reported a SIC for MIB by taking a magnesium poly(phosphazene-sulfonates)-based polymer.[185] It has been shown that TFSI-based polymers can enhance the ionic conductivity by decreasing the Mg^{2+}-polymer interaction.[186–189] For polymers based on 1-butyl-3-methylimidazolium poly(4-styrenesulfonyl trifluormethansulfonylimide) (BMIPSTFSI) and the magnesiated analogue $Mg(PSTFSI)_2$ the incorporation of small ratios of $Mg(PSTFSI)_2$ to BMIP-STFSI was found to just rarely change the ionic conductivity and the thermal and structural properties.[187] Schaefer and coworkers investigated the ion coordination in a poly(ethylene glycol) diacrylate (PEGDA) STIFSIX (X= Li, Na, K, Mg, Ca) crosslinked polymer matrix for various counterions, where a lower ionic conductivity and higher percentages of unpaired STFSI anions and larger dissociation energies for divalent cations were reported.[186] Another prominent class of SICs, so far mainly investigated for their use in LIBs, are poly(borate)-based electrolytes, that are characterized by borates as counter ions.[190,191] A borate based SIC for MIBs was investigated by Du and coworkers, where a crosslinked polytetrahydrofuran-borate-based PE (PTB) was

synthesized.[164] Herein, a coulombic efficiency of nearly 100% for over 250 cycles at 0.5 C and a specific capacity of 74.3 mA h g^{-1} was reported testing a Mo_6S_8||PTB||Mg cell. A summary of further SICs for MIBs applications is given in Table 6.

Table 6: Summary of SICs in MIBs.

Additive	**Polymer host**	**σ [Scm^{-1}]**	**t^+_{Mg}**	**Cell characteristics**	**References**
-	Magnesium poly(phosphazenesulfonates)	$\approx 10^{-7}$	-		185
-	PEO-P[$(STFSI)_2Mg$]	$\approx 10^{-9} – 10^{-5}$ (30 - 130°C)	-		189
-	PEO-P[$(STFSI)_2Mg$]	$\approx 10^{-9} – 10^{-7}$	-		188
-	$(Mg(PSTFSI))_2$ BMIPSTFSI	3.8 10^{-5} (80°C)	-		187
-	PEGDA-STFSIMg	$\approx 10^{-12} – 10^{-6}$ (-20 – 100°C)	-		186
THF	PTB	4.76 10^{-4} (RT)	0.73	Charge/discharge characteristics Mg||Mo_4S_8	164

A second possibility to use SICs over polyanions as matrix is to incorporate uncharged anion receptors into the polymer. The receptors can reversibly capture the mobile counter anion and form the corresponding immobilized anion and thereby increase the t^+ (schematically illustrated in Scheme 3). Such anion receptors are can be ammonium groups, amide hydrogen atoms or Lewis acids based on aluminum or boron moieties.[183] Best to our knowledge, only Yamamoto *et al.* investigated anion receptors with $Mg(ClO_4)_2$, $Mg(TFSI)_2$ and $Mg(Tf)_2$ for MIB applications.[192] They reported an increase in t^+_{Mg} for $Mg(ClO_4)_2$ > $Mg(TF)_2$ >> $Mg(TFSI)_2$ for a crosslinked poly(ethylene glycol) (cPEG) network with borate centers. The increasing interaction was explained by the harder character of the ClO_4^- and Tf^- compared to $TFSI^-$.

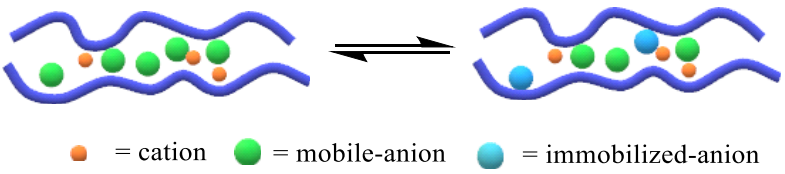

Scheme 3: Schematic illustration of polymer-based electrolytes with Lewis acids as anion traps.

1.3.4 Dual-salt polymer electrolytes

Dual-salt electrolytes were investigated for both MLHBs and as PEs for MIBs. Best to my knowledge, two publications describe dual-salt PEs for MIB and were published by *Tominaga et al.* and Buchmeiser *et al.*.[193,194] Tominaga focused on poly(ethylene carbonate) (PEC) and incorporated $Mg(TFSI)_2$ and LiTFSI in various concentration.[193] They reported higher current densities in CVs for the lithium-containing electrolytes compared to the reference material. Buchmeiser *et al.* obtained similar results, when investigating a crosslinked poly(tetrahydrofuran) (PTHF):$Mg(BH_4)_2$:$LiBH_4$:TiO_2 electrolyte.[194] Their constant current experiments at 0.1 to 0.4 mA cm^{-2} performed on low potentials (< 0.2 V) over 1100 of cycles at room temperature in Mg||Mg cells, but also high cycle ability in Mg-S batteries with various sulfur cathodes.

1.4 Polymer synthesis

Synthetic polymers are still dominant in PEs compared to natural polymers because of their wide variety and low costs. They can be synthesized by either step-growth or chain-growth approaches. Step-growth polymerizations are characterized by a high degree of polymerization (P_n) only when high conversions can be reached, whereas chain-growth yield high P_n at low conversions.

A prominent example for step-growth polymerizations is the polycondensation, while in chain-growth polymerizations the free-radical polymerizations (FRP) or cationic polymerizations is applied. Living polymerizations, like the anionic ring-opening polymerization (AROP), are also chain-growth polymerizations but are named separately. As defined by IUPAC living polymerizations have no termination or side reactions, leading to dispersities $Đ$ of 1 as well as a linear increase in P_n over conversion.[195] The "living" character further enables the synthesis of more complex structures, for example multi-block copolymers, in which two or more different monomers are polymerized step-wise.[196] Nevertheless, living polymerizations are limited in regards to monomers and reactions conditions, because of its (moisture) sensitivity and low functional-group tolerance. Generally, solvents with high grade of purity and strict inert reaction conditions are necessary. Controlled radical polymerizations (CRPs) have been developed to overcome these limitations by combining the benefits of radical polymerizations (e.g., high water tolerance, functional tolerance and monomer diversity) and living polymerizations (low dispersity and polymer architecture). The most prominent CRPs are the atom-transfer radical polymerization (ATRP), the nitroxide-mediated polymerization (NMP) and the reversible addition-fragmentation chain transfer (RAFT) process. Similar to the living polymerization, termination and side reactions are supressed, which leads to a linear P_n to conversion correlation. In the following chapters AROP, CRP and RAFT are further discussed.

1.4.1 Reversible addition-fragmentation chain transfer polymerization

RAFT as one of most recent controlled radical methodologies was firstly reported in 1995 by the Commonwealth Scientific and Industrial Research Organization (CISRO) and contemporaneously Rhodia in France developed a similar process, termed MADIX.[197,198] Similar to the other methods CRP, ATRP, NMP, and living polymerizations RAFT relies upon a kinetic strategy to control architecture and molecular weight (see Scheme 4).[199]

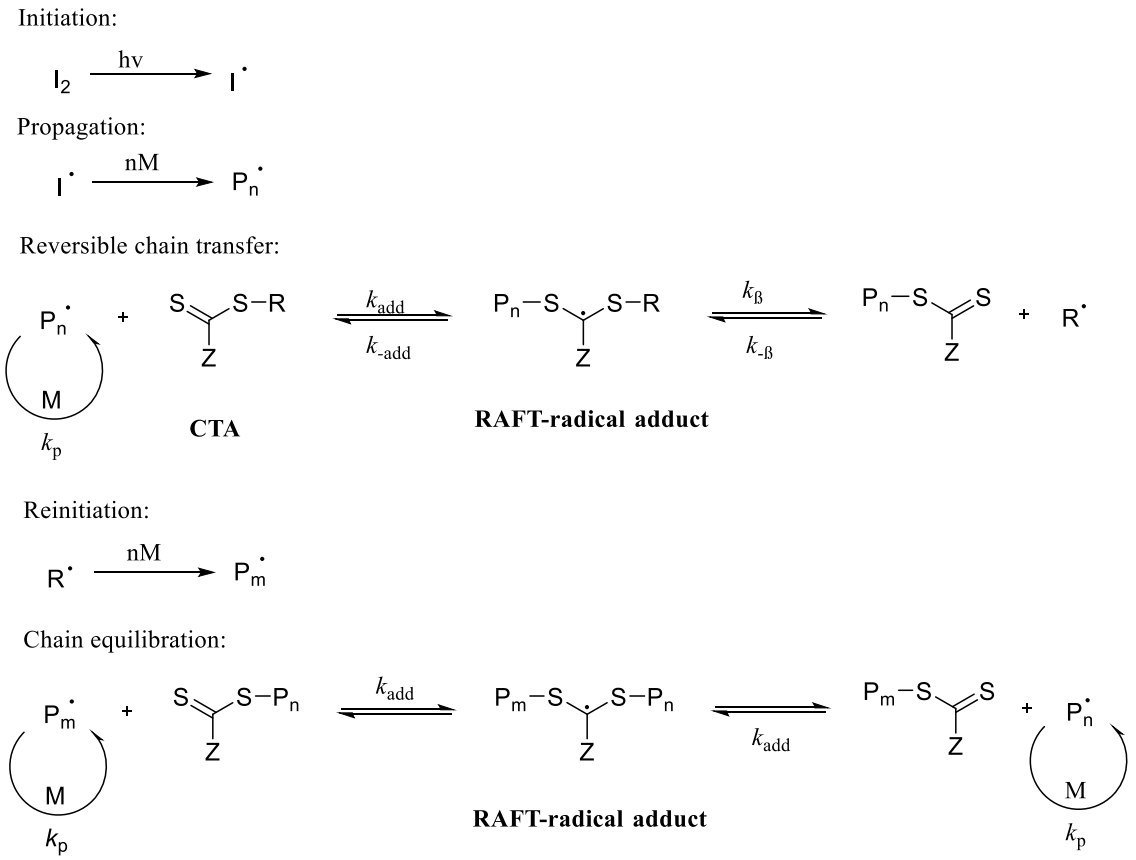

Scheme 4: Mechanism of RAFT polymerization with initiation, propagation, reversible chain transfer, reinitiation and chain equilibration.

The RAFT polymerization relies of the reversible exchange of two propagating radicals $P_n^{\bullet}$ and $P_m^{\bullet}$ via the RAFT radical adduct. After the initiation and first propagation process the propagating polymer $P_n^{\bullet}$ is formed. $P_n^{\bullet}$ forms a RAFT-radical adduct by addition with a dithioester (RAFT agent or chain-transfer agent (CTA)), which can further fragmentate back into $P_n^{\bullet}$ or another propagating radical $R^{\bullet}$ and dithioester. The radicals released by fragmentation are active intermediated, which can undergo chain growth. The lifetime of the propagating radicals ($R^{\bullet}/P_{n/m}^{\bullet}$) are hereby reduced by forming an equilibrium between $R^{\bullet}/P_{n/m}^{\bullet}$ and the low reactive RAFT-radical adduct, where $k_{add} >> k_{-add}$, $k_{\beta} << k_{-\beta}$ and $k_{add} >> k_{-add}$, respectively.

Due to the mechanism, the design of the CTA and specifically the leaving group R and activating group Z are from an outstanding importance to control the radical polymerization. The weak S-R bond favors its homolytic cleavage followed by the formation of a thioester. Thus, R should be a preferable leaving group while providing good polymerization reinitiating properties. DFT calculations suggested, that steric and polar groups, respectively, affect the chain transfer.[200] R groups bearing π-acceptors (CN or Ph) or α-CH_3 groups stabilizes the radicals $R^{\bullet}$ or $P_n^{\bullet}$ but destabilize the corresponding CTA agent by steric interactions. Therefore, too stable radicals, which are good

leaving groups, are not necessarily sufficient, because the subsequent reinitiating step is disfavored. Compatible R groups and monomers are listed in Scheme 5 as well as their addition/fragmentation rates.[201]

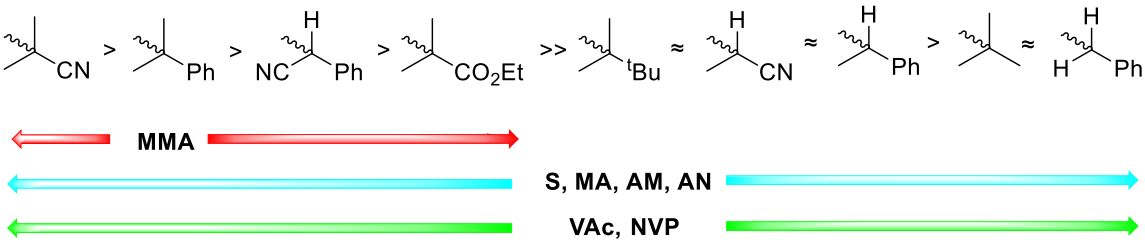

Scheme 5: Fragmentation rates decreases from left to right. Guidelines for selection of RAFT agents for various polymerizations.

Besides R, the second substituent Z effects the stability of the C=S bond in the RAFT agent and the RAFT-radical adduct. In Scheme 6 the order of fragmentation efficiency can be seen, where Z = NR_2 or OR favors fragmentation over Z = SR to Z = CN, Ph or CF_3 exhibit low fragmentation efficiencies.[202] The RAFT agent is stabilized for Z = OR, NR_2 and SR through delocalization of electron density into the C=S bond. On contrary, the RAFT agent is destabilized by σ-withdrawing effects. Furthermore, the lone-pair donors SR were found to express an overall stabilization, but only if the lone-pair donation of the substituent Z is stronger than of SR.[199] Therefore, only amino groups fulfill the requirements for enhanced CTA stability, whereas alkoxy groups do not enhance the stability, due to their σ-withdrawing character.

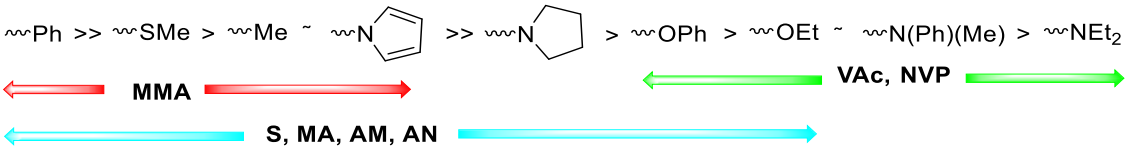

Scheme 6: Addition rates decrease and fragmentation rates increase from left to right. Guidelines for selection of RAFT agents for various polymerizations. Dotted lines indicate partial control.

Suitable R and Z groups depend on the monomer of choice. In general, the CTA should provide high k_{add} and a reactive C=S bond, high fragmentation rate of the CTA-radical adduct (high k_β), a favored formation of the CTA-radical adduct over the formation of the radicals $R^\cdot$ and $P^\cdot$ ($k_\beta > k_{-add}$) and efficient polymer reinitiation by $R^\cdot/P_n^\cdot$. A list of compatible R and Z groups for selected monomers as methyl methacrylates (MMAs), vinyl alcohols (VAcs), N-vinylpyrrolidone (NVPs), styrene (S), methacrylates (MAs) and acrylonitrile (AN) are provided in Scheme 5 and Scheme 6, respectively. The general chemical structures of dithioesters-based CTAs are shown in Scheme 7A.

Scheme 7: General chemical structures of RAFT agents/CTA. A) Dithioesters and B) trithiocarbonates.

As an example, 4-cyano-1-hydroxypent-4-yl dithobenzoate was reported as efficient CTA in the polymerization of MMA, whereas 2-cyano-2-propyl benzodithioate (CPDB) was used in polymerizing poly(ethylene glycol) monomethylether (PEGMA).[203,204] 2-Cyanoprop-2-yl 2,3,4,5,6-pentafluoro dithiobenzoate was also tested for the polymerization of MMA, while benzyl dithioisonicotinate was used to polymerize S.[205,206] The scope of CTAs was further extended to trithiocarbonates, as schematically shown in Scheme 7B. Those trithiocarbonates commonly bear alkylthio substituents as Z, which lead to a lower activity and hydrolytic degradation. For example, Chiefari and coworkers used 2-cyano-2-propyl dodecyl trithiocarbanate (CPDT) for the polymerization of styrene, *S*,*S*-bis(α,α'-dimethyl-α''-acetic acid) trithiocarbonate for *N*-isopropylacrylamide (NIPAM) or acrylic acid (AA) and dibutyl trithiocarbonate for S.[197,207,208] Depending on the chosen CTA, RAFT polymers can further be modified by either end group removal, ω-end modification, thermal modification, aminolysis or hetero-Diels-Alder.[209] Additionally, various architectures are available such as multi-block copolymer, branched copolymers or surface grafted copolymers, which are for major interest in fine tuning material properties and applications.[210]

1.4.2 Anionic ring-opening polymerization

Ring-opening polymerizations (ROP) is a subcategory of chain-growth polymerizations, in which cyclic monomers are polymerized. ROP is divided into radical ROP, cationic ROP (CROP), ring-opening metathesis polymerization (ROMP) and anionic ROP (AROP).[211] To overcome the entropy loss during the polymerization radical ROP is mainly aided by the enthalpy differences between the single C-C and double bounds C=C of olefines. Vice versa, ionic ROP as AROP, cationic ROP or ROMP are mostly driven by the ring strain and associated steric considerations.[195] In ROP olefines, ethers, thioethers, amines, lactones, thiolactones, lactams, disulfides, carbonates and silicones are typically applied monomers among others.[196,211–216] Noteworthy, P. Flory was honored in 1974 with the Nobel Prize in Chemistry for the investigation of AROP.[217] The living character of AROP is one of the outstanding benefits, enabling low dispersities and multi block structures.[218] Accordingly, AROP requires water-free conditions and high purity grades of educts. Accessible monomers are heterocyclic monomers as ether, siloxane, lactam, lactone and carboante.[196,213,216]

AROP of polycarbonates

Polycarbonates and thus cyclic carbonate monomers were in focus of interest due to their wide field of applications like elastomers, sealants, foams, coating adhesives and PEs in MIBs and LIBs.[213,218] Aliphatic polycarbonates were found to be also biocompatible and biodegradable, which is beneficial in case of sustainable material circular economy.

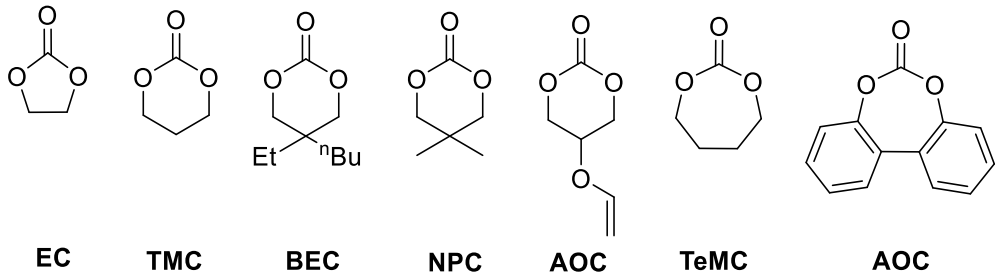

Scheme 8: Chemical structure of various 5-, 6- and 7-membered cyclic carbonates.

The most reports were on 5- ,6- or 7-membered cyclic carbonates as shown in Scheme 8. 7-Membered cycles, as annulated cyclic carbonate (AOC), are reacting faster compared to 6- and 5-membered, due to their relatively high ring strain.[218,219] Because of the ring strain the monomer synthesis and storage is much more challenging compared to the 5- and 6-member cycles, which is their major drawback. With 5-membered cycles, such as EC, difficulties are high polymerization temperatures (above 150 °C), low yields (about 50% conversion) and formation of alkylene oxide units as side products.[218,220] In between, 6-membered cycles polymerize already at moderate temperatures to high molar masses and an overall high number of monomers are noticeable benefits. Common 6-membered cycles are trimethyl carbonate (TMC), 2-butyl-2-ethyl-1,3-dioxan-2-one (BEC) or 5-allyloxy-1,3-dioxan-2-one (AOC).[221,222] Although the conversion is higher compared to 5-membered cycles the polymerization does not go to full conversion because of its equilibrium character, see Scheme 9.[218] The polymerization conversion depends on the substitution, where bulky substituents lead to higher monomer concentrations at equilibrium state.[223,224]

Initiation:

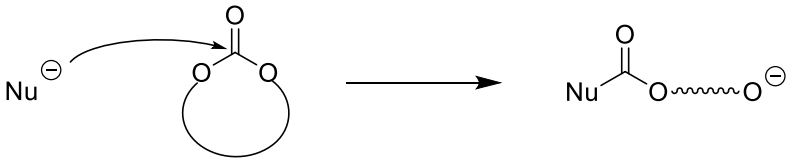

Monomer M

Propagation:

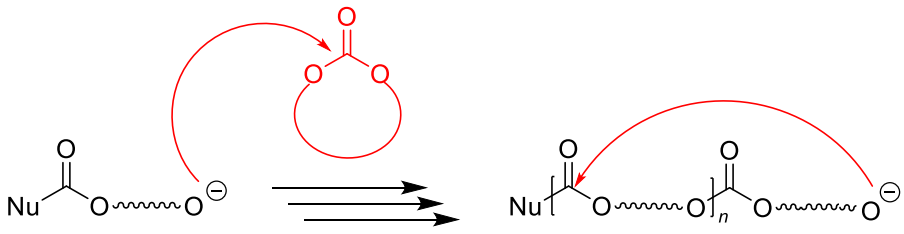

kinetic product

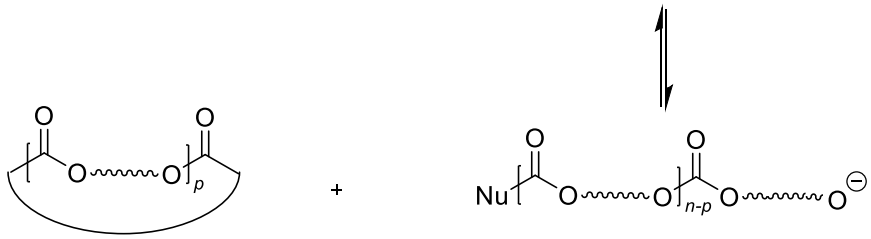

side-product **thermodynamic product**

Scheme 9: AROP mechanism of cyclic carbonates.

The initiation is accessible via an anionic process or zwitterionic polymerization mechanism.[195] In the ionic process inorganic bases such as alkali metal oxides undergo a nucleophilic attack on the carbonyl carbon followed by the ring-opening and the formation of an alcoholate.[223,224] Alcoholates and carbanions initiators contain mostly alkali and alkaline counterions, therefore the zwitterionic process was developed and firstly reported by Jaacks and Mathes in 1970s to avoid metallic impurities.[225] Instead of metal-based initiators organic nucleophiles are taken, where a zwitterionic compound is formed after the nucleophilic attack. Established organic initiators are 1,8-diazabicyclo[5.4.0]undec-7-ene (DBU), 1,4-diazabicyclo[2.2.2]octane (DABCO), 4-dimethylaminopyridine (DMAP) and phosphazene.[226–229] Phosphazene as described by Boileau and Illy in 2011 form zwitterionic intermediate by its strong basicity but low non-nucleophilicity, deprotonating e.g., alcohols and acting as counterion.[226] Further initiation occur in initiator-free AROP by self-initiation, but are limited in the scope of monomers. For example, TMC was reported to polymerize in bulk above 100 °C, whereas for NPC no polymerization was observed.[222] TMC was suggested to polymerize by a zwitterionic initiation process via AROP, as a stable

trialoxycarbenium intermediate was formed. On the one hand, AROP is a living polymerization, on the other hand side reactions in the propagation process were observed. While the resulting polymer is the kinetic product, a thermodynamic favoured product, a cyclic oligomers, can be formed by back-biting (Scheme 9), instead.[230] Furthermore, the formation of ether as defects can occur in 5-membered cycles.[213] Vogdanis and Heitz observed those defects, when polymerizing ethylene carbonate (EC) with dibutyl(ethylendioxy)tin in bulk at 150 – 200 °C. Hereby, the EC repeating unit content was not higher than 48 mol%.[220] The defect was explained by a decarboxylation process of an end-functionalized carbonate, which was formed by a nucleophilic attack of a propagating molecule on the methyl carbon instead on the carbonyl carbon. Further drawbacks have to be considered, when designing multifunctional polycarbonates by AROP because AROP is compatible with various functionalities but are also limited to nucleophilic moieties. Parzuchowski *et al.* reported a crosslinked polymer when using unprotected hydroxy groups, but no crosslinked product, if a protecting group (e.g. trimethylsilyl chloride) is used or post-modifications with mercaptoethanol were taken.[221] The design of a 5-membered cyclic bearing multifunctional polycarbonates was also reported, allowing the polymerization of bicyclic carbonates at low temperatures.[231]

1.5 Graft polymers

The given polymerization techniques enable the control of diverse monomers and architectures as cyclic polymers star polymers, dendrimers, hyperbranched polymers and graft polymers. Those architectures effectively influence the materials properties, which highlights their interest in industry and academia.[232]

Graft polymers can either be designed when polymers chains are connected to linear polymers or to planar surfaces or particles. The functionalization of particles and surfaces, which are mostly inorganic materials, are chosen to tune their properties in adhesion, coating, painting, coloring, lamination, packaging, colloid stabilaztion.[233] Surface grafting benefits are its high density, exact localization and long-term chemical stability compared to other techniques.[233] Therefore, their field of applications include membrane separation, bio-medical, fuel cells, sensors, optical and catalysis.[234,235] Polymers linked to polymers, also named grafted polymers, are characterized by three parameters, which impacts their bulk morphology and mechanical properties most.[232] Firstly be the molecular weight of the main chain, secondly by the weight of the graft chain and thirdly by the placement or density of the graft chain.

Three grafting techniques are established for the synthesis of grafted materials: *grafting onto*, *grafting through* and *grafting from* (Scheme 10). For the grafting onto approach already prepared polymers are added to the corresponding surface or polymer. This can either be done by nucleophilic substitutions or additions including so called `click reactions´. This approach allows good control over the polymer weights and architecture but are limited in regards of graft density or length of the added polymer.

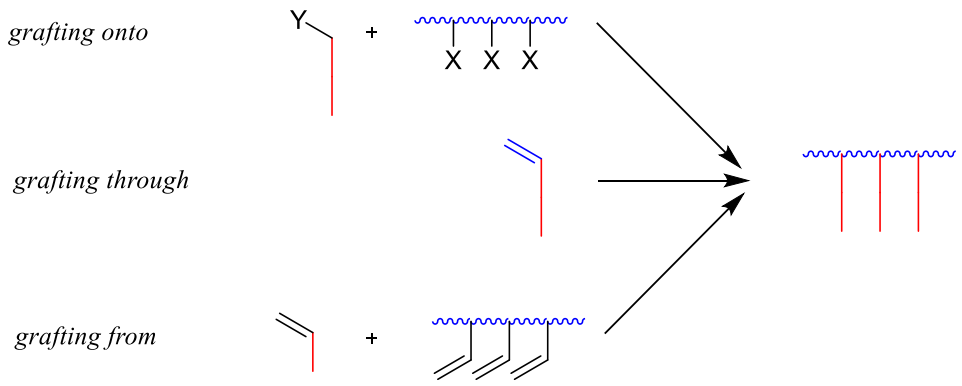

Scheme 10: Grafting approaches illustrations.

In the grafting through approach the grafted polymer backbone is build up by macromonomers. In here, the sidechains contain polymerizable functionalities, which build up the graft polymers

backbone. This allows the separate design and synthesis of the macromolecules before and open the opportunity for complex structures. Furthermore, the grafting density and polymer architecture are easy to control. However, the degree of polymerization and conversion strongly depends on the macromonomer size and reactivity of the polymerizable group.

The third approach, grafting from, takes advantage of polymerizing selected monomers from a polymer backbone. This requires polymerizable moieties in the backbone, which are used in following steps to build up the graft polymer. The approach benefit is its high grafting position and density control and, but also lead to higher dispersity of the polymer side chains.

Motivation and Goal

Polymers are of great interest as solid electrolytes for magnesium ion batteries due to their mechanical stability and processability. However, they are limited by their low ionic conductivity, electrode compatibility and charge-discharge reversibility. Established approaches to improve the electrochemical properties of polymer electrolytes, e.g., ion transport, stability, transference numbers, were already part of interest in lithium batteries. This includes the use of dual salt systems, polymer-in-salt electrolytes, single-ion conductors, grafted polymers and anion receptors. Polymer-in-salt electrolytes display improved properties such as their high ionic conductivity. Single-ion conductors and anion-receptor functionalized polymer electrolytes have shown superior ion transference numbers extended by their ability to reduce salt polarization ingredients and dendrite growth. Grafted polymers were in focus of research due to their ability to reduce crystallinity and increased chain flexibility besides mechanical stability.

All those approaches have been successfully applied on lithium batteries. However, their magnesium-based alternatives have been barely investigated and reported in literature. Magnesium batteries represent an attractive alternative to LIBs due to the high abundance of magnesium on earth as well as its low costs.

To gain further insights, multiple approaches were combined and investigated within this thesis to overcome the drawback of polymer electrolytes. The single-ion conductor approach was investigated to increase the transference number. Hereby, dual salt electrolytes have been synthesized, which enables reversible magnesium plating/stripping. Furthermore, polymer electrolytes with anion receptors have been studied to combine the benefits of polymer electrolytes and single-ion conductors to address the dilemma of low transference number on the one hand and reduced ionic conductivity.

The combination of different approaches shall provide a detail insight into their abilities and effects on the polymer ion coordination, morphological and electrochemical properties, eventually showing their opportunities and limitations.

Results and Discussion

1.6 Borate-Crosslinked Single-Ion Conducting Copolymer Electrolytes for Magnesium Battery Applications

Magnesium-lithium hybrid electrolytes were one appropriate approach for enhanced MIBs as reported by Buchmeiser *et al.* and Tominaga *et al.*.[193,194] While, Buchmeiser *et al.* focused on a crosslinked PTHF-$LiBH_4$-$Mg(BH_4)_2$ GPE performing with low plating/stripping potentials and longtime cyclability, Tominga and coworkers proved the enhanced effect of LiTFSI on a PEC-$Mg(TFSI)_2$ PE by CV measurements for various LiTFSI concentrations. Still, there is room for improvements, therefore, the design of magnesium-lithium dual-salt SPEs is the focus of the present study.

The polymer design was chosen to be a single-ion conductor because on the one hand only a limited number of reports on magnesium-lithium dual-salt single-ion conductors-only were published to the best of my knowledge.[67] On the other hand, dendrite formation was still observed not only for TFSI-based electrolytes but also for triphenolateborohydride-, magnesium monocarborane- (MMC) and magnesium bis(hexamethyldisilazide)-based ($Mg(HMDS)_2$) electrolytes.[26,236–238] SICs are known to reduce dendrite formation caused by polarization ingredients.[183] To further enhance the electrochemical performance and mechanical stability, grafted copolymers were crosslinked to crosslinked SICs (Scheme 11).

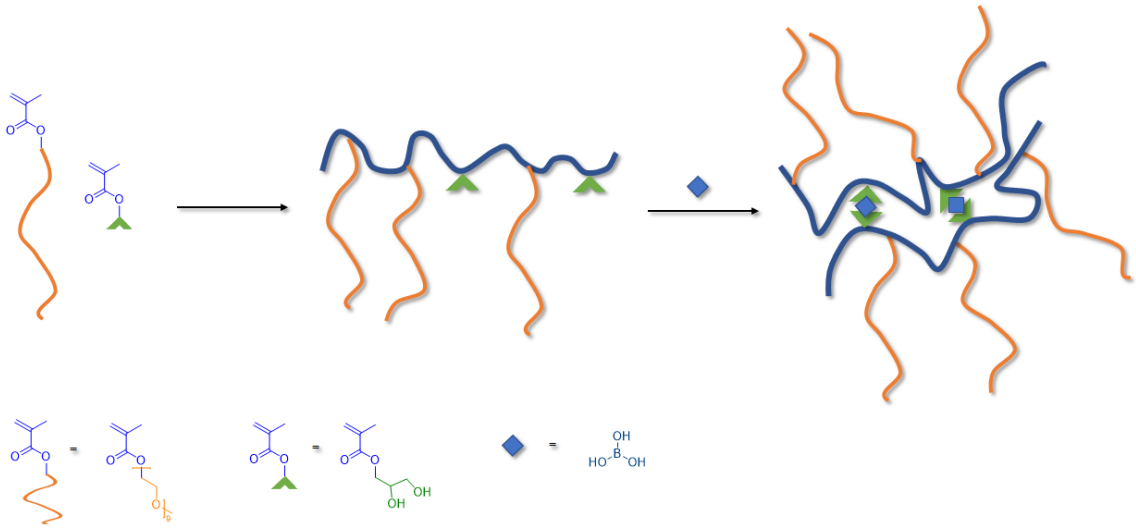

Scheme 11. Schematic synthesis illustration of a crosslinked SIC from grafted copolymers.

1.6.1 Synthesis

The synthetic procedure and selected results were developed by Nico Zuber for his Master thesis under my supervision.[239] In the first step, magnesium-based SICs were synthesized and optimized towards its thermal and electrochemical performance prior the preparation of the magnesium-lithium dual-salt electrolytes.

Crosslinked SICs were investigated, upon the RAFT copolymerization of $PEGMA_x$ (x = 500 and 950 g mol^{-1}) and solketal methacrylate (SMA) (Scheme 12). The crosslinking and grafting approach also reduce the crystallization of the PEG chains to increase the ionic conductivity.[67,166] SMA was taken as crosslinking point in the PE after a post-modification step and $PEGMA_x$ was copolymerized to increase the flexibility of the electrolyte films. After deprotection of the acetal group under acidic conditions (**1-diol** to **4-diol**), the SICs were formed by condensation reaction of boric acid and LiOH and/or $Mg(OEt)_2$ (Scheme 12). A partly decomposition of the RAFT agent in the deprotection step has to be assumed.

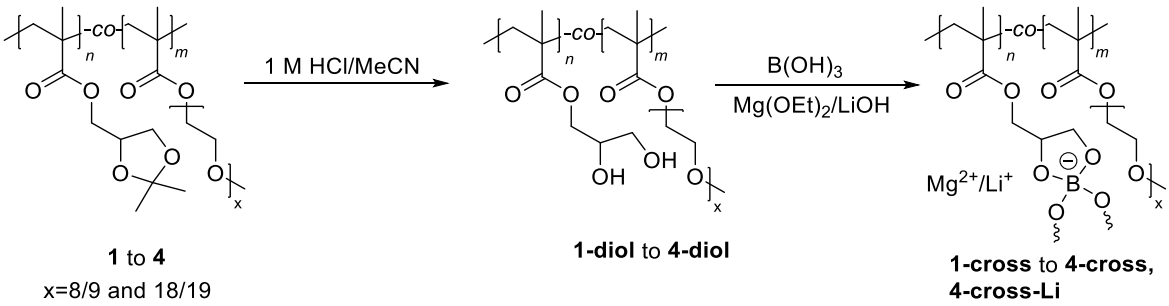

Scheme 12: Schematic synthesis of self-standing films **1-cross** to **4-cross**.

The monomers were polymerized by RAFT polymerization with high ratios of SMA (larger 60 mol%), which were required to form solid and self-standing electrolyte films upon the cross-linking process. $PEGMA_x$ with molecular weights larger 950 g mol^{-1} were not accessible because only low conversions (such as, 50 %) were obtained under these conditions. To optimize the ionic conductivity of the SICs, four different polymers were synthesized, which differs in architecture, $PEGMA_x$ molecular weight and monomer ratio. Block copolymers were synthesized by a macro-RAFT approach. The SMA:$PEGMA_x$ ratio was determined for the polymers **1** to **4** by ^{1}H-NMR spectroscopy, integrating the methyl groups of $PEGMA_x$ at 3.3 ppm and of the acetal group at 1.42 – 1.24 ppm. The complete hydrolysis of the acetale group was observed by ^{1}H-NMR (Figure 5).

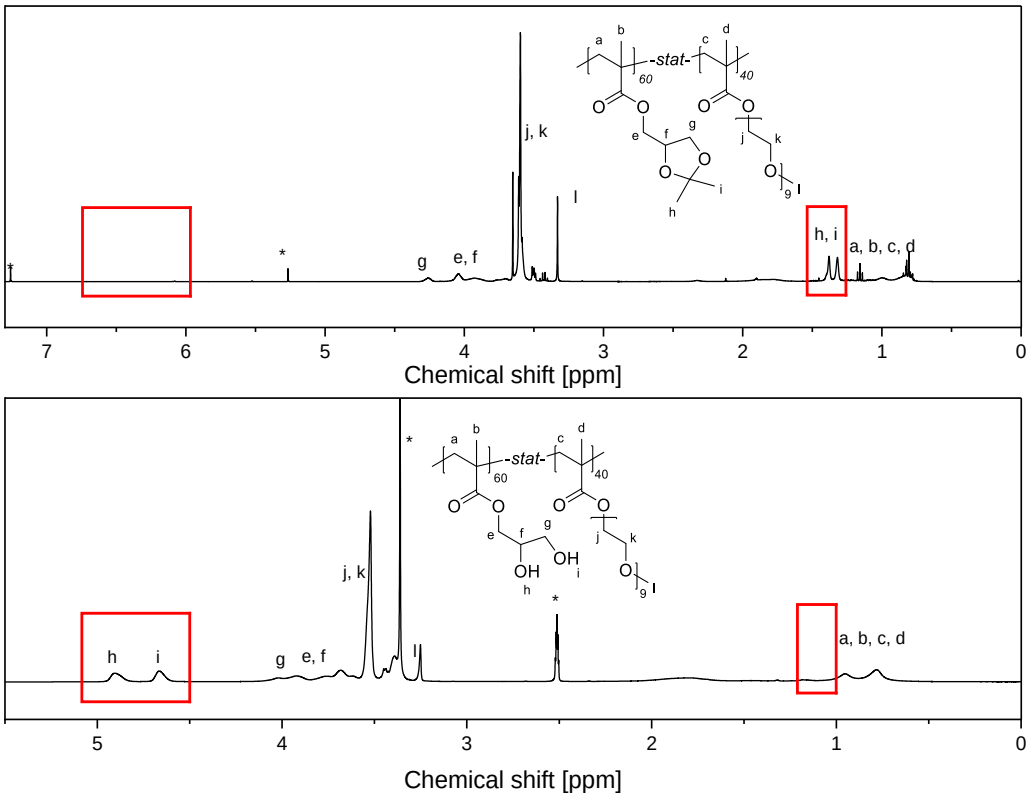

Figure 5: Exemplary, ^{1}H-NMR of **1** and **1 diol** in $CDCl_3$ and DMSO-d_6, respectively.

The polymers **1-diol** to **4-diol** SEC and ^{1}H-NMR results are concluded in Table 7.

Table 7: Molecular weight of $PEGMA_x$, Comonomer ratio, architecture, dispersity (M_n/M_w) and M_n of **1-diol** to **4-diol**. * Determined by gel permeations chromatography with DMAc as eluent.

	M_n (PEG-MA$_x$) [g mol^{-1}]	**Architecture**	**SMA:PEGMA$_x$ ratio [mol%]**	**M_n/M_w***	**M_n* [g mol^{-1}]**
1-diol	500	Statistic	58:42	1.35	47 900
2-diol	500	Statistic	73:27	1.17	21 200
3-diol	500	Block	82:18	1.2	25 300
4-diol	950	Statistic	76:24	1.46	32 800

In Figure 6 photos of the final self-standing solid films are shown.

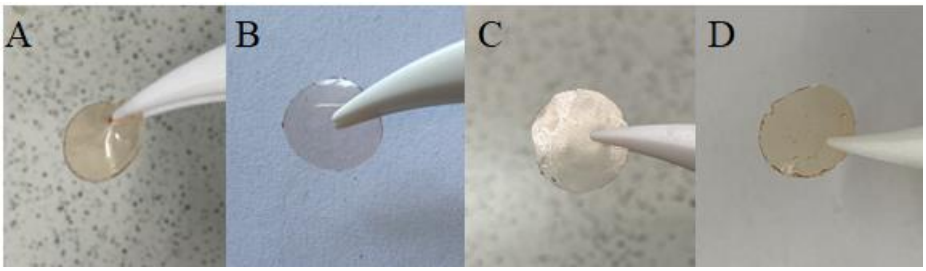

Figure 6: Pictures at room temperature of A) **1-cross** and B) **2-cross**, C) **3-cross** and D) **4-cross**.

In the SEC chromatograms, the formation of polymers with twice the number average molecular weight were detected, which were explained by the formation of disulfide linked polymers after the aminolysis of the RAFT agent in the eluent DMAc (Figure 7). Therefore, a unimodal distribution were assumed for the polymer itself, rather bimodal in amine-free solvents.

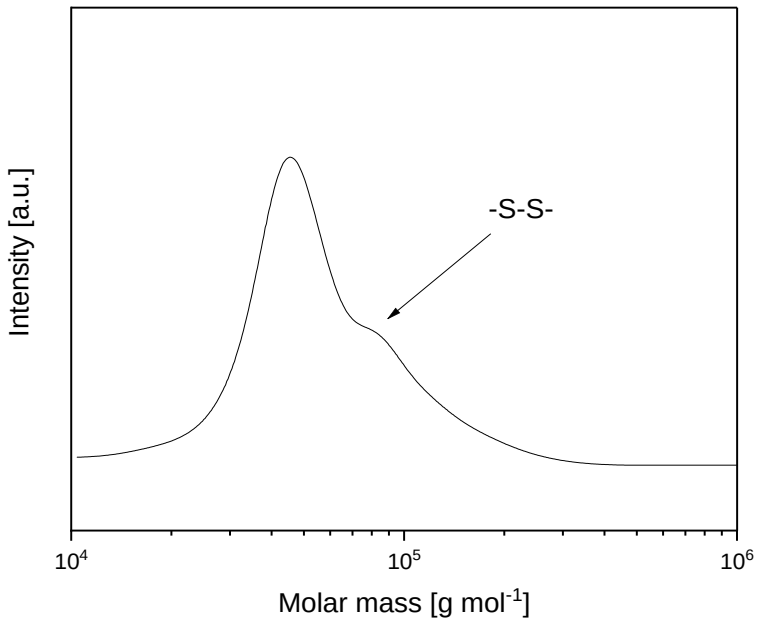

Figure 7: SEC spectrum of **1-diol**. The second peak correspond to disulfide linked polymers after aminolysis in the eluent DMAc.

The full conversion of boric acid and the respective crosslinking efficiency were confirmed by ^{11}B NMR and FT-IR (Figure 8). In ^{11}B-NMR signals at 10.1 ppm were detected corresponding to the five-membered borate-diol complex.[240] In FT-IR the O-H vibrations between 4000 to 3200 cm^{-1} disappeared and therefore, the complete conversion and the formation of only SICs was shown (Figure 8A).

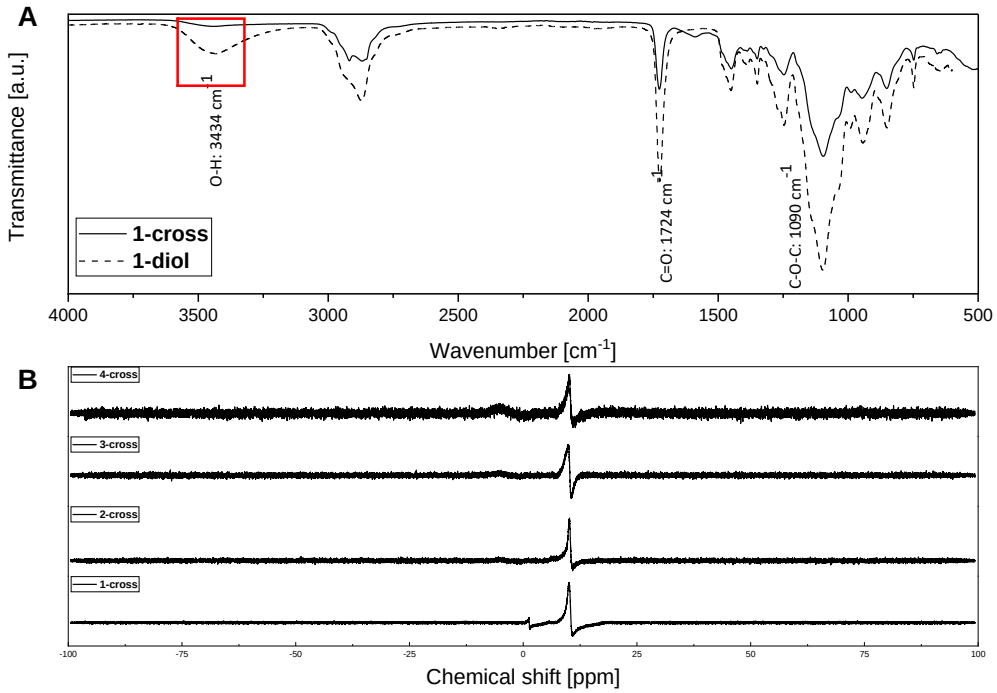

Figure 8: Prove of crosslinking. A) Disappearance of O-H vibrations at 3434 cm^{-1} in FT-IR spectra of 1 and 1-diol. B) ^{11}B-NMR of **1-cross** to **4-cross** in DMSO-d_6.

The resulting SICs (**1-cross** to **4-cross**) are summarized in Table 8. For further comparison, the Mg^{2+} concentration is given as ratio of the number of ethylene glycol repeating units [EO] and number of Mg^{2+} ([EO]:[Mg]).

Table 8: Comonomer ratios of **1-cross** to **4-cross** in molar, weight and in glycol ether repeating units to Mg^{2+} [EO]:[Mg].

	SMA:PEGMA$_x$ [mol%]	**[EO]:[Mg] ratio**	**SMA:PEGMA$_x$ [wt. %]**
1-cross	58:42	20.6	30:70
2-cross	73:27	10.5	46:54
3-cross	82:18	6.1	59:41
4-cross	76:24	21.4	35:65

As reference system a lithium-based SIC was synthesized based on the polymer **4** and **4-diol**, named **4-cross-Li**. The thermal properties, coordination environment and electrochemical performance were analyzed in the following chapter by TGA, DSC, FT-IR and impedance spectroscopy experiments.

1.6.2 Thermal properties

By TGA, decomposition temperatures (T_ds) at degradations at 5 % for the crosslinked SICs were measured and found to be between 260 °C to 280 °C (Figure 9). Those T_d were slightly higher compared to other reported borate based PEs by *Dai* and colleagues, who investigated crosslinked poly(ethylene glycol) methyl methacrylate borates with T_d = 235°C.[241]

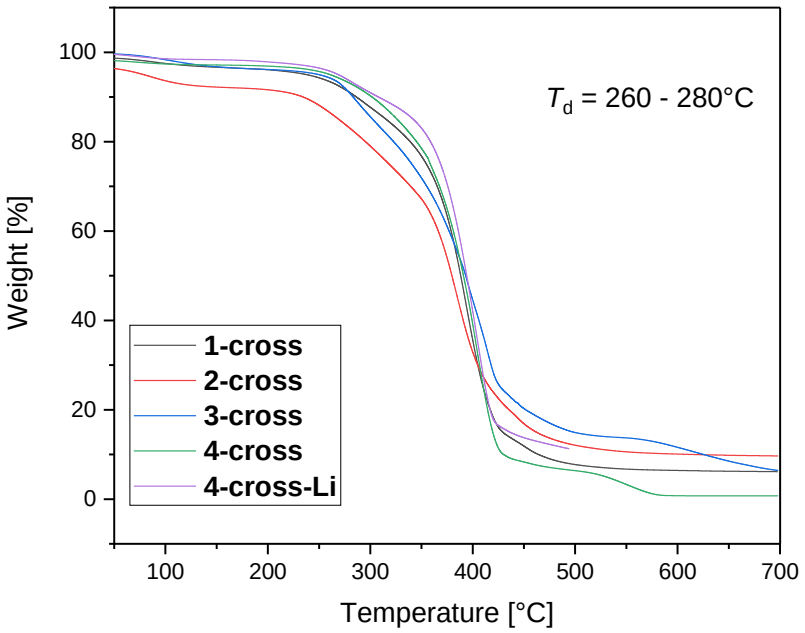

Figure 9: TGA spectra with the resulting T_ds of **1-cross** to **4-cross** and **4-cross-Li**.

DSC measurements revealed for **4-cross** and **4-cross-Li**, containing $PEGMA_{950}$, crystalline structures due to their melting points (T_ms) (Figure 10). **4-cross** had one T_m at about 30 °C, whereas **4-cross-Li** had two crystalline domains at -63 °C and -5 °C. The T_m at 35 °C for **4-cross** was related to semi-crystalline PEG chains because $PEGMA_{950}$ showed also a T_m at 35 °C.[242] The similar T_m of **4-cross** suggested, that neither Mg^{2+} nor borate anions showed an effect on the crystallinity and therefore only a limited PEG to Mg^{2+} interaction. In contrast to this, two different crystalline domains with two T_m were detected for **4-cross-Li** assigned to different PEG phases. The lower T_ms indicated weaker PEG-PEG interactions most likely caused by plasticizing effects of the lithium borate with two different concentrations. The copolymerization of $PEGMA_{500}$ instead of $PEGMA_{950}$ leaded to the formation of amorphous instead of crystalline domains because only glass transition temperatures (T_g) were seen (**1-cross** to **3-cross**). The T_g decreases slightly with increasing $PEGMA_{500}$ ratio from **1-cross** (-48 °C) to **2-cross** (-40 °C). Furthermore, block

architecture decreases significantly the T_g when focusing on **3-cross** (-62 °C) explained by larger PEG domains.

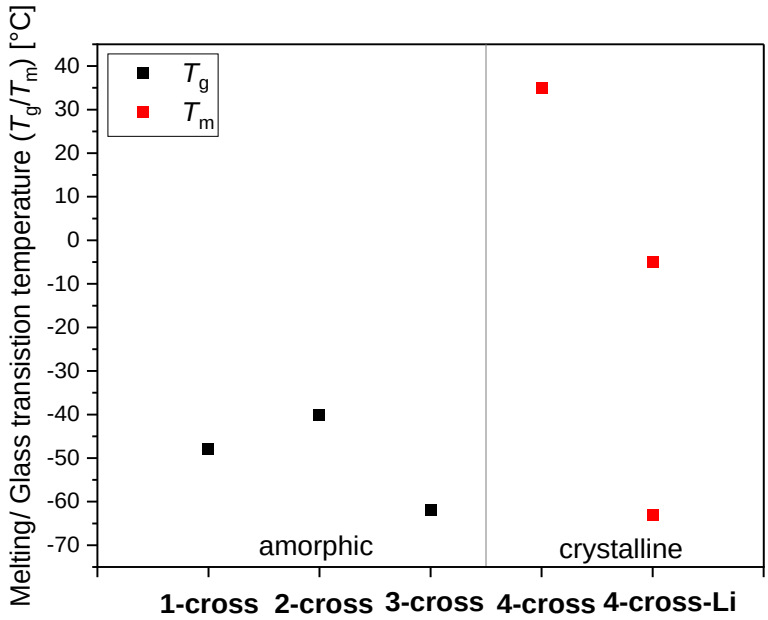

Figure 10: Glass transition temperatures and melting temperatures of **1-cross** to **4-cross-Li**.

1.6.3 Ion coordination

Conclusions about the coordination behaviour and environment between Li^+/Mg^{2+} and the polymer matrix, respectively, can be deducted from FT-IR spectra, when comparing shifts of certain vibrations (Figure 11).

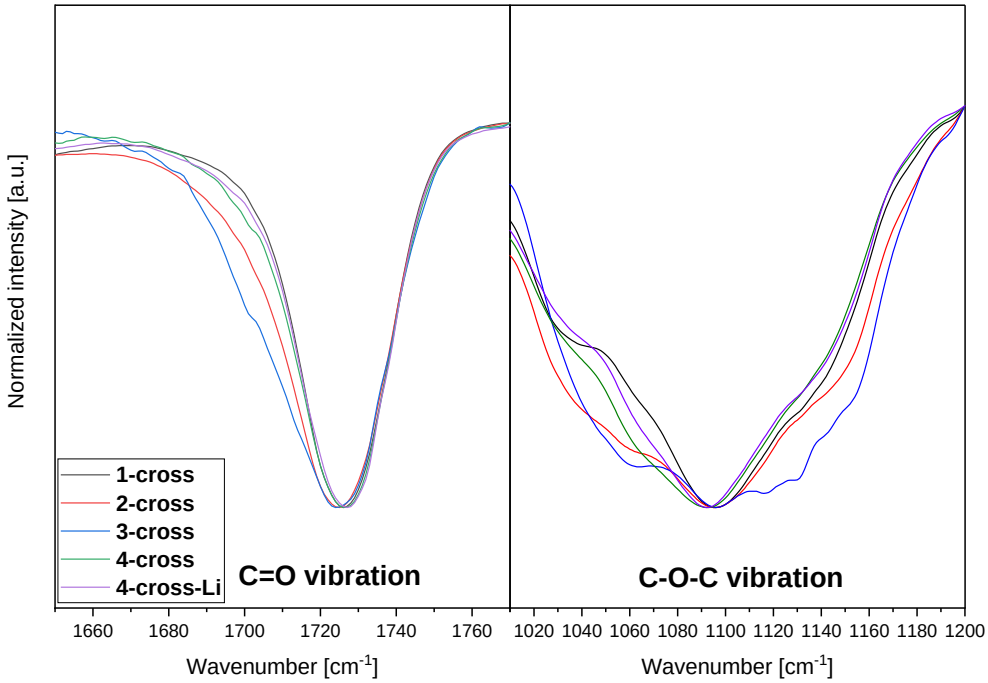

Figure 11: Normalized FT-IR spectra of **1-cross** to **4-cross-Li** between 1650 to 1770 cm^{-1} and 1010 to 1200 cm^{-1}.

Significant vibrations were identified for C-O-C at 1096 cm^{-1} and C=O at 1723 cm^{-1} (Figure 11).[243] The carbonyl vibrations of the SICs (**1-cross** to **4-cross-Li**) occurred at 1723 ± 1 cm^{-1} being in the similar range as the non-crosslinked polymers, **1-diol** to **4-diol** (1723 ± 1 cm^{-1}), which suggested no cation-carbonyl coordination. The C-O-C vibrations occurred at 1096 ± 0 cm^{-1} for **1-cross**, **2-cross** und **3-cross** and at 1092 ± 1 cm^{-1} for **4-cross** and **4-cross-Li** containing $PEGMA_{950}$. The C-O-C vibrations stayed unchanged compared to the non-crosslinked polymers (**1-diol** to **4-diol**) therefore, no or only a limited cation coordination to the PEG chain was suggested as well. Due to the absence of any coordination of cations to the PEG chain or the carbonyl groups it was assumed that the major number of Mg^{2+} and Li^{+} were coordinated to the borate anion indicating a low ion dissociation. For **4-cross** these assumptions are in good agreement to the DSC results also indicating no significant interaction between the PEG chains and the Mg^{2+}. The preferred cation coordination to the borate anion might be traced back to the high crosslinking ratio but also by the low delocalization of the negative charge at the borate anion.

1.6.4 Electrochemical properties

Ionic conductivities (σ) were derived from electrochemical impedance spectroscopy measurements for temperatures between 0 °C and 70 °C and discussed towards architectural, monomer ratio and in terms of $PEGMA_x$ ratio (Figure 12). For **2-cross** even at 70 °C no ionic conductivity

could be calculated, due to extremely slow ion transport and thus the absence of R_b in the Nyquist plots. The magnesium concentration is predetermined by the monomer fractions and was given as a ratio of the number of ether moieties of the $PEGMA_x$ sidechain in relation to the number of magnesium cations, denoted as [EO]:[Mg] (Table 8). The [EO]:[Mg] ratio was the highest for **1-cross** and **4-cross** with 21.4 and 20.6, respectively, which also showed higher ionic conductivity in contrast to **2-cross** ([EO:Mg] = 10.5) and **3-cross** ([EO:Mg] = 6.1) independent of temperature. Ion mobilities in PEG containing PE were reported to appear by a segmental motion mechanism and therefore the chain mobility is a critical parameter.[192,243] The higher ionic conductivity of **4-cross** (4.99 10^{-9} S cm^{-1} at 70 °C) in comparison to **1-cross** (4.95 10^{-10} S cm^{-1} at 70 °C), although both feature roughly the same PEG fraction, can be explained by its longer PEG chain and therefore higher chain mobility. The higher flexibility of $PEGMA_{950}$ compared to $PEGMA_{500}$ has already been reported for lithium based SPEs before.[244] For $PEGMA_{500}$ containing SICs, **1-cross** to **3-cross**, **1-cross** performed with the highest ionic conductivity at 70 °C (4.91 10^{-10} Scm^{-1}) followed by **3-cross** (9.61 10^{-11} Scm^{-1}) and **2-cross**. The given order is congruent with the DSC results, with the highest and lowest T_g for **2-cross** and **3-cross**. Therefore, the order of ionic conductivity can be explained by the T_g and chain mobility. In literature the beneficial effect of block architecture was already reported supporting this observation.[245] A critical temperature (T_σ) could also be observed, where ionic conductivities could not be calculated based on used EIS parameters. Those T_σs were found to be the lowest for **4-cross** with ~ 30 °C and increased over **1-cross** (~ 40 °C) to **3-cross** (~ 60 °C), whereas for **2-cross** no T_σ could be detected up to 70 °C. The T_σ for **4-cross** correlated with its T_m at 35 °C, which showed no ion mobility below T_m due to the crystallized and immobile PEG chains. Crystalline areas are known for PEG-based electrolytes to reduce ionic conductivity.[246] No T_σ for the lithium-based SIC (**4-cross-Li**) were seen because the T_m was below the measured temperature range. In addition, ionic conductivities between 3.32 10^{-7} S cm^{-1} (0 °C) and 6.14 10^{-5} S cm^{-1} (70 °C) were measured, which is a factor of 10^4 S cm^{-1} higher in contrast to the magnesium-based **4-cross** (4.99 10^{-9} S cm^{-1} at 70 °C). This exorbitant higher ionic conductivity for **4-cross-Li** could be traced back to the significantly higher charge density and harder character of Mg^{2+} due to its divalent character and therefore a much stronger Mg^{2+}-polymer coordination, resulting into lower ion mobility.[189] Although the ionic conductivity should be mainly caused by the mobility of Mg^{2+} as result of the SIC approach only low ionic conductivities of about 10^{-9} to 10^{-11} S cm^{-1} were measured for the solid magnesium-based SICs. Therefore, gel and quasi-solid SICs were prepared by incorporating 50 wt.% of ether PC or $PEGDME_{500}$ into the polymer matrix. The incorporation of organic additives, such as plasticizers, were an already established technique to tune polymer electrolytes and leads to gel-polymer

electrolytes (GPEs) with improved ionic conductivities.[67,247] This common strategy is expected to enhance the ion transport by increasing ion dissociation and segmental motion of the PEG side-chains.[248] Consequently, this approach resulted in an increased ionic conductivity up to 8.02 10^{-7} S cm^{-1} for **4-cross-PC** and 2.05 10^{-7} S cm^{-1} for **4-cross-PEGDME$_{500}$** at 70 °C and 1.69 10^{-7} S cm^{-1} and 1.75 10^{-8} S cm^{-1} at 20 °C, respectively. Additionally, the shape of **4-cross-PEGDME$_{500}$** and **4-cross-PC** follow a more convex profile, which is a hint for an ionic conductivity by segmental motion of polymer chains instead of ion hopping underlining the given conclusions.[249] The sudden increase in ionic conductivity for **4-cross-Li** at 20 °C might be related to a reduced chain mobility close to the first T_m. and is therefore a result of the phase transformation.[250] The higher ionic conductivity of **4-cross-PC** in comparison to **4-cross-PEGDME$_{500}$** can be explained by the larger dielectric constant of PC and lower viscosity compared to polyether, which leads to increased ionic conductivity as shown also by other researchers before.[251,252] Another reason is the coordination environment identified as critical parameter for ionic conductivity.[253,254] PEGDME$_{500}$ as linear polyether like DME or tetraethylene glycol dimethyl ether (tetraglyme) is expected to coordinate by ether moieties to Mg^{2+} but is not limited to one Mg^{2+} as schematically presented by Tuerxun and colleagues.[255] Because of the chelating effect the complexation of larger polyether is thermodynamically favoured, hence being an argument for possible stronger coordination and larger complexes of PEGDME$_{500}$ to Mg^{2+} compared to the monodentate ligand PC. Ultimately, the combination of all before mentioned effects lead to the lower ionic conductivity of **4-cross-PEGDME$_{500}$** over **4-cross-PC**.[256]

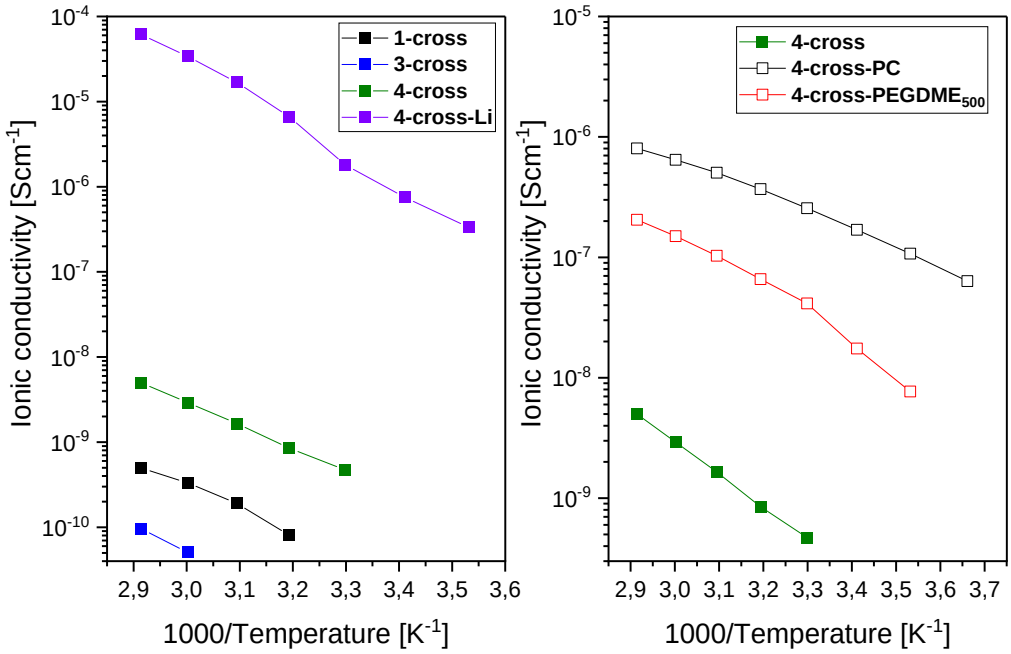

Figure 12: Temperature dependent ionic conductivity of solid polymer electrolytes **1-cross**, **2-cross**, **3-cross**, **4-cross** and **4-cross-Li**. GPE with 50 wt. % of PC (**4-cross-PC**) and quasi-solid SIC with 50 wt,% PEGDME$_{500}$ (**4-cross-PEGDME$_{500}$**). Filled symbols correspond to SPEs and empty symbols to GPEs.

Since SICs are supposed to benefit from a high transference number $t^{+/-}$, spectating solely the ionic conductivity is not sufficient to judge on their ion transport properties. Thus, polarization measurements were conducted for **4-cross-PC** and **4-cross-PEGDME$_{500}$** and their corresponding lithium derivatives (**4-cross-Li-PC** and 4-**cross-Li-PEGDME$_{500}$**) in symmetric Mg||Mg or Li||Li cell setup with an applied potential of 500 mV and 10 mV at 80 °C (Figure 13). DC polarization experiments were conducted by Evan´s method to determine lithium transference numbers (t^{+}_{Li}) and magnesium transference numbers (t^{+}_{Mg}). The transference number was calculated by following equation 2:

$$t^{+} = \frac{I_{SS}}{I_{0,pol}} \frac{\Delta V - R_0 I_{0,pol}}{\Delta V - R_{SS} I_{SS}} \qquad \text{Eq. 2}$$

ΔV was the polarization potential, R_{SS} and I_{SS} were the surface resistance after polarization and the steady-state current, respectively. R_0 and $I_{0,pol}$ were the surface resistance and initial current before polarization. To validate $I_{0,pol}$, $I_{0,cal}$ was calculated by Ohmic law (equation 3),where $I_{SS}/I_{0,pol}$ has to be equal to $I_{SS}/I_{0,cal}$.

$$I_{0,cal} = \frac{U}{R_0} \qquad \text{Eq. 3}$$

For the SICs **4-cross-PC** and **4-cross-PEGDME$_{500}$** the given restrictions for equation 2, as low ion dissociation are not full filled. Furthermore, the ratios of $I_{SS}/I_{0,Pol}$ = 0.0027 and $I_{SS}/I_{0,cal}$ = 0.1 for **4-cross-PC** and for **4-cross-PEGDME$_{500}$** $I_{SS}/I_{0,Pol}$ = 0.018 and $I_{SS}/I_{0,cal}$ = 0.18 strongly differ from each other, therefore no reliable t^{+}_{Mg} could be calculated. The discrepancy between $I_{0,cal}$ and $I_{0,Pol}$ might be explained by several effects. On the one hand, $I_{0,cal}$ was calculated by fits with limited numbers of data point due to the used EIS parameters and high surface resistances. On the other hand, a passivation of deposited Mg on the surface might lead to higher $I_{0,Pol}$. The results of the polarization experiments are given in Figure 13. For the lithiated SICs, **4-cross-Li-PC**/-**PEGMA$_{500}$**, $I_{0,Pol}$ and $I_{0,cal}$ were found to be nearly identical and with larger I_{SS}/I_0 ratios of $I_{SS}/I_{0,Pol}$ = 0.92 and $I_{SS}/I_{0,cal}$ = 0.92 for **4-cross-Li-PC** and $I_{SS}/I_{0,Pol}$ = 0.68 and $I_{SS}/I_{0,cal}$ = 0.65 for **4-cross-Li-PEGDME$_{500}$** (Table 16 and Table 17). Based on the equation 2 t^{+}_{Li} of 0.92 and 0.66 were calculated for **4-cross-Li-PC** and **4-cross-Li-PEGDME$_{500}$,** respectively, indicating mainly Li^{+} mobility and therefore successful SIC synthesis. This results are in the range of literature reported borate-based SICs (e.g. t^{+}_{Li} of 0.58 and 0.97).[243,257]

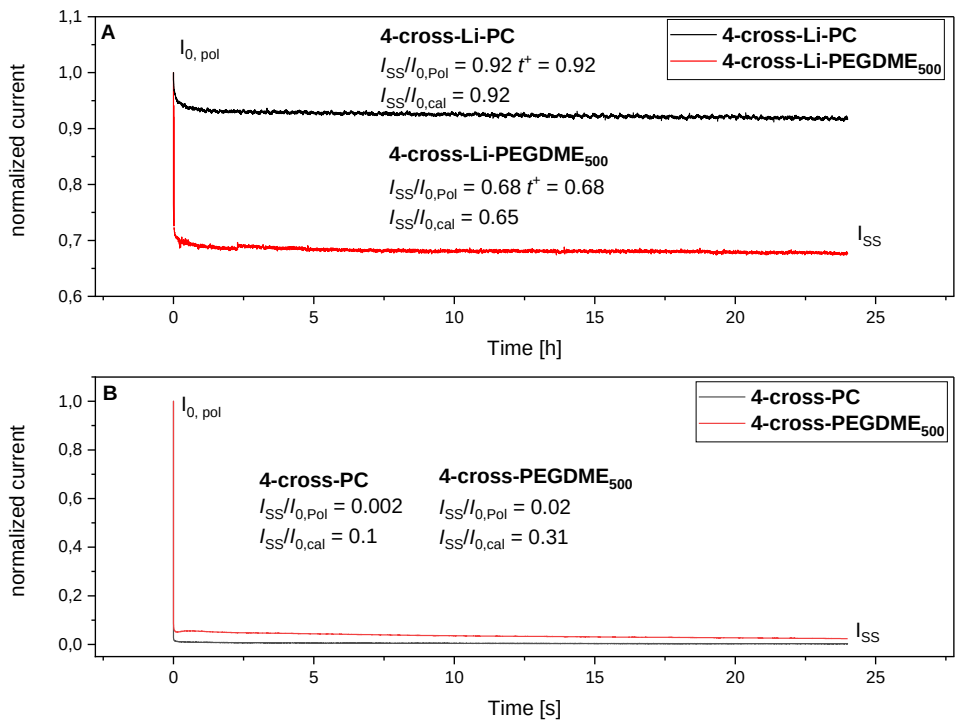

Figure 13: A) Polarization plot with normalized currents of A) **4-cross-PC** and **4-cross-PEGDME$_{500}$** B) **4-cross-Li-PC** and **4-cross-Li-PEGDME$_{500}$**.

To determine the oxidative stability of **4-cross-PC** and **4-cross-PEGDME$_{500}$**, linear sweep voltammetry measurements in Mg||SS cells (Figure 14) were performed. For **4-cross-PC** an oxidative stability up to 1.2 V vs Mg/Mg^{2+} and **4-cross-PEGDME$_{500}$** up to 2.7 V vs Mg/Mg^{2+} was found. A similar trend was also observed by Kim *et al.* who measured the stability oxidative stability against SS for liquid electrolytes (0.5 M $Mg(ClO_4)_2$) with values over 3.5 V vs Mg/Mg^{2+} for triglyme, which was found to be significantly larger than for PC with 2.4 V.[252]

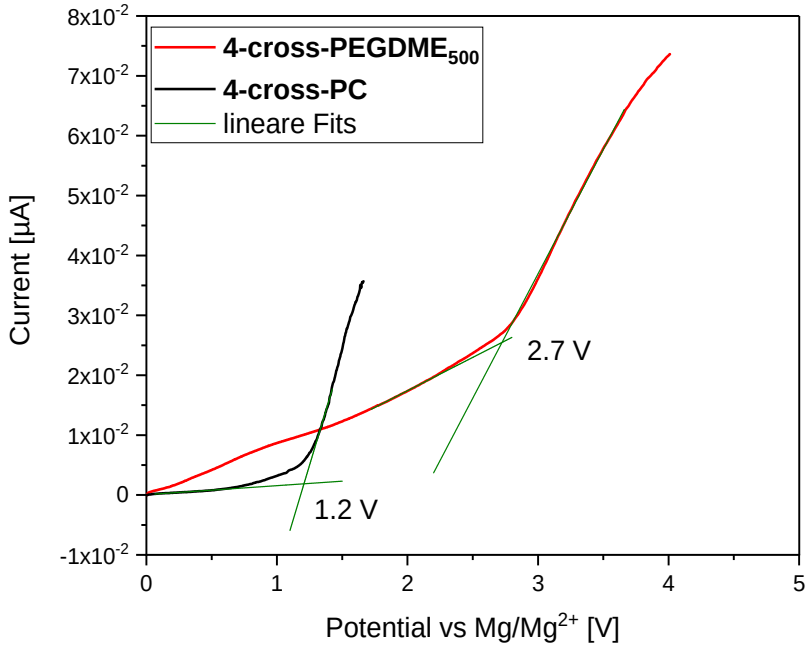

Figure 14: LSV spectra of **4-cross-PEGDME$_{500}$** and **4-cross-PC** in Mg||SS cell.

Lastly, plating/stripping experiments with magnesium-metal anodes were conducted to verify the Mg^{2+} transport abilities of **4-cross** and its gel-SICs **4-cross-PC** and **4-cross-PEGDME$_{500}$**. Subsequently, measurements were performed at 80 °C with a plating/stripping time of 1 h each. The first measurements were carried out at a current density of 0.1 µA cm^{-2} for **4-cross-PC** and **4-cross-PEGDME$_{500}$** and 0.01 µA cm^{-2} for **4-cross** (Figure 15), respectively. However, **4-cross** did not show any Mg/Mg^{2+} deposition, probably caused by extreme polarization, whereas in contrast to this **4-cross-PC** and **4-cross-PEGDME$_{500}$** featured a reversible Mg^{2+}/Mg decomposition for 50 cycles. Herein, **4-cross-PC** had an initial plating/stripping overpotential of about 0.5 V with a constant increase to 1.7 V for the 50th cycle, while **4-cross-PEGDME$_{500}$** started with an overpotential of about 0.5 V for the first cycle and increased to 1.5 V for the 50th cycle. Thus, both GPEs revealed similar overpotentials independent of the additive, which leads to the assumption that the stripping-plating behaviour is mainly dominated by the low Mg^{2+} conductivity as a result of a low ion dissociation. The latter is demonstrated by the tremendous increase of the plating/stripping overpotential, which was mentioned for other PE systems before and reveals the high reactivity of magnesium anodes.[137] The absence of Mg/Mg^{2+} decomposition for **4-cross** even at lower current densities compared to **4-cross-PC** and **4-cross-PEGDME$_{500}$** could be explained by the significantly lower ionic conductivity and Mg^{2+} mobility as well as low ion dissociation as explained in the previous chapter hindering Mg/Mg^{2+} deposition. Further reports of PEs and their

applications in magnesium batteries dealt with gel/gel-composite PVdF-HFP electrolytes at current densities of 0.05 to 0.2 mA cm^{-2} mentioning stripping/plating overpotentials of 0.15 V to 0.31 V.[137,258] Deivanayagam and colleagues performed galvanostatic measurements on PVdF-HFP:TiO_2:$Mg(ClO_4)_2$:1-buty-l-methylpyrrolidinium TFSI (Pyr_{14}-TFSI) composites with ratios of 0.3:0.1:1:0.75 wt.%, whereas Mesallam *et al.* focused on PVDF:$MgBr_2$:tetryglyme of 1:0.6:0.5 wt%.[137,258] These two PEs showed reversible plating/stripping, in sharp contrast to **4-cross-PC/PEGDME$_{500}$**, with higher current densities in the range of hundreds of microampere instead of nanoampere and lower overpotentials mainly caused by their significantly higher ionic conductivity, lower Mg^{2+}-polymer interaction and higher ion dissociation than **4-cross-PC** and **4-cross-PEGDME$_{500}$**.

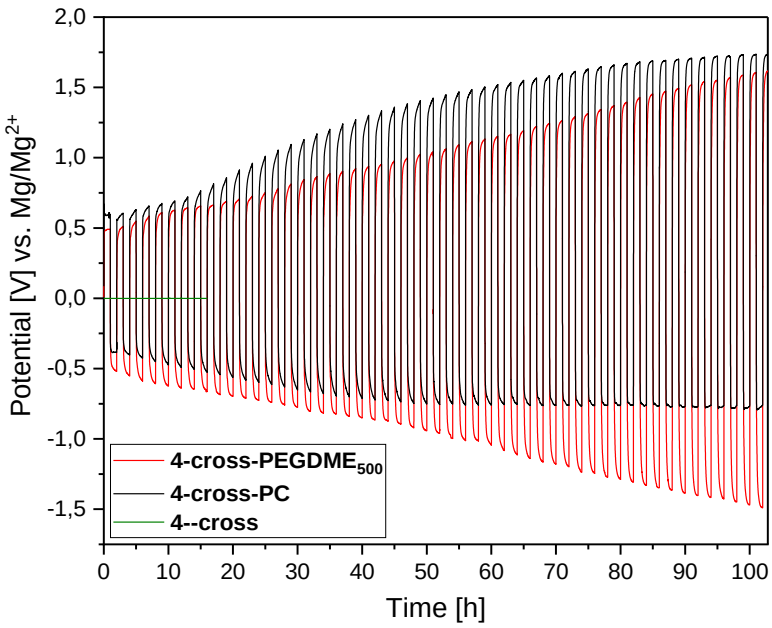

Figure 15 Plating/stripping measurements at 0.1 µA cm^{-2} and 80 °C of **4-cross-PEGDME$_{500}$**, **4-cross-PC** and at 0.01 µA cm^{-2} at 80 °C of **4-cross** against symmetric Mg electrodes.

1.6.5 Magnesium-lithium dual-salt polymer electrolytes

To further improve the Mg^{2+} transport abilities and plating/stripping behaviour, magnesium-lithium dual-salt SICs were prepared with [Mg^{2+}]:[Li^{+}] (**4-cross-PC-Li-Mg 1:1** and **4-cross-PC-Li-Mg 2:1**) ratios of 1:1 and 1:2 and 50 wt.% PC (Scheme 13).

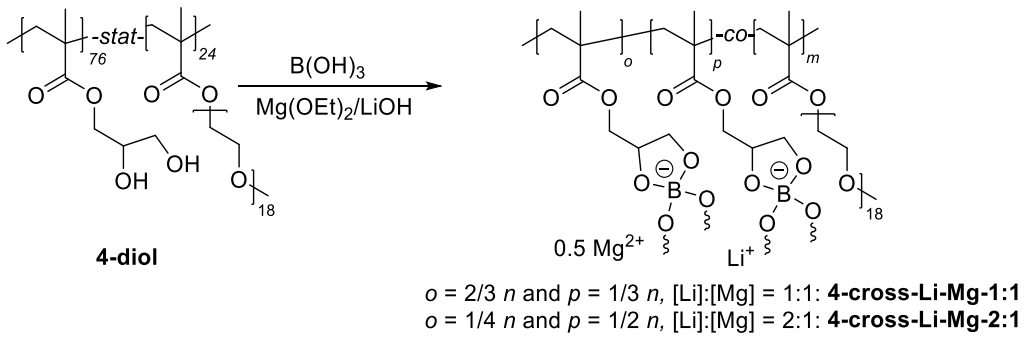

Scheme 13: Schematic synthesis of **4-cross-PC-Li-Mg 1:1** and **4-cross-PC-Li-Mg 2:1**.

Furthermore, a SIC, containing a 50 wt.% 1 M LiTFSI-PC solution, was also investigated (**4-cross-PC-LiTFSI**). Because **4-cross-PC** and **4-cross-PEGDME$_{500}$** had a similar performance at 0.1µA cm^{-2} in regard to cycle stability and overpotentials further experiments focused on **4-cross-PC**, due to its higher ionic conductivities. The measurements were carried out at various current densities, 0.01, 0.05, 0.1, 0.5, 1, 10 µA cm^{-2}, with 6 plating/stripping cycles each current (Figure 16).

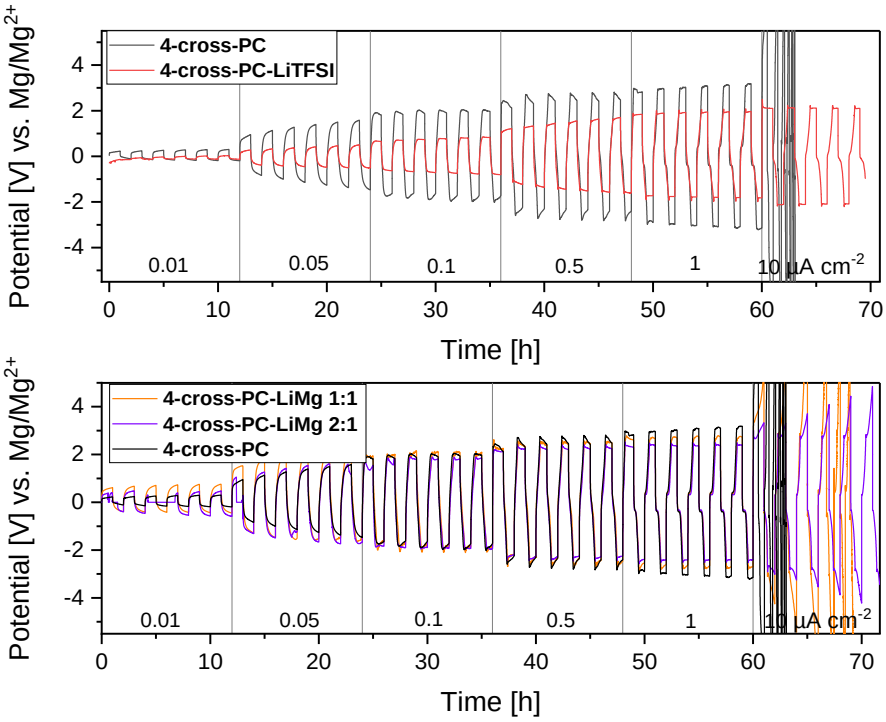

Figure 16. Plating/stripping measurements at 0.01, 0.05, 0.1, 0.5, 1 and 10 µA cm^{-2} and 80 °C of **4-cross-PC**, **4-cross-PC-LiTFSI**, **4-cross-PC-Li-Mg 1:1** and **4-cross-PC-Li-Mg 2:1**.

The reference system **4-cross-PC** had an initial plating/stripping potential of 0.2 V at 0.01 µA cm^{-2} and reached a maximum current density of 1 µA cm^{-2}, plating/stripping potential of 3.1 V, before reaching the cut-off voltage of 10 V. The addition of LiTFSI significantly decreases the

plating/striping potential at all current densities (1.9 V at 1 µA cm^{-2}) but also increased the possible current densities up to 10 µA cm^{-2} (2 V). Furthermore, in the first 3 cycles some pre-conditioning processes occurred because a fluctuating of the potential over the plating and stripping processes were detected before stabilizing. Those pre-conditioning process could be explained by lithium adsorption on the magnesium electrode surface having a similar effect as Cl^-, which are known to adsorb at the magnesium surface and to reduce the formation of a passivation layer.[259] **4-cross-PC-Li-Mg 2:1** performed with slightly lower plating/stripping potentials compared to **4-cross-PC-Li-Mg 1:1** but higher than **4-cross-PC-LiTFSI**. Comparing the dual-salt SICs to **4-cross-PC**, two distinctive segments can be seen at lower and higher currents. At lower currents the plating/stripping potentials of **4-cross-PC** were lower compared with the hybrid SICs but with an inverse behaviour at higher currents, where **4-cross-PC-Li-Mg 1:1** and **4-cross-PC-Li-Mg 2:1** performed with lower potentials. The plating/stripping potential of **4-cross-PC-Li-Mg 1:1** was higher for densities up to 0.05 µA cm^{-2} (1.8 V) before similar potentials were detected between 0.1 to 0.5 µA cm^{-2} (2 and 2.6 V) and 2.6 V at higher current density (1 µA cm^{-2}). **4-cross-PC-Li-Mg 2:1** showed a similar behaviour with higher plating/stripping potential at 0.01 µA cm^{-2} (0.6 V) and similar potentials between 0.05 and 0.5 µA cm^{-2} (1.3 and 2.4 V) but at higher current densities lower potentials of 2.4 V (1 µA cm^{-2}) and between 3.37 to 4.7 V (10 µA cm^{-2}) were seen.

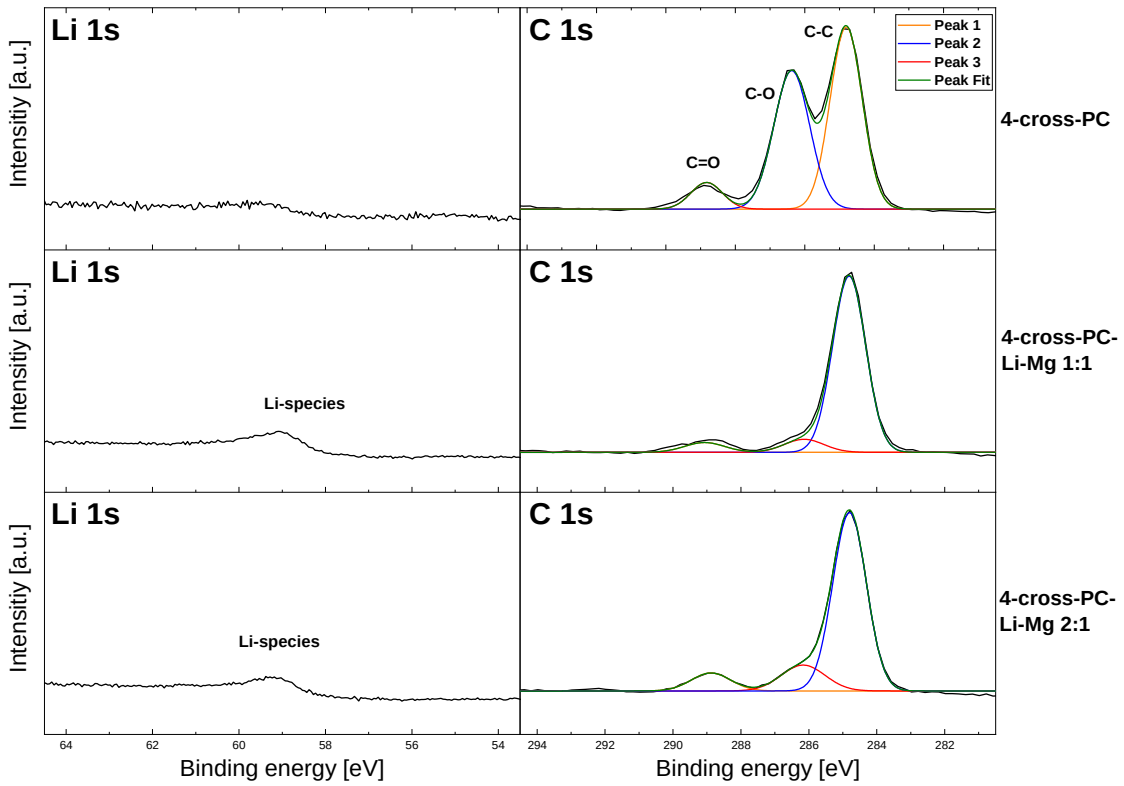

Figure 17: Li 1s and C 1s XPS spectra of the magnesium electrode surface after 13 cycles at 0.1 µA cm^{-2} in a Mg||Mg cell.

The importance of the electrode composition was part of interest for magnesium but also MLHB. Tang and coworkers assigned an enhanced long-cycle stability of a MLHB to shuttle effects and a beneficial SEI formation caused by Li^+ and lithium-containing SEI.[59] Therefore, XPS measurements of the magnesium metal electrodes were performed in cooperation with Dr. Zhixuan Wei from university Gießen for **4-cross-PC**, **4-cross-PC-Li-Mg 1:1** and **4-cross-PC-Li-Mg 2:1** after 13 cycles at 0.1 µA cm^{-2} (Figure 99). The resulting Li 1s, C 1s, Mg 2s and O 1s XPS spectra are shown in Figure 17 and Figure 18. In the Li 1s XPS spectra the occurrence of Li-species on the magnesium electrode surface for the dual-salt electrolytes were seen at 59 eV and assigned to carbonates as reported by Oswald and coworkers.[260] This observation is in good agreement to the reports of Tang and coworkers, thus a lithium-containing surface can be assumed.[59] Furthermore, for all three electrolytes organic decomposition products were seen in the C 1s spectra, which only differs in the ratios of the binding energies assigned to C-C, C-O and C=O, respectively (at about 284.8, 286.4 and 288.8 eV) (Table 15).[261]

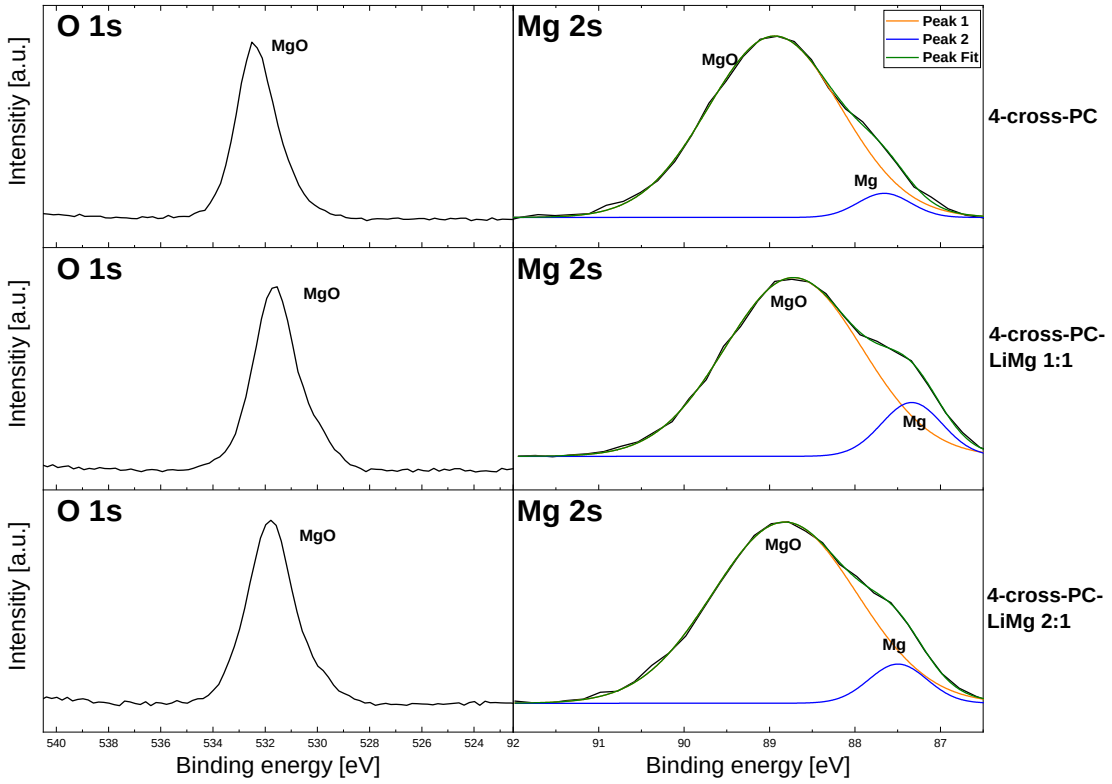

Figure 18: O 1s and Mg 2s XPS spectra of the magnesium electrode surface after 13 cycles at 0.1 µA cm^{-2} in a Mg||Mg cell.

Similar observations were made for all three electrolytes in the 1s O XPS spectra (Figure 18), where oxide was observed at 532 eV.[261] The formation of MgO was also revealed by 2s Mg, where two peaks at about 87.5 and 89 eV were detected. Those were assigned to MgO (89 eV)

and to metallic magnesium for the lower binding energy as reported by Parambath and coworkers.[261] The ratio of metallic magnesium was significantly lower, which indicates a nearly complete oxidation of magnesium on the surface for all three samples. However, a slightly higher ratio of metallic magnesium to oxide can be found for the dual-salt electrolytes (5:95 and about 10:90). Considering the plating/stripping experiments and XPS results, the lower plating/stripping potentials at higher current densities for the dual-salt electrolytes could be explained by the formation of lithium-containing species on the magnesium electrodes surface. Nevertheless, the high degree of oxidation and decomposition of the electrodes surface leaded to only a minor decrease in potential at higher current densities. At lower current densities no effect of the lithium-containing surface was assumed, due to the higher potentials for the dual-salt electrolytes. Instead, the lower Mg^{2+} concentration might increase the plating/stripping potential and were more dominant than the effect of the lithium. To overcome those issues the addition of higher amounts Li^{+} seem to be necessary, indicated by **4-cross-PC-LiTFSI** and comparing **4-cross-PC-Li-Mg 1:1/2:1** to each other.

1.6.6 Recapitulation

Herein, solid crosslinked, borate-based SICs were synthesized and characterized as electrolytes either Li^+, Mg^{2+} or both as cations. The comonomer ratio and architecture of $PEGMA_x$ was investigated and the borate anion to be the best in **4-cross**, where higher ratios of $PEGMA_x$ and chain length support ion transport. An overall, low ion dissociation and strong borate-anion to cation interaction were recognized in those systems, which limits the ion transport (about 10^{-9} S cm^{-2}) and inhibits reversible magnesium plating and stripping.

Therefore, GPEs with $PEGDME_{500}$ and PC as additive were investigated with moderate ion transport (about 10^{-6} S cm^{-2}) but high t^+_{Li} up to 0.92, which underline the formation of SIC. The exchange of Mg^{2+} by Li^+ of PC-based SICs and the synthesis of Li-Mg-hybrids SICs with [Li]:[Mg] ratios of 1:1 and 2:1 was further part of interest. The dual-salt electrolytes lead to higher plating/stripping potentials at low currents discussed in the context of XPS electrode surface measurements. The higher potentials at lower currents were suggested to be caused by the lower Mg^{2+} concentration on the one hand. But the lower potentials at higher current densities were explained by the formation of lithium-containing species at the electrode surface on the other hand. Additionally, with increasing Li^+ concentration a strong decrease in potentials were seen, incorporating 1M LiTFSI:PC solution into **4-cross**. Consequently, fundamentals to dual-salt SICs were set to gain knowledge to their performance in MIBs in regards of polymer design and Mg^{2+}/Li^+ concentrations.

1.7 Additive-free Copolymer Electrolytes with Borate Anion Receptors for Magnesium Ion Batteries

In this chapter the focus lays on the synthesis of anion receptor functionalized SPEs instead of SICs described in the previous chapter. Anion receptors are in general classic salt-in-polymer electrolytes but also combine partly the characteristics of SICs´ immobilized anions. *Yamamoto et al.* investigated anion receptors for MIBs based on cPEG networks of different PEG chain lengths and with various magnesium salts.[192] As anion receptor a borate-based Lewis-acid was chosen, which was immobilized by a crosslinking approach. An overall improved ion transference number and increased anion-to-receptor interaction depending on the receptor design and concentration was reported.[263,264]

Therefore, the knowledge towards PEs with electron withdrawing functionalities was expanded to increase the anion-receptor interaction. To do so, two new monomers as anion receptors were copolymerized by a *graft-through* method as schematically shown in Scheme 14.

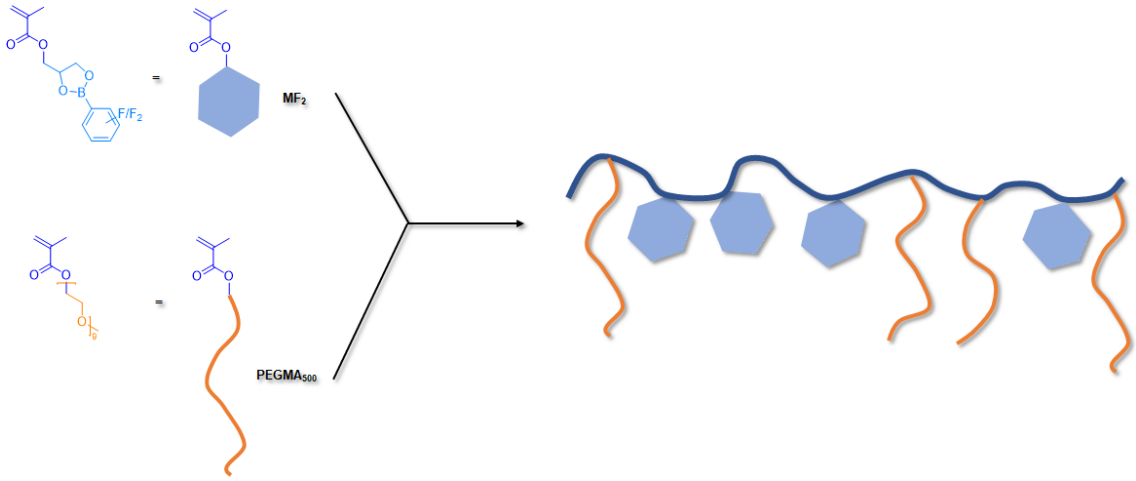

Scheme 14: Schematical illustration of the synthesis of grafted copolymers with anion receptors.

1.7.1 Synthesis

The anion receptor monomer was designed as a methacrylate derivate, which provides compatibility with numerous comonomers and commercial-available RAFT agents. The monomers **MF** and **MF$_2$** were synthesized by condensation reaction of 4-fluorophenyl boronic acid and 2,4-difluorophenyl boronic acid and 2,3-dihydroxypropyl methacrylate (**SMA-diol**), starting from glycidyl methacrylate, as schematically represented in Scheme 15.

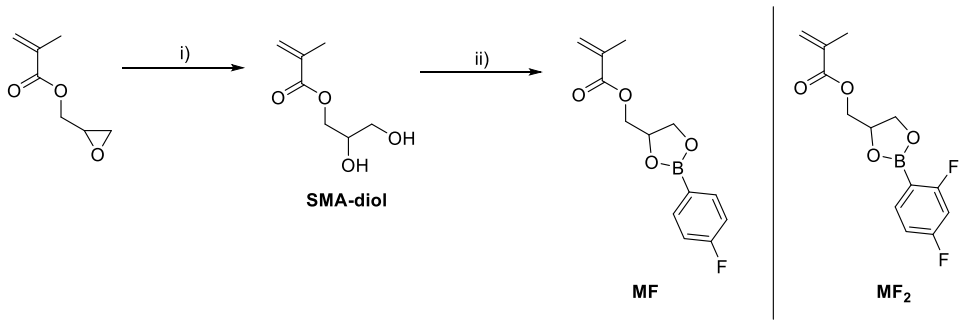

Scheme 15: Monomer synthesis of of the monomers **MF** and **MF₂**. i) 80°C, 16 h in H_2O ii) Molsieves 3Å , 16 h, MeCN, 2,4-difluorophenylboronic acid/4-fluorophenylboronic acid as reported by Wang and coworkers.[265]

Phenylboronic acids and its fluorinated derivatives were selected as starting materials because of their low costs, commercial availability and moderate water stability. When working with fluorinated phenylboronic acids, the decomposition, hydro deboronation, of those in aqueous media has to be considered (Scheme 16).[266] The decomposition ratio increases with increasing degree of fluorination and depends on the substituent position. The ortho position was reported to be the most effective position for the hydrodeboroantion.[266]

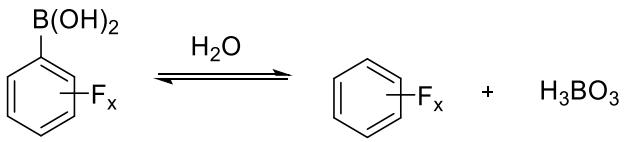

Scheme 16: Decomposition of multifluorinated arylborates in aqueous environment.

Thus, 4-fluorophenyl boronic acid and 2,4-difluorophenyl boronic acid were chosen as starting materials for **MF** and **MF₂** synthesis, because no decomposition products were detected during the polymerization process by ^{11}B-NMR and ^{19}F-NMR (Figure 19).

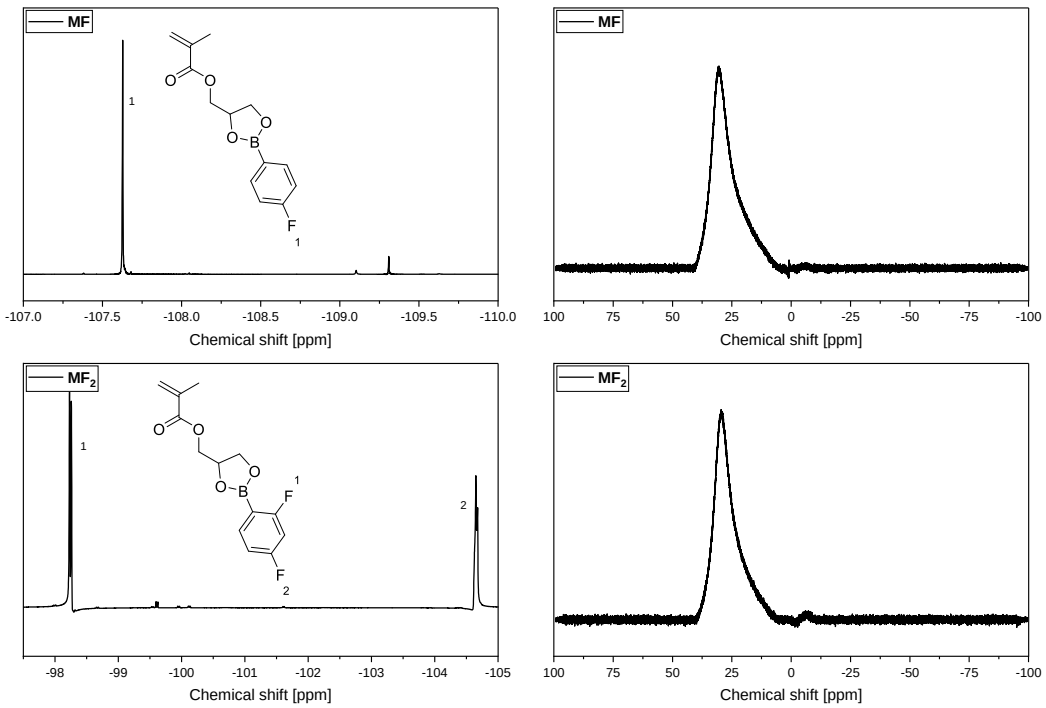

Figure 19: ^{19}F-NMR and ^{11}B-NMR of **MF** in $CDCl_3$ and **MF₂** in DMSO-d_6.

The monomers **MF** and **MF₂** were polymerized by RAFT polymerization under water-free conditions as presented in Scheme 17.

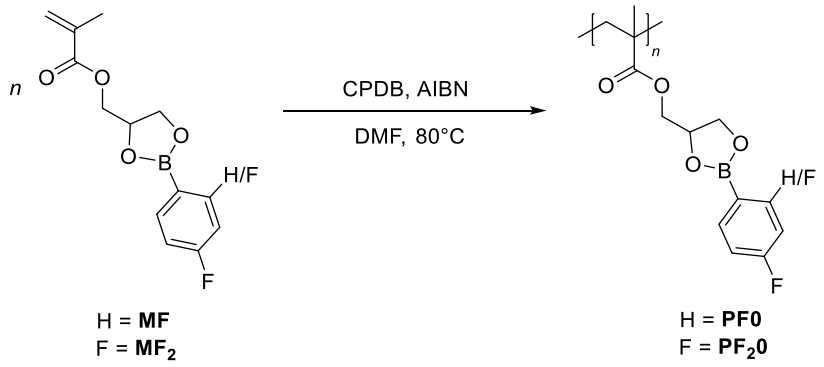

Scheme 17: Polymerization conditions of polymers **PF₂0** and **PF0.**

The successful polymerization of **PF0** and **PF₂0** was confirmed ^{1}H-NMR and ^{19}F-NMR (Figure 20).

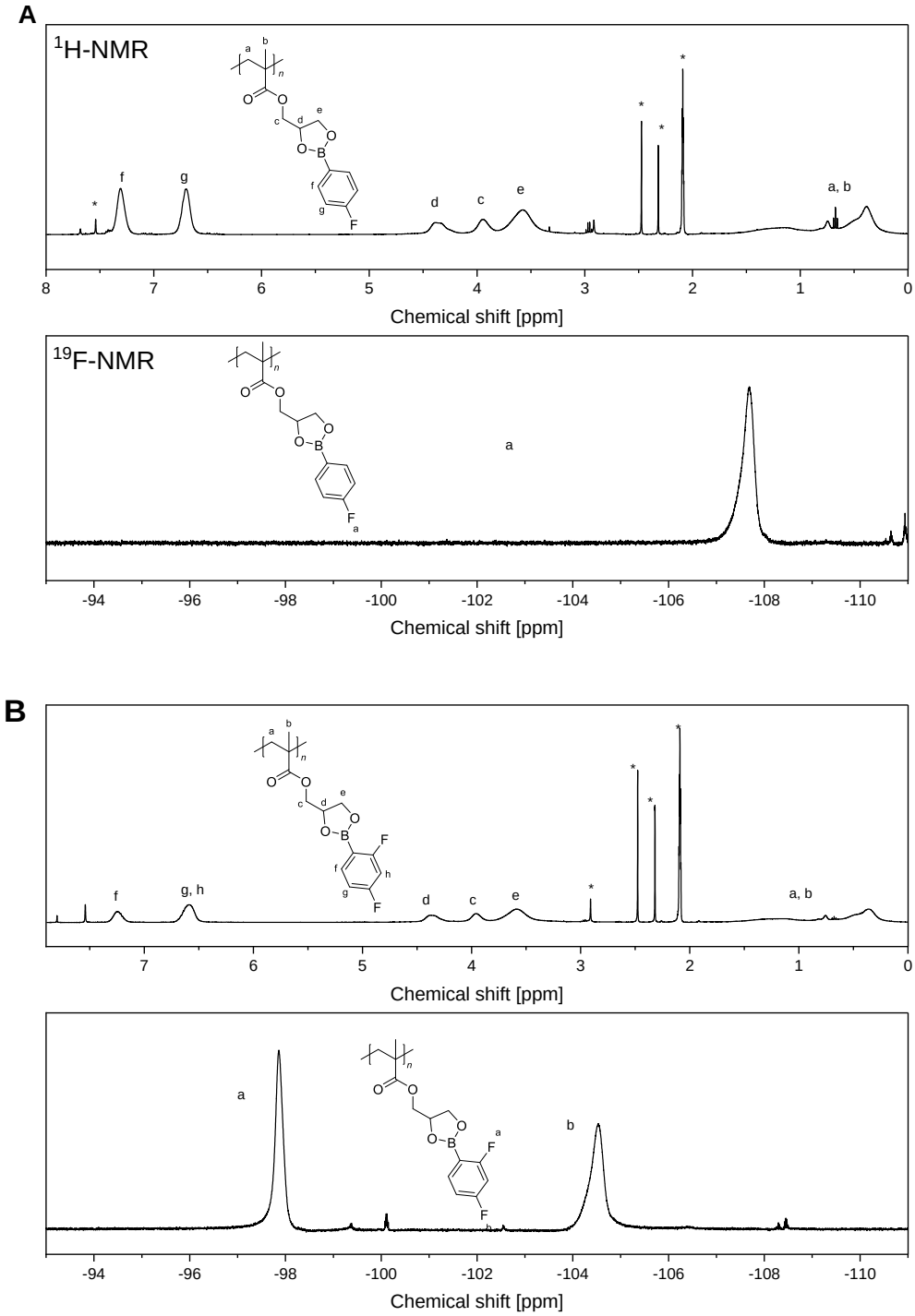

Figure 20: A) ^{1}H-NMR and ^{19}F-NMR spectra of **PF0** in toluene-d_8. B) ^{1}H-NMR and ^{19}F-NMR spectra of **PF$_2$0** in toluene-d_8. * corresponds to solvent signals.

The polymers were further analyzed by SEC, where for **PF$_2$0** a second peak appeared twice the number average molecular weight of the first peak and was assigned to disulfide connected polymers after aminolysis of the RAFT agent by the eluent DMAc (Figure 21).

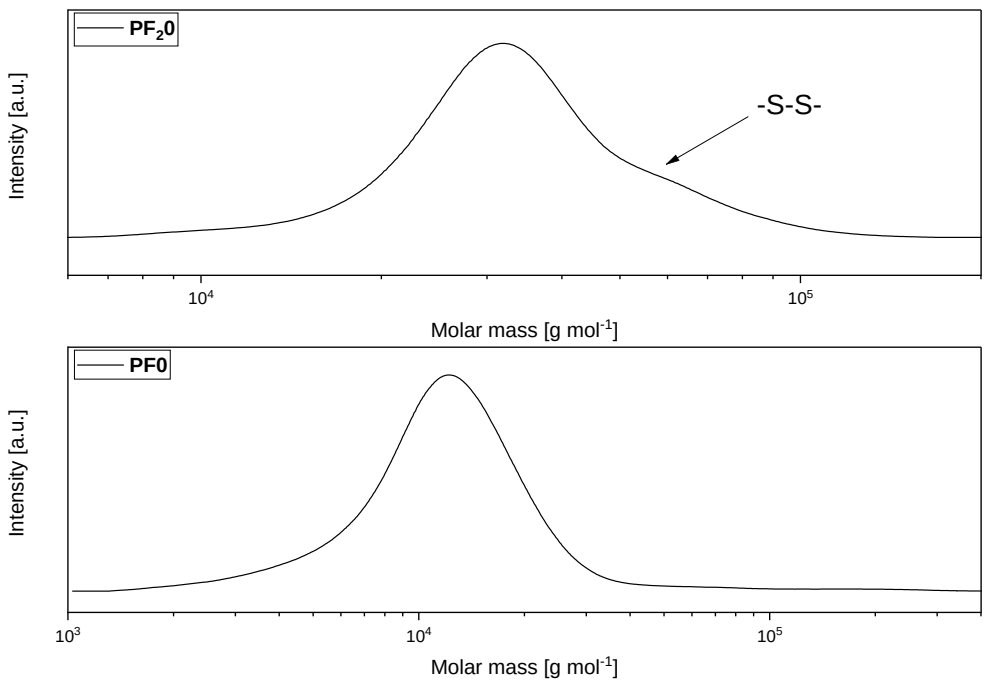

Figure 21: SEC spectra of **$PF_2$0** and **PF0**. The second peak correspond to disulfide linked polymers after aminolysis in the eluent DMAc.

While the monomers **MF** and **MF_2** were stable against non-dried solvents, the corresponding polymers **PF0** and **$PF_2$0** decomposed in the presence of water in solution, although they were stable under ambient conditions. Therefore, the polymers were always handled under water-free conditions inside a glovebox with H_2O and O_2 concentration below 0.5 ppm, when brought into solution. **PF0** and **$PF_2$0** were brittle solid materials thus, several approaches were evaluated to gain a self-standing and flexible PE. Therefore, the formation of polymer blends within PVDF-HFP were tested but led to inhomogeneous films with phase separations. Similar observations were done testing additives such as SN. Instead of preparing PEs by additives, copolymers were synthesized by copolymerization with $PEGMA_x$ (x = molecular weight) (Scheme 18), because it enhanced its flexibility, when forming homogenous films. Further, grafted PEO chains showed a lower crystallinity compared to linear PEG and therefore enhanced ionic conductivity as reported by Morita *et al.*.[166,167] The polymers were named as **PF_2X** with **P** for polymer, F_2 for the 2,4-difluorophenyl functionality and **b** correspond to block architecture. In the first step, the comonomer ratio was optimized for **MF_2** and $PEGMA_{500}$ using RAFT polymerization. Self-standing films only were formed for polymers with comonomer rations larger 70 mol% **MF_2**. However, below 70 mol% **MF_2** only highly viscous materials were formed, which was not further considered. Three different statistic copolymers between 70 to 92 mol% **MF_2** were synthesized

investigated as well as reference polymers with 0 and 100 mol% **MF₂**. Additionally, a block copolymer **PF₂3b** was prepared to consider the effect of architecture.

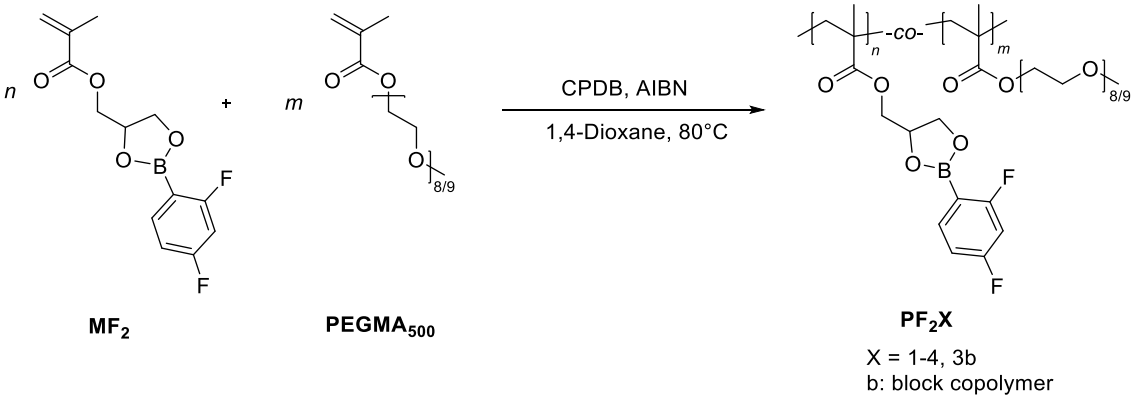

Scheme 18: Polymerization conditions of **PF₂X** with X = 1-4 and 3b.

The successful synthesis of **PF₂X** (X = 0 to 4 and 3b) was proven by ^{1}H-NMR and ^{19}F-NMR spectroscopy (Figure 22). In ^{19}F-NMR spectra, the fluorine signals appeared at -97.9 ppm and -104.6 ppm, which is in good agreement with the literature and prove no hydrolyzation of the borate sidechain.[267] By ^{1}H-NMR the comonomer ratio can be calculated by evaluation the integral values of the *ortho*-proton (7.7 ppm) and the PEGMA methyl end group (3.2 ppm).

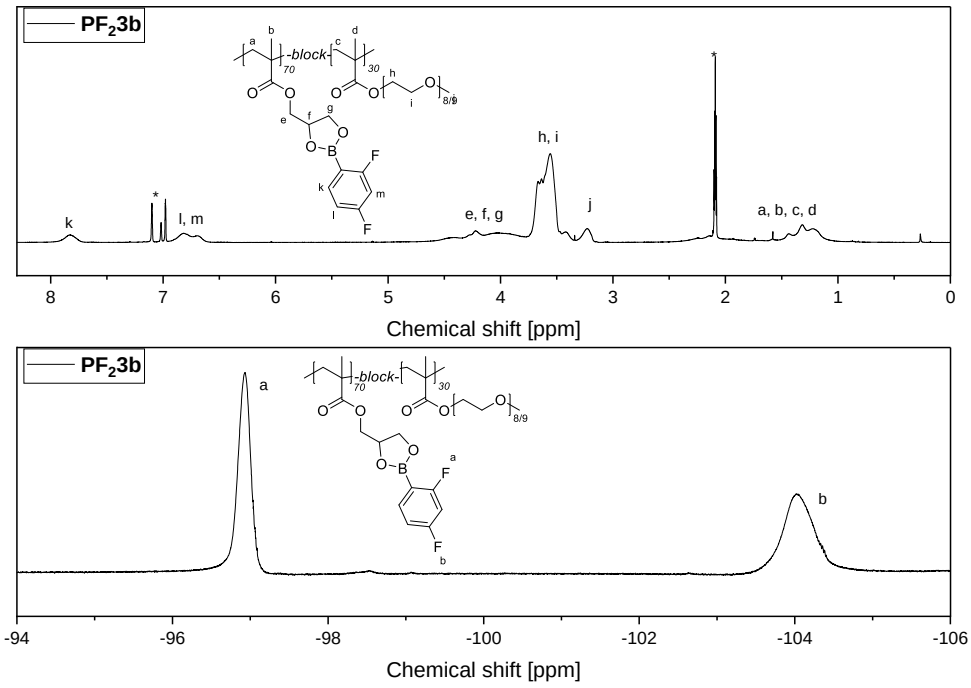

Figure 22: ^{1}H-NMR and ^{19}F-NMR of **PF₂3b** in toluene-d_8.

The polymers were further characterized by SEC and DSC, and the results are presented in Table 9 and Figure 23. Similar to **PF$_2$0** and **PF0** the formation of disulfide linked polymers were observed for **PF$_2$3b**. Therefore, a bimodal distribution, rather unimodal distribution was observed.

Table 9: Structure, glass transition temperture (T_g), comonomer ratio, avarage molare mass (M_n) and dispersity (M_n/M_w) of the random copolymers **PF$_2$X** with X = 0-4 and of the block copolymers **PF$_2$3b**.

	Structure	**Copolymer ratio (MF/MF$_2$:PEGMA$_{500}$) [mol%]**	**M_n [g mol^{-1}]**	**M_n/M_w**	**T_g [°C]**
PF$_2$0	Homo	100:0	19 600	1.48	62
PF$_2$1	Statistic	91:9	31 300	1.25	24
PF$_2$2	Statistic	86:14	34 100	1.21	7
PF$_2$3	Statistic	68:32	29 700	1.16	-29
PF$_2$3b	Block	70:30	29 700	1.27	-22
PF$_2$4	Homo	0:100	30 000	1.22	-52

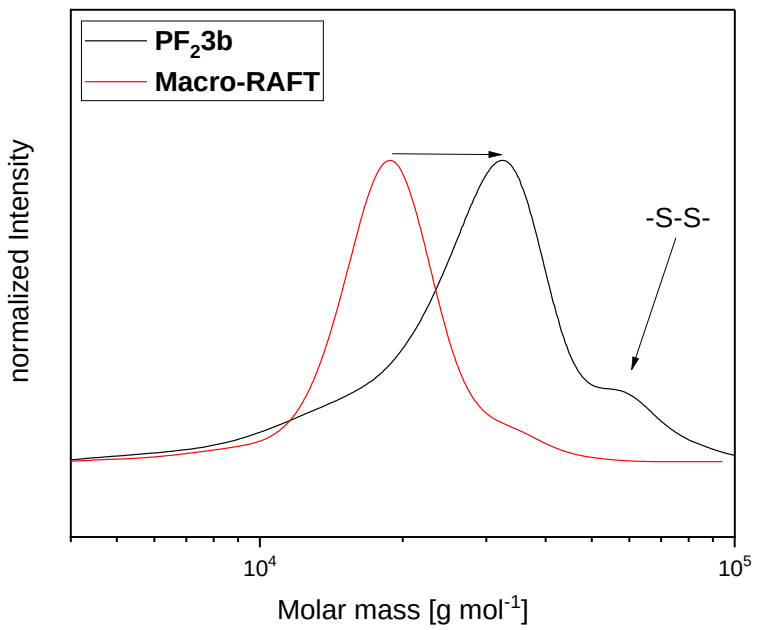

Figure 23: SEC spectrum of the chain extension of **PF$_2$3b**. The second peak correspond to disulfide linked polymers after aminolysis in the eluent DMAc.

The T_g increased with increasing monomer **MF$_2$** ratio between -52 °C (**PF$_2$4**) and 62 °C (**PF$_2$0**), with a minimum for **PF$_2$3** (-22 °C) (Table 9,Figure 24). A decrease in T_g lead to an increase in chain flexibility and an increasing in ionic conductivity. Therefore, a block architecture was tested for **PF$_2$3**, named as **PF$_2$3b** (b represents block architecture). For **PF$_2$3b** also only one T_g (-26 °C)

was found, which was lower compared to all tested statistic copolymers. Therefore, one macroscopic domain was assumed, indicating similar Flory interaction parameters ($\chi_{MF2PEGMA500}N$) ($\chi_{MF2PEGMA500}$ is equal to the effective interaction energy between **MF₂** and $PEGMA_{500}$, N is the degree of polymerization) because for local segregation ($\chi_{MF2PEGMA500}N$) > $(\chi_{MF2PEGMA500}N)_t$ is valid.[268] Therefore, a similar polarity of **MF₂** to $PEGMA_{500}$ was concluded. The block copolymer **PF₂3b** had a lower T_g compared to **PF₂3**, which was potentially caused by larger nanoscaled PEG domains. **PF₂3b** was further used for optimizing the ionic conductivity, having the overall lowest T_g.

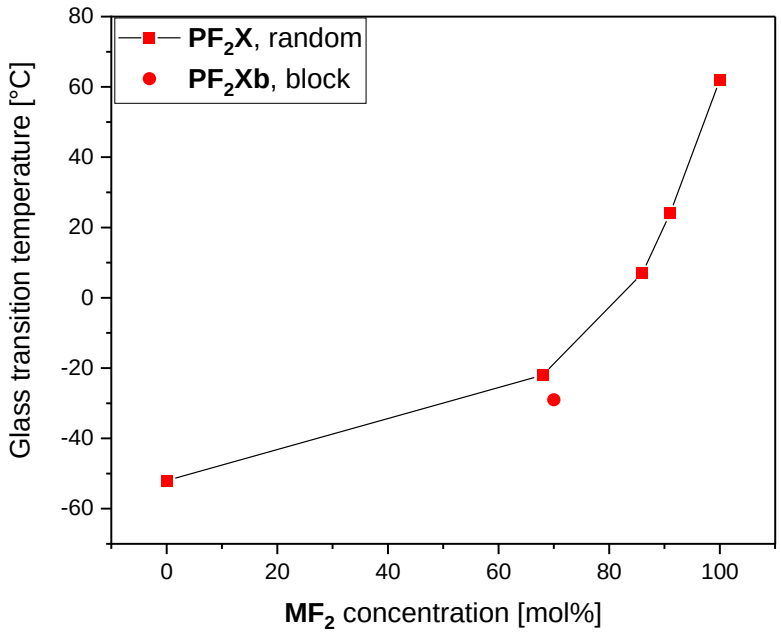

Figure 24: Glass transition temperatures of copolymers at various **MF₂** concentrations.

1.7.2 Electrochemical properties

In the first step, the PEs architecture, comonomer ratio and magnesium salt concentration was optimized for the monomer **MF₂** (Table 9).

PEs based on **PF₂3b** were named as **EF₂3b,** where **E** stands for electrolyte. They were tested with $Mg(TFSI)_2$ concentrations [Mg] referenced to the number of ether functionalities [EO] with 10:1 (**EF₂3bIow**), 25:1 (**EF₂3b**) and 10:1 (**EF₂3bhigh**) [EO]:[Mg]. A picture of **EF₂3b** can be seen in Figure 100. The temperature dependent ionic conductivity between 0 °C to 70 °C is presented in Figure 25, where the highest ionic conductivity was found for a 25:1 [EO]:[Mg] ratio (7.5 10^{-7}

S cm^{-1} at 70 °C and 3.5 10^{-10} S cm^{-1} at 0 °C). The observation of a local maximum in the salt concentration dependent ionic conductivity has been reported by Aziz *et al.* for Mg(TFSI)$_2$-polycarbonate electrolytes.[97] The increase of ionic conductivity of **EF$_2$3blow** to **EF$_2$3b** is contributed to a greater number of charge carriers as reported by Aziz *et al.* before. With further increase in Mg(TFSI)$_2$ concertation, the formation of ion pairs and aggregates was reported, reducing the number of mobile charge carriers and therefore the ionic conductivity.[97]

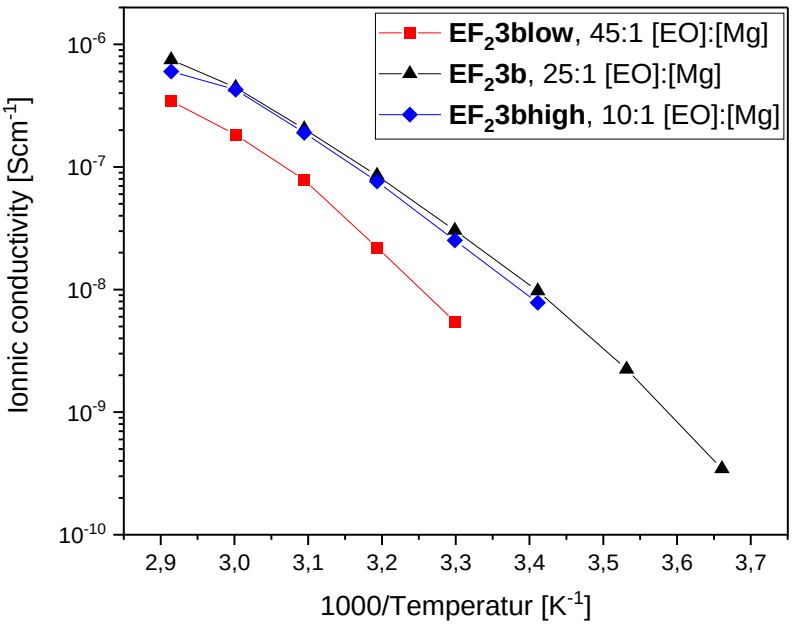

Figure 25: Ionic conductivity of **PF$_2$3b**-based electrolytes with various concentration of Mg(TFSI)$_2$.

Based on these results, polymer electrolytes **EF$_2$X** (X = 0 to 4) were prepared with Mg(TFSI)$_2$ concentration of 25:1 [EO]:[Mg] and characterized by DSC. The measured T_gs increased for all polymers with random architecture (Figure 26), but slightly decreased for **EF$_2$3b** (-31 °C). One possible explanation for the significant change in T_g is the formation of quasi-ionic crosslinking between ether sidechains and cations, which has already been reported for lithium-based electrolytes.[269] In the case of **EF$_2$3b**, the lower T_g could also be explained by a plasticizing effect of Mg(TFSI)$_2$.[97]

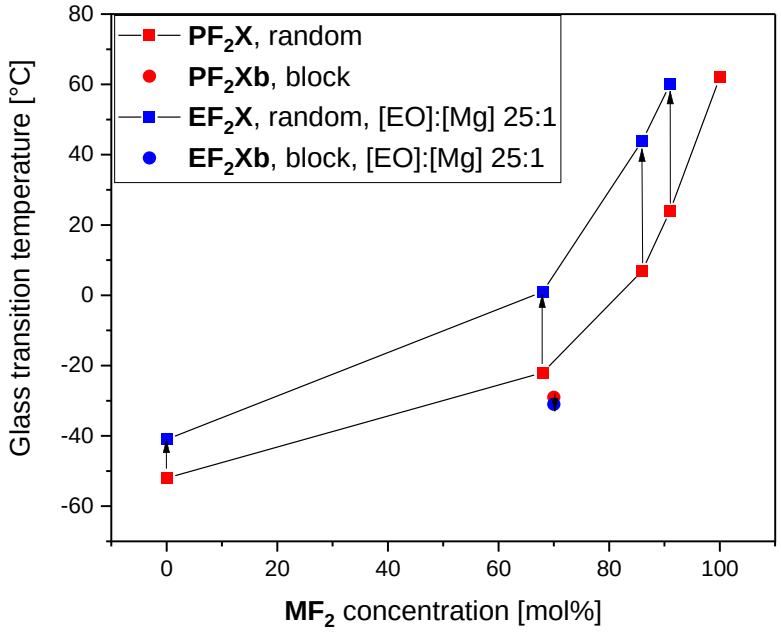

Figure 26: Glass transition temperatures of copolymers at various $\mathbf{MF_2}$ concentrations.

To further compare the copolymer architecture, reference electrolytes were prepared based on the homopolymers $\mathbf{PF_20}$ and $\mathbf{PF_24}$, resulting into $\mathbf{EF_24}$ and a blend electrolyte (**Eblend70**) with 25:1 [EO]:[Mg] $Mg(TFSI)_2$. **Eblend70** was prepared by $\mathbf{PF_20}$ and $\mathbf{PF_24}$ (70:30 mol%) and was unable to form a self-standing film. DSC measurements of **Eblend70** revealed two separated T_gs at -38 °C and 76 °C, respectively, indicating an inhomogeneous material distribution and macroscopic segregation. In the case of $\mathbf{EF_20}$, the T_g also increased with the addition of $Mg(TFSI)_2$ to -39 °C, therefore quasi-ionic crosslinking is assumed as discussed above and was found to be a liquid material at room temperature, whereas **Eblend70** was a granular, sticky material. This stands in contrast to the corresponding copolymers $\mathbf{EF_23}$ and $\mathbf{EF_23b}$, which formed self-standing films.

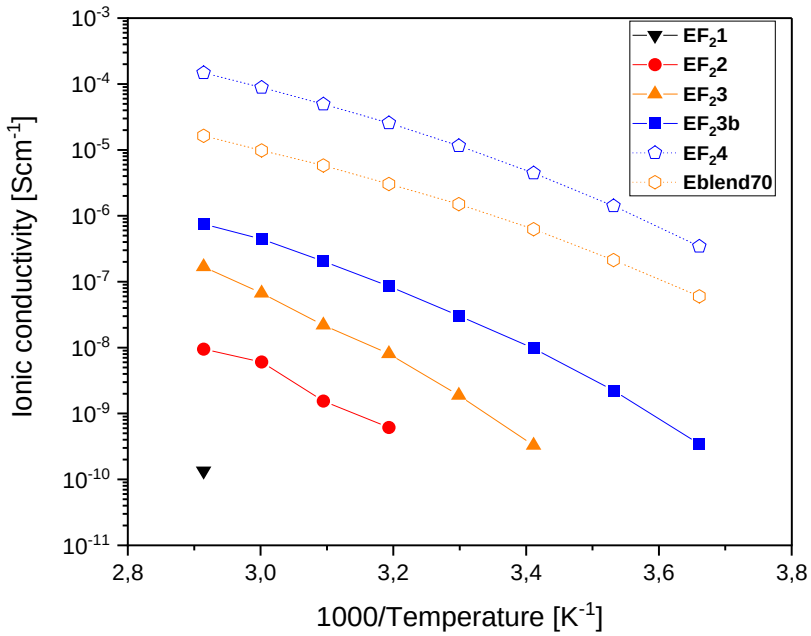

Figure 27: Ionic conductivity of **PF₂X** (X = 1 – 4 and 3b) at constant 25:1 [EO]:[Mg] rations of $Mg(TFSI)_2$ and of the reference material **Eblend70**. Filled symbols are assigned to self-standing materials and empty symbols to partly viscous and viscous materials.

The liquid and partly-liquid character of **Eblend70** and **EF₂4** also explained their significantly higher ionic conductivities (6 10^{-8} and 1.6 10^{-5} S cm^{-1} at 0 and 70 °C (**Eblend70**)) and 3.4 10^{-7} and 1.5 10^{-4} S cm^{-1} (**EF₂4**)) compared to the solid electrolytes **EF₂X** (X = 1-4 and 3b) as shown in Figure 27. **PF₂3b** was found to exhibit the highest ionic conductivity of all polymer electrolytes investigated in this study. The higher ionic conductivity of the block over random architecture could be explained by the lower T_g, enabling higher chain mobility. Following this argumentation **EF₂3** showed a higher ionic conductivity than **EF₂2** and **EF₂1**. Therefore, **EF₂3b** was used for further investigations of the salt effect.

1.7.3 Effect of degree of fluorination and counter anion on the electrochemical performance

For comparison, the monofluorinated polymer (**PF3b**) was synthesized based on the best performing polymer **PF₂3b** (

Table 10).

Table 10: Glass transition temperture (T_g), avarage molare mass (M_n) and dispersity (M_w/M_n) of block copolymers **$PF_2$3b** and **PF3b**.

	Structure	Copolymer ratio (MF/MF_2:$PEGMA_{500}$) [mol%]	M_n [g mol^{-1}]	M_w/M_n	T_g [°C]
$PF_2$3b	Block	70:30	29 700	1.27	-22
PF3b	Block	68:32	24 400	1.30	-32

Further investigations were performed towards the choice of salt, where $Mg(ClO_4)_2$ was chosen besides $Mg(TFSI)_2$ (**$EF_2$3b $Mg(ClO_4)_2$** and **EF3b $Mg(ClO_4)_2$**) because of the higher nucleophilic character of ClO_4^- over $TFSI^-$. Thus, a stronger polymer to ClO_4^- coordination compared to $TFSI^-$ was expected. The chosen concentration was 25:1 [EO]:[Mg], which was found to be the optimum concentration as discussed before **(**Figure 25**)**. As reference materials LiTFSI and $LiClO_4$ were also investigated to validate the differences between monovalent and divalent cations, named **$EF_2$3b LiTFSI/$LiClO_4$** and **EF3b LiTFSI/$LiClO_4$**. PEs with salts containing more nucleophilic anions as $Mg(OEt)_2$ were not accessible due to side-reactions, such as nucleophilic substitution at the aromatic system.

The ion coordination was analyzed by FT-IR, focusing on the area of 1800 to 500 cm^{-1} (Figure 28). In this area significant vibrations were found, corresponding to B-O, C=O, C-O-C, C-F and aromatic C-C bond vibrations. Vibrations assigned to the polymers **$PF_2$3b** and **PF3b** were the asymmetric stretching B-O vibrations at 1350 cm^{-1}, which were reported for phenylboronic acid and pentafluorophenylboronic acid to appear at 1370 cm^{-1} and 1350 cm^{-1}, respectively.[270,271] The aromatic C-C stretching vibrations were reported by Varsanyi to appear between 1625 and 1430 cm^{-1} for phenylboronic acid.[272] Based on their report and theoretical DFT simulations for 4-fluorophenylboronic acid by Erdogdu and coworkers, those aromatic C-C vibrations were assigned to transmittance bands at 1608, 1593 1427 cm^{-1}, respectively.[273] Further, aromatic C-H vibrations were assigned to signals at 851 cm^{-1} based on the report by Erdogdu and colleagues.[273] The carbonyl C=O vibration was assigned to signals at 1728 cm^{-1}, while C-O-C symmetric and asymmetric stretch vibrations occurred at 1105 cm^{-1} based on the reports of Soydan and Wieczorek.[274,275] Significant vibrations corresponding to the anions were C-F vibrations ($TFSI^-$)

and Cl-O vibrations (ClO_4^-) at 1185 and 1080 cm^{-1}.[276] The Cl-O vibration was found to strongly overlap with the polymer signals specifically O-C-O vibrations (Figure 104), therefore no definitive assignment of this vibration was possible. Similar to LiTFSI/$LiClO_4$-based electrolyte the same observations were done $Mg(TFSI)_2$ and $Mg(ClO_4)_2$. The C-O-C vibration at 1085 cm^{-1} for all **EF$_2$3b** and **EF70b** showed no differences in wavenumber compared to the polymers **PF$_2$3b** and **PF3b**, indicating no or only limited Mg^{2+} to PEG coordination. This suggestion is consistent with the decrease in T_g by DSC for **EF$_2$3b**, where no quasi-ionic crosslinking but a plasticizing effect of $Mg(TFSI)_2$ was concluded. For further vibrations at 1728 and 1350 cm^{-1} (C=O and B-O vibrations) no shifts were seen, indicating no changes in the coordination environment. In case of B-O, this indicates no anion coordination or formation of borate anions and therefore only a limited anion trap character was confirmed. Nevertheless, for **EF70b** shifts of aromatic C-C and C-H vibrations at 1608, 1593, 1427 and 851 cm^{-1} were found with the addition of lithium and magnesium salts. The aromatic C-C vibration at 1593 cm^{-1} shifted towards higher and the aromatic C-H vibration at 851 cm^{-1} to smaller wavenumbers. Additionally, the aromatic vibrations at 1427 and 1608 cm^{-1} decreased significantly, indicating an overall change in the electronic environment of the aromatic group, which leaded to the suggestion of salt coordination. Although no conclusion for ClO_4^- salts can be given due to overlapping with other vibrations, $TFSI^-$ had a characteristic and separated C-F signal at 1190 cm^{-1} (Figure 103). The C-F vibration appeared with the addition of $Mg(TFSI)_2$ and LiTFSI, in the **EF3b** spectra at 1185 cm^{-1}. This vibration was red shifted towards lower wavenumbers compared to the pure LiTFSI salt (1190 cm^{-1}) or to the reported wavenumber by Rey *et al.* (1195 cm^{-1}).[276] This indicates a stronger Mg^{2+} to $TFSI^-$ coordination in the electrolyte compared to the TFSI- salts. Moreover, Hambali and coworkers assigned C-F vibration at 1138 and 1195 cm^{-1} to aggregates, assuming mainly the formations of aggregates in **EF$_2$3b/-LiTFSI** and **EF3b/-LiTFSI**.[277] Considering both effects for the aromatic and TFSI vibrations, a coordination of $TFSI^-$ aggregates to the 4-fluorophenyl group can be assumed. This observation stands in sharp contrast to the **PF$_2$3b**-based electrolytes, because in here no shifts were seen for the polymer related vibrations, either for magnesium-based electrolytes nor lithium-based electrolytes. Solely, the appearance of C-F vibrations at 1185 cm^{-1} was seen for **EF$_2$3b** and **EF$_2$3b LiTFSI**, indicating a similar coordination structure as in **EF3b/-LiTFSI** and the formation of aggregates. The absence of changes in the spectra related to the polymer (**PF$_2$3b**) itself indicates a lower polymer-salt interaction for **EF$_2$3b** compared to **EF3b**. This might be explained by the lower electron density of the aromatic 2,4-diflurophenyl group compared to the 4-fluorophenyl group. Additionally, a similar coordination behavior was also assumed for the electrolytes

containing ClO_4^- and $TFSI^-$ anions, due to the similar wavenumbers of C-O-C, C=O, B-O, C-C and C-H vibrations in **EF70b** and **EF$_2$3b**.

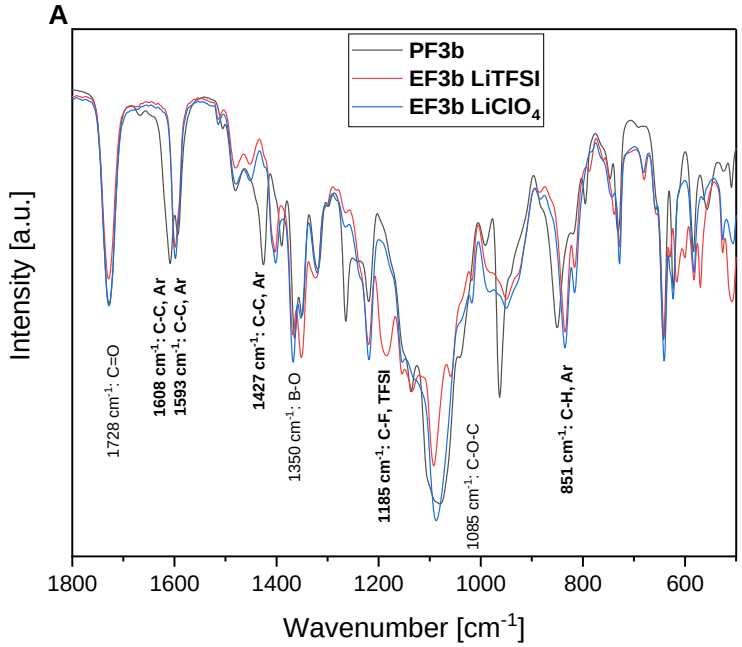

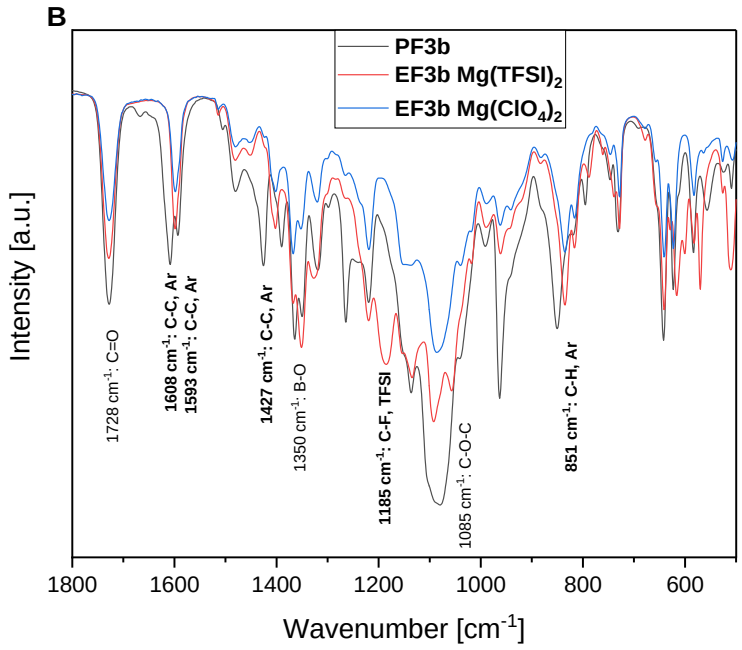

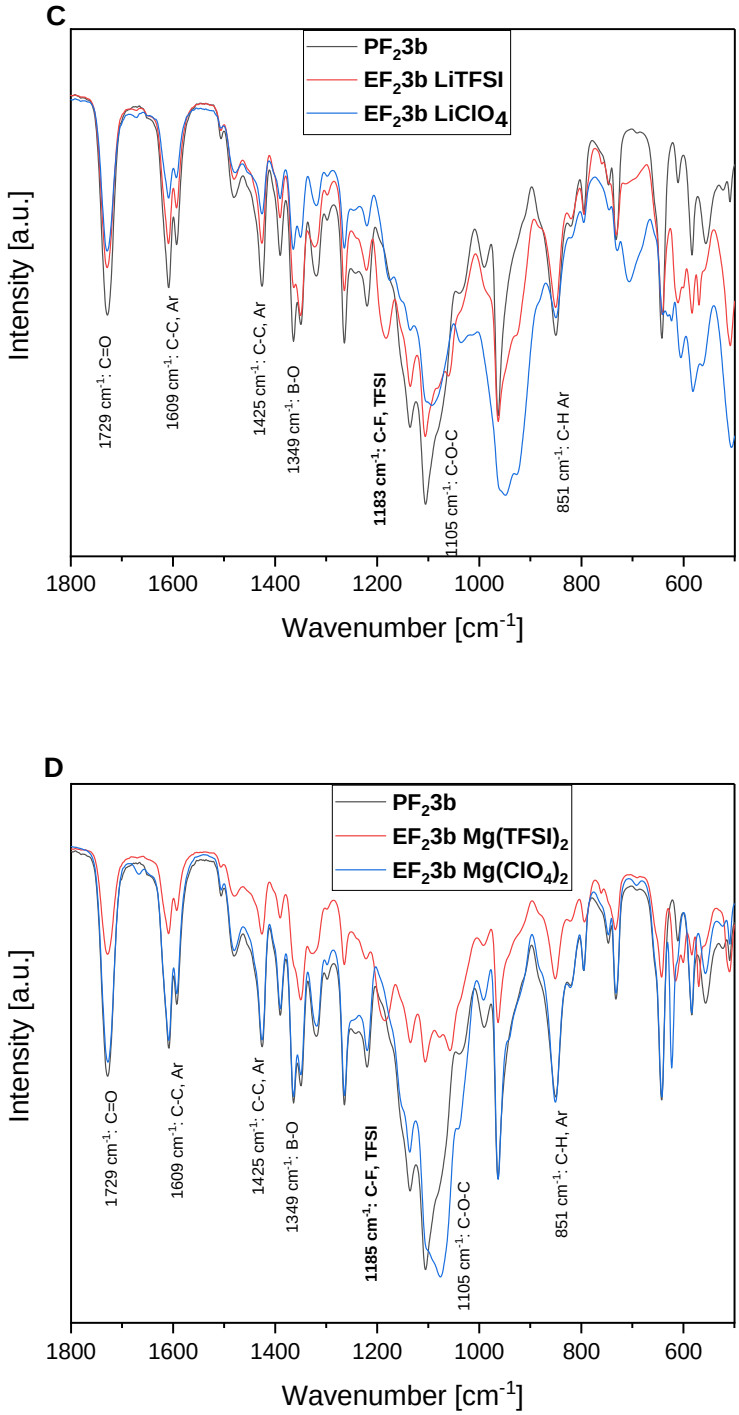

Figure 28: FT-IR spectra between 1800 to 500 cm^{-1} of A+B) **PF3b**-based and C+D) **$PF_2$3b**-based electrolytes containing $Mg(TFSI)_2$, $Mg(ClO_4)_2$, LiTFSI and $LiClO_4$. The bolded vibrations represent shifts compared to the polymers **PF3b**,**$PF_2$3b** and TFSI-, ClO_4-salts.

All eight samples were analyzed by DSC and the results are presented in Figure 29. For the **PF3b**-based electrolytes the addition of Li-salt showed no change in T_g, whereas for $Mg(TFSI)_2$ a

reduction and for $Mg(ClO_4)_2$ an increase could be observed. Compared to this, **$EF_2$3b**, **$EF_2$3b $Mg(ClO_4)_2$**, **$EF_2$3b LiTFSI** showed no change in T_g but for **$EF_2$3b $LiClO_4$** the T_g decreased to -20 °C. Due to the absence of any trends, a complex morphology depending on the polymer properties, cation and anion can be assumed for **PF3b**-based electrolytes. But in case of **$PF_2$3b**-based electrolytes the morphology seems to be stronger affected by Mg-salts than of Li-salt possibly caused by the higher number of anions compared to the lithium salt.

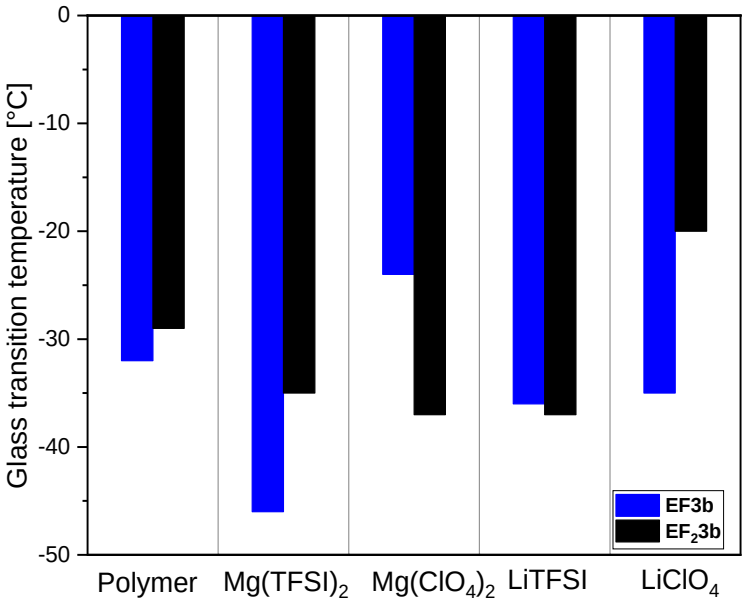

Figure 29: Glass transition temperatures of **$PF_2$3b**-based and **PF3b**-based electrolytes at constant 25:1 [EO]:[Mg]/[Li] rations of various magnesium and lithium salts.

Ionic conductivity measurements were also investigated between 0 and 70 °C similar to the previous electrolytes, where for constant [EO]:[Mg/Li] ratios of 25:1 four different salts were tested ($Mg(TFSI)_2$, $Mg(ClO_4)_2$, LiTFSI and $LiClO_4$) (Figure 30). The electrolytes based on **$PF_2$3b** and **PF3b** performed between 0 °C to 70 °C in a similar range and followed the same trend for all investigated salts ($Mg(ClO_4)_2$, LiTFSI and $LiClO_4$). The lowest ionic conductivities were seen for $Mg(ClO_4)_2$ electrolytes (about 10^{-10} S cm^{-1} at 30 °C) followed by $LiClO_4$ (about 4 10^{-9} S cm^{-1} at 30 °C) and LiTFSI-based systems (about 7 10^{-8} S cm^{-1} at 30 °C). $LiClO_4$-based electrolytes showed higher ionic conductivities than $Mg(ClO_4)_2$-based ones, presumably caused by the higher charge density of Mg^{2+} over Li^+. Similar to this, $TFSI^-$ salts had a higher dissociation constant compared to ClO_4^-, being a less nucleophilic anion, therefore the LiTFSI-based PEs performed with higher ion conductivity compared to $LiClO_4$-based PEs. Only the electrolytes with

$Mg(TFSI)_2$, **$EF_2$3b** and **EF3b**, showed some discrepancy, where for **EF3b** a higher ionic conductivity was determine (7.6 10^{-8} to 3 10^{-8} S cm^{-1} at 30 °C). **$EF_2$3b** exhibited a lower ionic conductivity compared to the LiTFSI-based electrolyte, but higher one than the $LiClO_4$-based system, which might be explained by the higher number of anions due to the divalent character of Mg^{2+} on the one hand, and the harder character of Mg^{2+}on the other hand. Interestingly, **EF3b** instead exhibited an ionic conductivity similar to the LiTFSI-based electrolyte, potentially caused by its lower T_g (-46 to -35 °C) as shown in Figure 29. Nevertheless, the overall ionic conductivity was still low compared to GPEs or PVDF-based systems.[87] This might be traced back to the formation of aggregates and the absence of Mg^{2+} to PEG coordination shown by FT-IR, but also the solid character of the electrolytes.

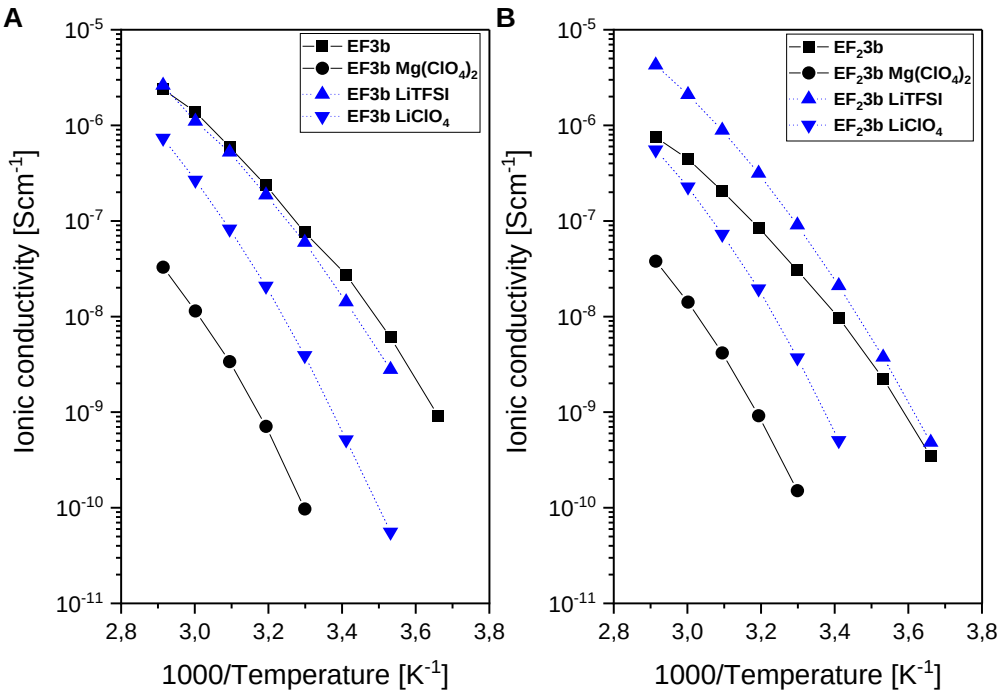

Figure 30: Ionic conductivity of A) **$PF_2$3b**-based and B) **PF3b**-based electrolytes at constant 25:1 [EO]:[Mg]/[Li] rations of various magnesium and lithium salts.

Ion transference numbers (t^+), in addition to other values, as ionic conductivity, electrochemical stability and plating/stripping potentials, are an important property for the electrochemical validation of an electrolyte. DC polarization experiments (Figure 32) were conducted by Evan´s method to determine lithium transference numbers (t^+_{Li}) and magnesium transference numbers (t^+_{Mg}). The transference number was calculated by equation 2. To validate $I_{0,pol}$, $I_{0,cal}$ was calculated by Ohmic law 3,where $I_{SS}/I_{0,pol}$ has to be equal to $I_{SS}/I_{0,cal}$. For all tested magnesium-based electrolytes independent of added salt no t^+_{Mg} could be given because $I_{SS}/I_{0,cal} \neq I_{SS}/I_{0,pol}$. The

discrepancy between $I_{SS}/I_{0,cal}$ and $I_{SS}/I_{0,pol}$ can be traced back to the extremely high surface resistance, caused by the passivation layer on the magnesium metal electrode (Figure 31). On top of that, in Evan´s methods complete ion dissociation was assumed, which was not entirely applicable in this case as shown by FT-IR spectroscopy. Further, high polarization potentials (ΔV = 500 mV) were used due to the high resistances, leading to low $I_{0,pol}$ and I_{SS}, although for Evan´s method low potentials of about 10 mV were required.

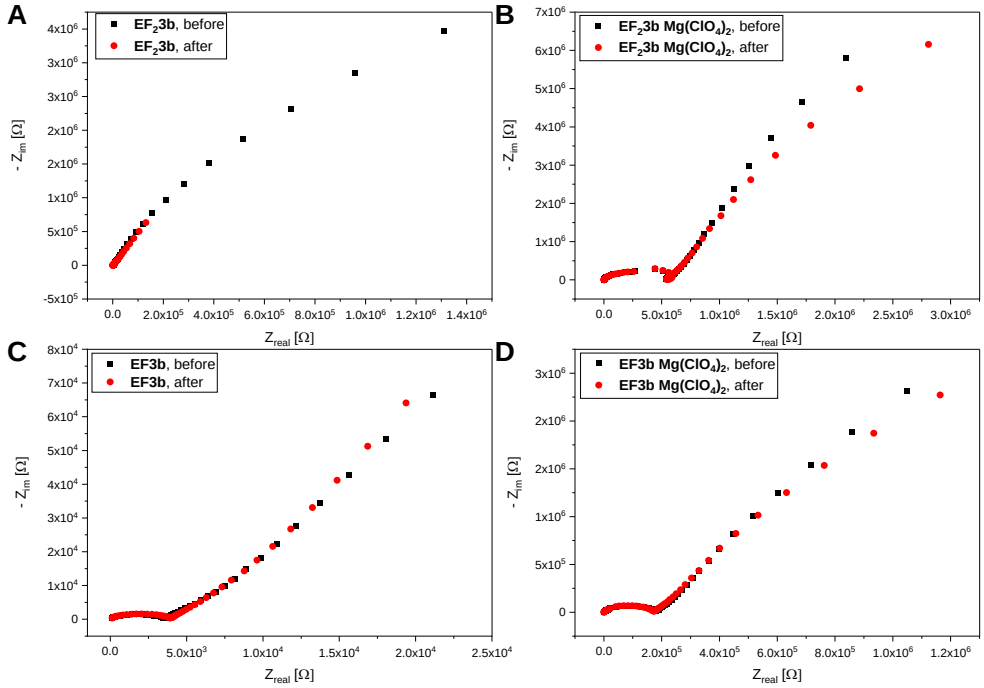

Figure 31: Impedance spectra before and after polarization (ΔV = 500 mV) in Mg||Mg cells for A+C) $Mg(TFSI)_2$ and B+D) $Mg(ClO_4)_2$ based electrolytes.

Therefore, only t^+_{Li} was calculated (Table 16 and Table 17), where $I_{SS}/I_{0,cal}$ was equal to $I_{SS}/I_{0,pol}$ validating the given results. **$EF_2$3b** showed no differences between $Mg(ClO_4)_2$ and $Mg(TFSI)_2$ (t^+_{Li} about 0.24) but significant differences were found for **EF3b**. **EF3b $LiClO_4$** had a higher lithium transference number (t^+_{Li} = 0.4) compared to **EF3b LiTFSI** (t^+_{Li} = 0.22), which led to the suggestion of stronger ClO_4^- to polymer interaction compared to $TFSI^-$ by its higher nucleophilicity. A stronger polymer to $LiClO_4$ interaction in **EF3b $LiClO_4$** over **$EF_2$3b $LiClO_4$** was already suggested by the FT-IR results. However, those t^+_{Li} values are still in the range of comparable PEG containing electrolytes, which were given to be below 0.5.[278] Although no t^+_{Mg} was calculated, it can be suggested, that t^+_{Mg} would be smaller than t^+_{Li}, due to a similar coordination behavior but harder character of Mg^{2+} by HSAB theory. Nevertheless, the results proof the successful synthesis of Lewis acid functionalized PEs as anion traps.

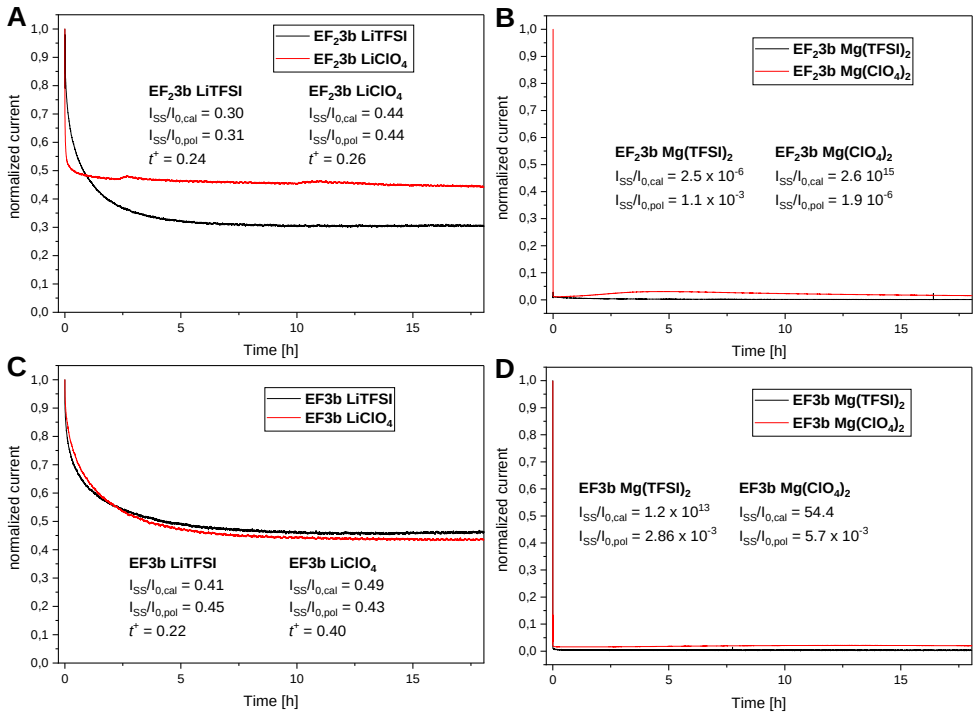

Figure 32: DC-Polarization spectra of A+B) **PF$_2$3b**-based and C+D) **PF3b**-based PEs. Steady-state currents I_{SS} divided by calculated and measured initial currents $I_{0,cal}$ and $I_{0,pol}$ for validation.

Plating and stripping potentials were determined by constant current experiments, applying different current densities of 0.01, 0.05, 0.1, 0.5, 1 and 10 µA cm^{-2} for 6 cycles each in a Mg||Mg cell setup (Figure 33). The plating/stripping time was 1 h each and were conducted with **EF$_2$3b**, **EF$_2$3b Mg(ClO$_4$)$_2$**, **EF3b** and **EF3b Mg(ClO$_4$)$_2$** at 80 °C. **EF3b** (1.2 V at 0.1 µA cm^{-2}) and **EF3b Mg(ClO$_4$)$_2$** (2.4 V at 0.1 µA cm^{-2}) showed higher plating/stripping potentials compared to the **PF$_2$3b**-based electrolytes up to 0.1 µA cm^{-2} (≈0.8 V at 0.1 µA cm^{-2}). The higher potential might be explained by the stronger interaction of the magnesium aggregates with the aromatic substituent observed by FT-IR. **EF$_2$3b** and **EF$_2$3b Mg(ClO$_4$)$_2$** had for low current densities up to 0.1 µA cm^{-2} a similar plating/stripping potential but deviate at 1 µA cm^{-2}. Meanwhile, **EF3b** had over the complete current density spectra a significant higher potential than **EF3b Mg(ClO$_4$)$_2$.** This indicates a stronger interaction between the polymer matrix with Mg(TFSI)$_2$ aggregates than Mg(ClO$_4$)$_2$. This observation was not seen for **EF$_2$3b** and **EF$_2$3b Mg(ClO$_4$)$_2$** at lower current densities up to 0.5 µA cm^{-1} because FT-IR indicated only a limited polymer-salt interaction. Meanwhile, **EF3b Mg(ClO$_4$)$_2$** and **EF$_2$3b** performed with only a slight increase in potential at 1 µA cm^{-2}, whereas **EF3b** and **EF$_2$3b Mg(ClO$_4$)$_2$** showed a strong increase in potentials. The overall increase in potential for **EF3b Mg(ClO$_4$)$_2$**, **EF$_2$3b**, **EF3b** and **EF$_2$3b Mg(ClO$_4$)$_2$** were traced back to the growth of passivation layer as reported by Mesallam *et al.*[279]

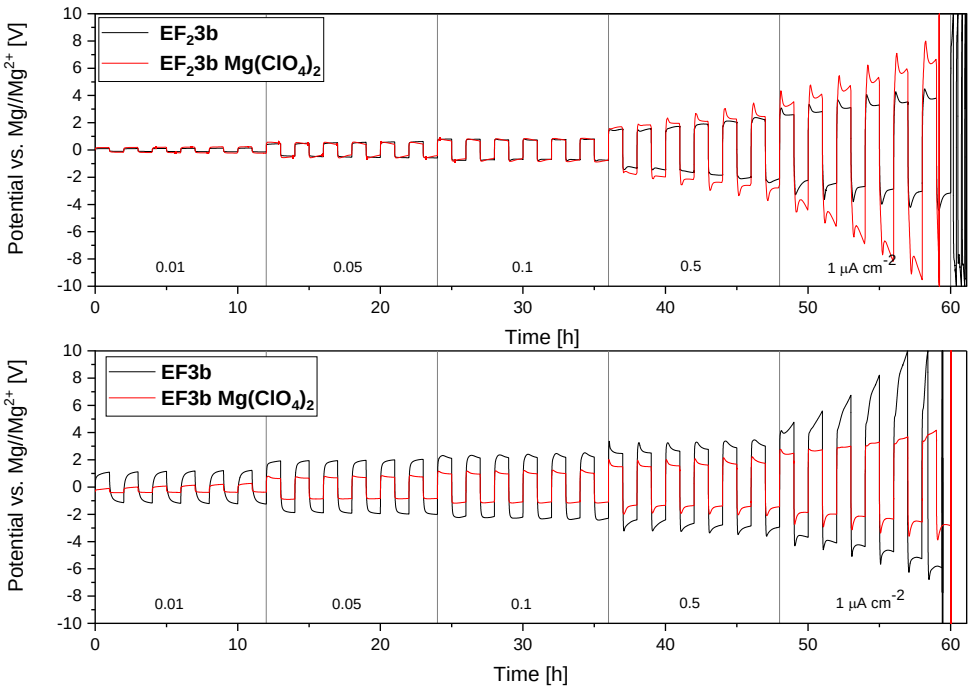

Figure 33: Constant current measurements at 0.01, 0.05, 0.1, 0.5, 1 and 10 µA cm^{-2} for 6 cycles each at 80°C in a Mg||Mg cell of **EF70b** and **EF70b Mg(ClO$_4$)$_2$** C) **EF$_2$3b** and **EF$_2$3b Mg(ClO$_4$)$_2$**.

Nevertheless, all four samples showed no plating/stripping behavior above 1 µA cm^{-1}, whereas the reference system **Eblend70** performed up to 10 µA cm^{-2} with even lower plating/stripping potentials (Figure 34). At 1 µA cm^{-2} **Eblend70** performed with a potential of about 1.1 V vs. Mg/Mg^{2+} instead of 4 V vs. Mg/Mg^{2+} (**EF$_2$3b**), which could be explained by the macroscopic segregation shown by DSC. The overall performance is still significant lower compared to a GPEs systems (PVDF:MgBr$_2$:tetraethylen glycol dimethylether) reported by Mesallam *et al.*.[279] But the results are in good agreement of other researchers, which reported an overall lower electrochemical performance of SPEs compared to GPEs.[67]

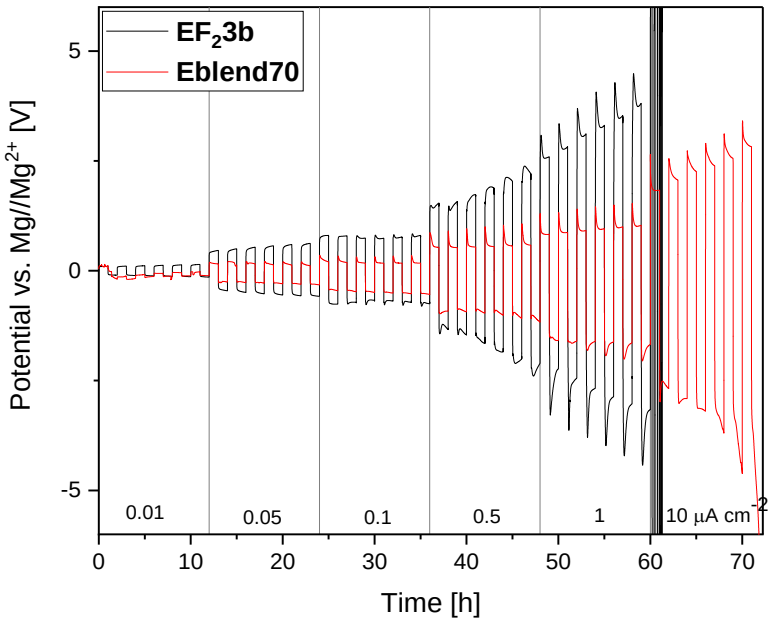

Figure 34: Constant current measurements at 0.01, 0.05, 0.1, 0.5, 1 and 10 µA cm^{-2} for 6 cycles each at 80°C in a Mg||Mg cell of **Eblend70.**

1.7.4 Cl^- containing polymer electrolytes

One approach to improve the plating-stripping potential is the addition of Cl^- to the system as described in chapter 1.2. Therefore, to the polymer **$PF_2$3b** $Mg(TFSI)_2$ and $MgCl_2$ in ratio of 2:1, (**$PF_2$3b $MgCl_2$**) were added in a concentration of 25:2 [EO]:[Mg]. The same plating and stripping conditions were applied as before, and the resulting spectra is shown in Figure 35.

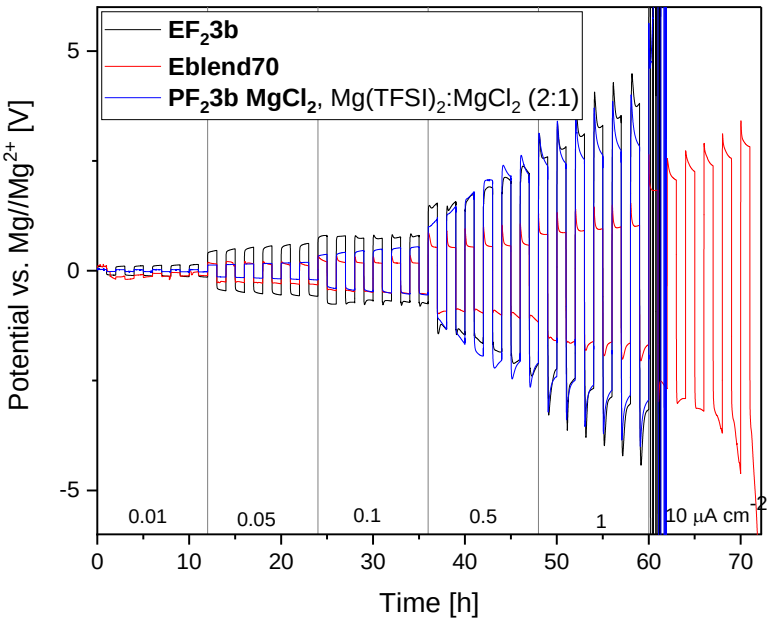

Figure 35: Constant current measurements at 0.01, 0.05, 0.1, 0.5, 1 and 10 µA cm^{-2} for 6 cycles each at 80°C in a Mg||Mg cell **$EF_2$3b $MgCl_2$**.

$PF_2$3b $MgCl_2$ performed with lower overpotentials between 0.01 to 0.1 µA cm^{-2} compared to **$EF_2$3b** but still higher compared to **Eblend70**. The performance was similar to **$EF_2$3b** at 0.5 and 1 µA cm^{-2} but did not show any reversible plating-stripping at 10 µA cm^{-2}. Overall Cl^- slightly improved the plating/stripping potential but still significantly higher potentials were measured at higher current densities compared to **Eblend70**.

1.7.5 Recapitulation

The successful synthesis of copolymers with anion receptors for magnesium ion batteries was conducted. The copolymers were polymerized by (2-(2,4-difluorophenyl)-1,3,2-dioxaborolan-4-yl)methyl methacrylate or (2-(4-fluorophenyl)-1,3,2-dioxaborolan-4-yl)methyl methacrylate and $PEGMA_{500}$ and the anion receptors were borate moieties. For $PEGMA_{500}$ contents between 30 to 5 mol% additive-free self-standing PEs were synthesized with random and block architecture as well as the corresponding homopolymers. The highest ionic conductivity was found for the block copolymer with 30 mol% $PEGMA_{500}$ of $3\ 10^{-8}$ S cm^{-1} at 30 °C containing $Mg(TFSI)_2$ (25:1 [EO]:[Mg]). Thus, PEs based on this polymer composition with four different salts ($Mg(TFSI)_2$, $Mg(ClO_4)_2$, LiTFSI and $LiClO_4$) were prepared, investigating the ion coordination, t^+_{Li} and magnesium plating-stripping potentials. FT-IR spectroscopy of the synthesized polymer electrolytes revealed a stronger interaction between salt aggregates and the polymer for monofluorinated polymers, compared to difluorinated ones. As a result, for the monofluorinated polymer electrolyte $t^+_{Li}(LiClO_4) > t^+_{Li}(LiTFSI)$ was detected, emphasizing a successful anion receptor for lithium systems. Furthermore, the monofluorinated polymer electrolytes performed with higher stripping/plating potentials in a Mg||Mg cell setup between current densities of 0.01 to 1 µAcm^{-2}, due to stronger interactions between the magnesium salts and the polymer matrix. Further, an enhanced plating/stripping behavior was recognized by the addition of $MgCl_2$. Consequently, advanced knowledge towards PEs with anion receptors were gained with focus on substituent effects on their ability in MIBs.

1.8 Magnesium polymer electrolytes based on polycarbonate poly(2-butyl-2-ethyltrimethylene-carbonate)

In this chapter, PEs with high ratios of salts were investigated towards the formation of polymer-in-salt electrolytes. Aliphatic polycarbonates were established matrixes for PISE in LIBs, due to their high chain flexibility and low T_g.[280] Therefore, poly(2-butyl-2-ethyltrimethylene-carbonate) (P(BEC)) was taken as matrix polymerized with two contrary magnesium salts, $Mg(B(HFIP)_4)_2$ and $Mg(TFSI)_2$.

Parts of this chapter and the corresponding parts in the experimental section were adapted with permission from a publication written by the author David A. Sundermann.[281]

P(BEC) was polymerized from the cyclic monomer (2-butyl-2-ethyltrimethylene carbonate (BEC)) by AROP (Scheme 19) for 24 h at monomer concentrations of 2 M.

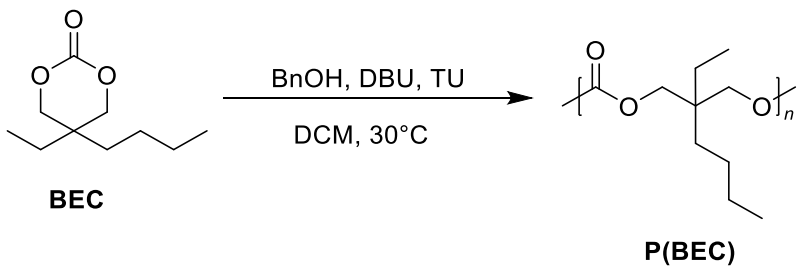

Scheme 19:Polymerization conditions of P(BEC).

As catalyst 1-(3,5-bis(trifluoromethyl)phenyl)-3-cyclohexylthiourea (TU) and 8-diazabicyclo(5.4.0)undec-7-ene (DBU) were used (Scheme 20) in ratio of 1 to 50 to the monomer concentration.

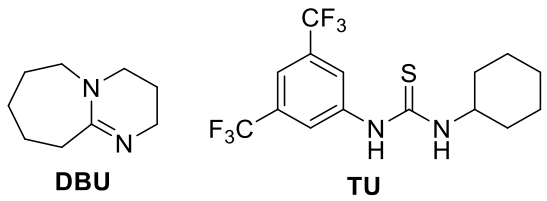

Scheme 20: Structure of co-catalyst DBU and TU.

By using ^{1}H-NMR spectroscopy, the degree of polymerization (average number of repeating units per chain) was calculated to be 22, by integrating and comparing the peak from the CH_2 of the benzyl alcohol at 5.07 ppm with peak from the CH_2 groups of the repeating units at 3.93 ppm

(Figure 36A). Based on SEC measurements, an M_n = 6 100 gmol^{-1}, equivalent to a degree of polymerization of 32, was estimated. Considering PMMA standards were used for calibration of the SEC, the results confirmed the ^{1}H-NMR result of about 22 repeating units per polymer.

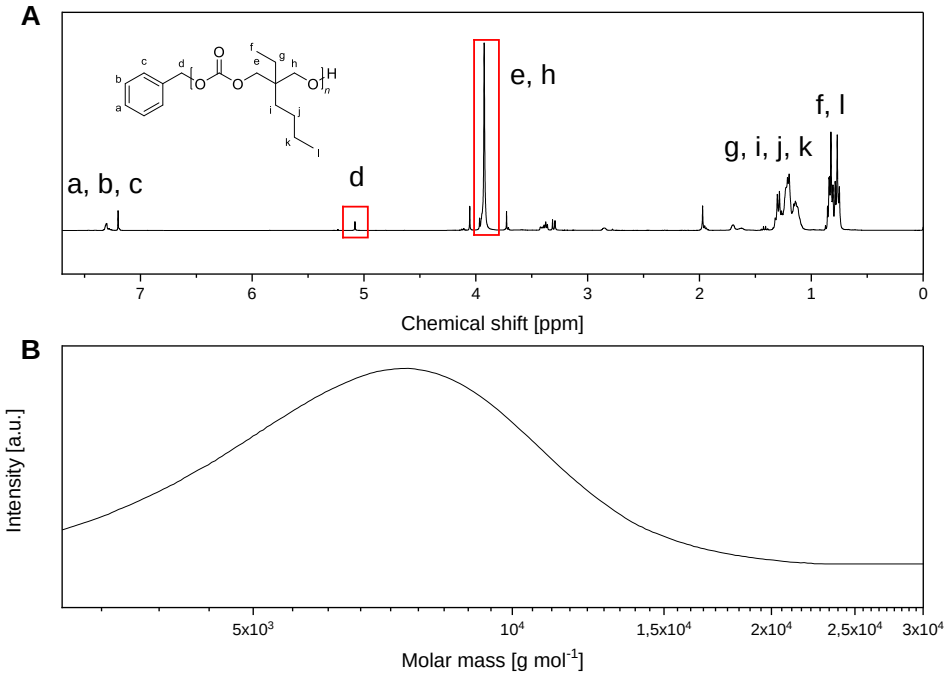

Figure 36: A) ^{1}H-NMR of P(BEC) in $CDCl_3$ with integrated areas for repeating unit calculations. * are assigned to solvents. B) SEC spectrum of P(BEC) in THF with PMMA standard. Partly reproduced with permission from ACS Omega, in press. Unpublished work copyright 2023 American Chemical Society.

$Mg(B(HFIP)_4)_2$ was synthesized as reported in literature, and the product was obtained in the form of $Mg(B(HFIP)_4)_2$-3 DME solids (Figure 91).[282] PEs were prepared by incorporating 5, 20, 30 and 40 mol% $Mg(TFSI)_2$ (**TFSI5** to **TFSI40**) or $Mg(B(HFIP)_4)_2$-3 DME (**HFIP5** to **HFIP40**) into the polymer matrix by solution casting method (Table 11). All PEs were solid and/or gum-like materials.

Table 11: Salt concentration, glass transition temperature (T_g) and ionic conductivity (σ) at 20 °C of **TFSI5** to **TFSI40** and **HFIP5** to **HFIP40**. -[1] is assigned to not measured and -[2] to not detected. Reproduced with permission from ACS Omega, in press. Unpublished work copyright 2023 American Chemical Society.

	Salt	**Mg:repeating unit ratio [mol%]**	**Salt concentration [wt.%]**
P(BEC)	-	0	0
	$Mg(TFSI)_2$	-[1]	-[1]
TFSI5		5	13.6
TFSI20		20	38.6
TFSI30		30	48.5
TFSI40		40	55.7
	$Mg(B(HFIP)_4)_2$-3 DME	-[1]	-[1]
HFIP5		5	27.1
HFIP20		20	59.8
HFIP30		30	69.0
HFIP40		40	74.8

1.8.1 Thermal properties

The polymer P(BEC) had a decomposition temperature ($T_{d,}$ 5%) of 166 °C (Figure 37), which was in a similar range as previously reported for polycarbonates.[193]

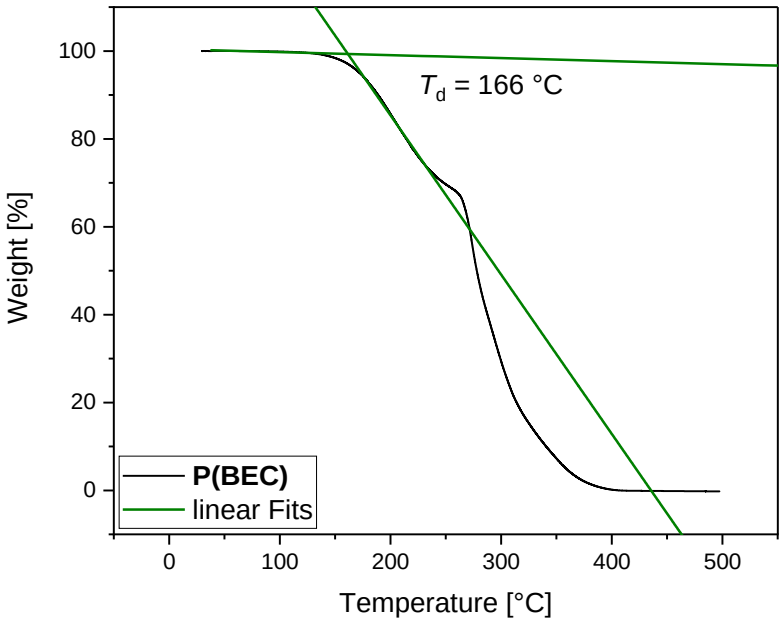

Figure 37: TGA measurement of P(BBC) between 50 to 500 °C at 10 °C per minute scan rate. Reproduced with permission from ACS Omega, in press. Unpublished work copyright 2023 American Chemical Society.

The physical properties of the P(BEC) and the corresponding PEs were analyzed by DSC (Figure 38), detecting for the pure polymer a glass transition temperature (T_g) of -10 °C. The addition of 5 mol% $Mg(TFSI)_2$ (**TFSI5**) to the polymer matrix led to a slight increase in T_g to about -7 °C. For **TFSI20** to **TFSI40** the T_g decreased to about -17 °C reaching a plateau, which indicated the formation of a stable phase being salt content independent. The decrease in T_g might be cause by plasticizing effect of the $TFSI^-$ anion as already reported elsewhere.[97,193] The addition of $Mg(B(HFIP)_4)_2$ lead to similar observation, where **HFIP5**, **HFIP20** and **HFIP30** showed only a slight decrease in T_g from -9 to -12 °C but a sudden drop for **HFIP40** to -42 °C. This rapid change in T_g hinted at a significant change in phase, suggesting the formation of polymer-in-salt electrolytes for **HFIP40**. In previous studies, a significant decrease in T_g was already reported for PEs with salt contents larger than 50 wt.%, which is traced back to the suppression of salt crystallization through the polymer-salt interaction.[283] Furthermore, no $Mg(B(HFIP)_4)_2$-3 DME complexes remained after the PE preparation due to the absence of any melting points corresponding to the salt complex.

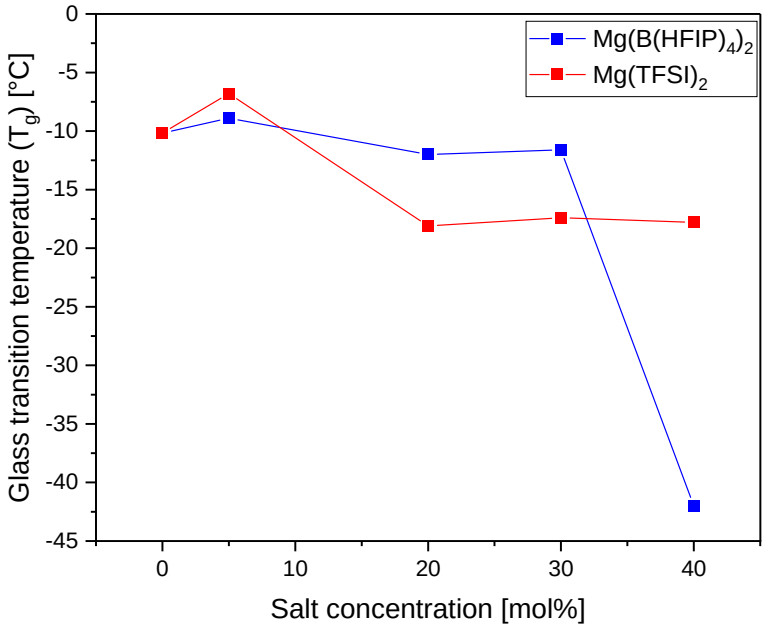

Figure 38: Glass transition temperatures of the studied P(BEC) electrolytes as a function of varying concentrations of magnesium salt measured for $Mg(TFSI)_2$ and $Mg(B(HFIP)_4)_2$. The data points were connected to guide the eye. Reproduced with permission from ACS Omega, in press. Unpublished work copyright 2023 American Chemical Society.

1.8.2 Ion coordination

Raman spectroscopy

The anion coordination behaviour was characterized by Raman spectroscopy (Figure 39 and Figure 40). For $Mg(TFSI)_2$, the focused was on analyzing changes in the C-F vibrations between 740 to 760 cm^{-1} and the polymer C-H vibrations between 2800 to 3000 cm^{-1}.[284] The polymer did not show Raman activity in the area of 750 cm^{-1}, and therefore these signals correspond only to the $TFSI^-$, where a shift towards higher wavenumbers and energies can be seen by an increase in $Mg(TFSI)_2$ concentration. Two overlapping vibrations were suggested with maxima at 744 cm^{-1} and 752 cm^{-1} corresponding to free $TFSI^-$ at 740 cm^{-1} and Mg^{2+} coordinated $TFSI^-$ at 752 cm^{-1} as previously reported.[284] By fitting the curves to Gaussian functions an increase of Mg^{2+} coordinated TFSI from 35.1 to 76.0% can be seen (Table 18 and Figure 39**)** with increasing salt concentration from 5 to 40 mol% $Mg(TFSI)_2$. For the C-H vibrations, a slight shift towards higher wavenumbers (2964 cm^{-1} to 2998 cm^{-1}) was also observed, indicating an increasing Mg-polymer interaction with increasing $Mg(TFSI)_2$ concentration.

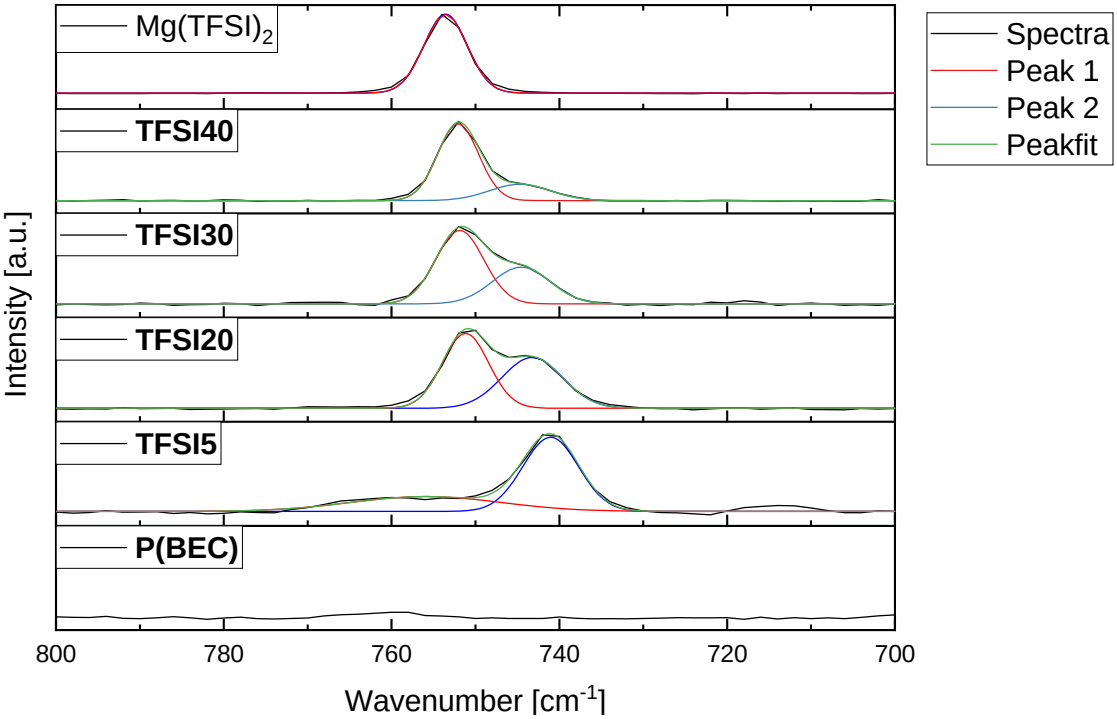

Figure 39: Raman spectra between 800 to 700 cm^{-1} with fitted Peaks 1 and 2. Reproduced with permission from ACS Omega, in press. Unpublished work copyright 2023 American Chemical Society.

An explanation considering both observations could be that in the first step the complexation of Mg^{2+} by the polymer was preferred leading to higher salt dissociation for **TFSI5** and therefore less ion pars or aggregates. With further increase in $Mg(TFSI)_2$ content the formation of ion pairs or aggregates increased because the coordination sites on the polymer chains were occupied. Thus, the preferred coordination number of 6 for Mg^{2+} could not be fulfilled by P(BEC), promoting the formation of aggregates and ion pairs.[128] Therefore, the higher T_g for **TFSI5** was caused by higher quasi-ionic cross-linking of the polymer by higher number of polymer-Mg complexes due to higher $Mg(TFSI)_2$ dissociation. With further increase in $Mg(TFSI)_2$ content the formation of ion pairs and aggregates occurred reducing the quasi-ionic cross-linking and leading to a decrease in T_g.[285] Compared to a PEC-based magnesium PE published in 2018, the ratio of free $TFSI^-$ is significant lower in P(BEC), where instead of 24% free $TFSI^-$ at 40 mol% 87% were reported.[97] This difference might be caused by the higher aliphatic character and therefore smaller dipole moment of P(BEC), compared to PEC enhancing the formation of ion pairs and aggregates.[286]

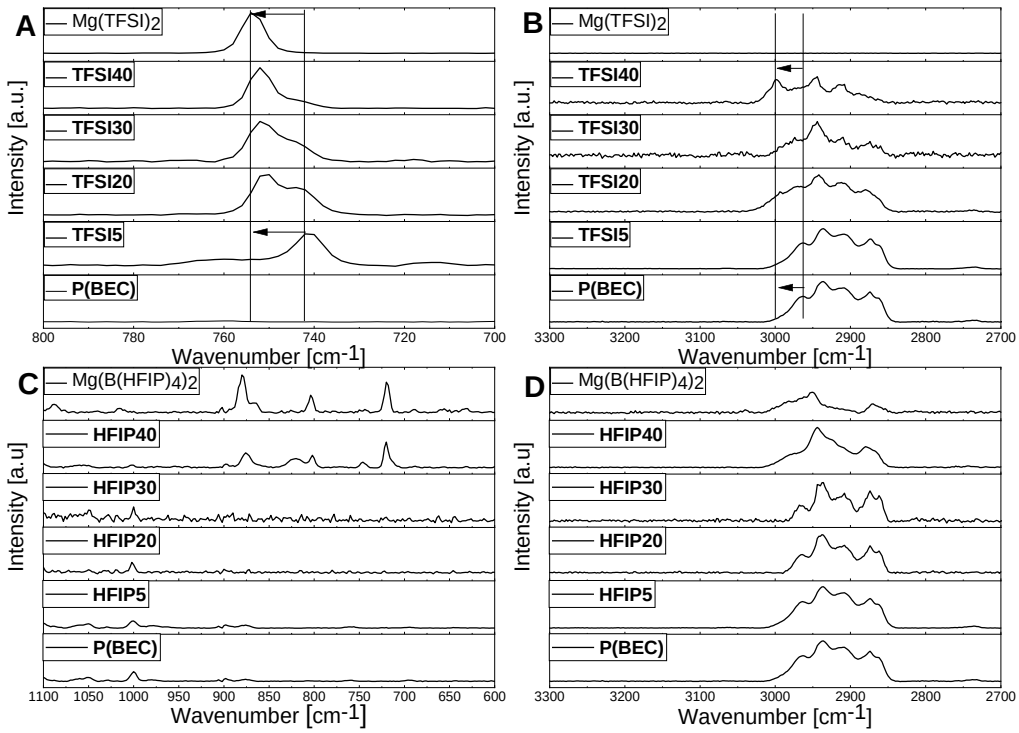

Figure 40: Raman spectra of A)+B) **TFSI5** to **TFSI40** and C+D) **HFIP5** to **HFIP40**. Reproduced with permission from ACS Omega, in press. Unpublished work copyright 2023 American Chemical Society.

In contrast to $Mg(TFSI)_2$, no significant shifts in the Raman spectra between 2800 to 3000 cm^{-1} were observed for the $Mg(B(HFIP)_4)_2$-containing PEs. $Mg(B(HFIP)_4)_2$-3 DME was Raman active in the area of 700 to 900 cm^{-1}, where vibration at 718 cm^{-1} and further vibrations at 804 and 880 cm^{-1} were detected. Based on previous reports, the vibrations at 880 cm^{-1} were C-O-C vibrations of DME, whereas the peaks at 804 and 718 cm^{-1} were assigned to B-O and C-F vibrations.[287] Overall those three signals only appeared for **HFIP40** without any shifting but were missing for the electrolytes with less than 40 mol% $Mg(B(HFIP)_4)_2$, suggesting a complete solvation of the salt below 30 mol%. Because no shifts of the signals at 880, 804, and 718 cm^{-1} were seen, it is inferred that a precipitation of $Mg(B(HFIP)_4)_2$-3DME salt occurred in **HFIP40**. The precipitation of salts was already reported in literature for lithium salts *e.g.* in poly(acrylonitrile-*co*-butyl acrylate) (P(AN-*co*-BuA)) at high salt contents.[180] However, the overall amount of DME and therefore $Mg(B(HFIP)_4)_2$-3DME in **HFIP40** is still suggested to be low due to the absence of any DME signals in ^{1}H-NMR (Figure 114) or any further T_g or T_m by DSC. Moreover, the Raman results underlines in combination with the DSC results the suggestion of a salt-in-polymer electrolyte for **HFIP40**.

Rheology

The given samples **TFSI5** to **TFSI40** and **HFIP5** to **HFIP40** were analyzed by dynamic strain sweep test (SST) and dynamic frequency sweep (DFS) to determine the storage (G') and loss (G'') moduli, representing the elastic and viscous parts of the materials as function of oscillation strain (γ) and angular frequency (ω). DFS studies were performed in the linear viscoelastic regime (LVE) with strain amplitudes between γ_0 = 0.02 and 10%. The PEs showed overall a complex rheological response being salt concentration, magnesium salt type and frequency dependent.

For SST measurements (Figure 42A and Figure 42B), the loss modulus G'' was mostly dominant over storage modulus G' for all PEs regardless of magnesium salts or concentrations, indicating more viscous than elastic materials.[288]

Based on these results, complex viscosities (η^*) (Figure 41) were calculated at ω = 0.32 rad s^{-1} and γ_0 = 10% to compare the different blends. The complex viscosity η^* increased constantly with increasing $Mg(B(HFIP)_4)_2$ concentration with reaching its maximum for **HFIP30** and then slightly decreasing again for **HFIP40**. Earlier polymer related publications, i.e. poly(ethylene-*co*-methacrylic acid) explained increasing viscosity by an increase in ionic interaction, in this case as quasi-ionic crosslinking.[289,290] The increase in η^* can therefore related to the increasing quasi-ionic crosslinking for **HFIP5** to **HFIP30**. The decrease in η^* for **HFIP40** is attributed to the precipitation of salt and decreases in T_g of **HFIP40**. Similarly, the η^* trend of **TFSI5** to **TFSI30** can be explained, where η^* decreased due to higher number of ion pairs and agglomerations and lower salt dissociation as discussed before. The large discrepancy between **TFSI40** and **TFSI30** may also be attributed to the formation of a polymer-in-salt situation, despite the lack of sharp decrease in T_g.

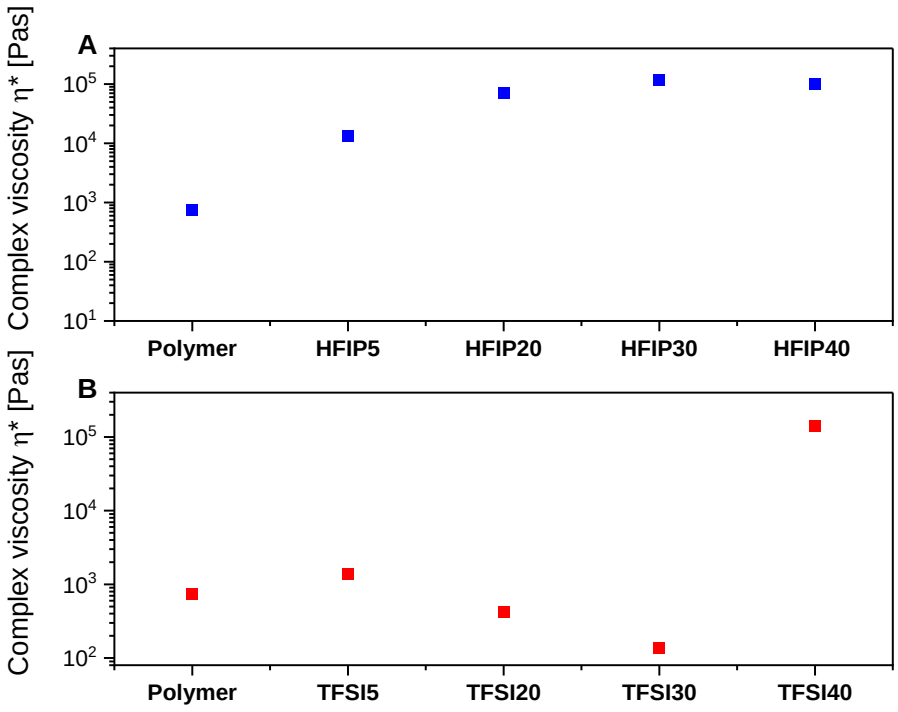

Figure 41: Complex viscosity at 20 °C by DFS measurements at γ_0 = 10% and ω = 0.32 rad s^{-1} for the given salt concentrations A) $Mg(B(HFIP)_4)_2$ and B) $Mg(TFSI)_2$. Reproduced with permission from ACS Omega, in press. Unpublished work copyright 2023 American Chemical Society.

Further structural information was found by interpreting the DFS experiments (Figure 42B and Figure 42D), where the corresponding slopes of linear fits for the parallel regime, i.e., are given in Table 18. For an ideal cross-linked system, a linear behaviour between angular frequency and storage and loss moduli with slope of -1 would be expected, however, with slopes ranging between -0.67 and -1.50 (Table 19) in the parallel area, a non-ideal behaviour seems to be present. For the PEs containing $Mg(TFSI)_2$, in the frequency range before, G' and G'' cross each other with increasing salt concentration resulting in close parallel behaviour, which is indicative for a structured material.[291] The crossover appearing for **TFSI40** at the highest frequency hints at entangled chains.[292] A parallel behaviour of G' and G'' can also be seen by incorporating $Mg(B(HFIP)_4)_2$ instead of $Mg(TFSI)_2$, where parallel regimes can be seen for **HFIP20** and high salt concentrations. Those, **HFIP20**, **HFIP30** and **HFIP40**, showed crossovers of G' and G'' at 452 rad s^{-1} indicating dominantly elastic properties at higher frequencies, which were salt concentration independent. Moreover, for **HFIP20** a second low frequency crossover of G' and G'' was found, whereas for the other samples, as e.g., **HFIP30**, a further crossover was indicated to occur at lower frequencies outside of the experimental frequency window. In literature such observations were explained by the formation of supramolecular dendritic aggregates of hydrogen-bonded supramolecular polymer networks.[293] Transferring this explanation to our system a

supramolecular ordered structure of Mg^{2+} coordinated and elongated polymers may be present. Observing the second crossover of *G´* and *G´´* to be for **HFIP20** at the highest frequency of all samples next to the assumption of entangled polymers by parallel *G´* and *G´´*, leads to the suggestion that for **HFIP20** the strongest interactions between the entangled polymers were present. The interactions related to this second crossover were assumed to be based on ionic interactions including quasi-ionic crosslinking and would therefore be reduced with increasing Mg-anion coordination or increasing distances between the elongated polymers. The quasi-ionic cross-linking was lower for **HFIP5** due to lower Mg^{2+} ion content, whereas for **HFIP30** and **HFIP20** the quasi-ionic cross-linking was decreased by increasing separation of the polymers due to the higher salt content.

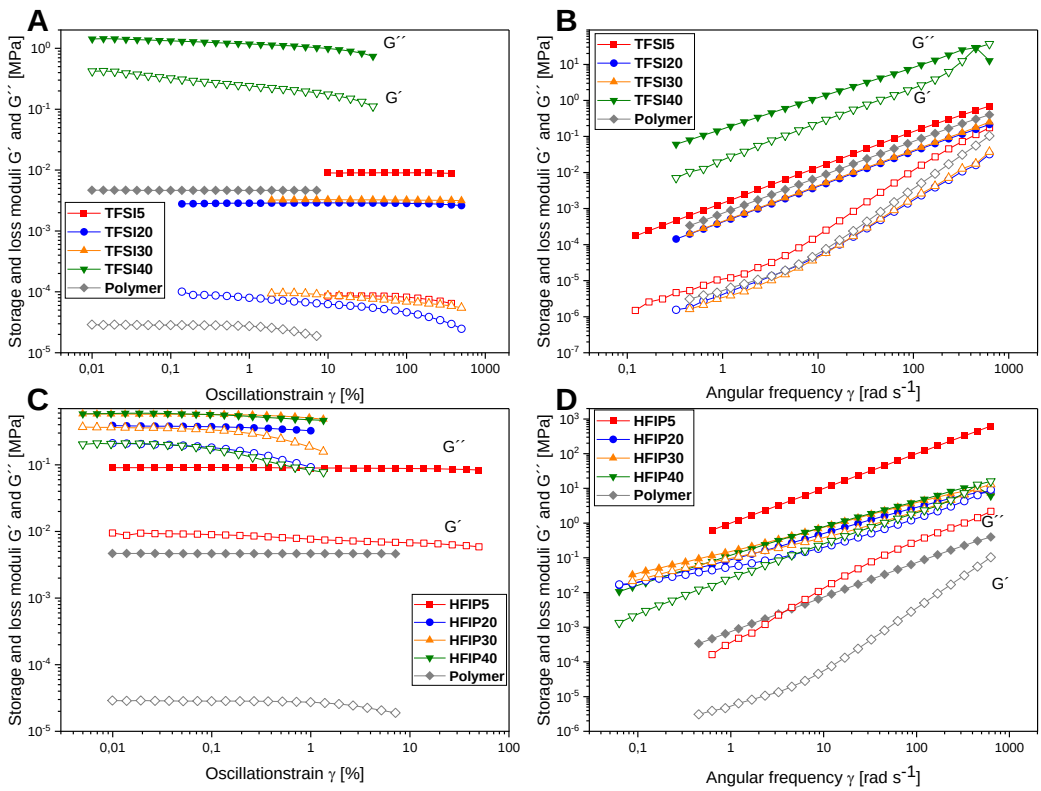

Figure 42: Rheological SST and DFS measurements at 20 °C with filled symbols for loss modulus G´´ and empty symbols for storage modulus G´ of A+B) **TFSI5** to **TFSI40** and C+D) **HFIP5** to HFIP40 as well as the neat polymeric matrix. Reproduced with permission from ACS Omega, in press. Unpublished work copyright 2023 American Chemical Society.

1.8.3 Electrochemical properties

Ionic conductivity (σ) measurements were performed between -20 to 120 °C (Figure 43) and further analyzed by fitting to Vogel-Fulcher-Tammann (VFT) equation, presented as equation 4.

$$\sigma = A_0 exp\,(-\frac{B}{R(T-T_0)}) \qquad \text{Eq. 4}$$

The VTF equation is commonly found to fit temperature dependent ionic conductivity for polymer electrolytes, where the ion mobility is influenced by segmental motion of the polymer host.[294]

For VFT analysis the results were plotted by ln(σ) against $(T\text{-}\ T_0)^{-1}$ as presented in Figure 116 and Table 12**.** For **TFSI5** to **TFSI40** ionic conductivity measurements resulted into maxima values of 2.7 10^{-7} S cm^{-1} for **TFSI5** at 20 °C followed by **TFSI20** with 6.4 10^{-9}, **TFSI30** with 1.0 10^{-9} and **TFSI40** with 5.4 10^{-10} Scm^{-1} at 20 °C. At 120 °C the maxima ionic conductivity has changed its order towards **TFSI20** followed by **TFSI5**, **TFSI40** and **TFSI30** (10^{-5} Scm^{-1}). The decreasing ionic conductivity with increasing $Mg(TFSI)_2$ concentration at 20 °C might be traced back to the aggregation of ions and the formation of ion clusters as reported for PEO-based PEs before.[295] An explanation of higher ionic conductivity of **TFSI20** and **TFSI40** over **TFSI5** and **TFSI30** at 120 °C were suggested by *B* and A_0. **TFSI40** and **TFSI20** were indicated to have a higher number of mobile charge carrier leading to higher ion conductivities at 120 °C. In contrast to this, the activation energy for segmental motion *B* seem to be more dominant at lower temperatures, explaining the higher ionic conductivity of **TFSI5** and **TFSI20**.

Table 12: Parameter T_0, A_0 and *B* from VTF plot for **TFSI5** to **TFSI40** and **HFIP5** to **HFIP40**. Reproduced with permission from ACS Omega, in press. Unpublished work copyright 2023 American Chemical Society.

	T_0 [K]	A_0 [S $cm^{-1}K^{-1}$]	B [$Jmol^{-1}K^{-1}$/eV]
TFSI5	216.35	0.003 ± 0.0006	5 872/0.14 ± 158/0.002
TFSI20	205.05	0.2 ± 0.05	12 487/0.15 ± 246/0.003
TFSI30	205.75	0.04 ± 0.02	12 511/0.15 ± 324/0.003
TFSI40	205.35	0.08 ± 0.04	13 247/0.17 ± 508/0.005
HFIP5	214.15	0.0007 ± 0.0002	13 319/0.06 ± 202/0.002
HFIP20	211.15	0.003 ± 0.0006	14 330/0.13 ± 217/0.002
HFIP30	211.55	0.0005 ± 0.0002	14 746/0.13 ± 98/0.001
HFIP40	181.15	2.78 ± 0.24	16 223/0.14 ± 98/0.001

When changing the focus from $Mg(TFSI)_2$ to $Mg(B(HFIP)_4)_2$ the ionic conductivity increased for the PEs with increasing salt concentration, where **HFIP5** to **HFIP20** exhibited ionic conductivities in the same order of magnitude. In contrast, **HFIP40** had a substantially higher (about 3 orders

of magnitude higher) ionic conductivity over the complete temperature range of -20 to 120 °C, between 1.8 10^{-10} and 2.5 10^{-4} S cm^{-1}. The large difference in ionic conductivity for **HFIP40** again hints at the formation of a polymer-in-salt electrolyte. Curvature is observed in Figure 43 for all the temperature-dependent ionic conductivity plots (**TFSI5**/**HFIP5** to **TFSI40** and **HFIP40**), so VFT plot analysis was conducted for all samples as shown in Figure 116. For the linearization of the VFT plots, only points for $T > 10$ °C were considered because at $T < T_g$ immobilization of polymer chains hinder ion mobility segmental motion. Overall, **HFIP5** to **HFIP20** showed in VFT plots similar values for B and A_0 explaining the overall similar performance. But in case of **HFIP40**, A_0 was several orders of magnitudes higher than for **HFIP30**, 2.78 $Scm^{-1}K^{-1}$ compared to 0.0005 S $cm^{-1}K^{-1}$. Such an increase in number of mobile charge carrier could be explained by the lower T_g of **HFIP40** being 30 °C below **HFIP30**. The high number of mobile charge carriers were also reported in a publication dealing with polymer-in-salt electrolytes, where for PAN co-polymers a dramatic increase in ionic conductivity were described.[283] Furthermore, comparing $Mg(B(HFIP)_4)_2$ to $Mg(TFSI)_2$ based PEs, the higher ionic conductivity for the $Mg(TFSI)_2$ electrolytes, except in the case of **HFIP40**, can be seen explained by their lower η^*.

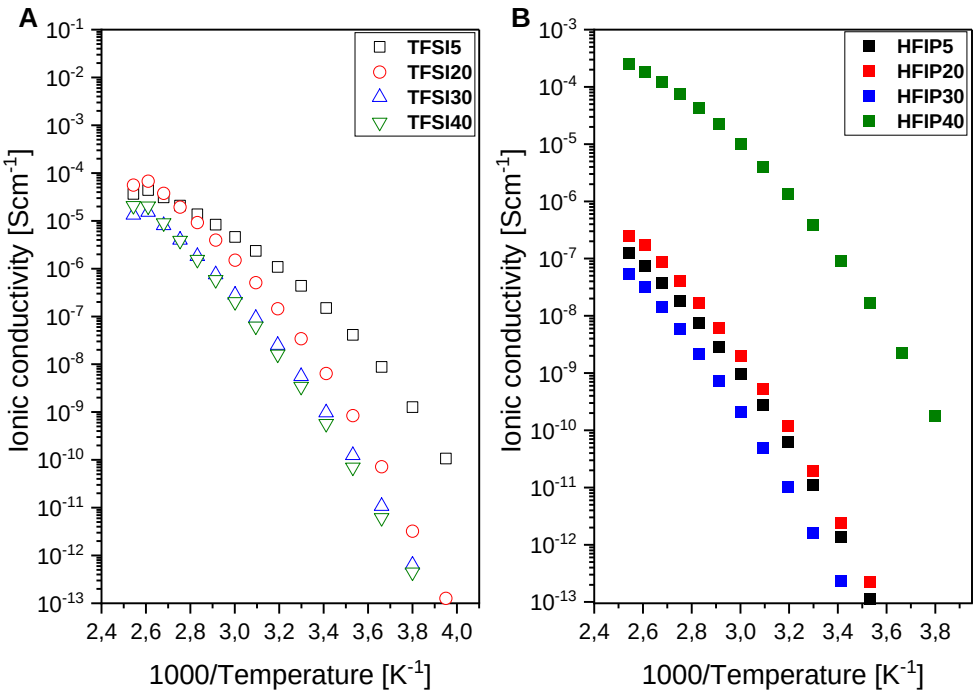

Figure 43: Temperature dependent conductivity measurements between -20 °C to 120 °C of A) **TFSI5** to **TFSI40** and B) **HFIP5** to **HFIP40**. Reproduced with permission from ACS Omega, in press. Unpublished work copyright 2023 American Chemical Society.

For the 40 mol% containing PEs, **TFSI40** and **HFIP40**, the electrochemical stability window was tested against magnesium metal by LSV on asymmetric Mg||SS cells. The results in Figure 44 and Figure 117 showed a much lower oxidative stability for **TFSI40**, which decomposed already at 3.6 V vs Mg/Mg^{2+} compared with **HFIP40** that did not show any decomposition behaviour up to 5.5 V vs. Mg/Mg^{2+}. The low stability of **TFSI40** might be because of the ionic aggregates and ion pairs, that are unstable against magnesium metal.[257,296] Wu and colleagues reported in 2021 for an LiTFSI-rich PE based on PEG ([EO:Li] = 0.5) also a declined in oxidation stability compared to lower concentrations.[297] The stability window of **HFIP40** was also larger than the reported potential for 1M $Mg(B(HFIP)_4)_2$ in DME solution reported in 2018 being 4 V.[46] Further, a higher stability for $Mg(B(HFIP)_4)_2$ over $Mg(TFSI)_2$-containing electrolytes was expected based on a prior publication.[287] Therefore, cyclic voltammetry measurements were performed for **HFIP40** on an asymmetric Mg||SS cell between -1 and 3 V as presented in Figure 44. A decrease in current with cycle number and a lack of stripping-plating peaks were observed and attributed to the formation of passivation layer on the magnesium surface. The growth and formation of the passivation layer was also detected by impedance spectroscopy before and after cyclic voltammetry, where an increase in surface resistance (R_s) was measured (Figure 118). Moreover, R_b seem to be quite high, being an argument for the low cyclability and the strong decrease in current. Therefore and because of the low cyclability, the results do not support the idea of an enhanced performance of $Mg(B(HFIP)_4)_2$-based polymer-in-salt electrolyte with regards to Mg plating or stripping efficacy.

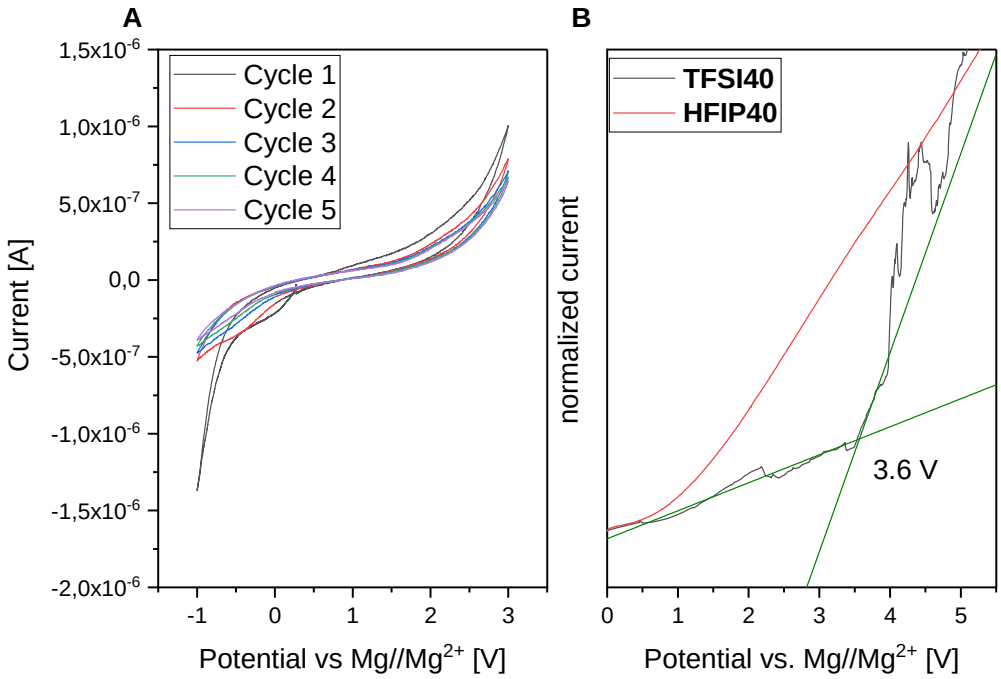

Figure 44: A) Cyclic voltammetry of **HFIP40** in asymmetric Mg||SS cell at 80 °C at 0.1 mVs^{-1} between -2 to 2 V. B) Electrochemical stability window in Mg||SS cell of **HFIP40** and **TFSI40** at 0.1 mVs^{-1} between 0 to 6 V. Reproduced with permission from ACS Omega, in press. Unpublished work copyright 2023 American Chemical Society.

1.8.4 Recapitulation

Here, polycarbonate based PEs containing P(BEC) as polymer matrix and either $Mg(TFSI)_2$ or $Mg(B(HFIP)_4)_2$ salt were prepared and characterized. The differing impact of anion character on the ion pair dissociation and agglomeration behaviour and the polymer-Mg coordination was shown, especially at high concentrations of 40 mol% magnesium salts (**TFSI40** and **HFIP40**). The incorporation of $Mg(TFSI)_2$ led to the formation of mainly polymer-Mg complexes at low concentrations followed by a substantial increase of polymer-Mg-TFSI complexes with increasing $Mg(TFSI)_2$ concentration. Nevertheless, outside of rheological measurements, the overall behaviour of **TFSI40** was like that of a salt-in-polymer.

The incorporation of $Mg(B(HFIP)_4)_2$ led to salt-in-polymer electrolyte behaviour at lower concentrations but polymer-in-salt behaviour at 40 mol%. **HFIP40** exhibited the highest ionic conductivity ($2.5\ 10^{-4}$ Scm^{-1} at 120 °C) of all samples and was found to have higher oxidative (> 5 V) stability than **TFSI40** (4.7 V). Still, **HFIP40** was not found to reversibly plat and strip magnesium metal. Therefore, use of this electrolyte with a magnesium anode may require use of artificial SEI to prevent anode passivation.

Consequently, the knowledge of salt-in-polymer electrolytes in MIBs was increased, where advances were made in regards of ion transport properties but no towards magnesium electrode compatibility.

Conclusion

The previous chapters of the present work discussed the development of well-defined polymer electrolytes for magnesium-ion batteries. I investigated multiple approaches and performance, focusing on the ionic conductivity, coordination environment, compatibility and reversibility with magnesium metal electrodes and further electrochemical and material characterization techniques.

In the first chapter, crosslinked self-standing single-ion conductors were developed based on PEO grafted copolymers with borate crosslinking points. Herein, the impact of architecture, PEO chain length and comonomer ratios on the ion transport properties and crystallinity was of interest. With increasing PEO chain length and weight ratio the ionic conductivity increases, whereas longer PEO sidechains lead to higher crystallization tendencies. Furthermore, GPEs with $PEGMA_{500}$ and PC as additives were prepared to further improve the electrochemical properties. For the GPEs high lithium transference numbers up to 0.9 underline the successful design of single-ion conductors and highlight their field of research. Based on these GPE, magnesium-lithium dual-salt electrolytes were prepared by exchanging magnesium- by lithium-ions and by the addition of LiTFSI. A two-part performance with higher potentials at lower current levels and lower potentials at high current levels was observed when comparing the dual-salt electrolytes to the magnesium-only single-ion conductor. A decrease of plating/stripping potentials at high current densities were traced back on the one hand to increasing lithium-ion concentrations and on the other hand to the magnesium electrodes surface composition. Lithium-containing decomposition products were found for the dual-salt electrolytes but did not hinder the formation of passivation layers by oxides and carbonates, which shows the necessity of further research in this field.

In the second chapter, PEO grafted copolymers with two different anion receptors, which differ in degree of fluorination, were developed as polymer electrolytes. Inhere, the ion transport properties are strongly affected by [EO]/[Mg] concentration, comonomer ratio, degree of fluorination and choice of salt. With increasing PEO ratio an increase in ionic conductivity was shown, which was caused by a decrease in T_g at the same time with a maximum at moderate $Mg(TFSI)_2$ concentrations. The successful design of anion receptors was proven by testing ClO_4^- and TFSI- with different nucleophilicity, which leaded to an increase in transference number for ClO_4^-. The effectiveness of the anion receptor mainly depends on the degree of fluorination and thus by its overall design. A higher degree of fluorination resulted into a lower anion receptor property, lower salt to polymer interaction and transference numbers.

In the third chapter, high salt containing polymer electrolytes were investigated for an aliphatic polycarbonate incorporating $Mg(TFSI)_2$ and $Mg(B(HFIP)_4)_2$ with contrary anion properties. With increasing salt concentrations, the formation of aggregates and ion pairs are supported as well as the elongation of the polycarbonate. Between 30 and 40 mol% $Mg(B(HFIP)_4)_2$ the formation of a polymer-in-salt electrolyte from salt-in-polymer electrolyte were seen due to its bulky anion but not for $Mg(TFSI)_2$. Although the polymer-in-salt electrolyte had an enhanced ionic conductivity over several magnitudes, only a low compatibility with magnesium metal electrodes due to a low plating/stripping reversibility.

In summary, fundamental knowledge to polymer electrolytes design in magnesium-ion batteries was developed as alternative to state-of-the-art LIBs and expands the knowledge for several approaches known in LIBs towards MIBs. Still certain drawbacks as poor reversibility, high plating/stripping potentials remains, which have to be considered in future research. In particular magnesium-lithium dual-salt electrolytes indicated an outstanding opportunity in polymer electrolyte design but struggle with the need of lithium. Thus, alternative dual-salt systems have to be in focus including sodium or potassium to overcome the abundance limitations.

Experimental Section

1.9 Chemicals

Boric acid (Sigma Aldrich, 99.5%), azobis(isobutyronitril) (AIBN, 98%, Sigma Aldrich), methacryloyl chloride (97%, Alfa), magnesium ethoxide (98%, Sigma Aldrich), 2-cyano-2-propyl dodecyl trithiocarbonate (CPDT, 97%, abcr GmbH), 1,4-dioxane (≥ 99%, TCI), 4-fluorophenylboronic acid (containing varying amounts of anhydride, TCI) glycidyl methacrylate (≥ 97%, Sigma Aldrich), triethylamine (99%, Acros), 2-cyano-2-propylbenzodithioat (CPBD, 97%, abcr GmbH), magnesium foil (99.9%, goodfellow, 0.1 mm thickness), 2,4-difluorophenylboronic acid (≥ 95%, Sigma Aldrich), ethylchloroformate (97%, Sigma Aldrich), 2-butyl-2-ethyl-1,3-propanediol (9 %, Sigma Aldrich), hexylamine (9 %, TCI), 3,5-bis(trifluoromethyl)phenyl isothiocyanate (>98%, Sigma Aldrich) and calcium hydride (95%, Sigma Aldrich) and D,L-isopropylidenglycerin (97%, solketal, Acros) were used as received.

Molsieve 3Å (Sigma Aldrich) was always used after activating at 120 °C and 10^{-3} mbar for 24 h.

Poly(ethylene glycol) methyl ether methacrylate ($PEGMA_{500}$ equals to M_n = 500 g mol^{-1}, Sigma Aldrich) and poly(ethylene glycol) methyl ether methacrylate ($PEGMA_{950}$ equals to M_n = 950 g mol^{-1}, Sigma Aldrich) were purified by basic aluminium oxide columns to eliminate stabilizers.

Poly(ethylene glycol) dimethylether ($PEGDME_{500}$ equals to M_n = 500 g mol^{-1}, Sigma Aldrich) and propylene carbonate (PC, 99.5%, Acros) were stored over activated molecular sieve (3 Å) inside the glovebox and dried for at least 3 days before used.

Lithium bis(trifluoromethane)sulfonimide (LiTFSI, 99.95%, Sigma Aldrich), lithium perchlorate ($LiClO_4$, 99.99%, Sigma Aldrich), magnesium perchlorate ($Mg(ClO_4)_2$, ACS reagent, Sigma Aldrich) and magnesium bis(trifluoromethane)sulfonylimide ($Mg(TFSI)_2$, >9 %, TCI) were dried at 200°C for 48 h at high vacuum (10^{-3} mbar) before using and were stored inside a glove box (MBraun Unilab, <0.5 ppm H_2O, <0.5 ppm O_2) under inert argon atmosphere.

Tetrahydrofuran (THF, anhydrous, 99.9%, Fisher) was dried with molecular sieves for at least a day before use.

All other solvents and reagents were of analytical grade or higher and were used without further purification.

The solvent for $Mg(B(HFIP)_4)_2$ synthesis, 1,2-dimethoxyethane (DME, 99.5%, inhibitor free, Sigma Aldrich) was stored over Na metal for a week, distilled under N_2 atmosphere, then dried with molecular sieves for a week in the glovebox prior to use.[282]

1.10 Instrumentation and general considerations

1.10.1 Instrumentations

Nuclear magnetic resonance spectroscopy (NMR)

Projects in chapters 1.6 and 1.7

NMR data was recorded with a Bruker Ascend III 400 MHz NMR at frequency of 400 MHz. The chemical shift for ^{1}H-NMR spectra was reported in parts per million (ppm) referenced to the characteristic solvent signal of DMSO-d_6 at 2.50 ppm (quintet), toluene-d_8 at 2.09 ppm (quintet) and $CDCl_3$ at 7.26 ppm (singlet).

Selected NMR samples were carried out in Young´s NMR tubes prepared under water-free conditions inside a glove box (MBraun Unilab, <0.5 ppm H_2O, <0.5 ppm O_2) under inert argon atmosphere.

Project in chapter 1.8

NMR data were recorded with a Bruker Ascend 400 MHz NMR. The chemical shift for ^{1}H-NMR spectra was reported in parts per million (ppm) referenced to the characteristic solvent signal of $CDCl_3$ at 7.26 ppm or DMSO-d_6 at 2.50 ppm.

Gel permeation chromatography (SEC)

Projects in chapters 1.6 and 1.7

The SEC elugrams were recorded with a PL-SEC 50 plus system equipped with a PLgel precolumn and two PLgel 5 µm Mixed-C columns as well as a differential refractive index (RI) detector. The operation temperature was set to 50 °C with a flow rate of 0.5 mL min^{-1}. The system was calibrated using poly(methyl methacrylate) (PMMA) standards ranging from 800 to 2.1 10^6 g mol^{-1}. Typically, 100 µL of a 2.0 $g \cdot L^{-1}$ sample solution in DMAc was injected onto the columns with a 0.32 $g \cdot L^{-1}$ LiBr solution in DMAc as eluent.

Project in chapter 1.8

The samples were prepared in an THF eluent at a concentration of 1 mg/mL and analyzed over PSS SDV 5 µm columns and an RI detector with a Tosoh EcoSEC pump at 35 °C and acquisition time of 35 min. PMMA reference material was used to estimate the molecular weight.

Infrared spectroscopy (FT-IR)

FT-IR measurements were recorded on a Bruker VERTEX 80 FT-IR spectrometer employing the PIKE MIRacle™ universal Attenuated Total Reflection (ATR) sampling accessory with diamond ATR crystal inside a glovebox with < 0.5 ppm H_2O and O_2 (MBraun Unilab).

Differential scanning calorimetry (DSC)

Projects in chapters 1.6 and 1.7

DSC measurements were conducted on a DSC Q200 (TA Instruments) in a range from −90 to 100 – 130 °C, with a scan rate of 5 K min^{-1} for all measurements with a pre-heating step before performing the measurement.

Project in chapter 1.8

DSC measurements were conducted on a DSC Q2000 V24 in a range from -100 to 125 °C, with a scan rate of 10 K min^{-1} for all measurements (pre-heating step to 130 °C and pre-cooling step to -100 °C before performing the measurement).

Thermogravimetric Analysis (TGA)

TGA measurements were performed on a TGA 5500 (TA Instruments) with a temperature ramp of 10 °K per minute from 50 °C to 700 °C under air or nitrogen atmosphere.

Electrochemical Impedance Spectroscopy (EIS)

Projects in chapters 1.6 and 1.7

For EIS measurements, coin cell-type cells (CR2032) were assembled, where the previously prepared polymer electrolytes were sandwiched between two stainless-steel electrodes using a Mylar foil spacer ring (thickness l = 100 µm, inner diameter = 10 mm) Subsequently, these cells were preconditioned in a temperature chamber (Binder MK53, controlled with a VMP300-based instrument of Bio-Logic Science Instruments SAS) with a preconditioning process of 20 to 70 °C to 0 °C. One hour after preconditioning was finished, the measurements were carried out by gradually increasing the temperature in 10 °C steps from 0 to 70 °C, with each temperature being maintained for 2 h to attain thermal equilibrium. The measurements were performed over a

frequency range of 1 MHz to 1 Hz with an amplitude of 10 mV. The ionic conductivity (σ) was calculated according to the equation 5;

$$\sigma = \frac{l}{A}\frac{1}{R_b} \qquad \text{Eq. 5}$$

R_b is the bulk resistance that can be accessed from the Nyquist plot, l is the film thickness ($l \approx 100$ µm), and A is the film area ($A = 7.85 \cdot 10^{-5}$ m^2). For each polymer at least three coin-cells were prepared and measured. For ionic conductivity values are averaged values of three different coin cells.

Project in chapter 1.8

Ionic conductivity was measured by using a broadband dielectric spectrometer with an Alpha A analyser, outfitted with a cryostat and Quatro temperature control unit (Novocontrol Technologies, Montabaur, Germany). The previously prepared PE samples were sandwiched between two stainless-steel electrodes using a Mylar foil spacer ring (thickness l = 100 µm, inner diameter = 8 mm). Coin cells (CR2032) were assembled and aged at 120°C overnight before measurement to improve contact between electrodes and the electrolyte. Ionic conductivity was measured over a frequency range of 10^7 to 10^{-1} Hz with an amplitude of 10 mV with a gradual increase in temperature from -10 to 120 °C in 10 °C steps and with a following reverse heating procedure cooled down to -10 °C. The temperature was stabilized at each point for 10 min within 0.5°C prior to each measurement. For each polymer, at least three coin cells were measured to derive an average ionic conductivity.

Temperature depending ionic conductivities typically are presented in Arrhenius plot with log(σ) vs. 1000/T. The resulting plots can either be described by Arrhenius plot or Vogel-Tammann-Fulcher-equation (VFT-equation), depending on the mechanism and nature of the electrolyte. Arrhenius plots are mostly found for liquid electrolytes, crystalline PEs, ceramics or glassy PEs.[70] Amorphous PEs are described by VFT-equation:

$$\sigma = A_0 e^{-\frac{B}{T-T_0}} \qquad \text{Eq. 4}$$

A_0 is the factor related to the number of mobile charge carriers, B is the pseudo-activation energy of segmental motion and T the temperature. T_0 is the Vogel temperature and can be estimated for a non-ideal glass as $T_0 = T_g$-50 °C.[70] The VFT-plots are often used to fit temperature dependent

ionic conductivity for polymer electrolytes, where the ion mobility is caused by segmental motion of the polymer host.

Transference number measurements (t^+)

Transference number (t^+) measurements) were done for coin cell-type cells (CR2032), where the previously prepared polymer electrolytes were sandwiched between two activated magnesium electrodes. For all electrochemical measurements Mylar foil spacer ring (thickness l = 100 µm, inner diameter = 10 mm) were used. Cells were conditioned in a temperature chamber (Binder MK53, controlled with a VMP300-based instrument of Bio-Logic Science Instruments SAS). Impedance measurements were conducted for 20 to 24 h before t^+ measurements, ensuring a stable interface. A DC polarization was applied with a polarization voltage of 0.5 V for t^+_{Mg} or 0.01 V for t^+_{Li} measurements. Additionally, impedance data were collected directly before and after the polarization over a frequency range of 1 MHz to 100 mHz with an amplitude of 10 mV. The results were discussed by $I_{SS}/I_{0,Pol}$ ratios, where the initial current, $I_{0,Pol}$ was validated by using Ohm´s law 3:

$$I_{0,cal} = \frac{\Delta U}{R_b} \qquad \text{Eq. 3}$$

I_{SS} are the initial and steady-state currents of the polarization plot, R_0 and R_{SS} are the surface resistance before and after polarization and ΔV is the applied potential. t^+_{Li} was calculated by equation 2, where $I_{SS}/I_{0,cal}$ equalled $I_{SS}/I_{0,Pol}$.

$$t^+ = \frac{I_{SS}}{I_{0,Pol}} \frac{(\Delta V - I_{SS}R_{SS})}{(\Delta V - I_{0,Pol}R_0)} \qquad \text{Eq. 2}$$

Linear Sweep Voltammetry (LSV)

LSV measurements were performed at 20 °C between 0 and 6 V vs. Mg/Mg^{2+} at a scan rate of 0.1 mVs^{-1}. Magnesium was used as counter and reference electrode, stainless steel as working electrode.

Constant current cycling measurements

Constant current cycling experiments were done for coin cell-type cells (CR2032), where the previously prepared polymer electrolytes were sandwiched between two activated magnesium electrodes. For all electrochemical measurements Mylar foil spacer ring (thickness l = 100 µm, inner diameter = 10 mm) were used. Cells were conditioned in a temperature chamber (Binder

MK53, controlled with a VMP300-based instrument of Bio-Logic Science Instruments SAS) at 80 °C. The constant currents were applied over 1 h while alternating between positive and negative current.

Experiments with various current densities were done a current densities of 0.01, 0.05, 0.1, 0.5, 1 and 10 µA cm^{-2} for 6 cycles each before increasing to the following current density.

For long time measurements a current density of 0.1 µA cm^{-2} was applied for over 50 cycles.

X-ray photon spectroscopy (XPS)

XPS measurements were done of magnesium electrodes after plating/stripping experiments carried out at 0.1 µA cm^{-2} at 80 °C for 13 cycles in symmetric Mg||Mg cell on a VMP-300 Bio-Logic potentiostat, with temperature control realized by a Weisstechnik climate chamber. measurements were carried out on a PHI 5000 VersaProbe II Scanning ESCA Microprobe (Physical Electronics) with a monochromatized Al Kα source (1486.6 eV), and the peaks were calibrated according to the binding energy of sp3-carbon (284.8 eV)

Raman spectroscopy

Samples were prepared in an argon filled glove box and sealed in quartz cuvettes Raman spectra were obtained using Jasco NRS-5100 with excitation laser with a wavelength of 532 nm. The signal was calibrated with a silicon wafer at a wavenumber of 520.7 cm^{-1}. Raman spectra were obtained with 5–10 scans for 1–2 min, which sums up to total scan time of around 10 min.

Rheology measurements

The rheological experiments were performed on a strain-controlled ARES-G2 rheometer (TA Instruments). For small-amplitude oscillatory shear (SAOS) measurements, parallel plates with a diameter of 13 mm were used, with temperature control with a Peltier at 20°C. Oscillatory strain sweeps (γ_0 = 0.01−100%) at a constant angular frequency of ω = 6.28 rad s^{-1} were conducted to determine the linear viscoelastic regime (LVE), followed by oscillatory frequency sweeps. Strain amplitudes between γ_0 = 0.02 and 10% were chosen for the frequency sweeps, depending on the LVE of blend.

Cyclic voltammetry (CV)

Electrochemical measurements were conducted using a PARSTAT MC1000 (Princeton Applied Research) potentiostat. Coin cells (CR2032) were assembled with the same spacer used for ionic conductivity measurement, wherein SS and Mg electrodes were used as working and counter

electrodes. CV measurements were performed between -2 to 2 V vs $Mg||Mg^{2+}$ for five cycles at 80 °C and a scan rate of 0.1 mVs^{-1}. Electrochemical impedance spectroscopy (EIS) measurements were conducted before and after CV measurements over a frequency range of 10^6 Hz to 10^{-1} Hz with an amplitude of 10 mV at 80 °C.

1.10.2 General polymer electrolyte film preparation

PE film preparation I- Projects in chapter 1.6

The PEs were prepared by a combined solution casting and cross-linking method. To do so, the deprotected polymers were cross-linked in methanol by the addition of boric acid (1.0 eq.) and magnesium ethanolate (0.5 eq.) based on the ratio of SMA in the copolymers. After homogenous solutions were obtained the solution was casted into a Teflon mold and the solvent was allowed to evaporate at room temperature and redissolved in methanol. The solving and casting procedure was repeated 5 times until homogenous films were obtained. Those films were cut into discs with a diameter of 1 cm and dried under high vacuum (10^{-3} mbar) at 60 °C for 72 h before insertion into a glovebox with argon atmosphere. Gel polymer electrolytes (GPEs) were prepared by swelling the polymer in 50 wt. % PC or $PEGDME_{500}$ for 15 min on the corresponding electrode inside the glovebox before cell assembling. All PEs were stored and further handled under argon atmosphere inside a glovebox with < 0.1 ppm O_2 and H_2O (MBraun Unilab).

PE film preparation II – Project in chapters 1.7

All polymer electrolytes were stored and prepared by a solution cast method under argon atmosphere inside a glovebox with < 0.5 ppm O_2 and H_2O concentration. Polymers were pre-dried at 60 °C for 72 h at high vacuum (10^{-3} mbar) before insertion into the glovebox with argon atmosphere. The corresponding polymer were dissolved into Acetone with salt concentrations of either 10:1, 25:1 or 45:1 [Mg]/[Li]:[EO]. The mixture was stirred until a clear solution was obtained and casted into a Teflon® bowl. The solvent was allowed to be evaporate before cutting disks with a diameter of 10 mm and drying for 72 h at 60 °C and high vacuum (10^{-3} mbar). All PEs were stored and further handled under argon atmosphere inside a glovebox with < 0.1 ppm O_2 and H_2O (MBraun Unilab).

PE film preparation III – Project in chapter 1.8

$Mg(B(HFIP)_4)_2$-3 DME and $Mg(TFSI)_2$ were combined with P(BEC) in THF at concentrations of 5, 20, 30 and 40 mol% magnesium salt to repeating unit, and electrolytes were prepared by solution casting under argon atmosphere. After the bulk solvent appeared to have evaporated, the electrolytes were dried for 24 h at room temperature under vacuum in an argon filled glovebox

followed by 48 h at 80 °C. All PEs were stored and further handled under argon atmosphere inside a glovebox with < 0.1 ppm O_2 and H_2O.

1.11 Experimental methods

1.11.1 Procedures for 'Borate crosslinked single-ion conducting copolymer electrolytes for magnesium battery applications'

The experimental procedures and analytical results were part of N. Zuber's Master thesis supervised by me, David Antonius Sundermann.[239]

Synthesis of Solketal methacrylate (SMA)

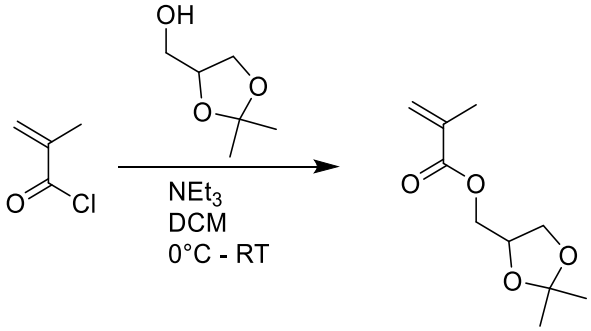

SMA was synthesized as previously reported.[298] Methacryloyl chloride (1.6 eq., 9.2 g, 88 mmol) was added to solketal (1 eq., 10.58 g, 53 mmol) and trimethylamine (1.6 eq., 22 ml, 88 mmol) in DCM (100 ml) at 0 °C and stirred for 16 h. After filtration the organic layer was washed with water and $NaHCO_{3(aq)}$ solution and dried over $MgSO_4$ before purification by vacuum distillation. Yield: 45%

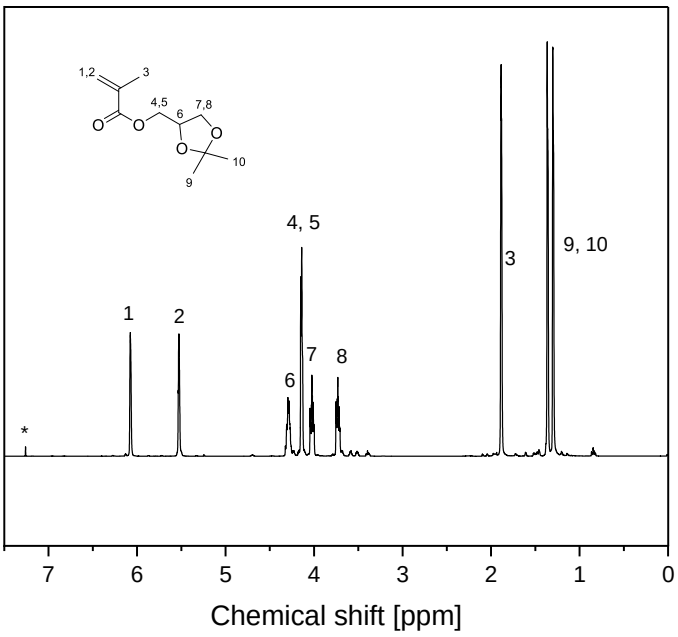

Figure 45: ^{1}H-NMR spectrum of **SMA** in $CDCl_3$. * is assigned to solvent.

^{1}H NMR (400 MHz, $CDCl_3$) δ/ppm 6.08 (s, 1H, C**H**$_2$CMe), 5.52 (s, 1H, C**H**$_2$CMe), 4.38 – 4.19 (dtd, *J* = 6.3, 4.7, 2.6 Hz, 1H, CH$_2$C**H**CH$_2$), 4.19 – 4.07 (td, *J* = 3.9, 3.0, 1.7 Hz, 2H, C**H**$_2$CHCH$_2$), 4.07 – 3.94 (ddd, *J* = 9.0, 6.5, 2.6 Hz, 1H, CH$_2$CHC**H**$_2$), 3.85 – 3.63 (tq, *J* = 6.1, 2.1 Hz, 1H, CH$_2$CHC**H**$_2$), 1.86 (s, 3H, CH$_2$C**Me**), 1.37 -1.3 (d, 6H, C**Me**$_2$).

Synthesis of polymers 1,2 and 4.

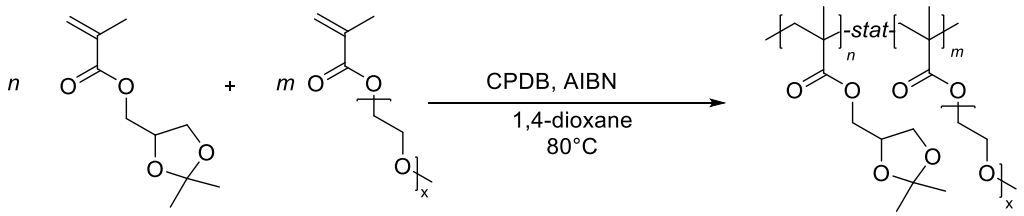

1: n = 58, m = 42, x = 8/9
2: n = 73, m = 27, x = 8/9
4: n = 76, m = 24, x= 18/19

General procedure polymers 1, 2 and 4: SMA (**1**: 60 eq., **2**: 80 eq., **4**: 80 eq.) and PEGMA$_{500/950}$ (**1**: 40 eq., **2**: 20 eq., **4**: 20 eq.) were copolymerized in 1,4-dioxane for 24 h at 80 °C after three cycles of freeze-pump thaw with a monomer to solvent concentration of 2 mol L^{-1} using AIBN (0.2 eq., 2.76 mg, 0.0168 mmol) as initiator and CPBD (1 eq.) as RAFT agent. Subsequently, the polymers were precipitated into cold petrol ether, redissolved in acetone, reprecipitated in petrol

ether tree times and then dried for 1 h at 40 °C under vacuum. The copolymer ratios are listed in Table 13. Yields: 75 – 83%.

Polymer **1**

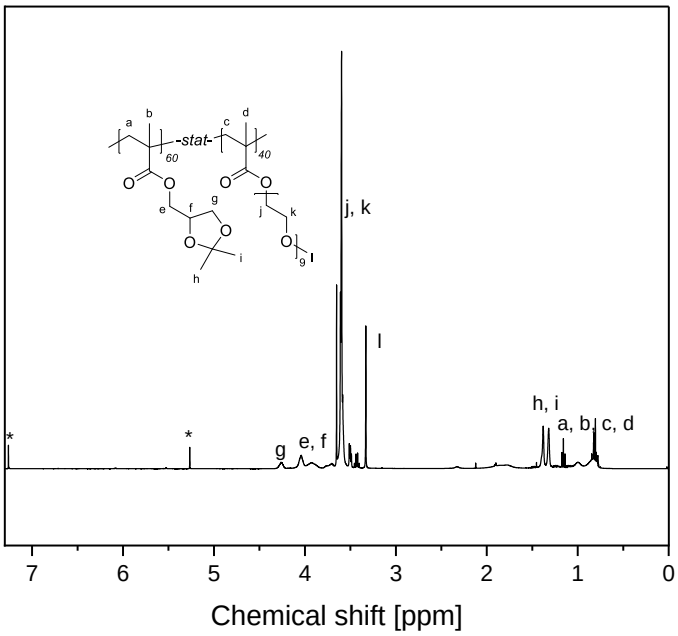

Figure 46: ^{1}H-NMR spectrum of **1** in $CDCl_3$. * is assigned to solvent.

^{1}H NMR (400 MHz, $CDCl_3$) δ/ppm 4.37 – 4.13 (m, 2H), 4.10 – 3.82 (m, 3H), 3.79 – 3.38 (m, 45H), 3.33 (s, 3H), 1.44 – 1.25 (m, 6H), 1.08 – 0.66 (m, 10H).

Polymer **2**

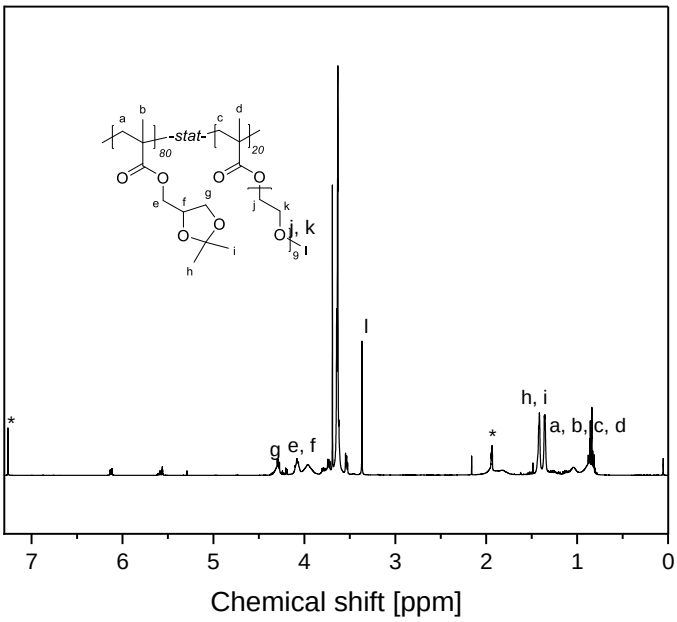

Figure 47: ^{1}H-NMR spectrum of **2** in $CDCl_3$. * is assigned to solvent.

^{1}H NMR (400 MHz, $CDCl_3$) δ/ppm 4.36 – 4.24 (m, 2H), 4.17 – 3.86 (m, 3H), 3.85 – 3.50 (m, 45H), 3.37 (s, 3H), 1.45 – 1.30 (m, 6H), 1.17 – 0.68 (m, 10H).

Polymer **4**

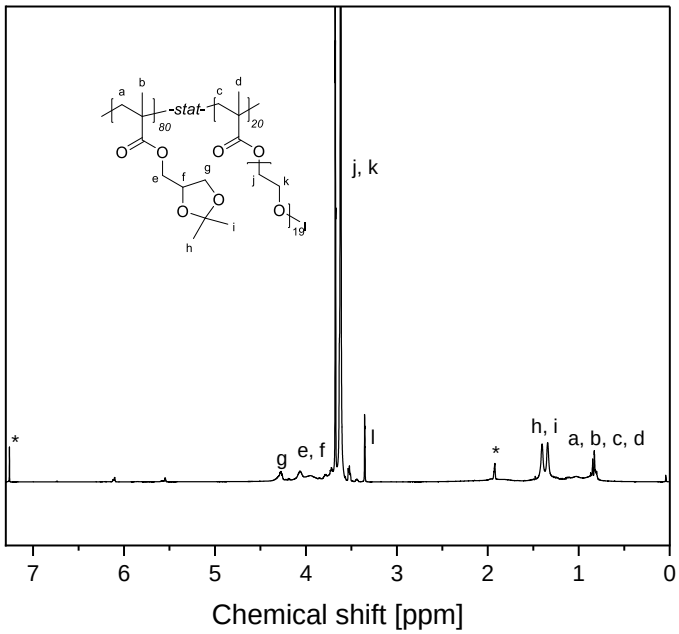

Figure 48: ^{1}H-NMR spectrum of **4** in $CDCl_3$. * is assigned to solvent.

^{1}H NMR (400 MHz, $CDCl_3$) δ/ppm 4.42 – 4.21 (m, 2H), 4.14 – 3.87 (m, 3H), 3.86 – 3.40 (m, 95H), 1.54 – 1.23 (m, 3H), 1.21 – 0.58 (m, 10H).

Synthesis of polymer 3

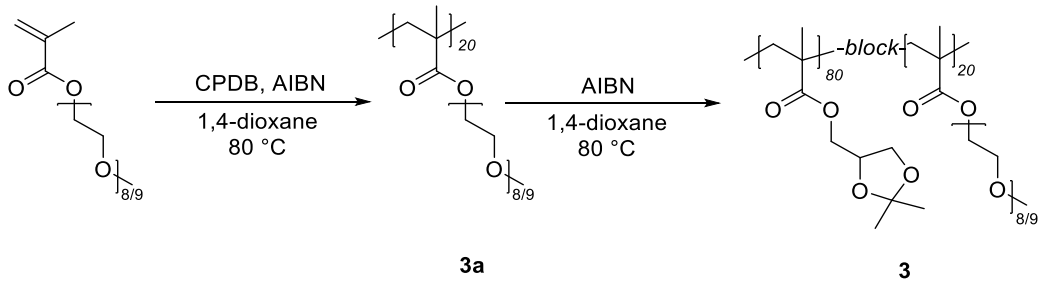

The block copolymers were synthesized in a two-step manner by a macro-RAFT agent approach. The macro-RAFT (**3a**) agent was synthesized by polymerizing $PEGMA_{500/950}$ (20 eq., 840 mg, 1.68 mmol) for 24 h at 80 °C in 1,4-dioxane (2 mol L^{-1}) using AIBN (0.2 eq., 2.76 mg, 0.0168 mmol) as initiator and CPDB (1 eq., 18.6 mg, 0.084 mmol) as RAFT agent. The polymerization was stopped by placing the flask in liquid nitrogen and precipitated once in petrol ether. In a

second step the macro-RAFT agent was copolymerized with SMA (80 eq., 1.34 g, 6.72 mmol) under same conditions as before. The copolymer ratios are listed in Table 13.

Polymer **3a**

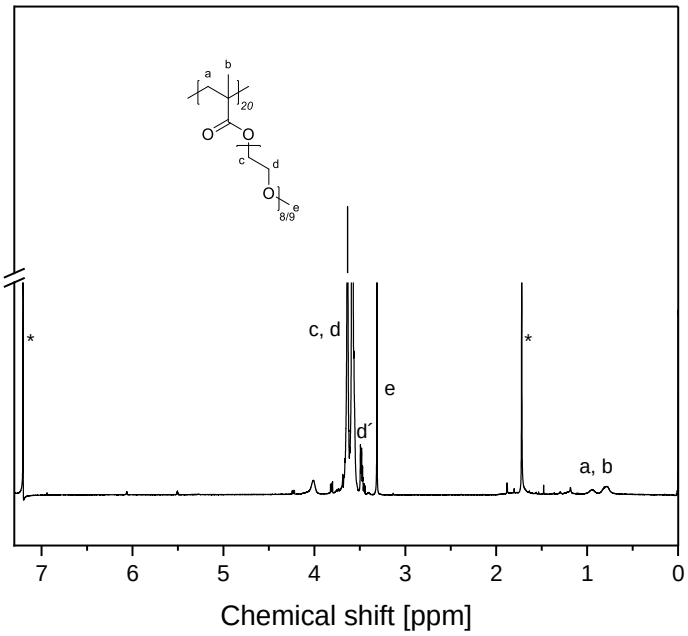

Figure 49: ^{1}H-NMR spectrum of **3a** in $CDCl_3$. * is assigned to solvent.

^{1}H NMR (400 MHz, $CDCl_3$) δ/ppm 3.62 – 3.52 (m, 45H), 3.49 (m, 2H), 3.31 (s, 3H), 1.10 – 0.48 (m, 5H).

Polymer **3**

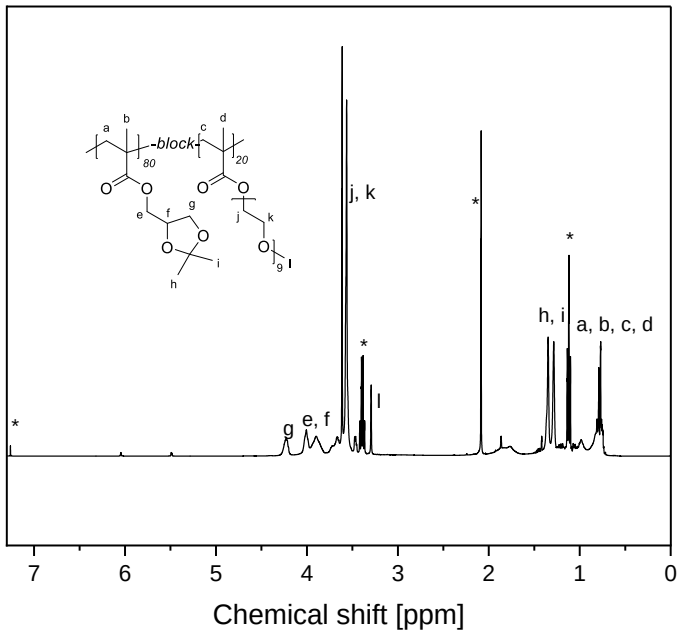

Figure 50: ^{1}H-NMR spectrum of **3** in $CDCl_3$. * is assigned to solvent.

^{1}H NMR (400 MHz, $CDCl_3$) δ/ppm 4.35 – 4.11 (m, 2H), 4.08 – 3.79 (m, 3H), 3.78 – 3.43 (m, 45H), 3.29 (s, 1H), 1.51 – 1.22 (m, 6H), 1.05 – 0.66 (m, 10H).

Table 13: M_n of PEGMA$_x$, architecture and comonomer ratio of polymers **1** to **4**. 1 Was calculated by the integrations of the SMA acetale groups (1.5 – 1.2 ppm) and the methyl end group of PEGMA$_x$ (3.3 ppm).

	M_n (PEGMA$_x$) [g mol^{-1}]	Architecture	SMA:PEGMA$_x$ [mol%][1]
1	500	Statistic	58:42
2	500	Statistic	73:27
3a	500	Macro-RAFT	0:100
3	500	Block	82:18
4	950	Statistic	76:24

Synthesis of polymers 1-diol to 4-diol

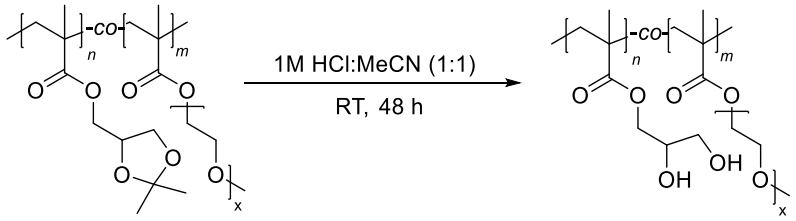

1, **1-diol**: n = 58, m = 42, x = 8/9
2, **2-diol**: n = 73, m = 27, x = 8/9
3, **3-diol**: n = 82, m = 18, x = 8/9
4, **4-diol**: n = 76, m = 24, x= 18/19

General procedure: The polymer was deprotected for 48 h in a 1 M $HCl_{(aq)}$/MeCN solution (1:1) and purified by dialysis in water employing a dialysis membrane with a molecular weight cut-off of 3 kDa for 3 days, while changing the water three times a day. Finally, the polymer was dried under vacuum at 40 °C for 2 days.

Polymer **1-diol**

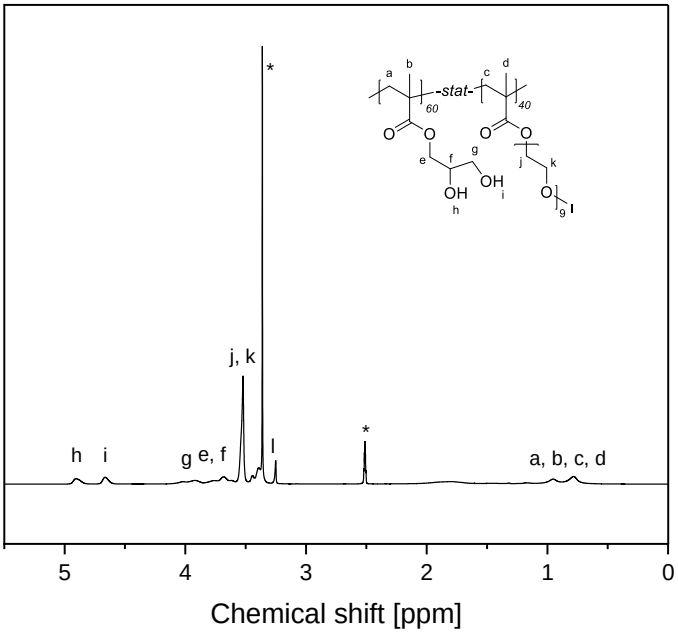

Figure 51: ^{1}H-NMR spectrum of **1-diol** in DMSO-d_6. * is assigned to solvent.

^{1}H NMR (400 MHz, DMSO-d_6) δ/ppm 4.90 (s, 1H), 4.66 (s, 1H), 3.97 (m, 2H), 3.72 (m, 3H), 3.53 (m, 45H), 3.25 (s, 3H), 2.07 – 0.47 (m, 10H).

SEC (PMMA-standard, DMAc): M_n = 47 900 g mol^{-1}, M_n/M_w = 1.35.

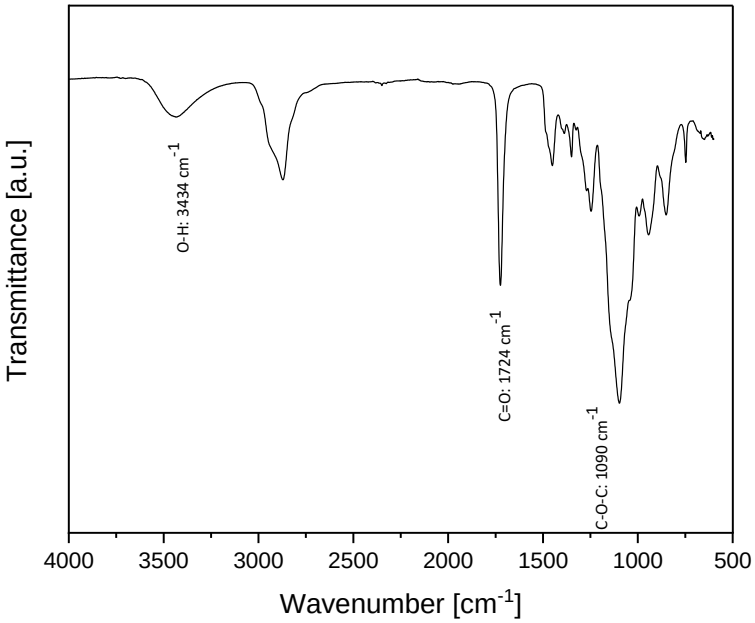

Figure 52: FT-IR spectra of **1-diol** between 4000 to 500 cm^{-1}.

Polymer **2-diol**

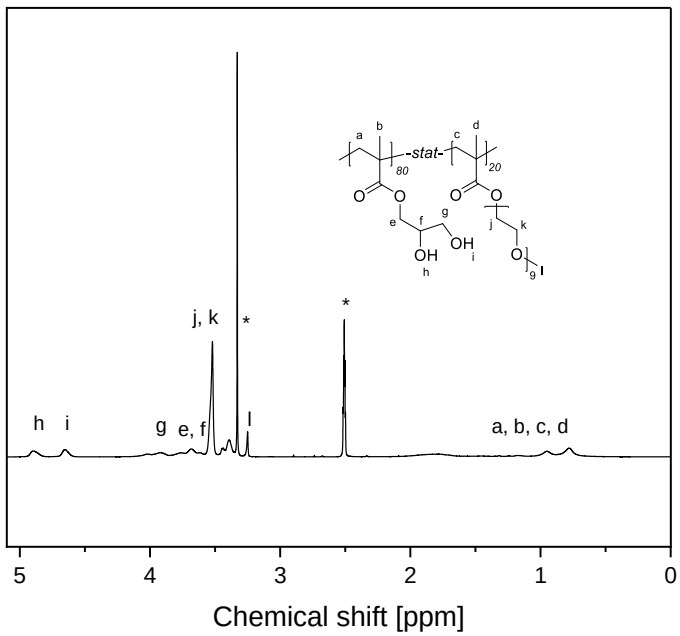

Figure 53: ^{1}H-NMR spectrum of **2-diol** in DMSO-d_6. * is assigned to solvent.

^{1}H NMR (400 MHz, DMSO-d_6) δ/ppm 4.89 (s, 1H), 4.65 (s, 1H), 4.21 - 3.7 (m, 2H), 3.68 (m, 3H), 3.57 – 3.36 (m, 40H), 3.25 (s, 3H), 0.87 (m, 10H).

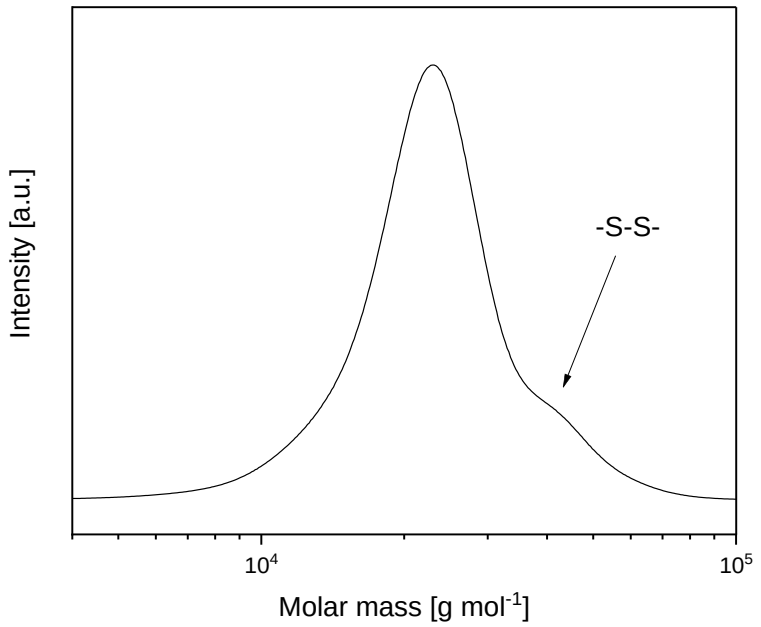

Figure 54: SEC spectrum of **2-diol**. The second peak correspond to disulfide linked polymers after aminolysis in the eluent DMAc.

SEC (PMMA-standard, DMAc): M_n = 21 200g mol^{-1}, M_n/M_w = 1.17.

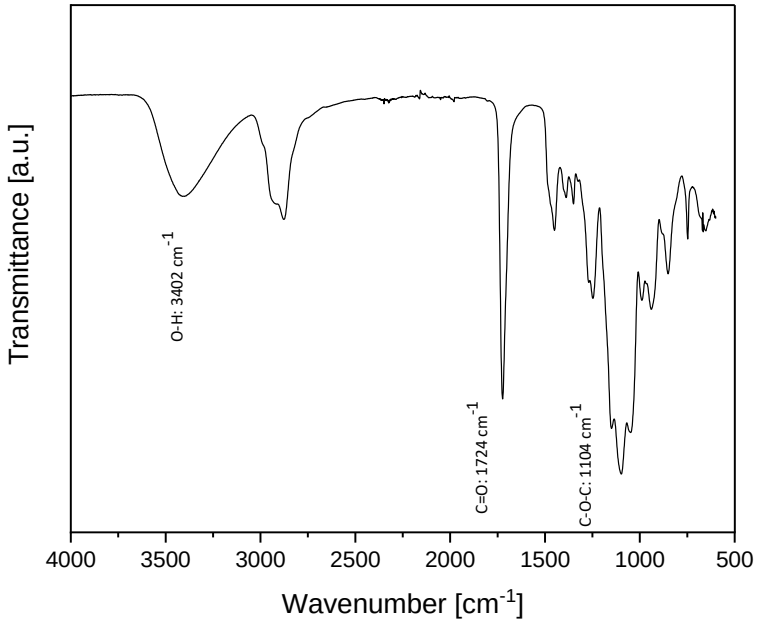

Figure 55: FT-IR spectra of **2-diol** between 4000 to 500 cm^{-1}.

Polymer **3-diol**

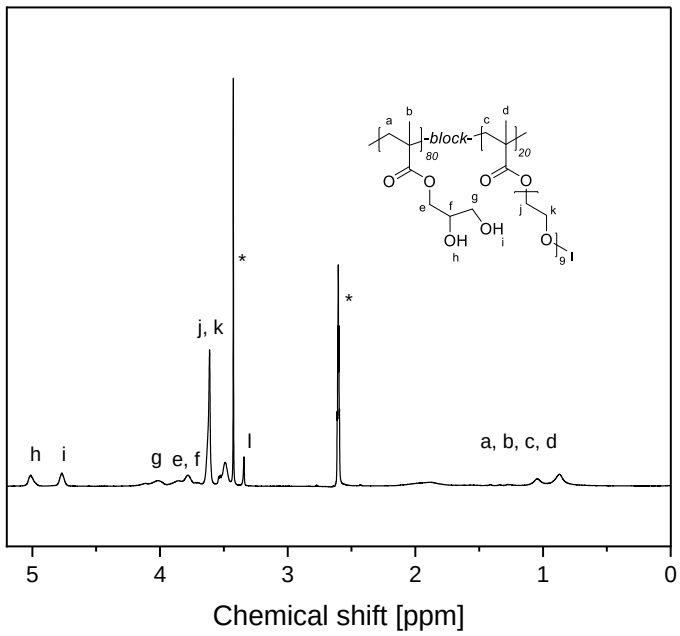

Figure 56: ^{1}H-NMR spectrum of **3-diol** in DMSO-d_6. * is assigned to solvent.

^{1}H NMR (400 MHz, DMSO-*d*$_6$) δ/ppm 5.01 (s, 1H), 4.77 (s, 1H), 4.27 – 3.93 (m, 2H), 3.93 – 3.68 (m, 3H), 3.68 – 3.46 (m, 40H), 3.43 (s, 3H), 1.45 – 0.55 (m, 10H).

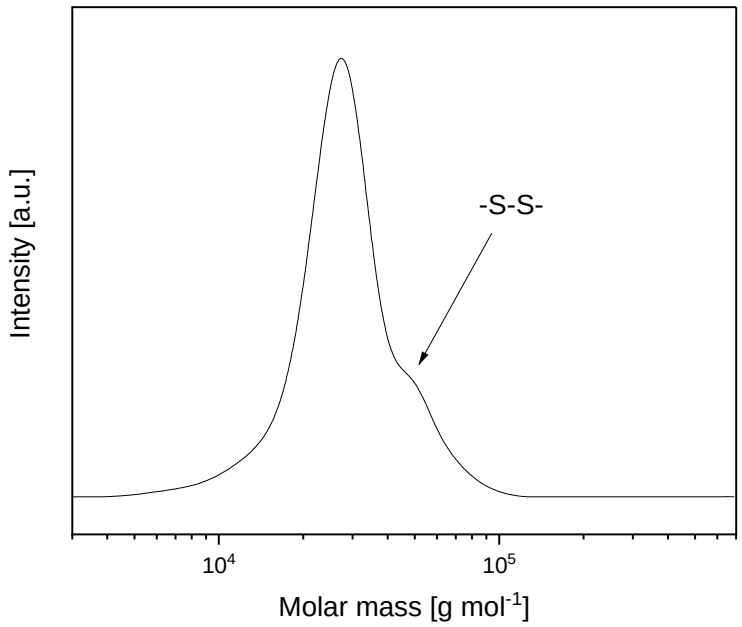

Figure 57: SEC spectrum of **3-diol**. The second peak correspond to disulfide linked polymers after aminolysis in the eluent DMAc.

SEC (PMMA-standard, DMAc): M_n = 25 300 g mol^{-1}, M_n/M_w = 1.20.

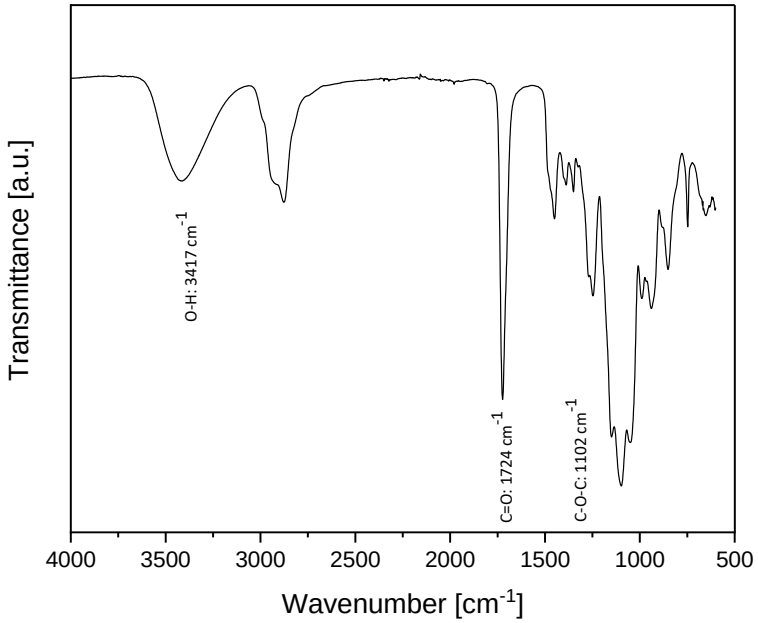

Figure 58: FT-IR spectra of **3-diol** between 4000 to 500 cm^{-1}.

Polymer **4-diol**

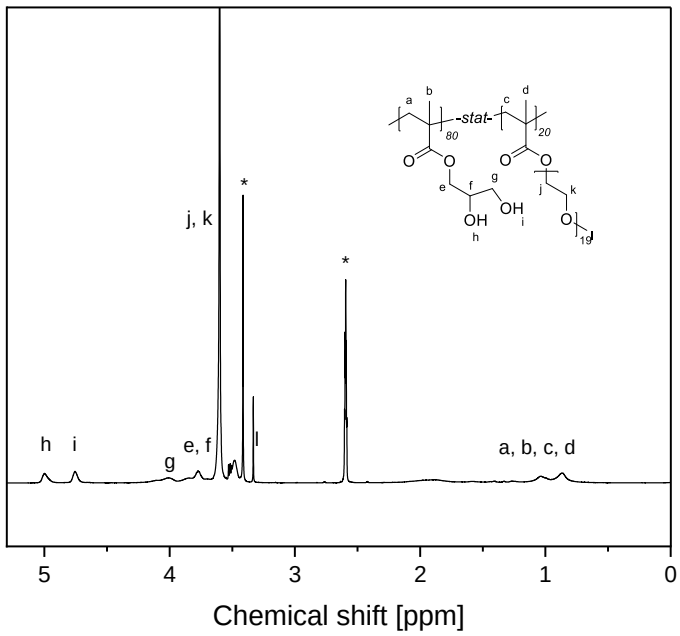

Figure 59: ^{1}H-NMR spectrum of **4-diol** in DMSO-d_6. * is assigned to solvent.

^{1}H NMR (400 MHz, DMSO-*d*$_6$) δ/ppm 5.00 (s, 1H), 4.75 (s, 1H), 4.27 – 3.94 (m, 2H), 3.93 – 3.68 (m, 3H), 3.65 – 3.45 (m, 95H), 3.41 (s, 3H), 1.57 – 0.56 (m, 10H).

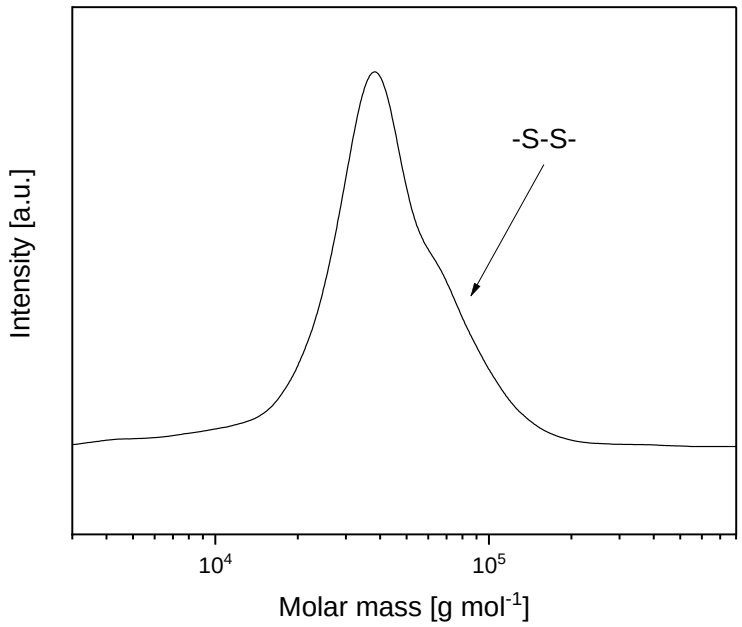

Figure 60: SEC spectrum of **4-diol**. The second peak correspond to disulfide linked polymers after aminolysis in the eluent DMAc.

SEC (PMMA-standard, DMAc): M_n = 32 800 g mol^{-1}, M_n/M_w = 1.46.

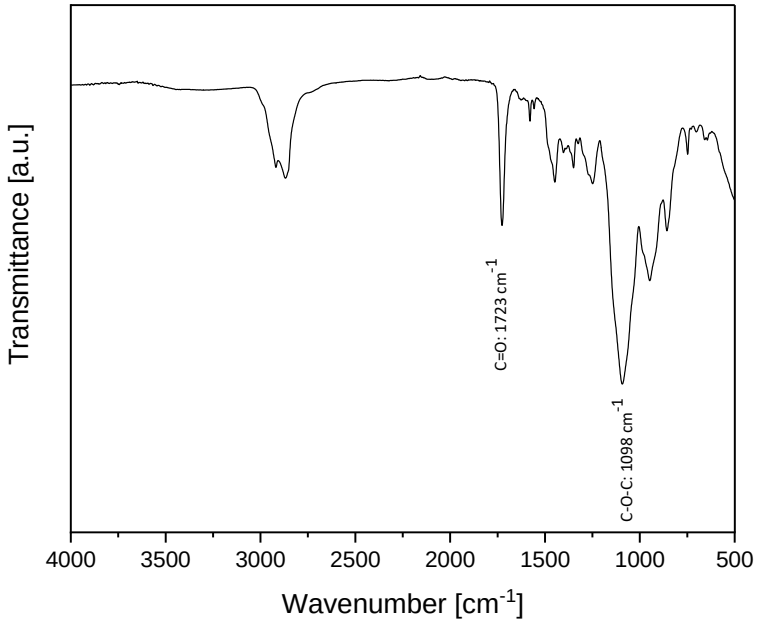

Figure 61: FT-IR spectra of **4-diol** between 4000 to 500 cm^{-1}.

Crosslinking procedure for 1-cross to 4-cross(-Li) and 4-cross-Li-Mg 1:1/2:1

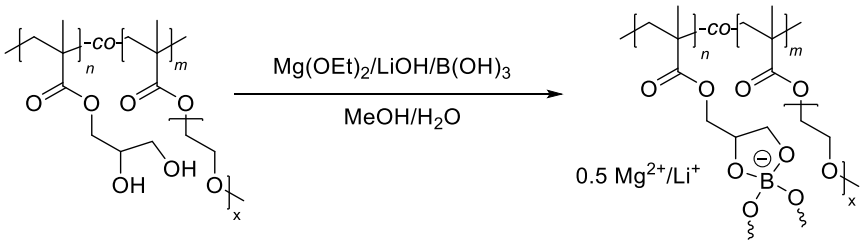

1-diol, **1-cross**: n = 58, m = 42, x = 8/9
2-diol, **2-cross**: n = 73, m = 27, x = 8/9
3-diol, **3-cross**: n = 82, m = 18, x = 8/9
4-diol, **4-cross**: n = 76, m = 24, x= 18/19

General procedure: The PEs were prepared by a combined solution casting and cross-linking method. To do so, the polymers **1-diol** to **4-diol** were crosslinked in methanol by the addition of $B(OH)_3$ (1.0 eq.) and $Mg(OEt)_2$ (**1-cross** to **4-cross**: 0.5 eq., **4-cross-Li-Mg 1:1**: 0.33 eq. and **4-cross-Li-Mg 2:1**: 0.25 eq.) and/or LiOH (**4-cross-Li**: 1 eq., **4-cross-Li-Mg 1:1**:0.33 eq. and **4-cross-Li-Mg 2:1**: 0.5 eq.) based on the ratio of SMA in the copolymers. After homogenous solutions were obtained the solution was casted into a Teflon mold and the solvent was allowed to evaporate at room temperature and redissolved in methanol. The solving and casting procedure was repeated 5 times until homogenous films were obtained.

Polymer **1-cross**

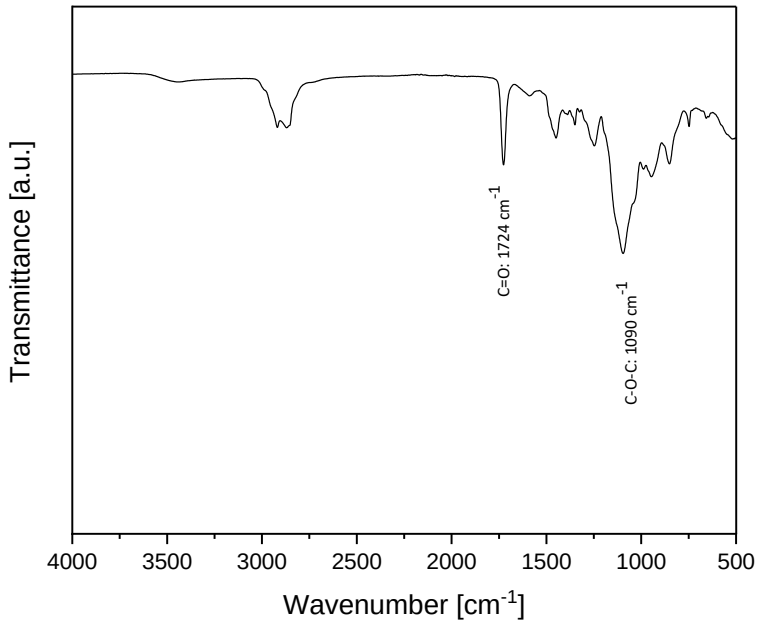

Figure 62: FT-IR spectra of **1-cross** between 4000 to 500 cm^{-1} under inert argon atmosphere.

^{11}B-NMR (128 MHz, DMSO-*d*$_6$) δ/ppm 10.1 (s). See Figure 8B.

Polymer **2-cross**

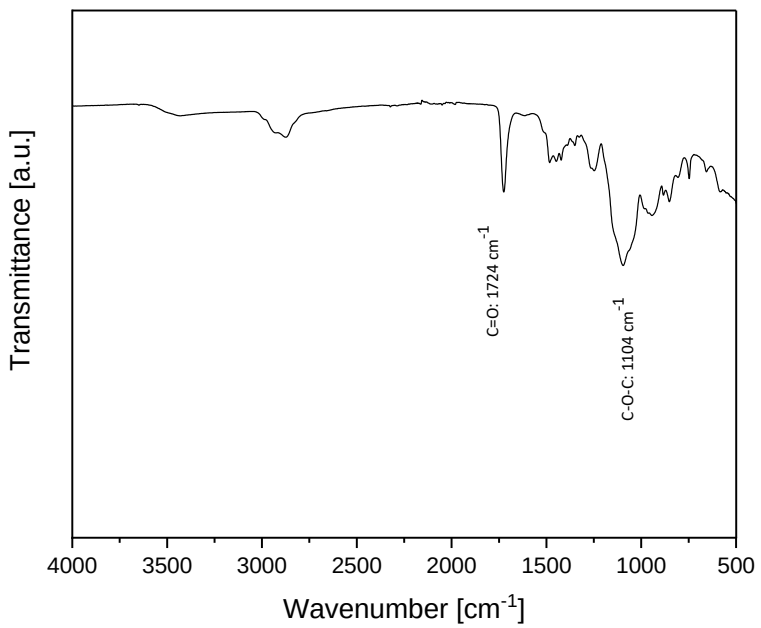

Figure 63: FT-IR spectra of **2-cross** between 4000 to 500 cm^{-1} under inert argon atmosphere.

^{11}B-NMR (128 MHz, DMSO-*d*$_6$) δ/ppm 10.1 (s). See Figure 8B.

Polymer **3-cross**

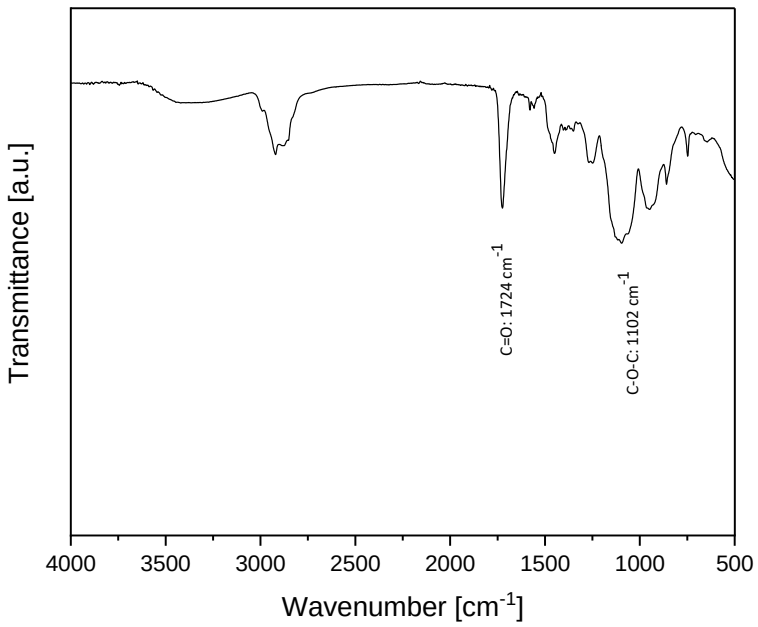

Figure 64: FT-IR spectra of **3-cross** between 4000 to 500 cm^{-1} under inert argon atmosphere.

^{11}B-NMR (128 MHz, DMSO-*d*$_6$) δ/ppm 10.1 (s). See Figure 8B.

Polymer **4-cross**

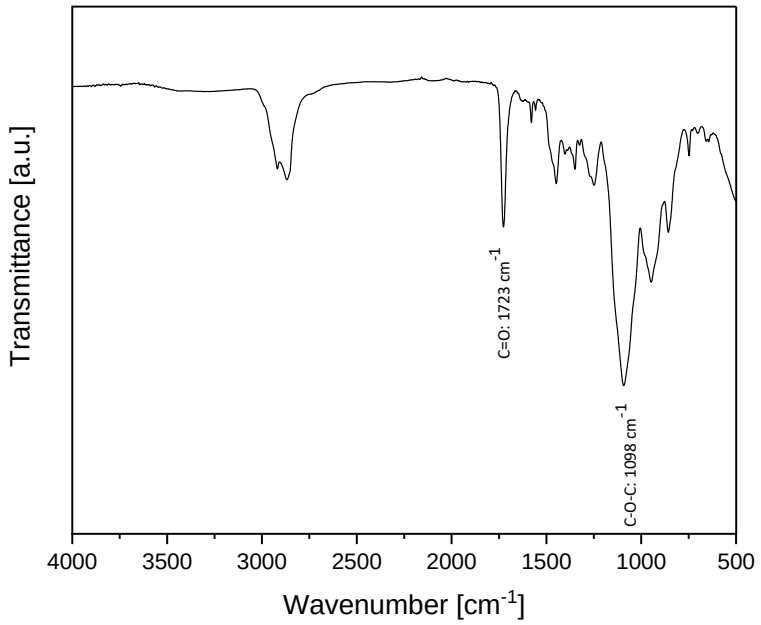

Figure 65: FT-IR spectra of **4-cross** between 4000 to 500 cm^{-1} under inert argon atmosphere.

^{11}B-NMR (128 MHz, DMSO-*d*$_6$) δ/ppm 10.1 (s). See Figure 8B.

Polymer **4-cross-Li**

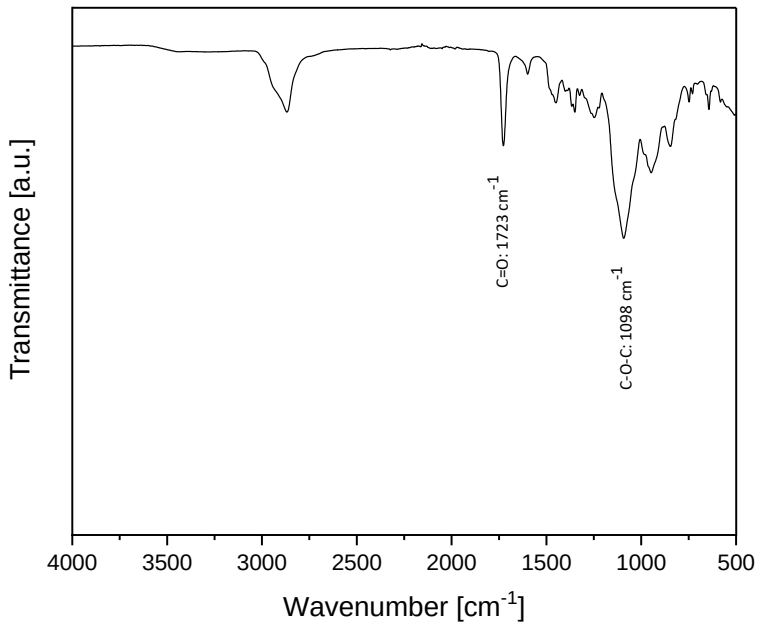

Figure 66: FT-IR spectra of **4-cross-Li** between 4000 to 500 cm^{-1} under inert argon atmosphere.

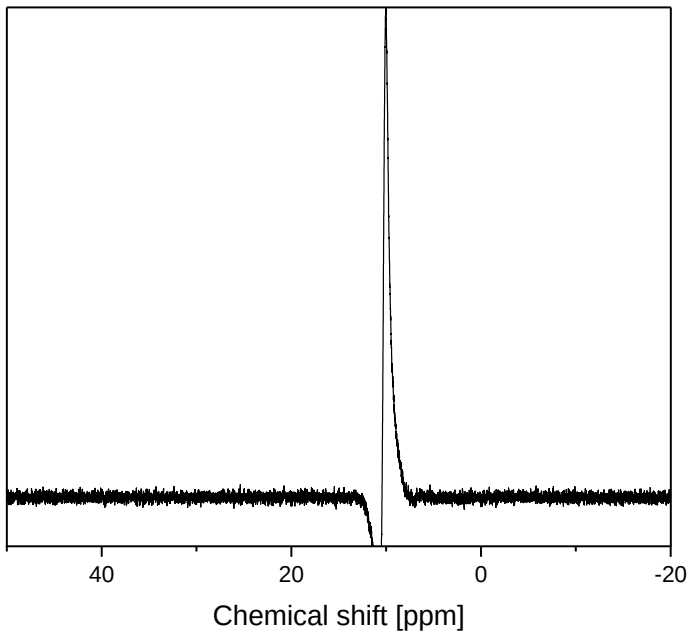

Figure 67: ^{11}B-NMR spectrum of **4-cross-Li** in DMSO-d_6.

^{11}B-NMR (128 MHz, DMSO-d_6) δ/ppm 10.1 (s).

Polymer **4-cross-Li-Mg-1:1**

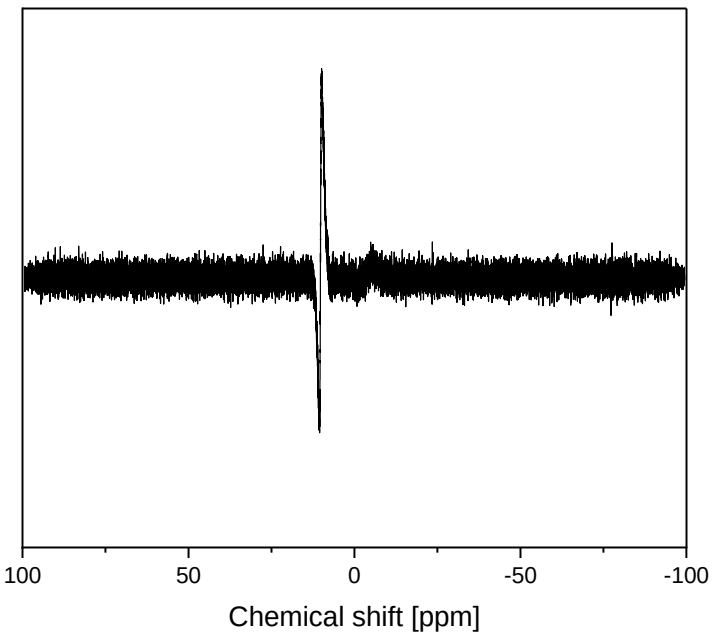

Figure 68: ^{11}B-NMR spectrum of **4-cross-LiMg-11** in DMSO-d_6.

^{11}B-NMR (128 MHz, DMSO-d_6) δ/ppm 10.1 (s).

Polymer **4-cross-Li-Mg-2:1**

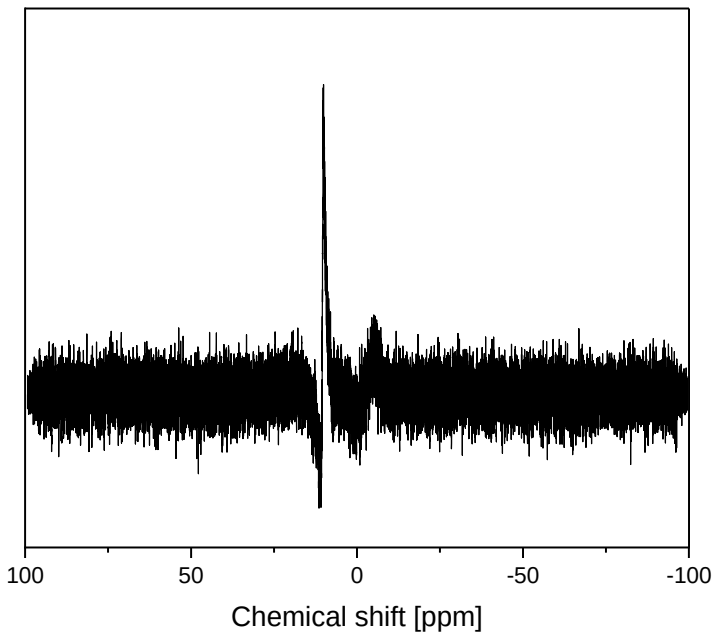

Figure 69: ^{11}B-NMR spectrum of **4-cross-LiMg-2:1** in DMSO-d_6.

^{11}B-NMR (128 MHz, DMSO-d_6) δ/ppm 10.1 (s).

1.11.2 Procedures for 'Additive-free copolymer electrolytes with borate anion receptors for magnesium ion batteries'

Synthesis of SMA-diol

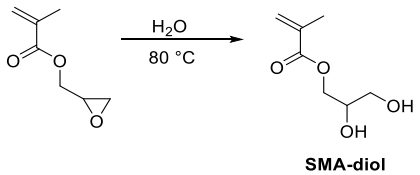

SMA-diol was synthesized as reported by Wang and coworkers.[265] Glycidyl methacrylate (10 mmol, 1.42 g) was stirred in 80 ml H_2O over night at 80 °C. The resulting product was extracted with EtOAc and washed twice with brine before purification by column chromatography (DCM:MeOH 30:1).

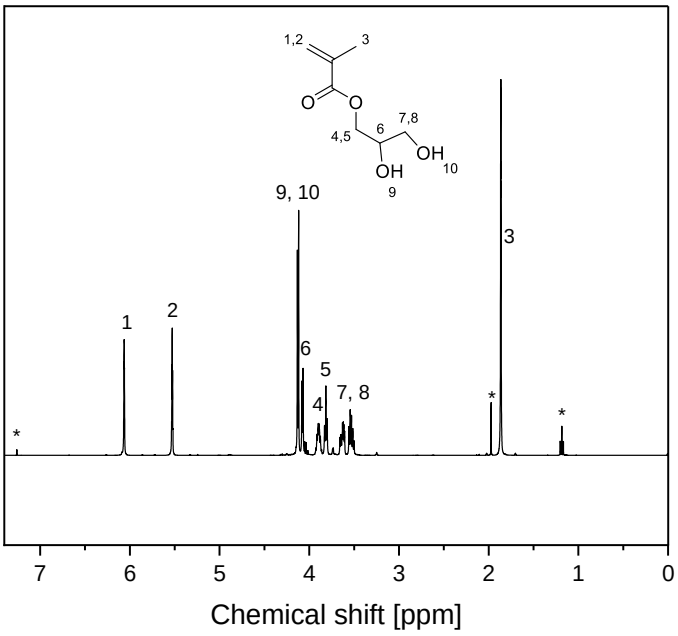

Figure 70: ^{1}H-NMR spectrum of **SMA-diol** in $CDCl_3$. * is assigned to solvent.

^{1}H NMR (400 MHz, $CDCl_3$) δ/ppm 6.13 – 5.97 (m, 1H, C**H**$_2$CMe), 5.61 – 5.47 (m, 1H, C**H**$_2$CMe), 3.95 – 3.85 (m, 2H, O**H**), 4.08 (d, *J* = 5.2 Hz, 1H, CH_2C**H**CH_2), 3.90 (qd, *J* = 5.5, 3.5 Hz, 1H, C**H**$_2$CHCH_2), 3.82 (t, *J* = 5.9 Hz, 1H, C**H**$_2$CHCH_2), 3.63 (ddd, *J* = 11.6, 6.0, 3.6 Hz, 1H, CH_2CHC**H**$_2$), 3.53 (dt, *J* = 11.7, 5.9 Hz, 1H, CH_2CHC**H**$_2$), 1.86 (s, 3H, CH_2C**Me**).

Synthesis of the Monomers MF and MF_2

Monomer **MF**

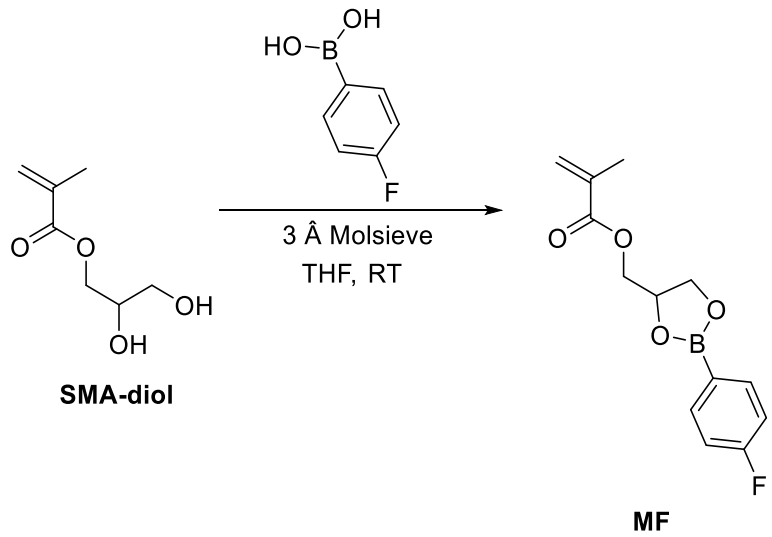

In a round bottom flask SMA-diol (1. eq., 3 g, 18.73 mmol) was added to a solution of 4-difluorophenylboronic acid (1. Eq., 2.62 g, 18.73 mmol) in 100 mL MeCN and was stirred over molsieve for 16 h at room temperature. The solution was filtrated and the solvent was evaporated under reduced pressure.

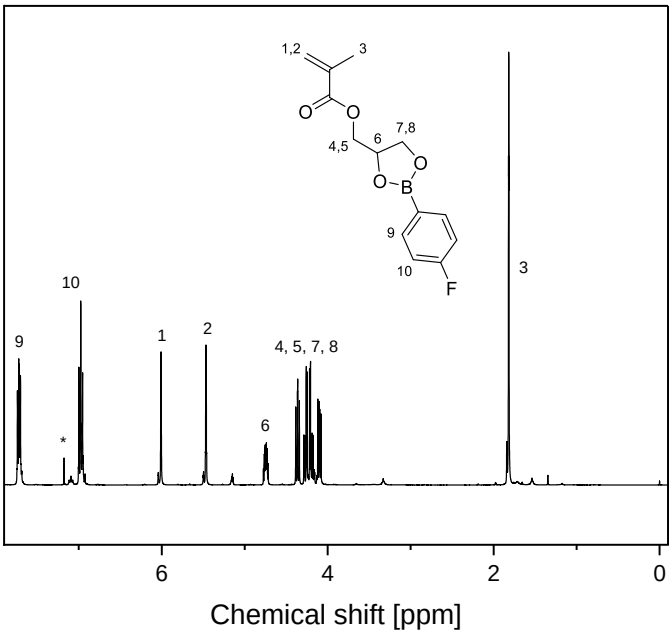

Figure 71: ^{1}H-NMR spectrum of **MF** in $CDCl_3$. * is assigned to solvent.

^{1}H NMR (400 MHz, $CDCl_3$) δ/ppm 7.79 – 7.63 (m, 2H, ortho-ArH), 7.03 – 6.89 (m, 2H, meta-ArH), 6.01 (q, *J* = 1.2 Hz, 1H, C**H**$_2$CMe), 5.57 – 5.41 (m, 1H, C**H**$_2$CMe), 4.75 (ddt, *J* = 8.3, 6.1, 4.2 Hz, 1H, CH$_2$C**H**CH$_2$), 4.36 (dd, *J* = 9.3, 8.3 Hz, 1H, C**H**$_2$CHCH$_2$), 4.30 – 4.15 (m, 2H, C**H**$_2$CHC**H**$_2$), 4.10 (dd, *J* = 9.3, 6.1 Hz, 1H, CH$_2$CHC**H**$_2$), 1.91 – 1.77 (m, 3H, CH$_2$C**Me**).

^{19}F NMR (376 MHz, $CDCl_3$) δ/ppm -107.63. See Figure 19.

^{11}B NMR (128 MHz, $CDCl_3$) δ/ppm 30.14 (s). See Figure 19.

Monomer **MF$_2$**

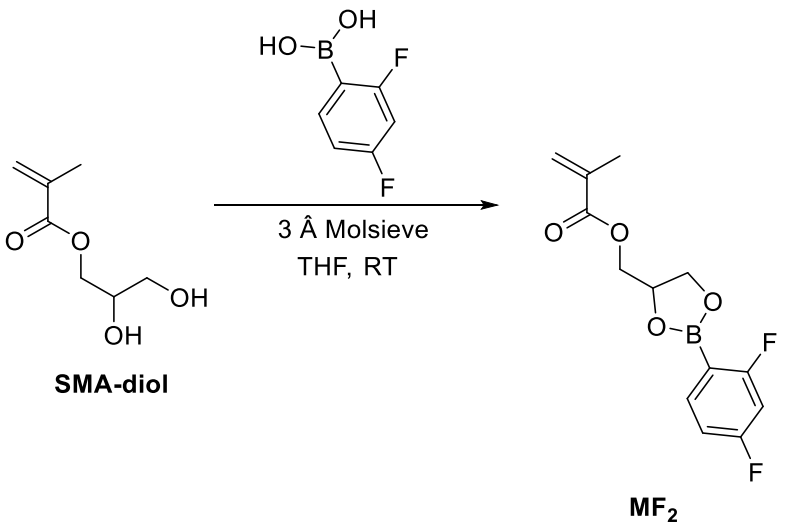

In a round bottom flask SMA-diol (1. eq., 3 g, 18.73 mmol) was added to a solution of 2,4-difluorophenylboronic acid (1. Eq., 2.96 g, 18.73 mmol) in 100 mL MeCN and was stirred over molsieve for 16 h at room temperature. The solution was filtrated and the solvent was evaporated under reduced pressure.

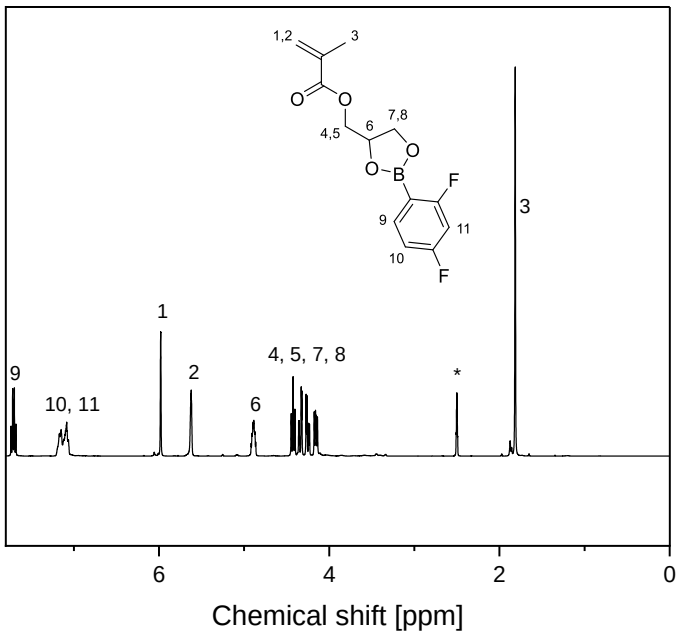

Figure 72: ^{1}H-NMR spectrum of **MF₂** in DMSO-d_6. * is assigned to solvent.

^{1}H NMR (400 MHz, DMSO-d_6) δ/ppm 7.71 (dt, J = 8.4, 7.2 Hz, 1H, ortho-ArH), 7.23 – 7.02 (m, 2H, meta-ArH), 6.01 – 5.95 (m, 1H, C**H**$_2$CMe), 5.62 (dq, J = 3.3, 1.7 Hz, 1H, C**H**$_2$CMe), 4.94 – 4.84 (m, 1H, CH$_2$C**H**CH$_2$), 4.43 (t, J = 8.8 Hz, 1H, C**H**$_2$CHCH$_2$), 4.34 (dd, J = 12.0, 3.1 Hz, 1H, C**H**$_2$CHCH$_2$), 4.25 – 4.12 (m, 2H, CH$_2$CHC**H**$_2$), 1.81 (s, 3H, CH$_2$C**Me**).

^{19}F NMR (376 MHz, DMSO-d_6) δ/ppm -98.24 (d, J = 10.9 Hz), -104.65 (t, J = 9.4 Hz). See Figure 19.

^{11}B NMR (128 MHz, DMSO-d_6) δ/ppm 30.46. See Figure 19.

Polymer synthesis of PF0 andPF$_2$0

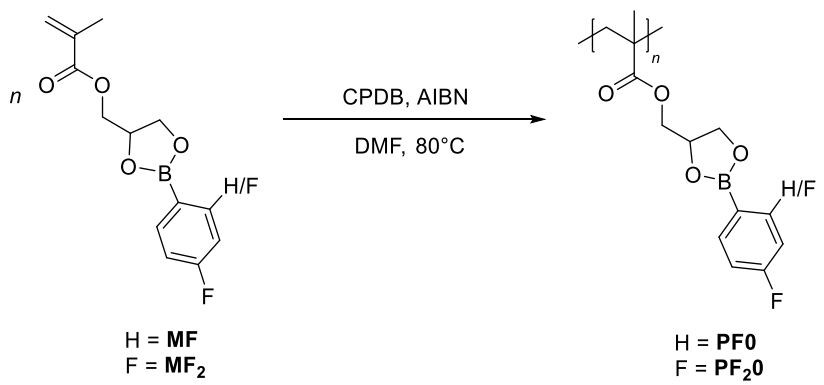

General procedures, $PF_2$0 and PF0. MF_2 (50 eq., 2.31 g, 2 mmol) or **MF** (50 eq., 528.1 mg, 2 mmol) were polymerized by RAFT polymerization in DMF with a concentration of 2 mmol mL^{-1} by AIBN (0.2 eq) and CPDT (1 eq.) for 24 h at 70 °C after three cycles of freeze-pump under water free conditions. The resulting polymer was precipitated into cold PE. Yields: 85%

Polymer **$PF_2$0**

^{1}H NMR (400 MHz, toluene-*d*$_8$) δ/ppm 7.22 (s, 1H), 6.62 (s, 2H), 4.36 (s, 1H), 3.96 (s, 1H), 3.59 (s, 3H), 1.74 – -0.02 (m, 5H). See Scheme 17B.

^{19}F NMR (377 MHz, toluene-*d*$_8$) δ -97.87 (s), -104.52 (s). See Figure 20.

SEC (PMMA-standard, DMAc): M_n = 19 600 g mol^{-1}, M_n/M_w = 1.48. See Figure 21.

Polymer **PF0**

^{1}H NMR (400 MHz, toluene-*d*$_8$) δ/ppm 7.33 (s, 2H), 6.72 (s, 2H), 4.37 (s, 1H), 3.45 (s, 1H), 1.81 – -0.03 (m, 5H). See Scheme 17A.

^{19}F NMR (377 MHz, toluene-*d*$_8$) δ/ppm -107.67 (s). See Figure 20.

SEC (PMMA-standard, DMAc): M_n = 9 800 g mol^{-1}, M_n/M_w = 1.52. See Figure 21.

Polymer synthesis of PF_2X with X = 1 - 4

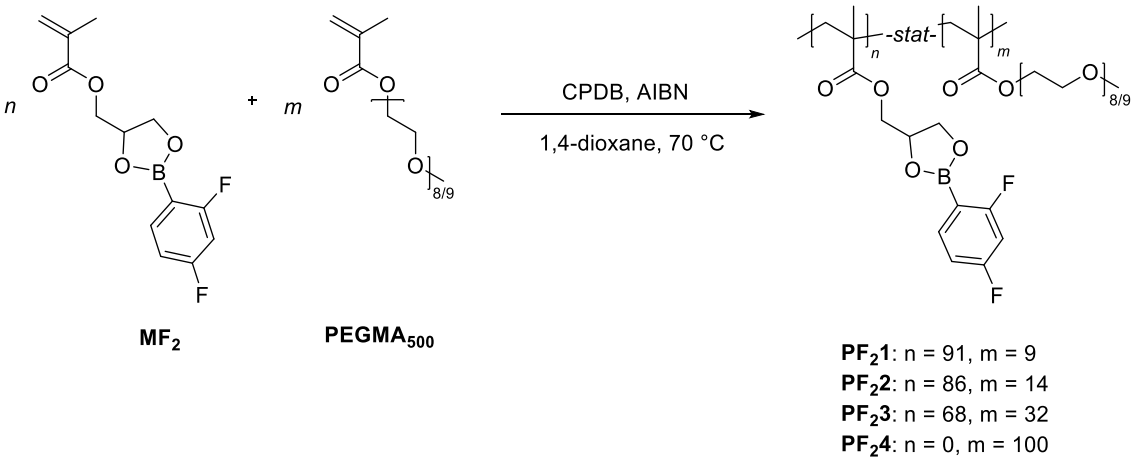

General procedures, PF_2X with X = 1 – 3. MF_2 (**$PF_2$1**:95 eq., **$PF_2$2**: 85 eq. and **$PF_2$3**: 70 eq.) was copolymerized by RAFT polymerization with $PEGMA_{500}$ (**$PF_2$1**:5 eq., **$PF_2$2**: 15 eq. and **$PF_2$3**: 30 eq.) in 1,4-dioxane with a concentration of 2 mmoL mL^{-1} for 24 h at 70 °C after three cycles of freeze-pump under water free conditions with AIBN (0.2 eq) and CPBD (1 eq., 10 mg, 0.045

mmol) as initiator and RAFT agent. The resulting polymer was once precipitated into cold PE. Yields: 75 - 80%.

Polymer **PF$_2$1**

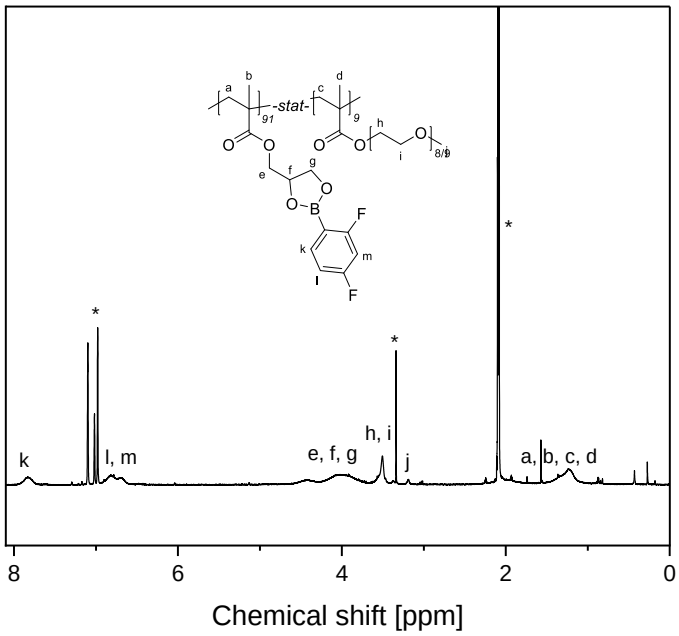

Figure 73: ^{1}H-NMR spectrum of **PF$_2$1** in toluene-d_8. * is assigned to solvent.

^{1}H NMR (400 MHz, toluene-d_8) δ/ppm 7.83 (s, 1H), 6.92 – 6.57 (m, 2H), 4.62 – 3.67 (m, 4H), 3.67 – 3.40 (m, 2H), 1.66 – 0.30 (m, 3H).

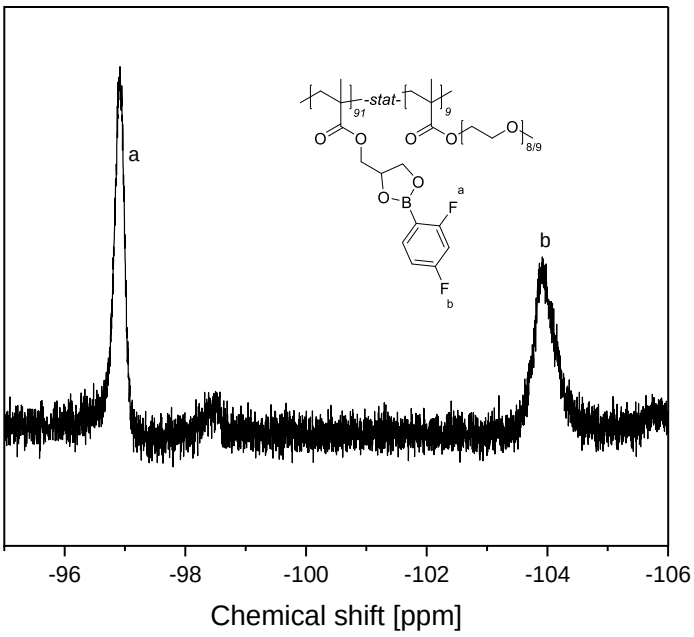

Figure 74: ^{19}F-NMR spectrum of **PF$_2$1** in toluene-*d$_8$*. * is assigned to solvent.

^{19}F NMR (377 MHz, toluene-*d$_8$*) δ/ppm -96.91 (s), -103.95 (s).

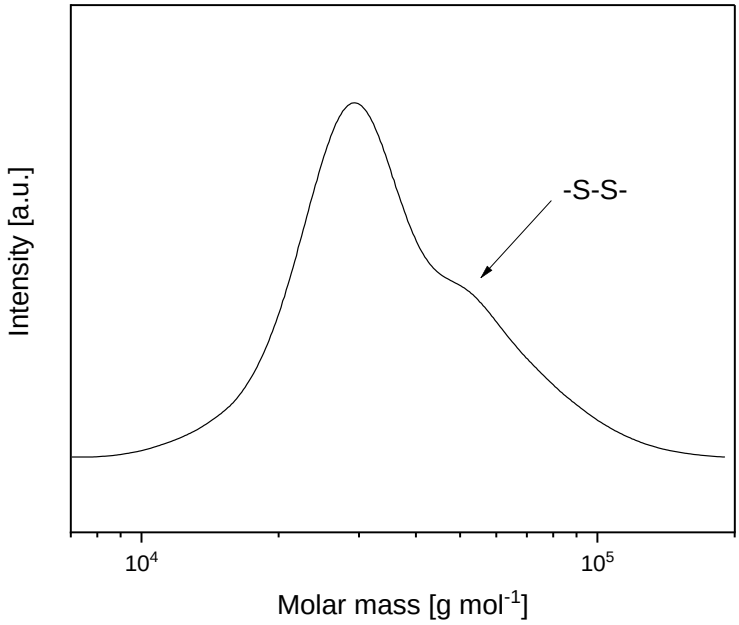

Figure 75: SEC spectrum of **PF$_2$1**. The second peak correspond to disulfide linked polymers after aminolysis in the eluent DMAc.

SEC (PMMA-standard, DMAc): M_n = 31 300 g mol^{-1}, M_n/M_w = 1.25.

Polymer **PF$_2$2**

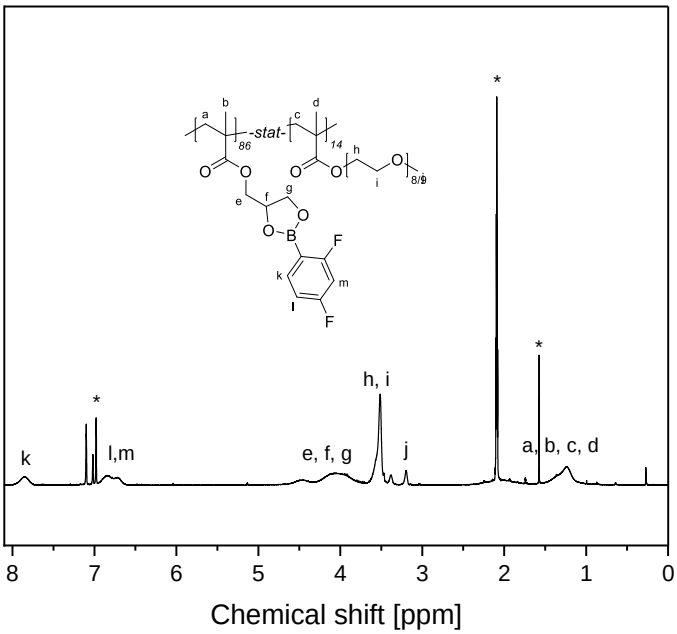

Figure 76: ^{1}H-NMR spectrum of **PF$_2$2** in toluene-d_8. * is assigned to solvent.

^{1}H NMR (400 MHz, toluene-d_8) δ/ppm 7.85 (s, 1H), 6.94 – 6.46 (m, 2H), 4.69 – 3.71 (m, 5H), 3.68 – 3.35 (m, 45H), 3.20 (s, 3H), 1.94 – 0.74 (m, 10H).

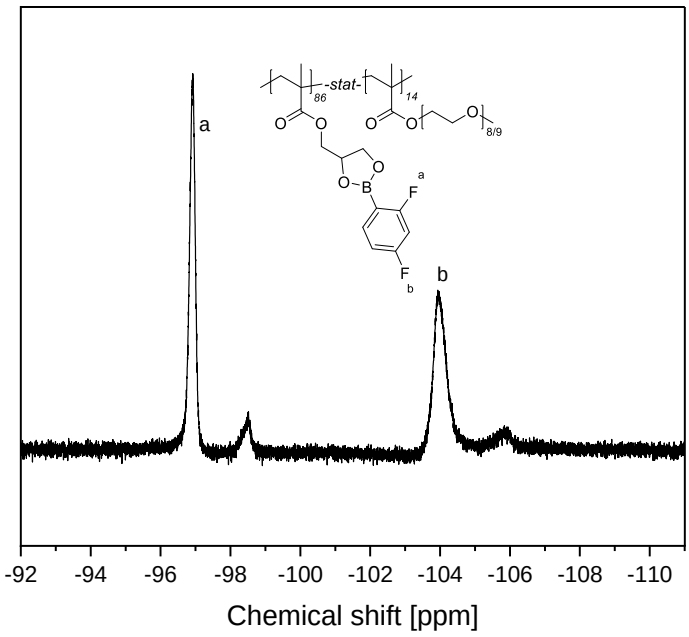

Figure 77: ^{19}F-NMR spectrum of **PF$_2$2** in toluene-*d$_8$*. * is assigned to solvent.

^{19}F NMR (377 MHz, toluene-*d$_8$*) δ/ppm -96.91 (s), -103.99 (s).

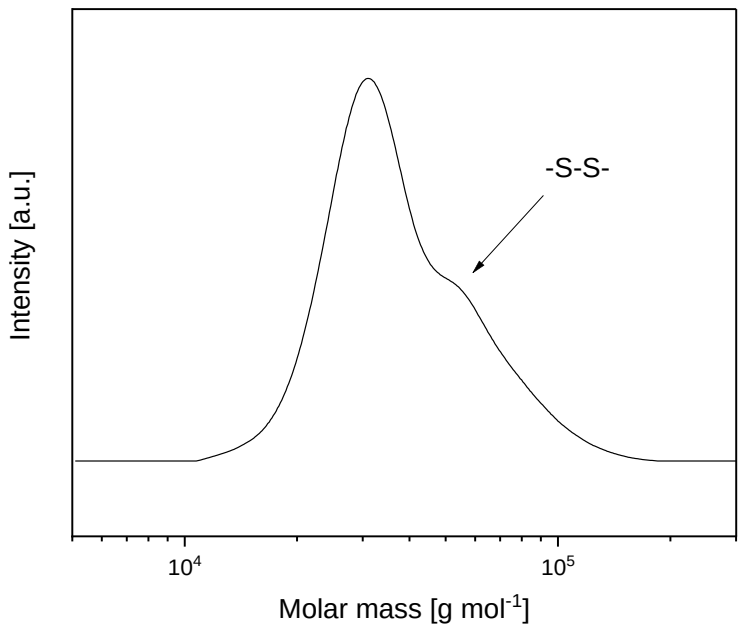

Figure 78: SEC spectrum of **PF$_2$2**. The second peak correspond to disulfide linked polymers after aminolysis in the eluent DMAc.

SEC (PMMA-standard, DMAc): M_n = 34 100 g mol^{-1}, M_n/M_w = 1.21.

Polymer **PF$_2$3**

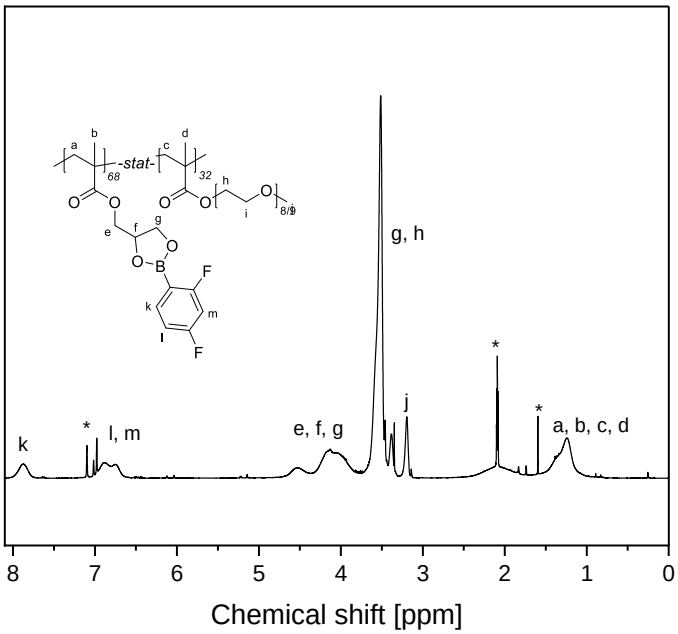

Figure 79: ^{1}H-NMR spectrum of **PF$_2$3** in toluene-d_8. * is assigned to solvent.

^{1}H NMR (400 MHz, toluene-d_8) δ/ppm 7.87 (s, 1H), 66.96 – 6.54 (m, 2H), 4.83 – 3.75 (m, 5H), 3.76 – 3.32 (m, 45H), 3.20 (s, 3H), 2.02 – 0.80 (m, 10H).

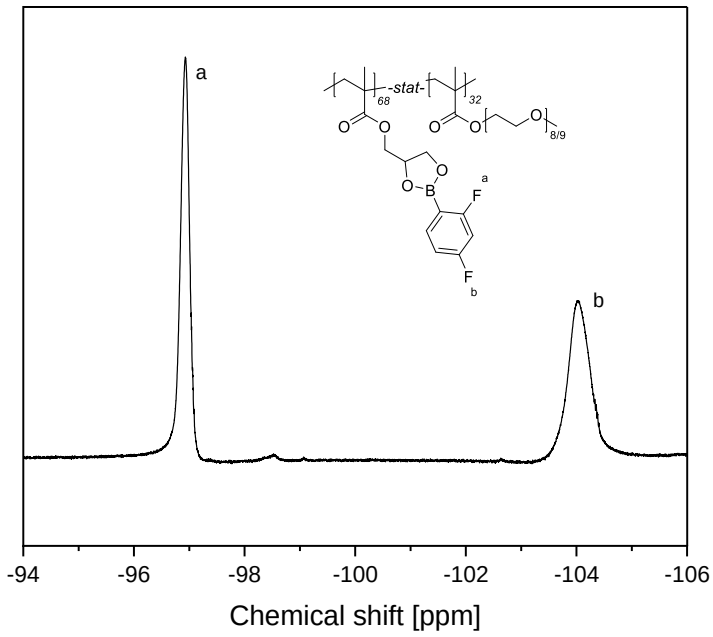

Figure 80: ^{19}F-NMR spectrum of **PF$_2$3** in toluene-*d$_8$*. * is assigned to solvent.

^{19}F NMR (377 MHz, toluene-*d$_8$*) δ/ppm -96.93 (s), -104.05 (s).

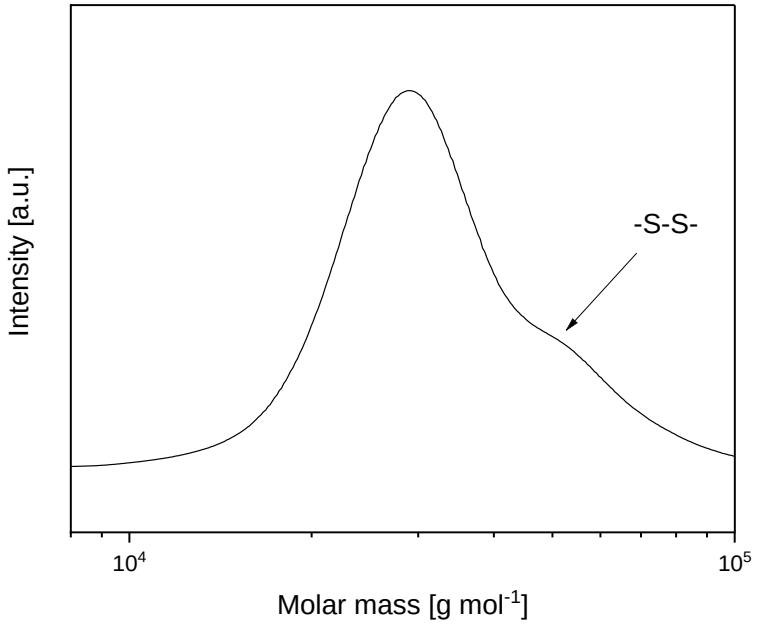

Figure 81: SEC spectrum of **PF$_2$3**. The second peak correspond to disulfide linked polymers after aminolysis in the eluent DMAc.

SEC (PMMA-standard, DMAc): M_n = 29 700 g mol^{-1}, M_n/M_w = 1.16.

Polymer **PF$_2$4**

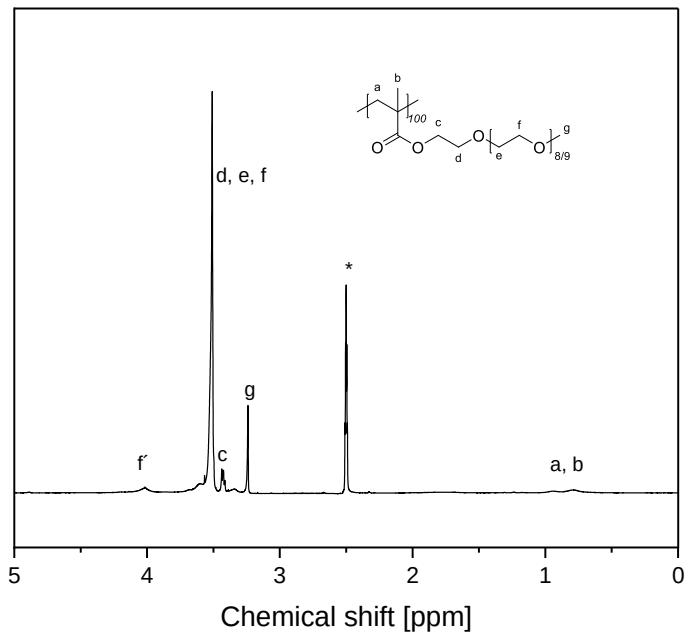

Figure 82: ^{1}H-NMR spectrum of **PF$_2$4** in DMSO-d_6. * is assigned to solvent.

^{1}H NMR (400 MHz, DMSO-d_6) δ/ppm 4.09 – 3.95 (m, 1H), 3.75 – 3.47 (m, 43H), 3.46 – 3.39 (m, 2H), 3.24 (s, 3H), 1.09 – 0.58 (m, 5H).

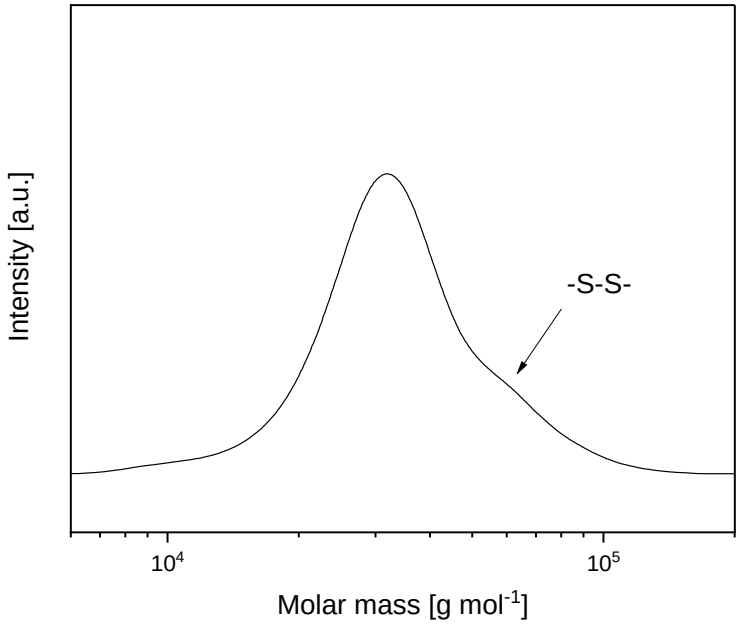

Figure 83: SEC spectrum of **PF$_2$4**. The second peak correspond to disulfide linked polymers after aminolysis in the eluent DMAc.

SEC (PMMA-standard, DMAc): M_n = 30 000 g mol^{-1}, M_n/M_w = 1.22.

Polymer synthesis of block copolymers PF3b and PF$_2$3b

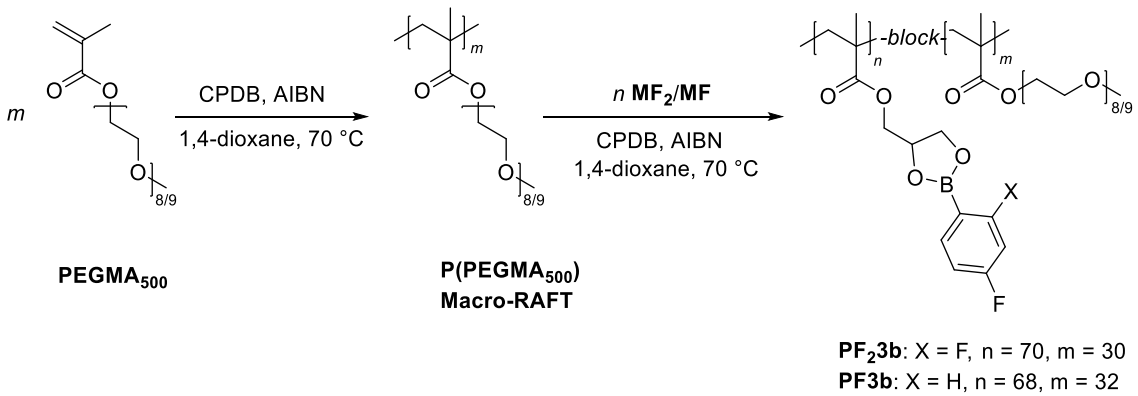

General procedures, block copolymers PF$_2$3b and PF3b. The block copolymers were synthesized in a two-step manner by a macro-RAFT agent approach. The macro-RAFT (**P(PEGMA$_{500}$)**) agent was synthesized by polymerizing PEGMA$_{500}$ (30 eq.) for 24 h at 80 °C in 1,4-dioxane under water-free conditions (2 mol L^{-1}) using AIBN (0.2 eq.,) as initiator and CPDB (1 eq., 10 mg, 0.045 mmol) as RAFT agent. The polymerization was stopped by placing the flask in liquid nitrogen and precipitated once in petrol ether. In a second step the macro-RAFT agent was

copolymerized with **MF** (70 eq., 834 mg, 6.72 mmol) or **MF$_2$** (70 eq., 892 mg, 3.16 mmol) under same conditions as before.

Polymer **PF3b**

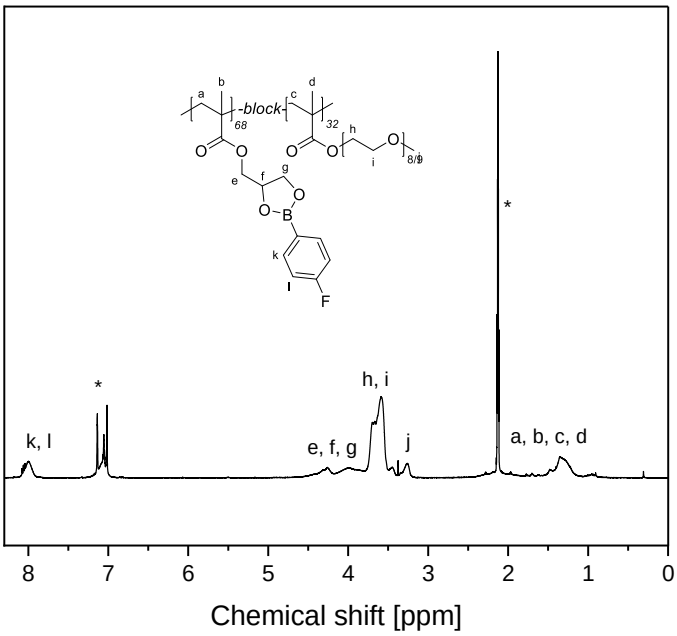

Figure 84: ^{1}H-NMR spectrum of **PF$_{3b}$** in toluene-d_8. * is assigned to solvent.

^{1}H NMR (400 MHz, toluene-d_8) δ/ppm 8.15 – 7.83 (m, 2H), 4.59 – 3.82 (m, 3H), 3.82 – 3.38 (m, 45H), 3.32 (s, 3H), 1.84 – 0.73 (m, 10H).

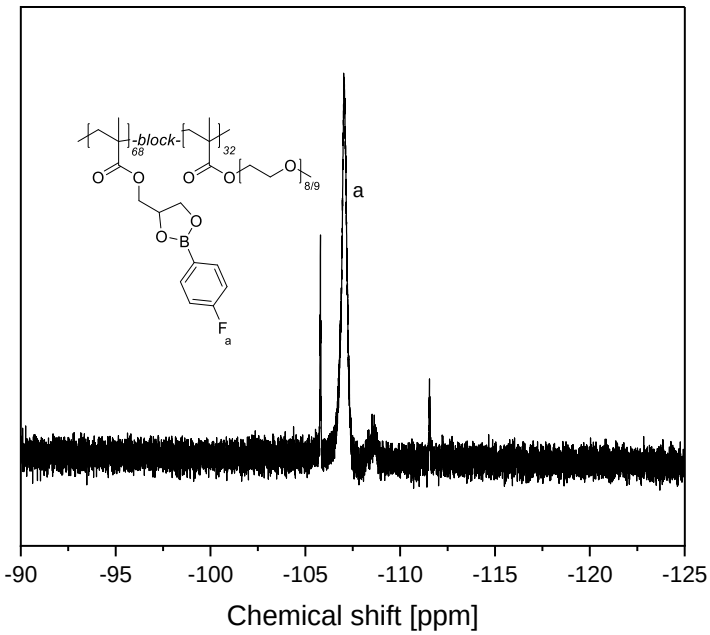

Figure 85: ^{19}F-NMR spectrum of **PF3b** in toluene-d_8. * is assigned to solvent.

^{19}F NMR (377 MHz, toluene-d_8) δ/ppm -107.02 (s).

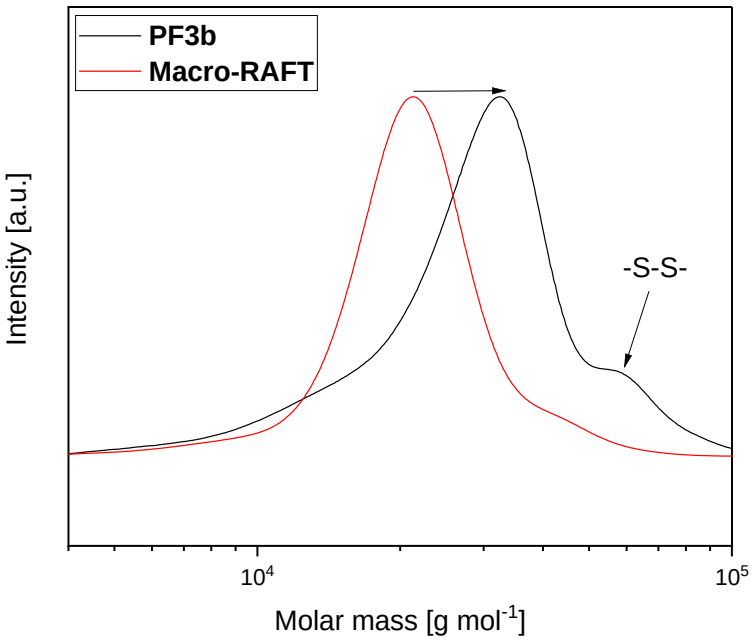

Figure 86: SEC spectrum of the chain extension of **PF3b**. The second peak correspond to disulfide linked polymers after aminolysis in the eluent DMAc.

SEC (PMMA-standard, DMAc): M_n = 24 400 g mol^{-1}, M_n/M_w = 1.3.

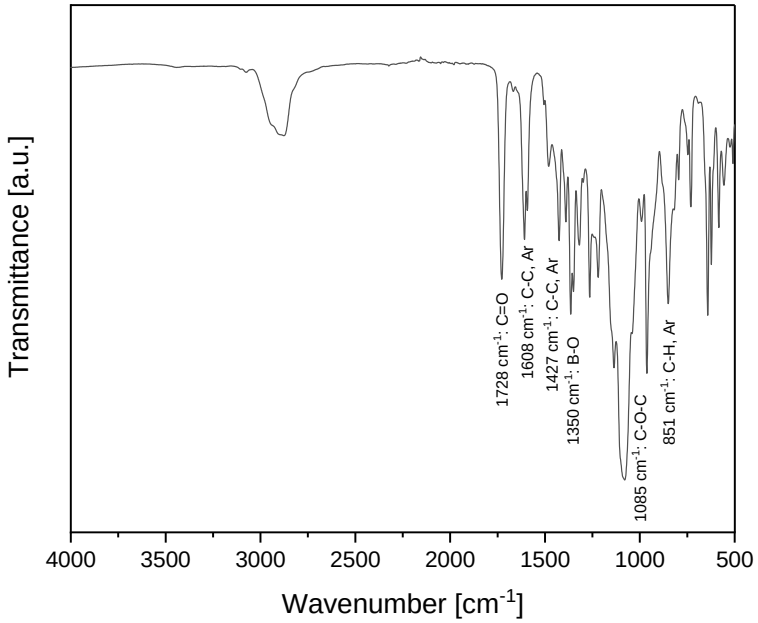

Figure 87: FT-IR spectra of **PF3b** between 4000 to 500 cm^{-1} under water-free argon atmosphere.

Polymer **$PF_2$3b**

^{1}H NMR (400 MHz, toluene-*d*$_8$) δ/ppm 7.83 (s, 1H), 6.91 – 6.52 (m, 2H), 4.68 – 3.79 (m, 5H), 3.78 – 3.33 (m, 45H), 3.23 (s, 3H), 1.96 – 0.71 (m, 10H). See Figure 22.

^{19}F NMR (377 MHz, toluene-*d*$_8$) δ -96.92 (s), -103.92 (s). See Figure 22.

SEC (PMMA-standard, DMAc): M_n = 24 400 g mol^{-1}, M_n/M_w = 1.30. See Figure 23.

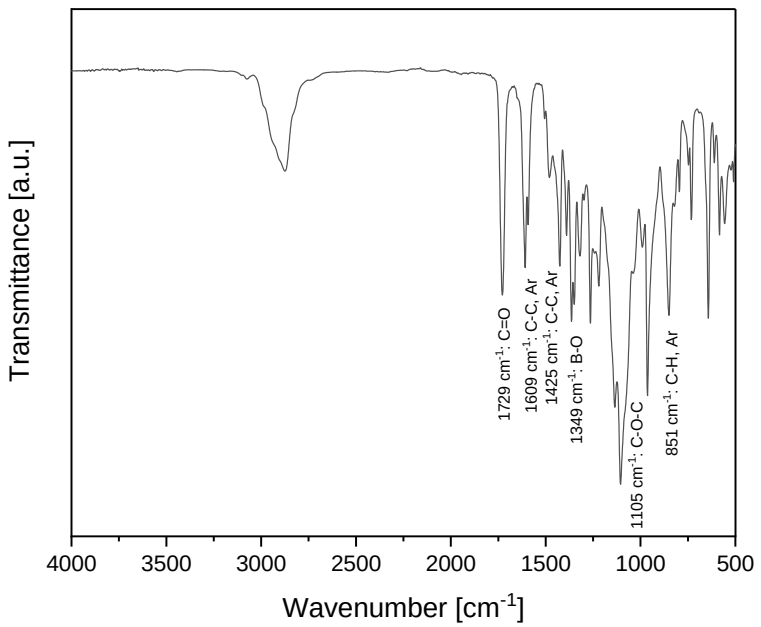

Figure 88: FT-IR spectra of **$PF_2$3b** between 4000 to 500 cm^{-1} under water-free argon atmosphere.

1.11.3 Procedures for 'Magnesium polymer electrolytes based on polycarbonate poly(2-butyl-2-ethyltrimethylene-carbonate)'

The results were partly reproduced with permission from ACS Omega, in press. Unpublished work copyright 2023 American Chemical Society.[281]

Monomer synthesis of (2-butyl-2-ethyltrimethylene carbonate (BEC))

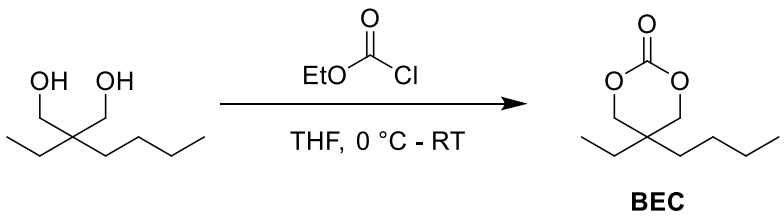

1 eq. 2-butyl-2-ethyl-1,3-propanediol (1 eq., 25 g, 156 mmol) was dissolved in 400 mL dry THF at 0 °C under inert gas. After adding 2 eq. ethyl chloroformate (2 eq., 29.8 mL, 312 mmol) to the mixture 2 eq. triethylamine (2 eq., 43.2 mL, 312 mmol) in 200 mL THF was added and the solution was stirred for 16 h at room temperature. The solution was filtered, concentrated and redissolved in 400 mL ethyl acetate. The organic layer was washed twice with 400 mL of 1M HCl and twice with deionized water. The resulting product was purified by fractionated distillation under reduced pressure, resulting in a colourless liquid. (Yield: 71%).

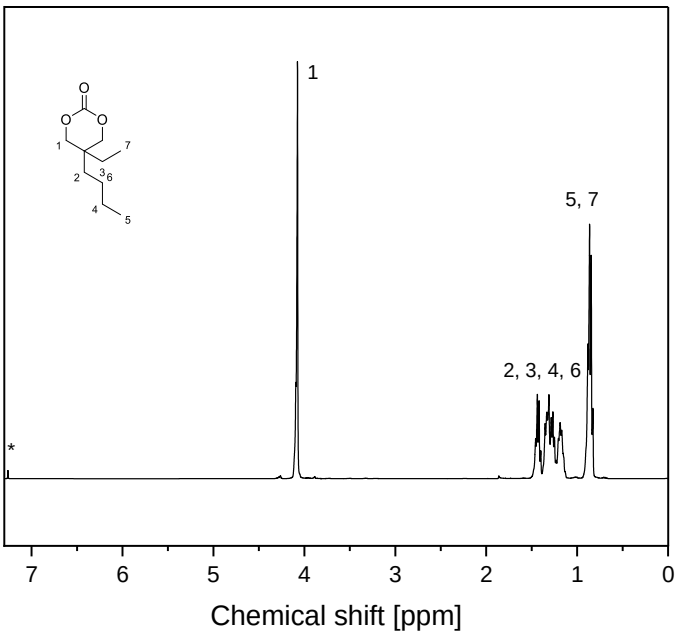

Figure 89: ^{1}H-NMR spectrum of **BEC** in $CDCl_3$. * is assigned to solvent.

^{1}H-NMR (400 MHz, $CDCl_3$) δ/ppm 0.63 - 1.05 (m, 4H, OC**H**$_2$C), 1.05 - 1.54 (m, 8H, Me), 4.1 (s, 6H, C**H**$_2$-segments in aliphatic chains).

Synthesis of 1-(3,5-bis(trifluoromethyl)phenyl)-3-cyclohexylthiourea (TU)

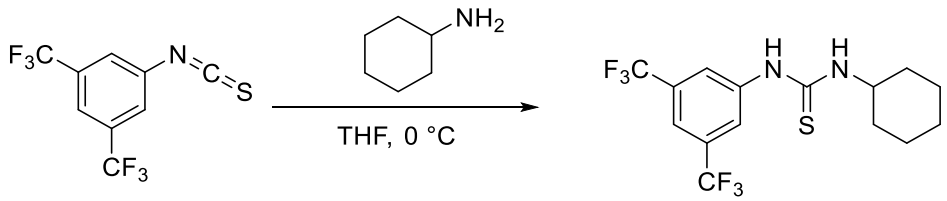

TU catalyst

TU was synthesized as described in a previous report.[299] Under an argon atmosphere, to a solution of 3,5-bis(trifluoromethyl)phenyl isothiocyanate (1 eq., 100 mg, 0.37 mmol) in dry THF (1.0 ml) was added cyclohexane amine (1 eq., 36.6 mg, 0.37 mmol) at 0 °C. After the reaction mixture was stirred for 3 h, the reaction mixture was concentrated in vacuo. The product was recrystallized by $CHCl_3$. Yield: 85%

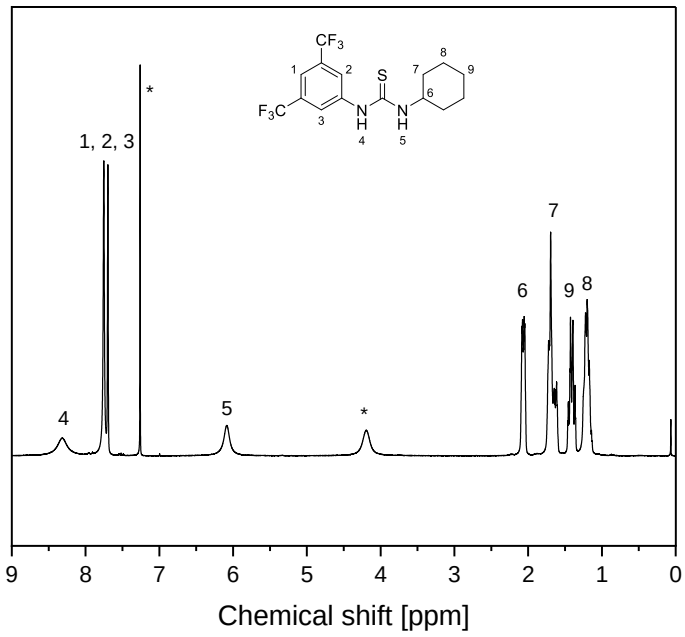

Figure 90: ^{1}H-NMR spectrum of **TU** in $CDCl_3$. * is assigned to solvent.

^{1}H NMR (400 MHz, $CDCl_3$) δ/ppm 8.32 (s, 1H, N**H**), 7.73 (m, 3H, ArH), 6.09 (s, 1H, N**H**), 2.06 (m, 2H, cyclohexan), 1.82 – 1.55 (m, 3H, cyclohexan), 1.55 – 1.30 (m, 3H, cyclohexan), 1.20 (m, 3H, cyclohexan).

Synthesis of magnesium tetrakis(hexafluoroisopropyloxy) borate, $Mg(B(HFIP)_4)_2$-3 DME

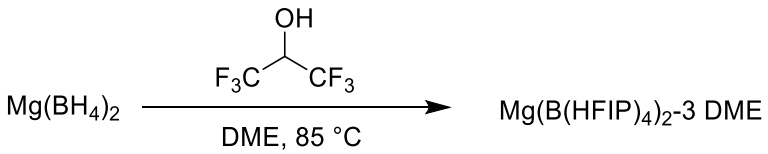

$Mg(B(HFIP)_4)_2$ was synthesized as reported in literature, and the product was obtained in the form of $Mg(B(HFIP)_4)_2$-3 DME solids.[282] Yield: 87%.

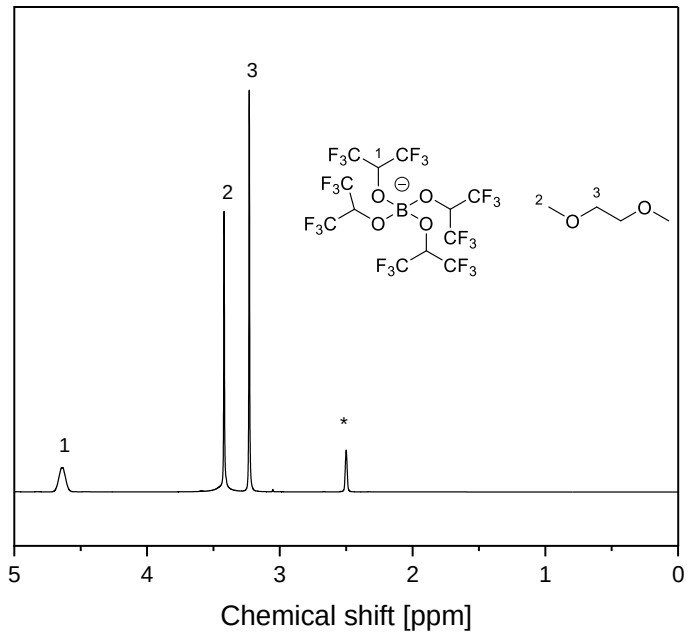

Figure 91: ^{1}H-NMR spectrum of $Mg(B(HFIP)_4)_2$-3 DME in DMSO-d_6. * is assigned to solvent.

^{1}H NMR (400 MHz, DMSO-d_6) δ/ppm 4.70 (s, C**H$_3$**), 3.47 (s, C**H$_2$**), 3.28 (s, CH, C**H**CF$_3$).

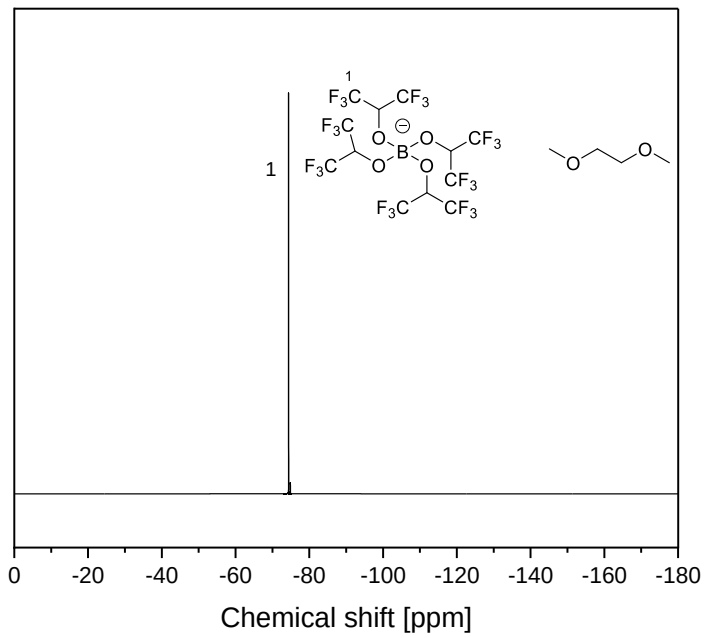

Figure 92: ^{19}F-NMR spectrum of $Mg(B(HFIP)_4)_2$-3 DME in DMSO-d_6.

^{19}F-NMR (376 MHz, DMSO-*d*$_6$) δ/ppm -74.3 (s, CF_3).

Synthesis of poly((2-butyl-2-ethyltrimethylene carbonate) (P(BEC))

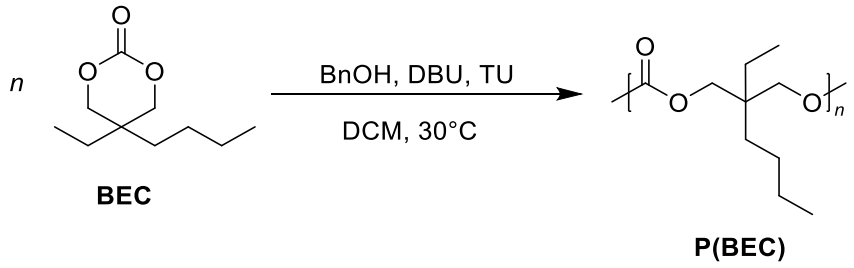

BEC (50 eq., 2 g, 10 mmol) was dissolved in dry DCM (5 mL) with TU catalyst (1 eq., 185 mg, 0.5 mmol) under inert gas. CaH_2 was added and the mixture stirred for 16 h. The solution was filtered afterwards to remove solids and heated up to 30 °C before 1,8-diazabicyclo(5.4.0)undec-7-ene (DBU) (1 eq., 74.7 µL, 0.5 mmol) and benzyl alcohol (0.4 eq., 20.7 µL, 0.2 mmol) was added. After 24 h the reaction was quenched by 1 mL of acetic acid and the polymer was precipitated into cold methanol two times. The polymer was dried for 24 h at 80 °C inside a glovebox before film preparation. Yield: 62%.

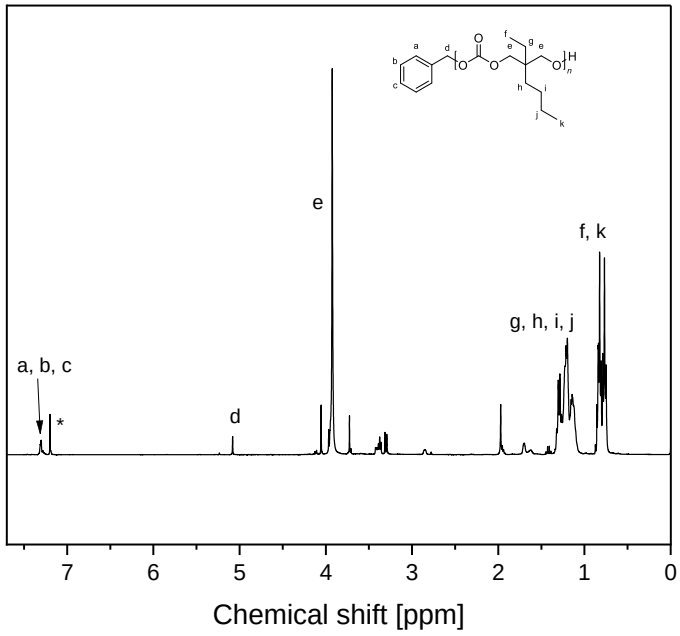

Figure 93: ^{1}H-NMR spectrum of **P(BEC)** in $CDCl_3$. * is assigned to solvent.

^{1}H NMR (400 MHz, $CDCl_3$) δ/ppm 7.34 - 7.26 (m, 5H), 3.93 (s, 6H), 1.33 - 1.06 (m, 8H), 0.90 - 0.72 (m, 6H).

SEC (PMMA-standard, DMAc): M_n = 6 100 g mol^{-1}, M_n/M_w = 1.13.

Abbreviations

1.12 List of Abbreviations

AIBN	2,2′-Azobis(2-methylpropionitrile)
AROP	Anionic ring-opening polymerization
Aq.	Aqueous
ATRP	Atom-transfer radical polymerization
a.u.	Arbitrary unit
b	Block
BEC	2-Butyl-2-ethyltrimethylene-carbonate
ClO_4^-	Perchlorate anion
CTA	Chain-transfer agent
CV	Cyclic voltammetry
Đ	Dispersity
DCM	Dichloromethane
DFS	Dynamic frequency sweep
DME	Dimethyl ether
DMSO	Dimethyl sulfoxide
DSC	Differential scanning calorimetry
Δ	Delta
EIS	Electrochemical impedance spectroscopy
EO	Ethylene oxide
FRP	Free radical polymerization
FT-IR	Fourier-transform infrared spectroscopy
GPE	Gel polymer electrolyte
G'	Storage moduli
G''	Loss moduli
HCl	Hydrochloric acid
IR	Infrared
LCO	$LiCoO_2$
$LiClO_4$	Litium perchlorate
LFP	$LiFePO_4$
LIB	Lithium-ion battery

LiOH	Lithium hydroxide
LiTFSI	Lithium bis(trifluoromethanesulfonyl)imide
LOE	Liquid organic electrolyte
LSV	Linear sweep voltammetry
M	Molar
MF	2-(4-fluorophenyl)-1,3,2-dioxaborolan-4-yl)methyl methacrylate
MF_2	(2-(2,4-Difluorophenyl)-1,3,2-dioxaborolan-4-yl)methyl methacrylate
M_n	Number-average molar mass
Mw	Weight-average molar mass
MeCN	Acetonitrile
MeOH	Methanol
$Mg(B(HFIP)_4)_2$	Magnesium tetrakis(hexafluoroisopropyloxy) borate
$Mg(ClO_4)_2$	Magnesium perchlorate
$Mg(OEt)_2$	Magnesium ethanolate
$Mg(TFSI)_2$	Magnesium bis(trifluromethanesulfonyl) imide
PE	Polymer electrolyte
PFX	$P(PEGMA_{500})$-stat-P(MF), where x refers to the MF ratio
PF_2X	$P(PEGMA_{500})$-stat-$P(MF_2)$, where x refers to the MF_2 ratio
PEG	Polyethylen glycol
$PEGDME_{500}$	Poly(ethylene glycol dimethyl ether) with M_n = 500 g mol^{-1}
$PEGMA_x$	Poly(ethylene glycol monomethyl ether) methyl methacrylate, x correspond to the molar mass
$P(PEGMA_x)$	Poly(ethylene glycol monomethyl ether) methacrylate, where x refers to the molar mass
ppm	Parts per million
PVDF	Poly(vinylidene fluoride)
PVDF-HFP	Poly(vinylidene fluoride-co- hexafluropropylene)
P(BEC)	Poly(2-butyl-2-ethyltrimethylene-carbonate)
RT	Room temperature
RAFT	Reversible addition-fragmentation chain transfer
ROP	Ring-opening polymerization
R_x	Resistance, where x defines bulk or surface resistance

σ	Ionic conductivity
SEC	Size exclusion chromatography
SEI	Solid electrolyte interphase
SMA	Solketal methacrylate
SMA-diol	Glycerol methacrylate
SN	Succinonitrile
SPE	Solid polymer electrolyte
SST	Strain sweep test
T_d	Decomposition temperature at 5 wt.% loss
$TFSI^-$	Trifluoromethanesulfonyl imide anion
T_g	Glass transition temperature
TGA	Thermogravimetric analysis
THF	Tetrahydrofuran
TU	1-(3,5-bis(trifluoromethyl)phenyl)-3-cyclohexylthiourea
t^+_{Mg}	Magnesium-ion transference number
t^+_{Li}	Lithium-ion transference number
VLE	linear viscoelastic regime
ω	Angular frequency
γ	Oscillation strain
[Mg]:[EO]	Ratio between Magnesium ion and the EO repeating units

List of Schemes, Figures and Tables

1.13 List of Figures

1.14 List of Schemes

1.15 List of Tables

Danksagung

Ein großer Dank gilt Prof. Dr. Patrick Théato für die Möglichkeit und Unterstützung an diesem interessanten und vielseitigen Thema meine Promotion durchzuführen.

Zusätzlich bedanke ich mich bei den Korreferenten, die meine Verteidigung und Abschluss meiner Promotion ermöglichten.

Beim POLiS Cluster und allen seinen Mitarbeitern bedanke ich mich ebenfalls für Ihre Unterstützung, aber auch bei der Ausrichtung einer Vielzahl an Konferenzen und Doktoranden Treffen. In diesem Kontext möchte ich Dr. Johannes Schnaidt nennen und danke Ihm für seine Hilfe und Organisatorische Unterstützung, die eine erfolgreiche Graduierten Schulen Konferenz erst ermöglichte.

Bei Prof. Dr. Jennifer Schaefer möchte ich mich besonders bedanken, da Sie mir eine außergewöhnliche Zeit in Notre Dame, USA ermöglichte und mit Ihrer wissenschaftlichen Expertise neue Blickwinkel ermöglichte. In diesem Kontext bedanke ich mich auch bei allen meinen Kollegen dort, ohne die eine solch schöne und produktive Zeit nicht möglich gewesen wäre. Ein besonderer Dank gilt dabei Bumjun Park der sich in dieser Zeit meiner besonders angenommen hatte und der mich stets wissenschaftlich aber auch freundschaftlich unterstützte.

Des Weiteren möchte ich unseren Technikerinnen Katharina Kuppinger, Klara Urbschaft und Birgit Huber für ihre stetige und unschätzbare Hilfe im alltäglichen Labor, ohne den dieser kaum zu schaffen gewesen wäre.

Auch Martina Ritter und Bärbel Seufert-Dausmann möchte ich herzlichst Danken. Ihr Arrangement in Corona Zeiten war ein wesentlicher Grund für meinen reibungslosen Auslandsaufenthalt in den USA. Darüber hinaus war Ihr Einsatz stets eine große Hilfe.

Bei Dr. Dominik Voll möchte ich mich für seine stete Ansprechbarkeit und Hilfe bedanken, die diese Arbeit ermöglicht hatte. Dr. Hatice Mutlu möchte ich ebenfalls meinen Dank aussprechen für Ihre Hilfsbereitschaft und wissenschaftliche Expertise, die mir aus vielen Zwickmühlen half und stets willkommen war.

Weiteren Kollegen, denen ich im Rahmen des POLiS Clusters für ihre Unterstützung danken möchte, sind Herr Prof. Dr. Maximilian Fichtner und Dr. Yanlei Xiu. Auch erwähnen und danken möchte ich meinen Kollegen der Magnesium Gruppe für unsere monatlichen Diskussionen und Gespräche.

Von herausragender Bedeutung und daher auch Dank gilt meinen Kooperationspartnern Dr. Zhixuan Wei, Valerian Hirschberg und Bumjun Park deren wissenschaftliche Expertise in vielen Gesprächen stets eine willkommene Hilfe waren und bei der Lösung diverser Probleme halfen.

Meinen Mitkollegen und Leidensgenossen möchte ich auch erwähnen und danken, da Sie erst das freudige und angenehme Arbeitsumfeld ermöglichten in dem ich täglich Arbeiten durfte. Dies schließt selbstverständlich meine langjährigen Laborkollegen Marvin, Nico und Isabella ein, die immer eine willkommene Ablenkung sein konnten. Aber auch Daniel, Alexander und Victoria mit denen sowohl wissenschaftliche als auch soziale Probleme morgens, mittags und auch abends, bei Wasser, Kaffee und Bier, bei Sonne, Regen aber auch Sturm diskutiert werden konnte. Auch möchte ich Yunji für seine stetige Hilfsbereitschaft und Andreas für seine wissenschaftliche Hilfe danken, so wie allen Studenten, die ich in meiner Zeit kennen lernen durfte.

Auch möchte ich meinen langjährigen Freunden Florian, Carina, Tobias, Lukas und Monika danken die mich schon zu Zeiten des Studiums begleitenten und unterstützen. Mit euch wäre die bisherige Zeit nicht ansatzweise so schön geworden.

Die dauerhaftesten und auch einer der wichtigsten Unterstützer ist meine Familie mit Mama, Ludger und meinen Geschwistern Manuel, Till und Esther. Diesen gilt mein tiefer Dank und Liebe, da Sie mich immer und überall anstandslos unterstützen.

Mein letzter und auch mit größtem Dank und Liebe gilt Katrin Glücks, welche mich gelegentlich zwar in Rage, aber in vielen anderen Gelegenheiten in Verzückung bringt. Ihre facettenreiche Unterstützung war während meiner Promotion ein wichtiger Faktor und Sie ist meine Liebe, die ich in meinem Leben nicht missen will.

References

(1) Weiss, P. Better Battery Management Boosts Electric Vehicle Prospects. *Engineering* **2021**, *7* (8), 1041–1043. DOI: 10.1016/j.eng.2021.06.010.

(2) G. Pistoia. *Battery operated devices and systems*:*From Portable Electronics to Industrial Products*; Elsevier B.V., 2009.

(3) Chen, H.; Cong, T. N.; Yang, W.; Tan, C.; Li, Y.; Ding, Y. Progress in electrical energy storage system: A critical review. *Progress in Natural Science* **2009**, *19* (3), 291–312. DOI: 10.1016/j.pnsc.2008.07.014.

(4) Koohi-Fayegh, S.; Rosen, M. A. A review of energy storage types, applications and recent developments. *Journal of Energy Storage* **2020**, *27*, 101047. DOI: 10.1016/j.est.2019.101047.

(5) Winter, M.; Barnett, B.; Xu, K. Before Li Ion Batteries. *Chemical reviews* **2018**, *118* (23), 11433–11456. DOI: 10.1021/acs.chemrev.8b00422.

(6) Wang, L.; Wu, Z.; Zou, J.; Gao, P.; Niu, X.; Li, H.; Chen, L. Li-free Cathode Materials for High Energy Density Lithium Batteries. *Joule* **2019**, *3* (9), 2086–2102. DOI: 10.1016/j.joule.2019.07.011.

(7) Cabana, J.; Monconduit, L.; Larcher, D.; Palacín, M. R. Beyond intercalation-based Li-ion batteries: the state of the art and challenges of electrode materials reacting through conversion reactions. *Advanced materials (Deerfield Beach, Fla.)* **2010**, *22* (35), E170-92. DOI: 10.1002/adma.201000717.

(8) International Energy Agency. Global EV Outlook 2019.

(9) Encyclopaedia Britannica. *Conte Alessandro Volta*, accessed 2014.

(10) Liu, C.; Neale, Z. G.; Cao, G. Understanding electrochemical potentials of cathode materials in rechargeable batteries. *Materials Today* **2016**, *19* (2), 109–123. DOI: 10.1016/j.mattod.2015.10.009.

(11) Zeng, X.; Li, M.; Abd El-Hady, D.; Alshitari, W.; Al-Bogami, A. S.; Lu, J.; Amine, K. Commercialization of Lithium Battery Technologies for Electric Vehicles. *Adv. Energy Mater.* **2019**, *9* (27), 1900161. DOI: 10.1002/aenm.201900161.

(12) Kim, T.; Song, W.; Son, D.-Y.; Ono, L. K.; Qi, Y. Lithium-ion batteries: outlook on present, future, and hybridized technologies. *J. Mater. Chem. A* **2019**, *7* (7), 2942–2964. DOI: 10.1039/C8TA10513H.

(13) Wang, Q.; Liu, B.; Shen, Y.; Wu, J.; Zhao, Z.; Zhong, C.; Hu, W. Confronting the Challenges in Lithium Anodes for Lithium Metal Batteries. *Advanced science* **2021**, *8* (17), e2101111. DOI: 10.1002/advs.202101111.

(14) Placke, T.; Kloepsch, R.; Dühnen, S.; Winter, M. Lithium ion, lithium metal, and alternative rechargeable battery technologies: the odyssey for high energy density. *J Solid State Electrochem* **2017**, *21* (7), 1939–1964. DOI: 10.1007/s10008-017-3610-7.

(15) Harry, K. J.; Hallinan, D. T.; Parkinson, D. Y.; MacDowell, A. A.; Balsara, N. P. Detection of subsurface structures underneath dendrites formed on cycled lithium metal electrodes. *Nature materials* **2014**, *13* (1), 69–73. DOI: 10.1038/nmat3793. Published Online: Nov. 24, 2013.

(16) Mauger, A.; Julien, C. Surface modifications of electrode materials for lithium-ion batteries: status and trends. *Ionics* **2014**, *20* (6), 751–787. DOI: 10.1007/s11581-014-1131-2.

(17) Luo, Y.; Guo, L.; Xiao, M.; Wang, S.; Ren, S.; Han, D.; Meng, Y. Strategies for inhibiting anode dendrite growth in lithium–sulfur batteries. *J. Mater. Chem. A* **2020**, *8* (9), 4629–4646. DOI: 10.1039/C9TA12910C.

(18) Takada, K. Progress and prospective of solid-state lithium batteries. *Acta Materialia* **2013**, *61* (3), 759–770. DOI: 10.1016/j.actamat.2012.10.034.

(19) Hubble, D.; Brown, D. E.; Zhao, Y.; Fang, C.; Lau, J.; McCloskey, B. D.; Liu, G. Liquid electrolyte development for low-temperature lithium-ion batteries. *Energy Environ. Sci.* **2022**, *15* (2), 550–578. DOI: 10.1039/D1EE01789F.

(20) Ue, M.; Uosaki, K. Recent progress in liquid electrolytes for lithium metal batteries. *Current Opinion in Electrochemistry* **2019**, *17*, 106–113. DOI: 10.1016/j.coelec.2019.05.001.

(21) L. Kulova, T. A Brief Review of Post-Lithium-Ion Batteries. *Int. J. Electrochem. Sci.* **2020**, 7242–7259. DOI: 10.20964/2020.08.22.

(22) Rajagopalan, R.; Tang, Y.; Ji, X.; Jia, C.; Wang, H. Advancements and Challenges in Potassium Ion Batteries: A Comprehensive Review. *Adv. Funct. Mater.* **2020**, *30* (12), 1909486. DOI: 10.1002/adfm.201909486.

(23) Shah, R.; Mittal, V.; Matsil, E.; Rosenkranz, A. Magnesium-ion batteries for electric vehicles: Current trends and future perspectives. *Advances in Mechanical Engineering* **2021**, *13* (3), 168781402110033. DOI: 10.1177/16878140211003398.

(24) Thomas D. Gregory,* Ronald J. Hoffman, and Richard C. Winterton. Nonaqueous Electrochemistry of Magnesium Applications to Energy Storage. *J. Electrochem. Soc.* **1990** (Vol 137 No 3), 775–780.

(25) Guo, M.; Yuan, C.; Zhang, T.; Yu, X. Solid-State Electrolytes for Rechargeable Magnesium-Ion Batteries: From Structure to Mechanism. *Small* **2022**, *18* (43), e2106981. DOI: 10.1002/smll.202106981. Published Online: Feb. 19, 2022.

(26) Eaves-Rathert, J.; Moyer, K.; Zohair, M.; Pint, C. L. Kinetic- versus Diffusion-Driven Three-Dimensional Growth in Magnesium Metal Battery Anodes. *Joule* **2020**, *4* (6), 1324–1336. DOI: 10.1016/j.joule.2020.05.007.

(27) Deivanayagam, R.; Ingram, B. J.; Shahbazian-Yassar, R. Progress in development of electrolytes for magnesium batteries. *Energy Storage Materials* **2019**, *21*, 136–153. DOI: 10.1016/j.ensm.2019.05.028.

(28) Mohtadi, R.; Tutusaus, O.; Arthur, T. S.; Zhao-Karger, Z.; Fichtner, M. The metamorphosis of rechargeable magnesium batteries. *Joule* **2021**, *5* (3), 581–617. DOI: 10.1016/j.joule.2020.12.021.

(29) Sun, Y.; Ai, F.; Lu, Y.-C. Electrolyte and Interphase Design for Magnesium Anode: Major Challenges and Perspectives. *Small* **2022**, *18* (43), e2200009. DOI: 10.1002/smll.202200009. Published Online: Mar. 22, 2022.

(30) Hiroko Kuwata, Masaki Matsuiand Nobuyuki Imanishiai. Passivation Layer Formation of Magnesium Metal Negative Electrodes for Rechargeable Magnesium Batteries. *Journal of the Electrochemical Society* **2017** (164 (13)), A3229-A3236.

(31) Dou, H.; Zhao, X.; Zhang, Y.; Zhao, W.; Yan, Y.; Ma, Z.-F.; Wang, X.; Yang, X. Revisiting the degradation of solid/electrolyte interfaces of magnesium metal anodes: Decisive role of interfacial composition. *Nano Energy* **2021**, *86*, 106087. DOI: 10.1016/j.nanoen.2021.106087.

(32) J. H. Connor, W. E. Reid, JR., G. B. Wood. Electrodeposition of Metals from Organic Solutions:V. E|ectrodeposition of Magnesium and Magnesium Alloys. *J. Electrochem. Soc.* **1957** (Vol. 104), 38–41.

(33) D. Aurbach, Z. Lu, A. Schechter, Y. Gofer, H. Gizbar, R. Turgeman. Prototype systems for rechargeable magnesium batteries. *Letters of Nature* **2000** (407), 724–727.

(34) Liang, Z.; Ban, C. Strategies to Enable Reversible Magnesium Electrochemistry: From Electrolytes to Artificial Solid-Electrolyte Interphases. *Angewandte Chemie (International ed. in English)* **2021**, *60* (20), 11036–11047. DOI: 10.1002/anie.202006472. Published Online: Jan. 28, 2021.

(35) Oren Mizrahi, Nir Amir, Elad Pollak, Orit Chusid, Vered Marks, Hugo Gottlieb, Liraz Larush, Ella Zinigrad, and Doron Aurbach. Electrolyte Solutions with a Wide

Electrochemical Window for Rechargeable Magnesium Batteries. *Journal of the Electrochemical Society* **2008** (155 (2)), A103-A109.

(36) Shunsuke Yagi, Akira Tanaka, Yuya Ichikawa, Tetsu Ichitsubo. Electrochemical Stability of Magnesium Battery Current Collectors in a Grignard Reagent-Based Electrolyte. *Journal of the Electrochemical Society* **2013** (160), C83-C88.

(37) He, S.; Nielson, K. V.; Luo, J.; Liu, T. L. Recent advances on MgCl2 based electrolytes for rechargeable Mg batteries. *Energy Storage Materials* **2017**, *8*, 184–188. DOI: 10.1016/j.ensm.2016.12.001.

(38) Pan, B.; Huang, J.; He, M.; Brombosz, S. M.; Vaughey, J. T.; Zhang, L.; Burrell, A. K.; Zhang, Z.; Liao, C. The Role of MgCl2 as a Lewis Base in ROMgCl-MgCl2 Electrolytes for Magnesium-Ion Batteries. *ChemSusChem* **2016**, *9* (6), 595–599. DOI: 10.1002/cssc.201501557. Published Online: Feb. 4, 2016.

(39) Baofei Pan et al. MgCl2: The Key Ingredient to Improve Chloride Containing Electrolytes for Rechargeable Magnesium-Ion Batteries. *J. Electrochem. Soc* **2016** (163), A1672-A1677.

(40) Robert E. Doe, Ruoban Han, Jaehee Hwang, Andrew J. Gmitter, vgeni Shterenberg, Hyun Deog Yoo, Nir Pourb and Doron Aurbach. Novel, electrolyte solutions comprising fully inorganic salts with high anodic stability for rechargeable magnesium batteries†. *Chem. Commun.* **2014** (50), 243–245.

(41) Liao, C.; Sa, N.; Key, B.; Burrell, A. K.; Cheng, L.; Curtiss, L. A.; Vaughey, J. T.; Woo, J.-J.; Hu, L.; Pan, B.; Zhang, Z. The unexpected discovery of the Mg(HMDS) 2 /MgCl 2 complex as a magnesium electrolyte for rechargeable magnesium batteries. *J. Mater. Chem. A* **2015**, *3* (11), 6082–6087. DOI: 10.1039/C5TA00118H.

(42) Nguyen, D.-T.; Eng, A. Y. S.; Horia, R.; Sofer, Z.; Handoko, A. D.; Ng, M.-F.; Seh, Z. W. Rechargeable magnesium batteries enabled by conventional electrolytes with multifunctional organic chloride additives. *Energy Storage Materials* **2022**, *45*, 1120–1132. DOI: 10.1016/j.ensm.2021.11.011.

(43) Attias, R.; Salama, M.; Hirsch, B.; Goffer, Y.; Aurbach, D. Anode-Electrolyte Interfaces in Secondary Magnesium Batteries. *Joule* **2019**, *3* (1), 27–52. DOI: 10.1016/j.joule.2018.10.028.

(44) Attias, R.; Chae, M. S.; Dlugatch, B.; Oliel, M.; Goffer, Y.; Aurbach, D. The Role of Surface Adsorbed Cl – Complexes in Rechargeable Magnesium Batteries. *ACS Catal.* **2020**, *10* (14), 7773–7784. DOI: 10.1021/acscatal.0c01956.

(45) Gofer, Y., Turgeman, R., Cohen, H., Aurbach, D. XPS investigation of surface chemistry of magnesium electrodes in contact with organic solutions of organochloroaluminate complex salts. *Langmuir* **2003** (Vol 19, Issue 6), 2344–2348.

(46) Zhao-Karger, Z.; Liu, R.; Dai, W.; Li, Z.; Diemant, T.; Vinayan, B. P.; Bonatto Minella, C.; Yu, X.; Manthiram, A.; Behm, R. J.; Ruben, M.; Fichtner, M. Toward Highly Reversible Magnesium–Sulfur Batteries with Efficient and Practical Mg[B(hfip) 4] 2 Electrolyte. *ACS Energy Lett.* **2018**, *3* (8), 2005–2013. DOI: 10.1021/acsenergylett.8b01061.

(47) Zhao, W.; Liu, Y.; Zhao, X.; Pan, Z.; Chen, J.; Zheng, S.; Qu, L.; Yang, X. Chloride-Free Electrolytes for High-Voltage Magnesium Metal Batteries: Challenges, Strategies, and Perspectives. *Chemistry* **2022**, e202203334. DOI: 10.1002/chem.202203334. Published Online: Nov. 21, 2022.

(48) Ren, W.; Cheng, M.; Wang, Y.; Zhang, D.; Yang, Y.; Yang, J.; Wang, J.; NuLi, Y. Boron–Based Electrolytes for Rechargeable Magnesium Batteries: Biography and Perspective. *Batteries & Supercaps* **2022**, *5* (9), 100450. DOI: 10.1002/batt.202200263.

(49) Mohtadi, R.; Matsui, M.; Arthur, T. S.; Hwang, S.-J. Magnesium Borohydride: From Hydrogen Storage to Magnesium Battery. *Angew. Chem.* **2012**, *124* (39), 9918–9921. DOI: 10.1002/ange.201204913.

(50) Kristensen, L. G.; Amdisen, M. B.; Skov, L. N.; Jensen, T. R. Fast magnesium ion conducting isopropylamine magnesium borohydride enhanced by hydrophobic interactions. *Physical chemistry chemical physics : PCCP* **2022**, *24* (30), 18185–18197. DOI: 10.1039/d1cp05063j. Published Online: Aug. 3, 2022.

(51) Jankowski, P.; Li, Z.; Zhao-Karger, Z.; Diemant, T.; Fichtner, M.; Vegge, T.; Lastra, J. M. G. Development of Magnesium Borate Electrolytes: Explaining the Success of Mg[B(hfip)4]2 Salt. *Energy Storage Materials* **2022**, *45* (4), 1133–1143. DOI: 10.1016/j.ensm.2021.11.012.

(52) Zhirong, Z.-K.; Maximilian, F. Magnesium-sulfur battery: its beginning and recent progress. *MRS Communications* **2017**, *7* (4), 770–784. DOI: 10.1557/mrc.2017.101.

(53) Zhao-Karger, Z.; Gil Bardaji, M. E.; Fuhr, O.; Fichtner, M. A new class of non-corrosive, highly efficient electrolytes for rechargeable magnesium batteries. *J. Mater. Chem. A* **2017**, *5* (22), 10815–10820. DOI: 10.1039/C7TA02237A.

(54) Pavčnik, T.; Lozinšek, M.; Pirnat, K.; Vizintin, A.; Mandai, T.; Aurbach, D.; Dominko, R.; Bitenc, J. On the Practical Applications of the Magnesium Fluorinated Alkoxyaluminate Electrolyte in Mg Battery Cells. *ACS applied materials & interfaces* **2022**, *14* (23), 26766–26774. DOI: 10.1021/acsami.2c05141. Published Online: Jun. 1, 2022.

(55) Lei, X.; Liang, X.; Yang, R.; Zhang, F.; Wang, C.; Lee, C.-S.; Tang, Y. Rational Design Strategy of Novel Energy Storage Systems: Toward High-Performance Rechargeable Magnesium Batteries. *Small* **2022**, *18* (22), e2200418. DOI: 10.1002/smll.202200418. Published Online: Mar. 21, 2022.

(56) Rashad, M.; Asif, M.; Wang, Y.; He, Z.; Ahmed, I. Recent advances in electrolytes and cathode materials for magnesium and hybrid-ion batteries. *Energy Storage Materials* **2020**, *25* (5), 342–375. DOI: 10.1016/j.ensm.2019.10.004.

(57) Yoo, H. D.; Liang, Y.; Li, Y.; Yao, Y. High areal capacity hybrid magnesium-lithium-ion battery with 99.9% Coulombic efficiency for large-scale energy storage. *ACS applied materials & interfaces* **2015**, *7* (12), 7001–7007. DOI: 10.1021/acsami.5b01206. Published Online: Mar. 23, 2015.

(58) Yagi, S.; Ichitsubo, T.; Shirai, Y.; Yanai, S.; Doi, T.; Murase, K.; Matsubara, E. A concept of dual-salt polyvalent-metal storage battery. *J. Mater. Chem. A* **2014**, *2* (4), 1144–1149. DOI: 10.1039/C3TA13668J.

(59) Tang, K.; Du, A.; Dong, S.; Cui, Z.; Liu, X.; Lu, C.; Zhao, J.; Zhou, X.; Cui, G. A Stable Solid Electrolyte Interphase for Magnesium Metal Anode Evolved from a Bulky Anion Lithium Salt. *Advanced materials (Deerfield Beach, Fla.)* **2020**, *32* (6), e1904987. DOI: 10.1002/adma.201904987. Published Online: Dec. 18, 2019.

(60) Li, Y.; An, Q.; Cheng, Y.; Liang, Y.; Ren, Y.; Sun, C.-J.; Dong, H.; Tang, Z.; Li, G.; Yao, Y. A high-voltage rechargeable magnesium-sodium hybrid battery. *Nano Energy* **2017**, *34*, 188–194. DOI: 10.1016/j.nanoen.2017.02.012.

(61) Mazdida Sulaiman, A. A. Rahman and N. S. Mohamed. Structural, Thermal and Conductivity Studies of Magnesium Nitrate – Alumina Composite Solid Electrolytes Prepared via Sol-Gel Method. *Int. J. Electrochem. Sci.* **2013** (8), 6647–6655.

(62) Sulaiman, M.; Che Su, N.; Mohamed, N. S. Sol-gel synthesis and characterization of β-MgSO4:Mg(NO3)2–MgO composite solid electrolyte. *Ionics* **2017**, *23* (2), 443–452. DOI: 10.1007/s11581-016-1854-3.

(63) Tamura, S.; Yamane, M.; Hoshino, Y.; Imanaka, N. Highly conducting divalent Mg2+ cation solid electrolytes with well-ordered three-dimensional network structure. *Journal of Solid State Chemistry* **2016**, *235*, 7–11. DOI: 10.1016/j.jssc.2015.12.008.

(64) Pieremanuele Canepa; Shou-Hang Bo; Gopalakrishnan Sai Gautam; Baris Key; William D. Richards; Tan Shi; Yaosen Tian; Yan Wang; Juchuan Li; Gerbrand Ceder. High magnesium mobility in ternary spinel chalcogenides. *Nature communications* **2017** (1759), 1–8.

(65) Zhan, Y.; Zhang, W.; Lei, B.; Liu, H.; Li, W. Recent Development of Mg Ion Solid Electrolyte. *Frontiers in chemistry* **2020**, *8*, 125. DOI: 10.3389/fchem.2020.00125. Published Online: Feb. 25, 2020.

(66) Park, S. S.; Tulchinsky, Y.; Dincă, M. Single-Ion Li+, Na+, and Mg2+ Solid Electrolytes Supported by a Mesoporous Anionic Cu-Azolate Metal-Organic Framework. *Journal of the American Chemical Society* **2017**, *139* (38), 13260–13263. DOI: 10.1021/jacs.7b06197. Published Online: Sep. 13, 2017.

(67) Park, B.; Schaefer, J. L. Review—Polymer Electrolytes for Magnesium Batteries: Forging Away from Analogs of Lithium Polymer Electrolytes and Towards the Rechargeable Magnesium Metal Polymer Battery. *J. Electrochem. Soc.* **2020**, *167* (7), 70545. DOI: 10.1149/1945-7111/ab7c71.

(68) Manuel Stephan, A.; Nahm, K. S. Review on composite polymer electrolytes for lithium batteries. *Polymer* **2006**, *47* (16), 5952–5964. DOI: 10.1016/j.polymer.2006.05.069.

(69) Long, L.; Wang, S.; Xiao, M.; Meng, Y. Polymer electrolytes for lithium polymer batteries. *J. Mater. Chem. A* **2016**, *4* (26), 10038–10069. DOI: 10.1039/C6TA02621D.

(70) Meng, N.; Lian, F.; Cui, G. Macromolecular Design of Lithium Conductive Polymer as Electrolyte for Solid-State Lithium Batteries. *Small* **2021**, *17* (3), e2005762. DOI: 10.1002/smll.202005762. Published Online: Dec. 21, 2020.

(71) M. J. Reddy, P. P. Chu. Ion pair formation and its effect in PEO: Mg solid polymer electrolyte system. *Journal of Power Sources* **2002** (109), 340–346.

(72) Kiruthika, S.; Malathi, M.; Selvasekarapandian, S.; Tamilarasan, K.; Maheshwari, T. Conducting biopolymer electrolyte based on pectin with magnesium chloride salt for magnesium battery application. *Polym. Bull.* **2020**, *77* (12), 6299–6317. DOI: 10.1007/s00289-019-03071-9.

(73) Kiruthika, S.; Malathi, M.; Selvasekarapandian, S.; Tamilarasan, K.; Moniha, V.; Manjuladevi, R. Eco-friendly biopolymer electrolyte, pectin with magnesium nitrate salt, for application in electrochemical devices. *J Solid State Electrochem* **2019**, *23* (7), 2181–2193. DOI: 10.1007/s10008-019-04313-6.

(74) Mahalakshmi, M.; Selvanayagam, S.; Selvasekarapandian, S.; Chandra, M. V. L.; Sangeetha, P.; Manjuladevi, R. Magnesium ion-conducting solid polymer electrolyte based on cellulose acetate with magnesium nitrate (Mg(NO3)2·6H2O) for electrochemical studies. *Ionics* **2020**, *26* (9), 4553–4565. DOI: 10.1007/s11581-020-03615-4.

(75) Mahalakshmi, M.; Selvanayagam, S.; Selvasekarapandian, S.; Moniha, V.; Manjuladevi, R.; Sangeetha, P. Characterization of biopolymer electrolytes based on cellulose acetate

with magnesium perchlorate (Mg(ClO4)2) for energy storage devices. *Journal of Science: Advanced Materials and Devices* **2019**, *4* (2), 276–284. DOI: 10.1016/j.jsamd.2019.04.006.

(76) Krupanidhi, S. B.; Gupta, V.; Sharma Kaushik, A.; Singh, A. K. *Advanced Functional Materials and Devices*, Vol. 14; Springer Singapore, 2022. DOI: 10.1007/978-981-16-5971-3.

(77) Koliyoor, J.; Ismayil; Hegde, S.; Vasachar, R.; Sanjeev, G. Novel solid biopolymer electrolyte based on methyl cellulose with enhanced ion transport properties. *J of Applied Polymer Sci* **2022**, *139* (12), 51826. DOI: 10.1002/app.51826.

(78) Shanmuga Priya, S.; Karthika, M.; Selvasekarapandian, S.; Manjuladevi, R.; Monisha, S. Study of biopolymer I-carrageenan with magnesium perchlorate. *Ionics* **2018**, *24* (12), 3861–3875. DOI: 10.1007/s11581-018-2535-1.

(79) Aziz, S. B.; Al-Zangana, S.; Woo, H. J.; Kadir, M.F.Z.; Abdullah, O. G. The compatibility of chitosan with divalent salts over monovalent salts for the preparation of solid polymer electrolytes. *Results in Physics* **2018**, *11* (4), 826–836. DOI: 10.1016/j.rinp.2018.10.040.

(80) Aziz, S. B.; Brza, M. A.; Hamsan, E. M. A. D. M. H.; Hadi, J. M.; Kadir, M. F. Z.; Abdulwahid, R. T. The Study of Electrical and Electrochemical Properties of Magnesium Ion Conducting CS: PVA Based Polymer Blend Electrolytes: Role of Lattice Energy of Magnesium Salts on EDLC Performance. *Molecules (Basel, Switzerland)* **2020**, *25* (19). DOI: 10.3390/molecules25194503. Published Online: Oct. 1, 2020.

(81) Alves, R. D.; Rodrigues, L. C.; Andrade, J. R.; Pawlicka, A.; Pereira, L.; Martins, R.; Fortunato, E.; Silva, M. M. Study and Characterization of a Novel Polymer Electrolyte Based on Agar Doped with Magnesium Triflate. *Molecular Crystals and Liquid Crystals* **2013**, *570* (1), 1–11. DOI: 10.1080/15421406.2012.703041.

(82) Manjuladevi, R.; Selvasekarapandian, S.; Thamilselvan, M.; Mangalam, R.; Monisha, S.; Selvin, P. C. A study on blend polymer electrolyte based on poly(vinyl alcohol)-poly (acrylonitrile) with magnesium nitrate for magnesium battery. *Ionics* **2018**, *24* (11), 3493–3506. DOI: 10.1007/s11581-018-2500-z.

(83) Sheha, E. M.; Nasr, M. M.; El-Mansy, M. K. The role of MgBr2 to enhance the ionic conductivity of PVA/PEDOT:PSS polymer composite. *Journal of advanced research* **2015**, *6* (4), 563–569. DOI: 10.1016/j.jare.2014.01.010.

(84) Suvarnna, K.; Kirubavathy, S. J.; Selvasekarapandian, S.; Krishna, M. V.; Ramaswamy, M. Corn silk extract–based solid-state biopolymer electrolyte and its application to electrochemical storage devices. *Ionics* **2022.** DOI: 10.1007/s11581-021-04415-0.

(85) Anilkumar, K. M.; Jinisha, B.; Manoj, M.; Jayalekshmi, S. Poly(ethylene oxide) (PEO) – Poly(vinyl pyrrolidone) (PVP) blend polymer based solid electrolyte membranes for developing solid state magnesium ion cells. *European Polymer Journal* **2017**, *89*, 249–262. DOI: 10.1016/j.eurpolymj.2017.02.004.

(86) Ramesh, S.; Lu, S.-C.; Morris, E. Towards magnesium ion conducting poly(vinylidene-fluoride-hexafluoropropylene)-based solid polymer electrolytes with great prospects: Ionic conductivity and dielectric behaviours. *Journal of the Taiwan Institute of Chemical Engineers* **2012**, *43* (5), 806–812. DOI: 10.1016/j.jtice.2012.04.004.

(87) Ponmani, S.; Prabhu, M. R. Development and study of solid polymer electrolytes based on PVdF-HFP/PVAc: Mg (ClO4)2 for Mg ion batteries. *J Mater Sci: Mater Electron* **2018**, *29* (17), 15086–15096. DOI: 10.1007/s10854-018-9649-0.

(88) L. L. Yang, A. R. McGhie, G. C. Farrington. Ionic Conductivity in Complexes of Poly(ethylene oxide) and MgCl2. *Journal of Electrochemical Society* **1986** (133), 1380.

(89) S. Ramalingaiah, D. S. Reddy, M. J. Reddy, E. Laxminarsaiah, U. V. S. Rao. Conductivity and discharge characteristic studies of novel polymer electrolyte based on PEO complexed with Mg(NO3)2. *Materials Letters* **1996** (29), 285–289.

(90) M. J. Reddy, P. P. Chu. Effect of Mg2+ on PEO morphology and conductivity. *Solid State Ionics* **2002** (149), 115–123.

(91) Patrick et al. Novel solid state polymeric batteries. *Solid State Ionics* **1986** (18 & 19), 1063–1067.

(92) A. Bakker, S. Geijji, J. Lindgren, K. Hermansson, M. M. Probst. Contact ion pair formation and ether oxygen coordination in the polymer electrolytes M[N(CF3SO2)2]PEOn for M = Mg, Ca, Sr and Ba. *Polymer* **1995** (Vol. 36 No 23), 4371–4378.

(93) Polu, A. R.; Kumar, R. Ionic Conductivity and Discharge Characteristic Studies of PVA-Mg(CH 3 COO) 2 Solid Polymer Electrolytes. *International Journal of Polymeric Materials and Polymeric Biomaterials* **2013**, *62* (2), 76–80. DOI: 10.1080/00914037.2012.664211.

(94) Jeong, S.-K.; Jo, Y.-K.; Jo, N.-J. Decoupled ion conduction mechanism of poly(vinyl alcohol) based Mg-conducting solid polymer electrolyte. *Electrochimica Acta* **2006**, *52* (4), 1549–1555. DOI: 10.1016/j.electacta.2006.02.061.

(95) A. R. Polu, R: Kumar. Preparation and characterization of pva based solid polymer electrolytes for electrochemical cell application. *Chinese Journal of Polymer Science* **2013** (31), 641–648.

(96) Basha, S. K. S.; Sundari, G. S.; Kumar, K. V.; Rao, M. C. Preparation and dielectric properties of PVP-based polymer electrolyte films for solid-state battery application. *Polym. Bull.* **2018**, *75* (3), 925–945. DOI: 10.1007/s00289-017-2072-5.

(97) Ab Aziz, A.; Tominaga, Y. Magnesium ion-conductive poly(ethylene carbonate) electrolytes. *Ionics* **2018**, *24* (11), 3475–3481. DOI: 10.1007/s11581-018-2482-x.

(98) P. Perumal, K. P. Abhilash, P. Sivaraj, P. C. Selvin. Study on Mg-ion conducting solid biopolymer electrolytes based on tamarind seed polysaccharide for magensium ion batteries. *Materials Research Bulletin* **2019** (118), 110490.

(99) Sadiq M., Raza M.M.H., Zulfequar M., Ali M., Ali J. Investigation of Magnesium Ion and Cellulose Acetate-Based Conducting Biopolymers: Electrical and Ion Transport Properties. In: Krupanidhi S.B., Gupta V., Sharma Kaushik A., Singh A.K. (eds). *Advanced Functional Materials and Devices. Springer Proceedings in Materials* **2022** (14), 17–26.

(100) Rathika, R.; Suthanthiraraj, S. A. Ionic Interactions and Dielectric Relaxation of PEO/PVDF-Mg[(CF3SO2)2N2)] Blend Electrolytes for Magnesium Ion Rechargeable Batteries. *Macromol. Res.* **2016**, *24* (5), 422–428. DOI: 10.1007/s13233-016-4053-1.

(101) A. Mallikarjun, M. Sangeetha, Maheshwar Reddy Mettu, M. Vikranth Reddy, M. Jaipal Reddy, J. Siva Kumar, T. Sreekanth. Morphological, Spectroscopic, Structural and Electrical Properties of Ion Conducting PMMA: PVDF-HFP Blend Polymer Electrolytes:In: Bindhu V., R. S. Tavares J.M., Talu S. (eds) Morphological Proceeding of Fourth International Conference on Intentive Material Science Applications. Advances in Sustainability Science and Technology. *Springer Singapore* **2022**, 401–416.

(102) Jeyabanu, K.; Siva, V.; Nallamuthu, N.; Selvanayagam, S.; Bahadur, S. A.; Manikandan, A. Investigation of Electrochemical Studies of Magnesium Ion Conducting Poly(vinyl alcohol)-Poly(vinyl pyrrolidone) Based Blend Polymers. *Journal of nanoscience and nanotechnology* **2018**, *18* (2), 1103–1109. DOI: 10.1166/jnn.2018.13969.

(103) Reddy Polu, A.; Kumar, R.; Vijaya Kumar, K. Ionic Conductivity And Electrochemical Cell Studies Of New Mg2+ ion Conducting PVA/PEG Based Polymer Blend Electrolytes. *AML* **2012**, *3* (5), 406–409. DOI: 10.5185/amlett.2012.6375.

(104) A. R. Polu, R: Kumar. AC impedance and dielectric spectroscopic studies of Mg2+ ion conducting PVA-PEG blended polymer electrolytes. *Bull Mater Sci* **2011** (34), 1063–1067.

(105) Manjuladevi, R.; Thamilselvan, M.; Selvasekarapandian, S.; Mangalam, R.; Premalatha, M.; Monisha, S. Mg-ion conducting blend polymer electrolyte based on poly(vinyl

alcohol)-poly (acrylonitrile) with magnesium perchlorate. *Solid State Ionics* **2017**, *308*, 90–100. DOI: 10.1016/j.ssi.2017.06.002.

(106) Manjuladevi, R.; Thamilselvan, M.; Selvasekarapandian, S.; Christopher Selvin, P.; Mangalam, R.; Monisha, S. Preparation and characterization of blend polymer electrolyte film based on poly(vinyl alcohol)-poly(acrylonitrile)/MgCl2 for energy storage devices. *Ionics* **2018**, *24* (4), 1083–1095. DOI: 10.1007/s11581-017-2273-9.

(107) Ramaswamy, M.; Malayandi, T.; Subramanian, S.; Srinivasalu, J.; Rangaswamy, M. Magnesium ion conducting polyvinyl alcohol–polyvinyl pyrrolidone-based blend polymer electrolyte. *Ionics* **2017**, *23* (7), 1771–1781. DOI: 10.1007/s11581-017-2023-z.

(108) T, P.; Ramalingam, A.; Selvasekarapandian, S.; Srikumar, S. R.; Manjuladevi, R. Mg-ion conducting triblock copolymer electrolyte based on poly(VdCl-co-AN-co-MMA) with magnesium nitrate. *Ionics* **2020**, *26* (2), 789–800. DOI: 10.1007/s11581-019-03244-6.

(109) Ponraj, T.; Ramalingam, A.; Selvasekarapandian, S.; Srikumar, S. R.; Manjuladevi, R. Plasticized solid polymer electrolyte based on triblock copolymer poly(vinylidene chloride-co-acrylonitrile-co-methyl methacrylate) for magnesium ion batteries. *Polym. Bull.* **2020**, *287* (6), 15. DOI: 10.1007/s00289-019-03091-5.

(110) N. Yoshimoto, Y. Tomonaga, M. Ishikawa, M. Morita. Ionic conductance of polymeric electrolytes consisting of magnesium salts dissolved in cross-linked polymer matrix with linear polyether. *Electrochimica Acta* **2001** (46), 1195–1200.

(111) Yoshizawa-Fujita, M.; Ota, R.; Ishii, J.; Takeoka, Y.; Rikukawa, M. Ion Conductive Behavior of Oligoether/Zwitterion Diblock Copolymers Containing Magnesium Salt. *Macro Chemistry & Physics* **2021**, 2100363. DOI: 10.1002/macp.202100363.

(112) Dissanayake, M.A.K.L.; Bandara, L.R.A.K.; Karaliyadda, L. H.; Jayathilaka, P.A.R.D.; Bokalawala, R.S.P. Thermal and electrical properties of solid polymer electrolyte PEO9 Mg(ClO4)2 incorporating nano-porous Al2O3 filler. *Solid State Ionics* **2006**, *177* (3-4), 343–346. DOI: 10.1016/j.ssi.2005.10.031.

(113) Sundar, M.; Selladurai, S. Effect of fillers on magnesium–poly(ethylene oxide) solid polymer electrolyte. *Ionics* **2006**, *12* (4-5), 281–286. DOI: 10.1007/s11581-006-0048-9.

(114) Agrawal, R. C.; Sahu, D. K.; Mahipal, Y. K.; Ashrafi, R. Investigations on ion transport properties of hot-press cast magnesium ion conducting Nano-Composite Polymer Electrolyte (NCPE) films: Effect of filler particle dispersal on room temperature conductivity. *Materials Chemistry and Physics* **2013**, *139* (2-3), 410–415. DOI: 10.1016/j.matchemphys.2012.12.056.

(115) Sharma, J.; Hashmi, S. Magnesium ion-conducting gel polymer electrolyte nanocomposites: Effect of active and passive nanofillers. *Polym. Compos.* **2019**, *40* (4), 1295–1306. DOI: 10.1002/pc.24853.

(116) ANJI REDDY POLU and RANVEER KUMAR. Preparation and characterization of PEG–Mg(CH3COO)2–CeO2 composite polymer electrolytes for battery application. *Bull. Mater. Sci.* **2014** (Vol 37, No 2), 309–314.

(117) Shahenoor Basha, S. K.; Sunita Sundari, G.; Vijay Kumar, K.; Rao, M. C. Optical and dielectric properties of PVP based composite polymer electrolyte films. *Polym. Sci. Ser. A* **2017**, *59* (4), 554–565. DOI: 10.1134/S0965545X17040095.

(118) Wu, N.; Wang, W.; Wei, Y.; Li, T. Studies on the Effect of Nano-Sized MgO in Magnesium-Ion Conducting Gel Polymer Electrolyte for Rechargeable Magnesium Batteries. *Energies* **2017**, *10* (8), 1215. DOI: 10.3390/en10081215.

(119) Zaky, M. M.; Eyssa, H. M.; Sadek, R. F. Improvement of the magnesium battery electrolyte properties through gamma irradiation of nano polymer electrolytes doped with magnesium oxide nanoparticles. *J Vinyl Addit Technol* **2019**, *25* (3), 243–254. DOI: 10.1002/vnl.21683.

(120) Oh, J.-S.; Ko, J.-M.; Kim, D.-W. Preparation and characterization of gel polymer electrolytes for solid state magnesium batteries. *Electrochimica Acta* **2004**, *50* (2-3), 903–906. DOI: 10.1016/j.electacta.2004.01.099.

(121) Polu, A. R.; Kumar, R. Mg^{2+}-ion conducting poly(ethylene glycol)-TiO_2 composite polymer electrolytes for solid-state batteries. *Mat Express* **2014**, *4* (1), 79–84. DOI: 10.1166/mex.2014.1143.

(122) Polu, A. R.; Kumar, R.; Kumar, K. V.; Jyothi, N. K. Effect of TiO[sub 2] ceramic filler on PEG-based composite polymer electrolytes for magnesium batteries. In ; AIP, 2013; pp 996–997. DOI: 10.1063/1.4791378.

(123) Helen, P. A.; Ajith, K.; Diana, M. I.; Lakshmi, D.; Selvin, P. C. Chitosan based biopolymer electrolyte reinforced with V2O5 filler for magnesium batteries: an inclusive investigation. *J Mater Sci: Mater Electron* **2022**, *33* (7), 3925–3937. DOI: 10.1007/s10854-021-07587-7.

(124) Ponmani, S.; Selvakumar, K.; Ramesh Prabhu, M. The effect of the geikeilite (MgTiO3) nanofiller concentration in PVdF-HFP/PVAc–based polymer blend electrolytes for magnesium ion battery. *Ionics* **2020**, *26* (5), 2353–2369. DOI: 10.1007/s11581-019-03341-6.

(125) Anji Reddy Polu, Ranveer Kumar. Preperation and characterization of PEG-Mg(OAc)2-CeO2 composite polymer electrolytes for battery application. *Bull. Mater. Sci.* **2014** (37), 309–314.

(126) Polu, A. R.; Kumar, R.; Kumar, K. V.; Jyothi, N. K. Effect of TiO2 ceramic filler on PEG-based composite polymer electrolytes for magnesium batteries. In *AIP Conference Proceedings*; pp 996–997. DOI: 10.1063/1.4791378.

(127) Nidhi, Sandhya Patel, R. Kumar. Synthesis and characterization of magnesium ion conductivity in PVDF based nanocomposite polymer electrolytes disperse with MgO. *Journal of Alloys and Compounds* **2019** (789), 6–14.

(128) Shao, Y.; Rajput, N. N.; Hu, J.; Hu, M.; Liu, T.; Wei, Z.; Gu, M.; Deng, X.; Xu, S.; Han, K. S.; Wang, J.; Nie, Z.; Li, G.; Zavadil, K. R.; Xiao, J.; Wang, C.; Henderson, W. A.; Zhang, J.-G.; Wang, Y.; Mueller, K. T.; Persson, K.; Liu, J. Nanocomposite polymer electrolyte for rechargeable magnesium batteries. *Nano Energy* **2015**, *12* (8), 750–759. DOI: 10.1016/j.nanoen.2014.12.028.

(129) C. Arbizzani, M. Biso, D. Cericola, M. Lazzari, F. Soavi, M. Mastragostino. Safe, high-energy supercapacitors based on solvent free ionic liquid electrolyte. *Journal of Power Sources* **2008** (Boluome 185, Issue 2), 1575–1579.

(130) Shukur, M. F.; Ithnin, R.; Kadir, M. F. Z. Ionic conductivity and dielectric properties of potato starch-magnesium acetate biopolymer electrolytes: the effect of glycerol and 1-butyl-3-methylimidazolium chloride. *Ionics* **2016**, *22* (7), 1113–1123. DOI: 10.1007/s11581-015-1627-4.

(131) J. W. Fergus, B. Mishra, D. Anderson, E. A. Sarver, N. R. Neelameggham, M. Latha, Ch. S. SandeepReddy, V. Kanakaiah, G. Venkateshwarlu, K. Srinivasulu, Ch. KotiReddy, D. Shailaja, J. Vatsala rani. Engineering Solutions for Sustainability: Materials and Resources II:Abstract: Rechargeable magnesium batteries with novel PVdF-PAN graft copolymer electrolyte membranes. *TMS (The Minerals, Metals & materilas Society)* **2015**, 261–274.

(132) Jia, X.; Yang, Y.; Wang, C.; Zhao, C.; Vijayaraghavan, R.; MacFarlane, D. R.; Forsyth, M.; Wallace, G. G. Biocompatible ionic liquid-biopolymer electrolyte-enabled thin and compact magnesium-air batteries. *ACS applied materials & interfaces* **2014**, *6* (23), 21110–21117. DOI: 10.1021/am505985z.

(133) Aravindan, V.; Karthikaselvi, G.; Vickraman, P.; Naganandhini, S. P. Polyvinylidene fluoride-based novel polymer electrolytes for magnesium-rechargeable batteries with

Mg(CF 3 SO 3) 2. *J. Appl. Polym. Sci.* **2009**, *112* (5), 3024–3029. DOI: 10.1002/app.29877.

(134) P. Vickraman, V. Aravindan, T. Srinivasan, M. Jayachandran. Polyvinylidenefluoride (PVdF) based novel polymer electrolytes complexed with Mg(ClO4)2. *The European Physical Jouranl - Applied Physics* **2009** (45), 11101.

(135) Watkins, T.; Kumar, A.; Buttry, D. A. Designer Ionic Liquids for Reversible Electrochemical Deposition/Dissolution of Magnesium. *Journal of the American Chemical Society* **2016**, *138* (2), 641–650. DOI: 10.1021/jacs.5b11031.

(136) Sarangika, H. N. M.; Dissanayake, M. A. K. L.; Senadeera, G. K. R.; Rathnayake, R. R. D. V.; Pitawala, H. M. J. C. Polyethylene oxide and ionic liquid-based solid polymer electrolyte for rechargeable magnesium batteries. *Ionics* **2017**, *23* (10), 2829–2835. DOI: 10.1007/s11581-016-1870-3.

(137) Deivanayagam, R.; Cheng, M.; Wang, M.; Vasudevan, V.; Foroozan, T.; Medhekar, N. V.; Shahbazian-Yassar, R. Composite Polymer Electrolyte for Highly Cyclable Room-Temperature Solid-State Magnesium Batteries. *ACS Appl. Energy Mater.* **2019**, *2* (11), 7980–7990. DOI: 10.1021/acsaem.9b01455.

(138) Yang, G.; Song, Y.; Wang, Q.; Zhang, L.; Deng, L. Review of ionic liquids containing, polymer/inorganic hybrid electrolytes for lithium metal batteries. *Materials & Design* **2020**, *190*, 108563. DOI: 10.1016/j.matdes.2020.108563.

(139) Pandey, G. P.; Hashmi, S. A. Experimental investigations of an ionic-liquid-based, magnesium ion conducting, polymer gel electrolyte. *Journal of Power Sources* **2009**, *187* (2), 627–634. DOI: 10.1016/j.jpowsour.2008.10.112.

(140) Vila, J.; Varela, L. M.; Cabeza, O. Cation and anion sizes influence in the temperature dependence of the electrical conductivity in nine imidazolium based ionic liquids. *Electrochimica Acta* **2007**, *52* (26), 7413–7417. DOI: 10.1016/j.electacta.2007.06.044.

(141) Hirankumar, G.; Mehta, N. Effect of incorporation of different plasticizers on structural and ion transport properties of PVA-LiClO4 based electrolytes. *Heliyon* **2018**, *4* (12), e00992. DOI: 10.1016/j.heliyon.2018.e00992. Published Online: Dec. 8, 2018.

(142) G. G. Kumar, N. Munichandraiah. Solid-state Mg/MnO2 cell empoying a gel polymer electrolyte of magnesium triflate **2000** (91), 157–160.

(143) G. G. Kumar, N. Munichandraiah. Reversibility of Mg/Mg2+ couple in a gel polymer electrolyte. *Electrochimica Acta* **1999** (44), 2663–2666.

(144) G. G. Kumar, N. Munichandraiah. A gel polymer electrolyte of magnesium triflate. *Solid State Ionics* **2000** (128), 203–210.

(145) G. G. Kumar, N. Munichandraiah. Effect of plasticizers on magnesium-poly(ethyleneoxide) polymer electrolyte. *Journal of Electroanalytical Chemistry* **2000** (495), 42–50.

(146) G. G. Kumar, N. Munichandraiah. Poly(methylmethacrylate)-magnesium triflate gel polymer electrolyte for solid state magnsium battery application. *Electrochimica Acta* **2002**, 1013–1022.

(147) Osman, Z.; Zainol, N. H.; Samin, S. M.; Chong, W. G.; Md Isa, K. B.; Othman, L.; Supa'at, I.; Sonsudin, F. Electrochemical Impedance Spectroscopy Studies of Magnesium-Based Polymethylmethacrylate Gel Polymer Electroytes. *Electrochimica Acta* **2014**, *131*, 148–153. DOI: 10.1016/j.electacta.2013.11.189.

(148) Zainol, N. H.; Osman, Z.; Othman, L.; Md. Isa, K. B. Transport and Morphological Properties of Gel Polymer Electrolytes Containing $Mg(CF_3SO_3)_2$. *AMR* **2013**, *686*, 137–144. DOI: 10.4028/www.scientific.net/AMR.686.137.

(149) G. G. Kumar, N. Munichandraiah. Solid-state rechargeable magnesium cell with poly(vinylidenefluoride)-magnesium triflate gel polymer electrolyte. *Journal of Power Sources* **2001** (102), 46–54.

(150) Hambali, D.; Zainol, N. H.; Othman, L.; Md Isa, K. B.; Osman, Z. Magnesium ion-conducting gel polymer electrolytes based on poly(vinylidene chloride-co-acrylonitrile) (PVdC-co-AN): a comparative study between magnesium trifluoromethanesulfonate (MgTf2) and magnesium bis(trifluoromethanesulfonimide) (Mg(TFSI)2). *Ionics* **2019**, *25* (3), 1187–1198. DOI: 10.1007/s11581-018-2666-4.

(151) Asmara, S. N.; Kufian, M. Z.; Majid, S. R.; Arof, A. K. Preparation and characterization of magnesium ion gel polymer electrolytes for application in electrical double layer capacitors. *Electrochimica Acta* **2011**, *57*, 91–97. DOI: 10.1016/j.electacta.2011.06.045.

(152) Yoshimoto, N.; Yakushiji, S.; Ishikawa, M.; Morita, M. Rechargeable magnesium batteries with polymeric gel electrolytes containing magnesium salts. *Electrochimica Acta* **2003**, *48* (14-16), 2317–2322. DOI: 10.1016/S0013-4686(03)00221-4.

(153) Pandey, G. P.; Agrawal, R. C.; Hashmi, S. A. Magnesium ion-conducting gel polymer electrolytes dispersed with fumed silica for rechargeable magnesium battery application. *J Solid State Electrochem* **2011**, *15* (10), 2253–2264. DOI: 10.1007/s10008-010-1240-4.

(154) Pandey, G. P.; Agrawal, R. C.; Hashmi, S. A. Magnesium ion-conducting gel polymer electrolytes dispersed with nanosized magnesium oxide. *Journal of Power Sources* **2009**, *190* (2), 563–572. DOI: 10.1016/j.jpowsour.2009.01.057.

(155) Sharma, J.; Hashmi, S. A. Magnesium ion transport in poly(ethylene oxide)-based polymer electrolyte containing plastic-crystalline succinonitrile. *J Solid State Electrochem* **2013**, *17* (8), 2283–2291. DOI: 10.1007/s10008-013-2104-5.

(156) Sharma, J.; Hashmi, S. A. Plastic crystal-incorporated magnesium ion conducting gel polymer electrolyte for battery application. *Bull Mater Sci* **2018**, *41* (6), 1623. DOI: 10.1007/s12034-018-1662-7.

(157) R. Gamal, Sh. I. Elkalashy, E. Sheha, M.M. El Kohly. Polymer electrolytes based on magnesium triflate for quasi-solid-state magnesium-sulfur batteries **2022**.

(158) Sheha, E.; Ahmad, F.; Zhang, P.; Wang, H.; Guo, Z. Effect of Magnesium Bromide on the electrical and electrochemical Properties of PVA and tetraethylene Glycol Dimethyl Ether Polymer Electrolyte for Solid State Magnesium Batteries. *Energy and Environment Focus* **2016** (5), 125–130.

(159) R. Gamal, e. Sheha, N. Shash, M. G. El-Shaarawy. Effect of plasticizer on electric and dielectric properties of PVA-MgBr2 based solid polymer electrolytes. *Journal of Basic and Enviromental Sciences* **2014** (1), 86–91.

(160) Bhatt, P. J.; Pathak, N.; Mishra, K.; Kanchan, D. K.; Kumar, D. Effect of Different Cations on Ion-Transport Behavior in Polymer Gel Electrolytes Intended for Application in Flexible Electrochemical Devices. *J. Electron. Mater.* **2022**, *51* (3), 1371–1384. DOI: 10.1007/s11664-021-09398-2.

(161) Tominaga, Y.; Kato, S.; Nishimura, N. Preparation and electrochemical characterization of magnesium gel electrolytes based on crosslinked Poly(tetrahydrofuran). *Polymer* **2021** (224), 123743. DOI: 10.1016/j.polymer.2021.123743.

(162) Mesallam, M.; Kamar, E. M.; Sharma, N.; Sheha, E. Synthesis and characterization of polyvinylidene fluoride/magnesium bromide polymer electrolyte for magnesium battery application. *Phys. Scr.* **2020**, *95* (11), 115805. DOI: 10.1088/1402-4896/abbcf4.

(163) Hamsan, M. H.; B. Aziz, S.; Nofal, M. M.; Brza, M. A.; Abdulwahid, R. T.; Hadi, J. M.; Karim, W. O.; Kadir, M.F.Z. Characteristics of EDLC device fabricated from plasticized chitosan:MgCl2 based polymer electrolyte. *Journal of Materials Research and Technology* **2020**, *9* (5), 10635–10646. DOI: 10.1016/j.jmrt.2020.07.096.

(164) Du, A.; Zhang, H.; Zhang, Z.; Zhao, J.; Cui, Z.; Zhao, Y.; Dong, S.; Wang, L.; Zhou, X.; Cui, G. A Crosslinked Polytetrahydrofuran-Borate-Based Polymer Electrolyte Enabling Wide-Working-Temperature-Range Rechargeable Magnesium Batteries. *Advanced materials (Deerfield Beach, Fla.)* **2019**, *31* (11), e1805930. DOI: 10.1002/adma.201805930.

(165) Mishra, K.; Kanchan, D. K.; Gohel, K.; Sharma, P.; Kumar, D. Urea-assisted ion-transport behavior in magnesium ion conducting solid polymer electrolyte membranes intended for magnesium batteries. *Chem. Pap.* **2021**, *41* (4), 146. DOI: 10.1007/s11696-021-01910-6.

(166) Morita, M.; Yoshimoto, N.; Yakushiji, S.; Ishikawa, M. Rechargeable Magnesium Batteries Using a Novel Polymeric Solid Electrolyte. *Electrochem. Solid-State Lett.* **2001**, *4* (11), A177. DOI: 10.1149/1.1403195.

(167) Yoshimoto, N.; Tomonaga, Y.; Ishikawa, M.; Morita, M. Ionic conductance of polymeric electrolytes consisting of magnesium salts dissolved in cross-linked polymer matrix with linear polyether. *Electrochimica Acta* **2001**, *46* (8), 1195–1200. DOI: 10.1016/S0013-4686(00)00705-2.

(168) Liping Wang, Zhenyou Li, Zhen Meng, Yanlei Xiu, Bosubabu Dasari, Zhirong Zhao-Karger, MaximilianFichtner. Designing Gel Polymer Electrolyte with Synergetic Properties for Rechargeable Magnesium Batteries. *Energy Storage Materials* **2022** (48), 155–163.

(169) R. Gamal, Sh. I. Elkalashy, E. Sheha and M. M. El Kholy. Polymer electrolytes based on magnesium triflate for quasi-solid-state magnesium-sulfur batteries. *Physica Scripta* **2022** (97), 65816.

(170) Tang, X.; Muchakayala, R.; Song, S.; Zhang, Z.; Polu, A. R. A study of structural, electrical and electrochemical properties of PVdF-HFP gel polymer electrolyte films for magnesium ion battery applications. *Journal of Industrial and Engineering Chemistry* **2016**, *37*, 67–74. DOI: 10.1016/j.jiec.2016.03.001.

(171) J. Wang, Z. Zhao, R. Muchakayala, S. Song. High-perfomance Mg-ion conducting poly(vinylalcohol) membranes: Preparation, characterization and application in supercapacitors. *Journal of Membrane Science* **2018** (555), 280–289.

(172) Wang, J.; Song, S.; Muchakayala, R.; Hu, X.; Liu, R. Structural, electrical, and electrochemical properties of PVA-based biodegradable gel polymer electrolyte membranes for Mg-ion battery applications. *Ionics* **2017**, *23* (7), 1759–1769. DOI: 10.1007/s11581-017-1988-y.

(173) Pandey, G. P.; Kumar, Y.; Hashmi, S. A. Ionic liquid incorporated PEO based polymer electrolyte for electrical double layer capacitors: A comparative study with lithium and magnesium systems. *Solid State Ionics* **2011**, *190* (1), 93–98. DOI: 10.1016/j.ssi.2011.03.018.

(174) Kumar, Y.; Hashmi, S. A.; Pandey, G. P. Ionic liquid mediated magnesium ion conduction in poly(ethylene oxide) based polymer electrolyte. *Electrochimica Acta* **2011**, *56* (11), 3864–3873. DOI: 10.1016/j.electacta.2011.02.035.

(175) Morita, M.; Shirai, T.; Yoshimoto, N.; Ishikawa, M. Ionic conductance behavior of polymeric gel electrolyte containing ionic liquid mixed with magnesium salt. *Journal of Power Sources* **2005**, *139* (1-2), 351–355. DOI: 10.1016/j.jpowsour.2004.07.028.

(176) Yoshimoto, N.; Shirai, T.; Morita, M. A novel polymeric gel electrolyte systems containing magnesium salt with ionic liquid. *Electrochimica Acta* **2005**, *50* (19), 3866–3871. DOI: 10.1016/j.electacta.2005.02.036.

(177) Rachna Mishra, N. Baskaran, P.A. Ramakrishnan, K.J. Rao. Lithium ion conduction in extreme polymer in salt regime. *Solid State Ionics* **1998** (112), 261–273.

(178) O.V. Bushkova , V.M. Zhukovsky, B.I. Lirova, A.L. Kruglyashov. Fast ionic transport in solid polymer electrolytes based on acrylonitrile copolymers. *Solid State Ionics* **1999** (119).

(179) Ferry, A.; Edman, L.; Forsyth, M.; MacFarlane, D. R.; Sun, J. Connectivity, ionic interactions, and migration in a fast-ion-conducting polymer-in-salt electrolyte based on poly(acrylonitrile) and LiCF3SO3. *Journal of Applied Physics* **1999**, *86* (4), 2346–2348. DOI: 10.1063/1.371053.

(180) Łasińska, A. K.; Marzantowicz, M.; Dygas, J. R.; Krok, F.; Florjańczyk, Z.; Tomaszewska, A.; Zygadło-Monikowska, E.; Żukowska, Z.; Lafont, U. Study of ageing effects in polymer-in-salt electrolytes based on poly(acrylonitrile-co-butyl acrylate) and lithium salts. *Electrochimica Acta* **2015**, *169*, 61–72. DOI: 10.1016/j.electacta.2015.04.023.

(181) Zhaoxiang Wang, Weidong Gao, Liquan Chen, Yujun Mo, Xuejie Huang. Study on roles of polyacrylonitrile in ‘‘salt-in-polymer’’ and ‘‘polymer-in-salt’’ electrolytes **2002** (154-155), 51–56.

(182) Diederichsen, K. M.; McShane, E. J.; McCloskey, B. D. Promising Routes to a High Li + Transference Number Electrolyte for Lithium Ion Batteries. *ACS Energy Lett.* **2017**, *2* (11), 2563–2575. DOI: 10.1021/acsenergylett.7b00792.

(183) Strauss, E.; Menkin, S.; Golodnitsky, D. On the way to high-conductivity single lithium-ion conductors. *J Solid State Electrochem* **2017**, *21* (7), 1879–1905. DOI: 10.1007/s10008-017-3638-8.

(184) Mayer, A.; Steinle, D.; Passerini, S.; Bresser, D. Block copolymers as (single-ion conducting) lithium battery electrolytes. *Nanotechnology* **2021**, *33* (6). DOI: 10.1088/1361-6528/ac2e21. Published Online: Nov. 15, 2021.

(185) Kaimin Chen/D. F. Shriver. Magnesium ion conducting polymeric electrolytes. *Chem. Mater.* **1991** (3), 771–772.

(186) Elmore, C.; Seidler, M.; Ford, H.; Merrill, L.; Upadhyay, S.; Schneider, W.; Schaefer, J. Ion Transport in Solvent-Free, Crosslinked, Single-Ion Conducting Polymer Electrolytes for Post-Lithium Ion Batteries. *Batteries* **2018**, *4* (2), 28. DOI: 10.3390/batteries4020028.

(187) Park, B.; Ford, H. O.; Merrill, L. C.; Liu, J.; Murphy, L. P.; Schaefer, J. L. Dual Cation Exchanged Poly(ionic liquid)s as Magnesium Conducting Electrolytes. *ACS Appl. Polym. Mater.* **2019**, *1* (11), 2907–2913. DOI: 10.1021/acsapm.9b00614.

(188) Rojas, A. A.; Thakker, K.; McEntush, K. D.; Inceoglu, S.; Stone, G. M.; Balsara, N. P. Dependence of Morphology, Shear Modulus, and Conductivity on the Composition of Lithiated and Magnesiated Single-Ion-Conducting Block Copolymer Electrolytes. *Macromolecules* **2017**, *50* (21), 8765–8776. DOI: 10.1021/acs.macromol.7b01686.

(189) Thelen, J. L.; Inceoglu, S.; Venkatesan, N. R.; Mackay, N. G.; Balsara, N. P. Relationship between Ion Dissociation, Melt Morphology, and Electrochemical Performance of Lithium and Magnesium Single-Ion Conducting Block Copolymers. *Macromolecules* **2016**, *49* (23), 9139–9147. DOI: 10.1021/acs.macromol.6b01886.

(190) Guzmán-González, G.; Vauthier, S.; Alvarez-Tirado, M.; Cotte, S.; Castro, L.; Guéguen, A.; Casado, N.; Mecerreyes, D. Single-Ion Lithium Conducting Polymers with High Ionic Conductivity Based on Borate Pendant Groups. *Angewandte Chemie* **2022**, *134* (7). DOI: 10.1002/ange.202114024.

(191) Dai, K.; Zheng, Y.; Wei, W. Organoboron-Containing Polymer Electrolytes for High-Performance Lithium Batteries. *Adv. Funct. Mater.* **2021**, *31* (13), 2008632. DOI: 10.1002/adfm.202008632.

(192) Saito, M.; Ikuta, H.; Uchimoto, Y.; Wakihara, M.; Yokoyama, S.; Yabe, T.; Yamamoto, M. Interaction between the Lewis Acid Group of a Borate Ester and Various Anion Species in a Polymer Electrolyte Containing Mg Salt. *J. Phys. Chem. B* **2003**, *107* (42), 11608–11614. DOI: 10.1021/jp034040b.

(193) Aziz, A. A.; Tominaga, Y. Effect of Li salt addition on electrochemical properties of poly(ethylene carbonate)-Mg salt electrolytes. *Polym J* **2019**, *51* (1), 61–67. DOI: 10.1038/s41428-018-0113-z.

(194) Wang, P.; Trück, J.; Häcker, J.; Schlosser, A.; Küster, K.; Starke, U.; Reinders, L.; Buchmeiser, M. R. A design concept for halogen-free Mg2+/Li+-dual salt-containing gel-polymer-electrolytes for rechargeable magnesium batteries. *Energy Storage Materials* **2022**, *49*, 509–517. DOI: 10.1016/j.ensm.2022.04.034.

(195) Penczek, S.; Pretula, J.; Slomkowski, S. Ring-opening polymerization. *Chemistry Teacher International* **2021**, *3* (2), 33–57. DOI: 10.1515/cti-2020-0028.

(196) Hashimoto, K. Ring-opening polymerization of lactams. Living anionic polymerization and its applications. *Progress in Polymer Science* **2000**, *25* (10), 1411–1462. DOI: 10.1016/S0079-6700(00)00018-6.

(197) J. Chiefari, Y. K. Chong, F. Ercole, J. Krstina, J. Jeffery, T. P. Le, R. T. A.Mayadunne, G. F. Meijs, C. L. Moad, G.Moad, E. Rizzardo, S. H. Thang. Living Free-Radical Polymerization by Reversible Addition-Fragmentation Chain Transfer: The RAFT Process. *Macromolecules* **1998** (31), 5559–5562.

(198) Taton, D.; Wilczewska, A.-Z.; Destarac, M. Direct Synthesis of Double Hydrophilic Statistical Di- and Triblock Copolymers Comprised of Acrylamide and Acrylic Acid Units via the MADIX Process. *Macromol. Rapid Commun.* **2001**, *22* (18), 1497. DOI: 10.1002/1521-3927(20011201)22:18<1497:AID-MARC1497>3.0.CO;2-M.

(199) Soares, J. B. P.; McKenna, T. F. L. *Polyolefin reaction engineering*; Wiley-VCH, 2012.

(200) Matyjaszewski, K.; Poli, R. Comparison of Bond Dissociation Energies of Dormant Species Relevant to Degenerative Transfer and Atom Transfer Radical Polymerization. *Macromolecules* **2005**, *38* (19), 8093–8100. DOI: 10.1021/ma0512049.

(201) Moad, G.; Rizzardo, E.; Thang, S. H. Living Radical Polymerization by the RAFT Process. *Aust. J. Chem.* **2005**, *58* (6), 379. DOI: 10.1071/CH05072.

(202) Rizzardo, E.; Chen, M.; Chong, B.; Moad, G.; Skidmore, M.; Thang, S. H. RAFT Polymerization: Adding to the Picture. *Macromol. Symp.* **2007**, *248* (1), 104–116. DOI: 10.1002/masy.200750211.

(203) Chong, Y. K.; Krstina, J.; Le, T. P. T.; Moad, G.; Postma, A.; Rizzardo, E.; Thang, S. H. Thiocarbonylthio Compounds [SC(Ph)S−R] in Free Radical Polymerization with Reversible Addition-Fragmentation Chain Transfer (RAFT Polymerization). Role of the Free-Radical Leaving Group (R). *Macromolecules* **2003**, *36* (7), 2256–2272. DOI: 10.1021/ma020882h.

(204) Rinaldi, D.; Hamaide, T.; Graillat, C.; D'Agosto, F.; Spitz, R.; Georges, S.; Mosquet, M.; Maitrasse, P. RAFT copolymerization of methacrylic acid and poly(ethylene glycol) methyl ether methacrylate in the presence of a hydrophobic chain transfer agent in organic

solution and in water. *J. Polym. Sci. A Polym. Chem.* **2009**, *47* (12), 3045–3055. DOI: 10.1002/pola.23374.

(205) Benaglia, M.; Rizzardo, E.; Alberti, A.; Guerra, M. Searching for More Effective Agents and Conditions for the RAFT Polymerization of MMA: Influence of Dithioester Substituents, Solvent, and Temperature. *Macromolecules* **2005**, *38* (8), 3129–3140. DOI: 10.1021/ma0480650.

(206) Alberti, A.; Benaglia, M.; Guerra, M.; Gulea, M.; Hapiot, P.; Laus, M.; Macciantelli, D.; Masson, S.; Postma, A.; Sparnacci, K. A Multidisciplinary Approach to the Use of Pyridinyl Dithioesters and Their N -Oxides as CTAs in the RAFT Polymerization of Styrene. Not the Chronicle of a Failure Foretold. *Macromolecules* **2005**, *38* (18), 7610–7618. DOI: 10.1021/ma050652d.

(207) Postma, A.; Davis, T. P.; Evans, R. A.; Li, G.; Moad, G.; O'Shea, M. S. Synthesis of Well-Defined Polystyrene with Primary Amine End Groups through the Use of Phthalimido-Functional RAFT Agents. *Macromolecules* **2006**, *39* (16), 5293–5306. DOI: 10.1021/ma060245h.

(208) Millard, P.-E.; Barner, L.; Stenzel, M. H.; Davis, T. P.; Barner-Kowollik, C.; Müller, A. H. E. RAFT Polymerization ofN-Isopropylacrylamide and Acrylic Acid underγ-Irradiation in Aqueous Media. *Macromol. Rapid Commun.* **2006**, *27* (11), 821–828. DOI: 10.1002/marc.200600115.

(209) Willcock, H.; O'Reilly, R. K. End group removal and modification of RAFT polymers. *Polym. Chem.* **2010**, *1* (2), 149–157. DOI: 10.1039/B9PY00340A.

(210) Gregory, A.; Stenzel, M. H. Complex polymer architectures via RAFT polymerization: From fundamental process to extending the scope using click chemistry and nature's building blocks. *Progress in Polymer Science* **2012**, *37* (1), 38–105. DOI: 10.1016/j.progpolymsci.2011.08.004.

(211) Nuyken, O.; Pask, S. Ring-Opening Polymerization—An Introductory Review. *Polymers* **2013**, *5* (2), 361–403. DOI: 10.3390/polym5020361.

(212) Brocas, A.-L.; Mantzaridis, C.; Tunc, D.; Carlotti, S. Polyether synthesis: From activated or metal-free anionic ring-opening polymerization of epoxides to functionalization. *Progress in Polymer Science* **2013**, *38* (6), 845–873. DOI: 10.1016/j.progpolymsci.2012.09.007.

(213) Suriano, F.; Coulembier, O.; Hedrick, J. L.; Dubois, P. Functionalized cyclic carbonates: from synthesis and metal-free catalyzed ring-opening polymerization to applications. *Polym. Chem.* **2011**, *2* (3), 528–533. DOI: 10.1039/C0PY00211A.

(214) Sarazin, Y.; Carpentier, J.-F. Discrete cationic complexes for ring-opening polymerization catalysis of cyclic esters and epoxides. *Chemical reviews* **2015**, *115* (9), 3564–3614. DOI: 10.1021/acs.chemrev.5b00033. Published Online: Apr. 21, 2015.

(215) M. E. Piotti. Ring opening metathesis polymerization. *Current Opinion in Solid State and Materials Science* **1999** (4), 539–547.

(216) Albertsson, A.-C.; Varma, I. K. Recent developments in ring opening polymerization of lactones for biomedical applications. *Biomacromolecules* **2003**, *4* (6), 1466–1486. DOI: 10.1021/bm034247a.

(217) Flory, P. J. Molecular Size Distribution in Ethylene Oxide Polymers. *Journal of the American Chemical Society* **1940** (62), 1561-1565.

(218) Hadjichristidis, N.; Hirao, A. *Anionic Polymerization*; Springer Japan, 2015. DOI: 10.1007/978-4-431-54186-8.

(219) T. Takata, H. Matsuoka, T. Endo. Synthesis and Anionic Ring-Opening Polymerization of a Novel Aromatic Cyclic Carboante Having Binapthyl Structure. *Chemistry Letters* **1991**, 2091–2094.

(220) Vogdanis, L.; Heitz, W. Carbon dioxide as a monomer, 3. The polymerization of ethylene carbonate. *Makromol. Chem., Rapid Commun.* **1986**, *7* (9), 543–547. DOI: 10.1002/marc.1986.030070901.

(221) Parzuchowski, P. G.; Jaroch, M.; Tryznowski, M.; Rokicki, G. Synthesis of New Glycerol-Based Hyperbranched Polycarbonates. *Macromolecules* **2008**, *41* (11), 3859–3865. DOI: 10.1021/ma8000912.

(222) Kricheldorf, H. R.; Lee, S.-R.; Weegen-Schulz, B. Polymers of carbonic acid, 12. Spontaneous and hematin-initiated polymerizations of trimethylene carbonate and neopentylene carbonate. *Macromol. Chem. Phys.* **1996**, *197* (3), 1043–1054. DOI: 10.1002/macp.1996.021970323.

(223) Matsuo, J.; Sanda, F.; Endo, T. A novel observation in anionic ring-opening polymerization behavior of cyclic carbonates having aromatic substituents. *Macromol. Chem. Phys.* **1998**, *199* (11), 2489–2494. DOI: 10.1002/(SICI)1521-3935(19981101)199:11<2489:AID-MACP2489>3.0.CO;2-V.

(224) Jyuhou Matsuo, Kazutaka Aoki, Fumio Sanda, and Takeshi Endo. Substituent Effect on the Anionic Equilibrium Polymerization of Six-Membered Cyclic Carbonates. *Macromolecules* **1998** (31), 4432–4438.

(225) Jaacks, V.; Mathes, N. Formation of macrozwitterions in the polymerization of β-lactones initiated by tertiary amines. 2nd communication on macrozwitterions1. *Makromol. Chem.* **1970**, *131* (1), 295–303. DOI: 10.1002/macp.1970.021310123.

(226) Boileau, S.; Illy, N. Activation in anionic polymerization: Why phosphazene bases are very exciting promoters. *Progress in Polymer Science* **2011**, *36* (9), 1132–1151. DOI: 10.1016/j.progpolymsci.2011.05.005.

(227) Baheti, P.; Rheinberger, T.; Gimello, O.; Bouilhac, C.; Wurm, F. R.; Lacroix-Desmazes, P.; Howdle, S. M. Clean synthesis of linear and star amphiphilic poly(ε-caprolactone)-block -poly(ethyl ethylene phosphonate) block copolymers: assessing self-assembly and surface activity. *Green Chem.* **2020**, *22* (10), 3248–3261. DOI: 10.1039/D0GC00819B.

(228) Park, N. H.; Voo, Z. X.; Yang, Y. Y.; Hedrick, J. L. Convergent Approach to Boronic Acid Functionalized Polycarbonates: Accessing New Dynamic Material Platforms. *ACS macro letters* **2017**, *6* (3), 252–256. DOI: 10.1021/acsmacrolett.6b00875. Published Online: Feb. 27, 2017.

(229) Sun, J.; Aly, K. I.; Kuckling, D. A novel one-pot process for the preparation of linear and hyperbranched polycarbonates of various diols and triols using dimethyl carbonate. *RSC Adv.* **2017**, *7* (21), 12550–12560. DOI: 10.1039/C7RA01317E.

(230) Abdel Baki, Z.; Dib, H.; Sahin, T. Overview: Polycarbonates via Ring-Opening Polymerization, Differences between Six- and Five-Membered Cyclic Carbonates: Inspiration for Green Alternatives. *Polymers* **2022**, *14* (10). DOI: 10.3390/polym14102031. Published Online: May. 16, 2022.

(231) Endo, T.; Kakimoto, K.; Ochiai, B.; Nagai, D. Synthesis and Chemical Recycling of a Polycarbonate Obtained by Anionic Ring-Opening Polymerization of a Bifunctional Cyclic Carbonate. *Macromolecules* **2005**, *38* (20), 8177–8182. DOI: 10.1021/ma050791v.

(232) Ito, S.; Goseki, R.; Ishizone, T.; Hirao, A. Synthesis of well-controlled graft polymers by living anionic polymerization towards exact graft polymers. *Polym. Chem.* **2014**, *5* (19), 5523. DOI: 10.1039/C4PY00584H.

(233) Koichi Kato, Emiko Uchida, En-Tang Kang, Yoshikimi Uyama, Yoshito Ikada. Polymer surface with graft chains. *Prog. Polym. Sci.* **2003** (28), 209–259.

(234) BHATTACHARYA, A. Grafting: a versatile means to modify polymersTechniques, factors and applications. *Progress in Polymer Science* **2004**, *29* (8), 767–814. DOI: 10.1016/j.progpolymsci.2004.05.002.

(235) Francis, R.; Joy, N.; Aparna, E. P.; Vijayan, R. Polymer Grafted Inorganic Nanoparticles, Preparation, Properties, and Applications: A Review. *Polymer Reviews* **2014**, *54* (2), 268–347. DOI: 10.1080/15583724.2013.870573.

(236) Hebié, S.; Ngo, H. P. K.; Leprêtre, J.-C.; Iojoiu, C.; Cointeaux, L.; Berthelot, R.; Alloin, F. Electrolyte Based on Easily Synthesized, Low Cost Triphenolate-Borohydride Salt for High Performance Mg(TFSI)2-Glyme Rechargeable Magnesium Batteries. *ACS applied materials & interfaces* **2017**, *9* (34), 28377–28385. DOI: 10.1021/acsami.7b06022. Published Online: Aug. 21, 2017.

(237) Singh, N.; Arthur, T. S.; Tutusaus, O.; Li, J.; Kisslinger, K.; Xin, H. L.; Stach, E. A.; Fan, X.; Mohtadi, R. Achieving High Cycling Rates via In Situ Generation of Active Nanocomposite Metal Anodes. *ACS Appl. Energy Mater.* **2018**, *1* (9), 4651–4661. DOI: 10.1021/acsaem.8b00794.

(238) Merrill, L. C.; Schaefer, J. L. The Influence of Interfacial Chemistry on Magnesium Electrodeposition in Non-nucleophilic Electrolytes Using Sulfone-Ether Mixtures. *Frontiers in chemistry* **2019**, *7*, 194. DOI: 10.3389/fchem.2019.00194. Published Online: Apr. 3, 2019.

(239) N. Zuber. Cross-linking of PEO-based polymers for solid-state electrolyte application:Master thesis **2021**.

(240) Coddington, J. M.; Taylor, M. J. High Field 11 B and 13 C Nmr Investigations of Aqueous Borate Solutions and Borate-Diol Complexes. *Journal of Coordination Chemistry* **1989**, *20* (1), 27–38. DOI: 10.1080/00958978909408845.

(241) Dai, K.; Ma, C.; Feng, Y.; Zhou, L.; Kuang, G.; Zhang, Y.; Lai, Y.; Cui, X.; Wei, W. A borate-rich, cross-linked gel polymer electrolyte with near-single ion conduction for lithium metal batteries. *J. Mater. Chem. A* **2019**, *7* (31), 18547–18557. DOI: 10.1039/C9TA05938E.

(242) Kaya, N. U.; Saloglu, D.; Guvenilir, Y. Photopolymerization of enzymatically synthesized methacrylated poly(caprolactone) with poly(ethylene glycol) macromonomer. *Journal of Macromolecular Science, Part A* **2019**, *56* (7), 658–666. DOI: 10.1080/10601325.2019.1594891.

(243) Tang, B.; Yang, Z.; Zhang, S. Poly(polyethylene glycol methyl ether methacrylate) as novel solid-solid phase change material for thermal energy storage. *J. Appl. Polym. Sci.* **2012**, *125* (2), 1377–1381. DOI: 10.1002/app.35287.

(244) Guzmán-González, G.; Ávila-Paredes, H. J.; Rivera, E.; González, I. Electrochemical Characterization of Single Lithium-Ion Conducting Polymer Electrolytes Based on sp3

Boron and Poly(ethylene glycol) Bridges. *ACS applied materials & interfaces* **2018**, *10* (36), 30247–30256. DOI: 10.1021/acsami.8b02519. Published Online: Aug. 30, 2018.

(245) Rosenbach, D.; Mödl, N.; Hahn, M.; Petry, J.; Danzer, M. A.; Thelakkat, M. Synthesis and Comparative Studies of Solvent-Free Brush Polymer Electrolytes for Lithium Batteries. *ACS Appl. Energy Mater.* **2019**, *2* (5), 3373–3388. DOI: 10.1021/acsaem.9b00211.

(246) Sang-Woog Ryu et al. Effect of Counter Ion Placement on Conductivity in Single-Ion Conducting Block Copolymer Electrolytes. *J. Electrochem. Soc.* **2005** (152 (1)), A158-A163.

(247) Xue, Z.; He, D.; Xie, X. Poly(ethylene oxide)-based electrolytes for lithium-ion batteries. *J. Mater. Chem. A* **2015**, *3* (38), 19218–19253. DOI: 10.1039/C5TA03471J.

(248) Manuel Stephan, A. Review on gel polymer electrolytes for lithium batteries. *European Polymer Journal* **2006**, *42* (1), 21–42. DOI: 10.1016/j.eurpolymj.2005.09.017.

(249) G. G. Kumar, N. Munichandraiah. Effect of plasticizers on magnesium-poly(etyhleneoxide) polymer electrolyte. *Journal of Electroanalytical Chemistry* **2000** (495), 42–50.

(250) Andrew L. Tipton, Mark C. Lonergan, Mark A. Ratner, and Duward F. Shriver. Conductivity and Dielectric Constant of PPO and PPO-Based Solid Electrolytes from Dc to 6 GHz. *J. Phys. Chem.* **1994** (98), 4148–4154.

(251) Stowe, M. K.; Liu, P.; Baker, G. L. Star Poly(ethylene oxide) as a Low Temperature Electrolyte and Crystallization Inhibitor. *Chem. Mater.* **2005**, *17* (26), 6555–6559. DOI: 10.1021/cm050673m.

(252) Merrill, L. C.; Ford, H. O.; Schaefer, J. L. Application of Single-Ion Conducting Gel Polymer Electrolytes in Magnesium Batteries. *ACS Appl. Energy Mater.* **2019**, *2* (9), 6355–6363. DOI: 10.1021/acsaem.9b00991.

(253) Kim, D. J.; Ryu, H. S.; Kim, I. P.; Cho, K. K.; Nam, T. H.; Kim, K. W.; Ahn, J. H.; Ahn, H. J. Electrochemical properties of magnesium electrolyte with organic solvent. *Phys. Scr.* **2007**, *T129*, 70–73. DOI: 10.1088/0031-8949/2007/T129/016.

(254) Muldoon, J.; Bucur, C. B.; Oliver, A. G.; Sugimoto, T.; Matsui, M.; Kim, H. S.; Allred, G. D.; Zajicek, J.; Kotani, Y. Electrolyte roadblocks to a magnesium rechargeable battery. *Energy Environ. Sci.* **2012**, *5* (3), 5941. DOI: 10.1039/c2ee03029b.

(255) Shao, Y.; Liu, T.; Li, G.; Gu, M.; Nie, Z.; Engelhard, M.; Xiao, J.; Lv, D.; Wang, C.; Zhang, J.-G.; Liu, J. Coordination chemistry in magnesium battery electrolytes: how ligands affect their performance. *Scientific reports* **2013**, *3*, 3130. DOI: 10.1038/srep03130. Published Online: Nov. 4, 2013.

(256) Tuerxun, F.; Abulizi, Y.; NuLi, Y.; Su, S.; Yang, J.; Wang, J. High concentration magnesium borohydride/tetraglyme electrolyte for rechargeable magnesium batteries. *Journal of Power Sources* **2015**, *276*, 255–261. DOI: 10.1016/j.jpowsour.2014.11.113.

(257) Rajput, N. N.; Qu, X.; Sa, N.; Burrell, A. K.; Persson, K. A. The coupling between stability and ion pair formation in magnesium electrolytes from first-principles quantum mechanics and classical molecular dynamics. *Journal of the American Chemical Society* **2015**, *137* (9), 3411–3420. DOI: 10.1021/jacs.5b01004. Published Online: Feb. 24, 2015.

(258) Zhu, Y.; Xiao, S.; Shi, Y.; Yang, Y.; Wu, Y. A trilayer poly(vinylidene fluoride)/polyborate/poly(vinylidene fluoride) gel polymer electrolyte with good performance for lithium ion batteries. *J. Mater. Chem. A* **2013**, *1* (26), 7790. DOI: 10.1039/c3ta00167a.

(259) Mesallam, M.; Kamar, E. M.; Sharma, N.; Sheha, E. Synthesis and characterization of polyvinylidene fluoride/magnesium bromide polymer electrolyte for magnesium battery application. *Phys. Scr.* **2020**, *95* (11), 115805. DOI: 10.1088/1402-4896/abbcf4.

(260) Jae-Hyun Cho, Su Jin Kim, Jinwoo Oh, Jung Hoon Ha, Kwang-Bum Kim, Kwan-Young Lee, and Jae Kyun Lee. Strategic Design of Highly Concentrated Electrolyte Solutions for Mg2+/Li+ Dual-Salt Hybrid Batteries. *J. Phys. Chem. C* **2018** (122, 49), 27866–27874.

(261) Oswald, S.; Thoss, F.; Zier, M.; Hoffmann, M.; Jaumann, T.; Herklotz, M.; Nikolowski, K.; Scheiba, F.; Kohl, M.; Giebeler, L.; Mikhailova, D.; Ehrenberg, H. Binding Energy Referencing for XPS in Alkali Metal-Based Battery Materials Research (II): Application to Complex Composite Electrodes. *Batteries* **2018**, *4* (3), 36. DOI: 10.3390/batteries4030036.

(262) Bhaghavathi Parambath, V.; Zhao-Karger, Z.; Diemant, T.; Jäckle, M.; Li, Z.; Scherer, T.; Gross, A.; Behm, R. J.; Fichtner, M. Investigation on the formation of Mg metal anode/electrolyte interfaces in Mg/S batteries with electrolyte additives. *J. Mater. Chem. A* **2020**, *8* (43), 22998–23010. DOI: 10.1039/D0TA05762B.

(263) J. McBreen, H.S. Lee, X.Q. Yang, X. Sun. New approaches to the design of polymer and liquid electrolytes for lithium batteries. *Journal of Power Sources* **2000** (89), 163–167.

(264) Lee, Y. M.; Seo, J. E.; Choi, N.-S.; Park, J.-K. Influence of tris(pentafluorophenyl) borane as an anion receptor on ionic conductivity of LiClO4-based electrolyte for lithium batteries. *Electrochimica Acta* **2005**, *50* (14), 2843–2848. DOI: 10.1016/j.electacta.2004.11.058.

(265) Wang, Z.; Gu, Y.; Ma, M.; Chen, M. Strong, Reconfigurable, and Recyclable Thermosets Cross-Linked by Polymer–Polymer Dynamic Interaction Based on Commodity Thermoplastics. *Macromolecules* **2020**, *53* (3), 956–964. DOI: 10.1021/acs.macromol.9b02325.

(266) Zarzeczańska, D.; Adamczyk-Woźniak, A.; Kulpa, A.; Ossowski, T.; Sporzyński, A. Fluorinated Boronic Acids: Acidity and Hydrolytic Stability of Fluorinated Phenylboronic Acids. *Eur. J. Inorg. Chem.* **2017**, *2017* (38-39), 4493–4498. DOI: 10.1002/ejic.201700546.

(267) Esteruelas, M. A.; Martínez, A.; Oliván, M.; Oñate, E. Direct C-H Borylation of Arenes Catalyzed by Saturated Hydride-Boryl-Iridium-POP Complexes: Kinetic Analysis of the Elemental Steps. *Chemistry (Weinheim an der Bergstrasse, Germany)* **2020**, *26* (55), 12632–12644. DOI: 10.1002/chem.202001838. Published Online: Sep. 7, 2020.

(268) La Olvera de Cruz, M. Theory of microphase separation in block copolymer solutions. *The Journal of Chemical Physics* **1989**, *90* (3), 1995–2002. DOI: 10.1063/1.456042.

(269) Andreas J. Butzelaar, Kun L. Liu, Philipp Röring, Gunther Brunklaus, Martin Winter, Patrick Theato. A Systematic Study of Vinyl Ether-Based Poly(Ethylene Oxide) SideChain Polymer Electrolytes **2021** (3), 1573–1582.

(270) J. A. Faniran and H. F. Shurvell. Infrared spectra of phenylboronic acid (normal and deuterated) and diphenyl phenylboronate.

(271) Kurt, M. An experimental and theoretical study of molecular structure and vibrational spectra of pentafluorophenylboronic acid molecule by density functional theory and ab initio Hartree Fock calculations. *Journal of Molecular Structure* **2008**, *874* (1-3), 159–169. DOI: 10.1016/j.molstruc.2007.03.050.

(272) G. Varsanyi. Assignments of Vibrational Spectra of Seven Hundred Benzene Derivatives. *Adam Hilger 1-2* **1974**.

(273) Erdogdu, Y.; Tahir Güllüoğlu, M.; Kurt, M. DFT, FT-Raman, FT-IR and NMR studies of 2-fluorophenylboronic acid. *J. Raman Spectrosc.* **2009**, *40* (11), 1615–1623. DOI: 10.1002/jrs.2309.

(274) Wieczorek, W.; Lipka, P.; Żukowska, G.; Wyciślik, H. Ionic Interactions in Polymeric Electrolytes Based on Low Molecular Weight Poly(ethylene glycol)s. *J. Phys. Chem. B* **1998**, *102* (36), 6968–6974. DOI: 10.1021/jp981397k.

(275) Soydan, A. M.; Bozkurt, A. Single-ion conductivity enhancement for the composite polymer electrolytes based on Li(PVAOB)/PPEGMA for lithium-ion batteries. *Ionics* **2018**, *24* (5), 1399–1405. DOI: 10.1007/s11581-017-2286-4.

(276) I. Rey, P. Johansson, J. Lindgren, J. C. Lasse`gues, J. Grondin, and L. Servant. Spectroscopic and Theoretical Study of (CF3SO2)2N- (TFSI-) and (CF3SO2)2NH (HTFSI). *J. Mater. Chem. A* **1998** (Vol. 102, No. 19), 3249–3258.

(277) Hambali, D.; Osman, Z.; Othman, L.; Isa, K. B. M.; Harudin, N. Magnesium (II) bis(trifluoromethanesulfonimide) doped PVdC-co-AN gel polymer electrolytes for rechargeable batteries. *J Polym Res* **2020**, *27* (6). DOI: 10.1007/s10965-020-02083-8.

(278) Xue, Z.; He, D.; Xie, X. Poly(ethylene oxide)-based electrolytes for lithium-ion batteries. *J. Mater. Chem. A* **2015**, *3* (38), 19218–19253. DOI: 10.1039/C5TA03471J.

(279) Mesallam, M.; Kamar, E. M.; Sharma, N.; Sheha, E. Synthesis and characterization of polyvinylidene fluoride/magnesium bromide polymer electrolyte for magnesium battery application. *Phys. Scr.* **2020**, *95* (11), 115805. DOI: 10.1088/1402-4896/abbcf4.

(280) Ebadi, M.; Eriksson, T.; Mandal, P.; Costa, L. T.; Araujo, C. M.; Mindemark, J.; Brandell, D. Restricted Ion Transport by Plasticizing Side Chains in Polycarbonate-Based Solid Electrolytes. *Macromolecules* **2020**, *53* (3), 764–774. DOI: 10.1021/acs.macromol.9b01912. Published Online: Jan. 31, 2020.

(281) David A. Sundermann, Bumjun Park, Valerian Hirschberg, Jennifer L. Schaefer, and Patrick Théato. Magnesium Polymer Electrolytes Based on the Polycarbonate Poly(2-butyl-2-ethyltrimethylene-carbonate). *ACS Omega* **2023**.

(282) He, P.; Ford, H. O.; Gonzalez, S.; Rodriguez, S.; Oliver, A. G.; Schaefer, J. L. Stability and Disproportionation of Magnesium Polysulfides and the Effects on the Mg-Polysulfide Flow Battery. *J. Electrochem. Soc.* **2021**, *168* (11), 110516. DOI: 10.1149/1945-7111/ac33e2.

(283) Florjańczyk, Z.; Zygadło-Monikowska, E.; Wieczorek, W.; Ryszawy, A.; Tomaszewska, A.; Fredman, K.; Golodnitsky, D.; Peled, E.; Scrosati, B. Polymer-in-Salt Electrolytes Based on Acrylonitrile/Butyl Acrylate Copolymers and Lithium Salts. *J. Phys. Chem. B* **2004**, *108* (39), 14907–14914. DOI: 10.1021/jp049195d.

(284) I. Rey, P. Johansson, J. Lindgren, J. C. Lasségues, J. Grondin, L. Servant. Spectroscopic and Theoretical Study of (CF3SO2)2N- (TFSI-) and (CF3SO2)NH (HTFSI). *J. Phys. Chem. A* **1998** (102), 3249–3258.

(285) Butzelaar, A. J.; Röring, P.; Mach, T. P.; Hoffmann, M.; Jeschull, F.; Wilhelm, M.; Winter, M.; Brunklaus, G.; Théato, P. Styrene-Based Poly(ethylene oxide) Side-Chain Block Copolymers as Solid Polymer Electrolytes for High-Voltage Lithium-Metal Batteries. *ACS applied materials & interfaces* **2021**, *13* (33), 39257–39270. DOI: 10.1021/acsami.1c08841. Published Online: Aug. 10, 2021.

(286) Wheatle, B. K.; Lynd, N. A.; Ganesan, V. Effect of Polymer Polarity on Ion Transport: A Competition between Ion Aggregation and Polymer Segmental Dynamics. *ACS macro letters* **2018**, *7* (10), 1149–1154. DOI: 10.1021/acsmacrolett.8b00594. Published Online: Sep. 10, 2018.

(287) Tuerxun, F.; Yamamoto, K.; Mandai, T.; Tateyama, Y.; Nakanishi, K.; Uchiyama, T.; Watanabe, T.; Tamenori, Y.; Kanamura, K.; Uchimoto, Y. Effect of Interaction among Magnesium Ions, Anion, and Solvent on Kinetics of the Magnesium Deposition Process. *J. Phys. Chem. C* **2020**, *124* (52), 28510–28519. DOI: 10.1021/acs.jpcc.0c08268.

(288) Srinivasa R. Raghavan, Michael W. Riley, Peter S. Fedkiw, and Saad A. Khan. Composite Polymer Electrolytes Based on Poly(ethylene glycol) and Hydrophobic Fumed Silica: Dynamic Rheology and Microstructure. *Chem. Mater.* **1998** (10), 244–251.

(289) Earnest, T. R.; Macknight, W. J. Effect of hydrogen bonding and ionic aggregation on the melt rheology of an ethylene–methacrylic acid copolymer and its sodium salt. *J. Polym. Sci. Polym. Phys. Ed.* **1978**, *16* (1), 143–157. DOI: 10.1002/pol.1978.180160113.

(290) Takahashi, T.; Watanabe, J.; Minagawa, K.; Koyama, K. Effect of ionic interaction on elongational viscosity of ethylene-based ionomer melts. *Polymer* **1994**, *35* (26), 5722–5728. DOI: 10.1016/S0032-3861(05)80047-3.

(291) Dintcheva, N. T.; Furlani, M.; Jayasundara, W. J. M. J. S. R.; Bandara, T. M. W. J.; Mellander, B.-E.; La Mantia, F. P. Rheological behavior of PAN-based electrolytic gel containing tetrahexylammonium and magnesium iodide for photoelectrochemical applications. *Rheol Acta* **2013**, *52* (10-12), 881–889. DOI: 10.1007/s00397-013-0727-1.

(292) G. Larson. *The Structure and Rheology of Complex Fluids*; Oxford University Press; Illustrated edition, 1998.

(293) Chen, S.; Döhler, D.; Binder, W. H. Rheology of hydrogen-bonded dendritic supramolecular polymer networks in the melt state. *Polymer* **2016**, *107*, 466–473. DOI: 10.1016/j.polymer.2016.08.046.

(294) G. G. Kumar, N. Munichandraiah. Effect of plasticizers on magnesium-poly(ethyleneoxide) polymer electrolyte. *Journal of Electroanalytical Chemistry* **2000** (495), 42–50.

(295) M. J. Reddy, P. P. Chu. Ion pair formation and its effect in PEO:Mg solid polymer electrolyte system. *Journal of Power Sources* **2002** (109), 340–346.

(296) Baskin, A.; Prendergast, D. Exploration of the Detailed Conditions for Reductive Stability of Mg(TFSI) 2 in Diglyme: Implications for Multivalent Electrolytes. *J. Phys. Chem. C* **2016**, *120* (7), 3583–3594. DOI: 10.1021/acs.jpcc.5b08999.

(297) Wu, H.; Gao, P.; Jia, H.; Zou, L.; Zhang, L.; Cao, X.; Engelhard, M. H.; Bowden, M. E.; Ding, M. S.; Hu, J.; Hu, D.; Burton, S. D.; Xu, K.; Wang, C.; Zhang, J.-G.; Xu, W. A Polymer-in-Salt Electrolyte with Enhanced Oxidative Stability for Lithium Metal Polymer Batteries. *ACS applied materials & interfaces* **2021**, *13* (27), 31583–31593. DOI: 10.1021/acsami.1c04637. Published Online: Jun. 25, 2021.

(298) Zhang, C.; Yang, Z.; Duong, N. T.; Li, X.; Nishiyama, Y.; Wu, Q.; Zhang, R.; Sun, P. Using Dynamic Bonds to Enhance the Mechanical Performance: From Microscopic Molecular Interactions to Macroscopic Properties. *Macromolecules* **2019**, *52* (13), 5014–5025. DOI: 10.1021/acs.macromol.9b00503.

(299) Dove, A. P.; Pratt, R. C.; Lohmeijer, B. G. G.; Waymouth, R. M.; Hedrick, J. L. Thiourea-based bifunctional organocatalysis: supramolecular recognition for living polymerization. *Journal of the American Chemical Society* **2005**, *127* (40), 13798–13799. DOI: 10.1021/ja0543346.

Appendix

Additional information and spectra for the different projects are given in the following.

1.16 Additional spectra and results for 'Borate crosslinked single-ion conducting copolymer electrolytes for magnesium battery applications'

Table 14: Initial and steady-state current densities ($I_{0,Pol}$ and I_{SS}) , resistances before and after polarization (R_0 and R_{SS}), bulk resistances (R_b) and the calculated initial current densities ($I_{0,cal}$). [a] Resistances fitted for **4-cross-PC** and **4-cross PEGDME$_{500}$** by equivalent circuit shown in Figure 94.

	4-cross-PC	**4-cross-PEGDME$_{500}$**	**4-cross-Li-PC**	**4-cross-Li-PEGDME$_{500}$**
I_{SS} [mA]	3.9 10^{-6}	8.1 10^{-6}	1.38 10^{-3}	0,18 10^{-3}
$I_{0,Pol}$ [mA]	1.44 10^{-3}	1.47 10^{-3}	1.50 10^{-3}	0.27 10^{-3}
R_b [Ω], before polarization [a]	9628.5	137 444	5 705	34 389.6
R_b [Ω], after polarization [a]	9024	139 740	5 612	31 972.8
R_0 [Ω] [a]	13.81 10^6	11.86 10^6	892.7	4 874
R_{SS} [Ω] [a]	13.9 10^6	17.05 10^6	1022	6034.2
$I_{0,cal}$ [mA]	3.9 10^{-5}	4.4 10^{-5}	1.51 10^{-3}	0.24 10^{-3}
$I_{SS}/I_{0,Pol}$	0.0027	0.018	0.92	0.68
$I_{SS}/I_{0,cal}$	0.1	0.18	0.91	0.65
t^+_{Li}	-	-	0.92	0.66

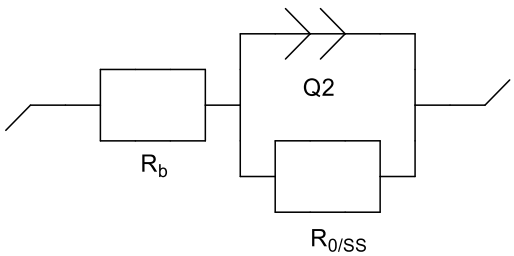

Figure 94: The equivalent circuit model of impedance spectroscopy employed for DC-polarization measurements **4-cross-PC** and **4-cross-PEGDME$_{500}$**.

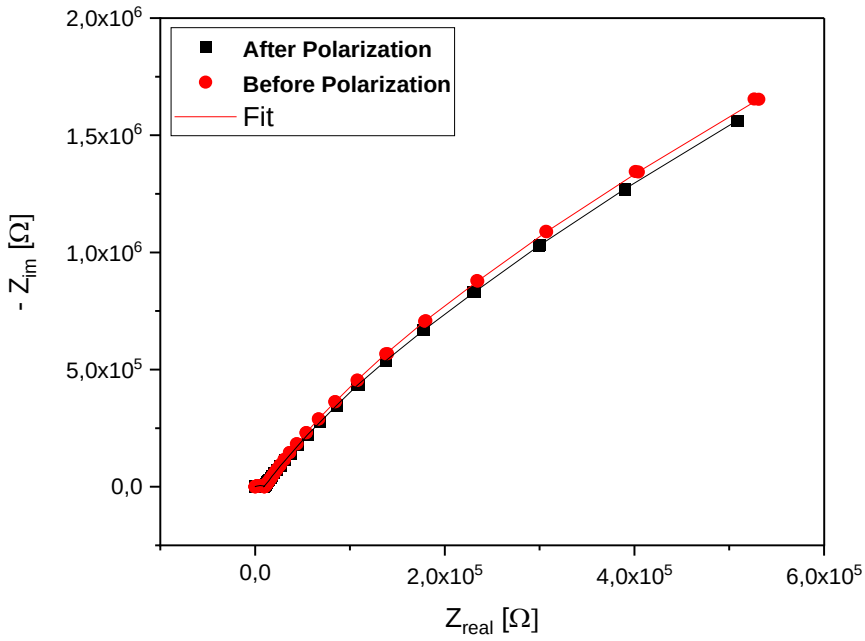

Figure 95: EIS spectra before and after polarization with FITs based on **4-cross-PC**. Plots fitted by equivalent circuit shown in Figure 94.

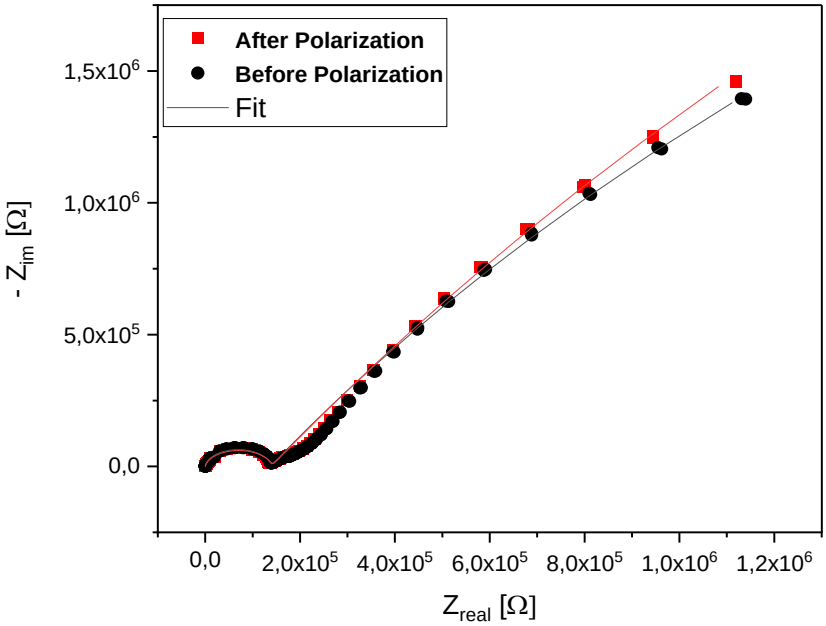

Figure 96: EIS spectra before and after polarization with FITs of **4-cross-PEGDME$_{500}$**. Plots fitted by equivalent circuit shown in Figure 94.

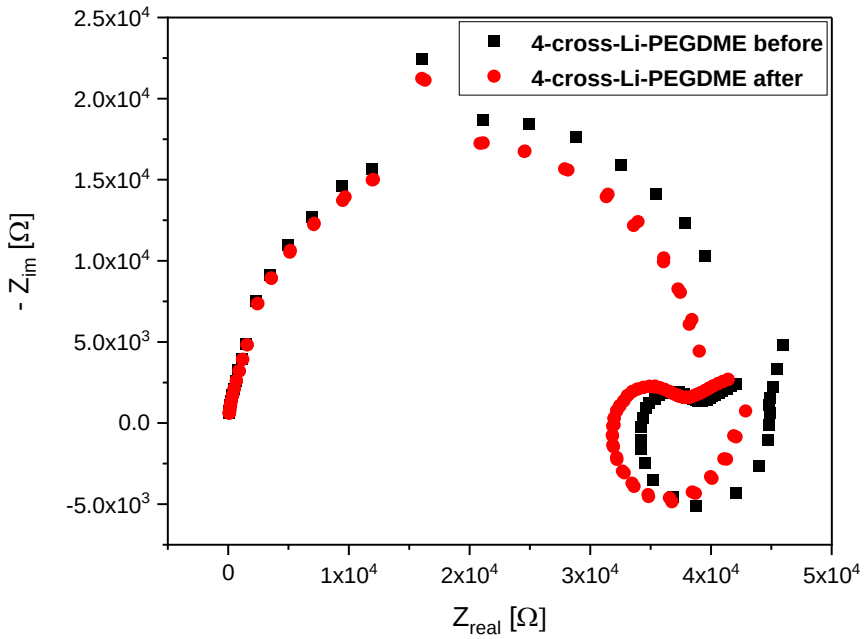

Figure 97: EIS spectra before and after polarization of **4-cross-Li-PEGDME$_{500}$**.

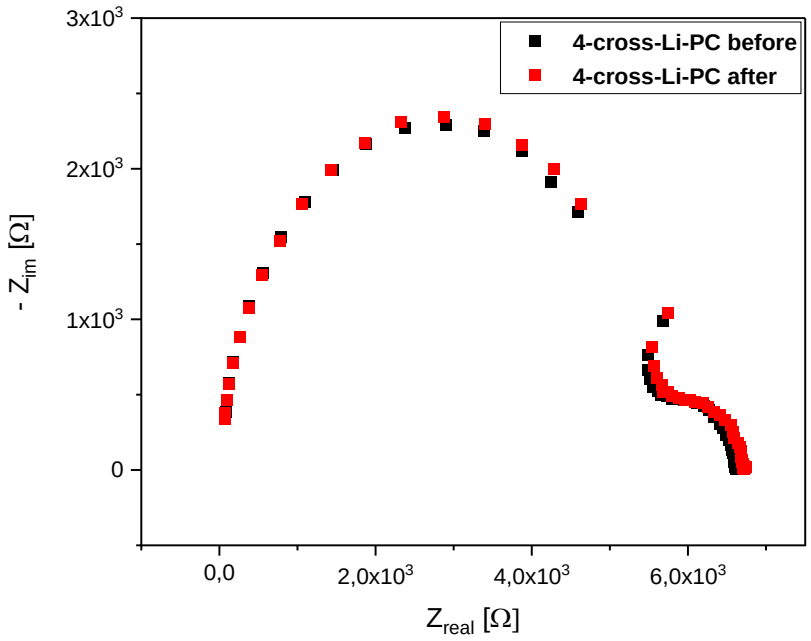

Figure 98: EIS spectra before and after polarization of **4-cross-Li-PC**.

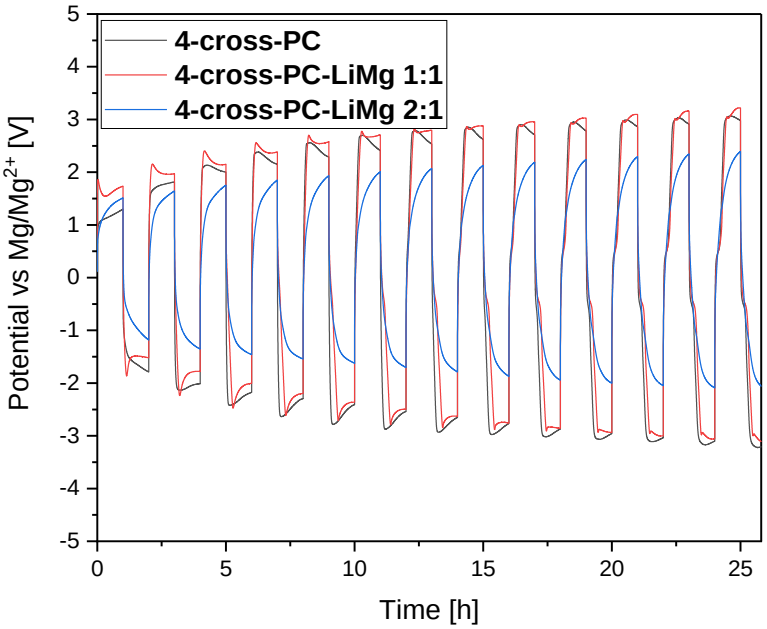

Figure 99: Pre-conditioning process at 0.1 µA cm^{-2} in symmetric Mg||Mg cell before measuring XPS.

Table 15: XPS Signal ratios of Mg 2s and C 1s of **4-cross**, **4-cross-PC-Li-Mg 1:1** and **4-cross-PC-Li-Mg 2:1** of magnesium electrode surface after pre-conditioning at 0.1 µA cm^{-2} in symmetric Mg||Mg cells.

Mg 2s	**Peak 1 [%]**	**Peak 2 [%]**
4-cross-PC	95.0	5.0
4-cross-PC-Li-Mg 1:1	88.2	11.8
4-cross-PC-Li-Mg 2:1	92.0	8.0

C 1s	**Peak 1 [%]**	**Peak 2 [%]**	**Peak 3 [%]**
4-cross-PC	50.2	42.6	7.2
4-cross-PC-Li-Mg 1:1	86.6	7.6	5.8
4-cross-PC-Li-Mg 2:1	76.5	14.4	9.0

1.17 Additional spectra and results for 'Additive-free copolymer electrolytes with borate anion receptors for magnesium ion batteries'

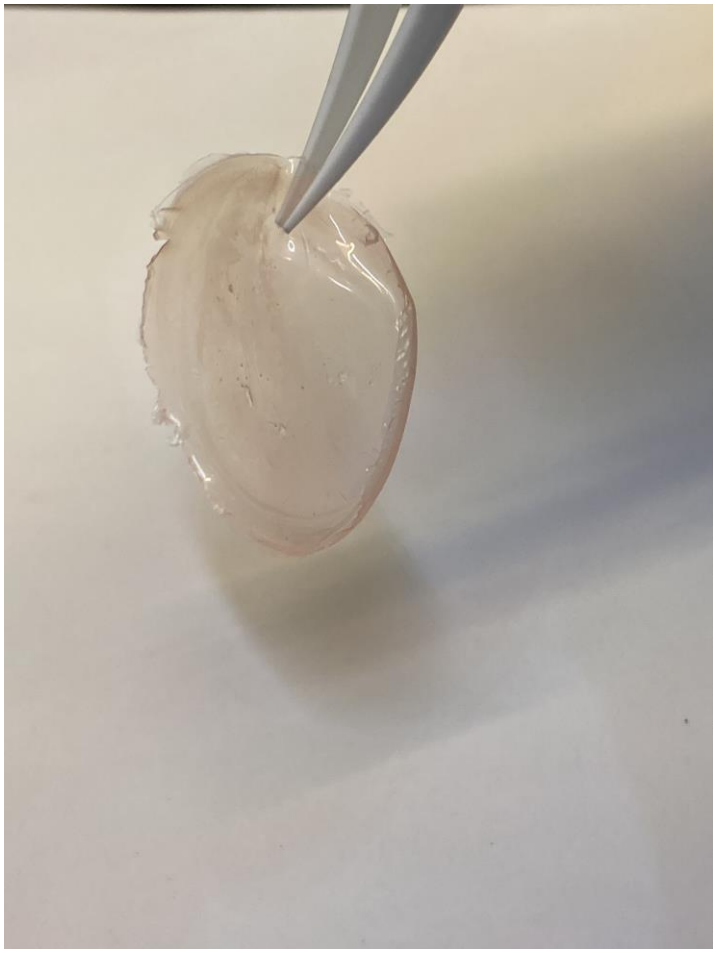

Figure 100: Picture of **EF$_2$3b**.

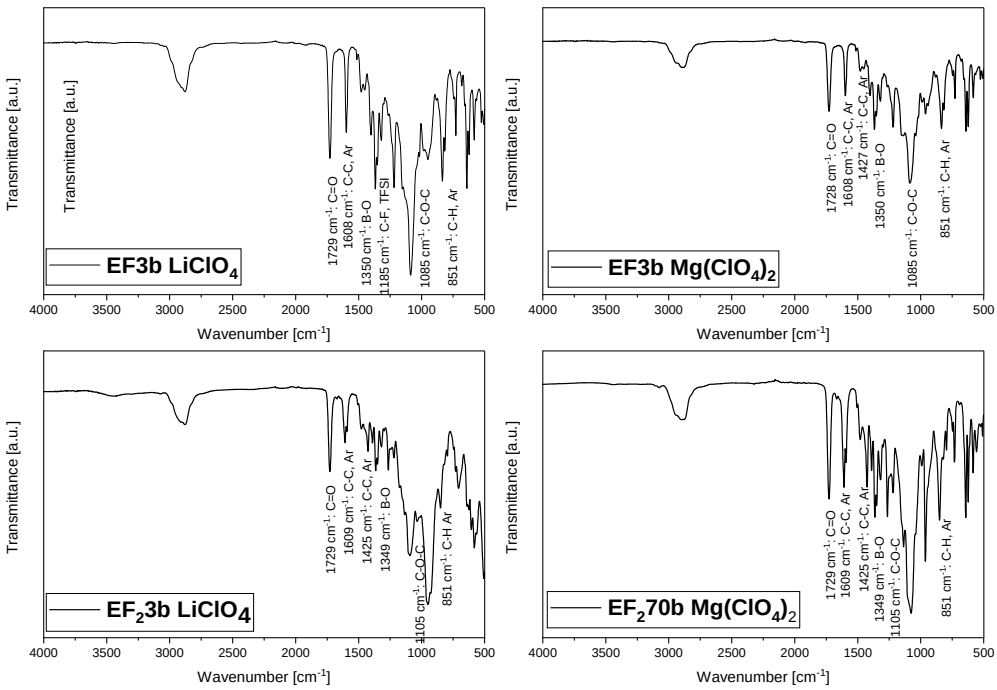

Figure 101: FT-IR spectra of, **EF3 Mg(ClO$_4$)$_2$**, **EF$_2$3 Mg(ClO$_4$)$_2$**, **EF3b LiClO$_4$** and **EF$_{23}$b LiClO$_4$**, between 4000 to 500 cm^{-1} under water-free argon atmosphere.

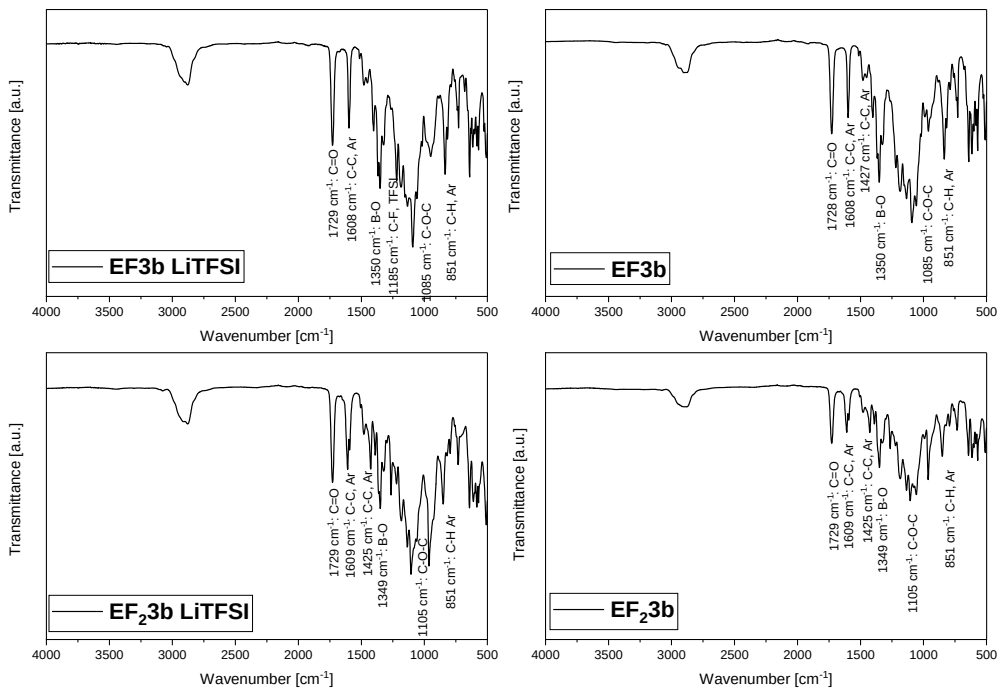

Figure 102: FT-IR spectra of **EF3b, EF$_2$3b**, **EF3b LiTFSI** and **EF$_2$3b LiTFSI** between 4000 to 500 cm^{-1} under water-free argon atmosphere.

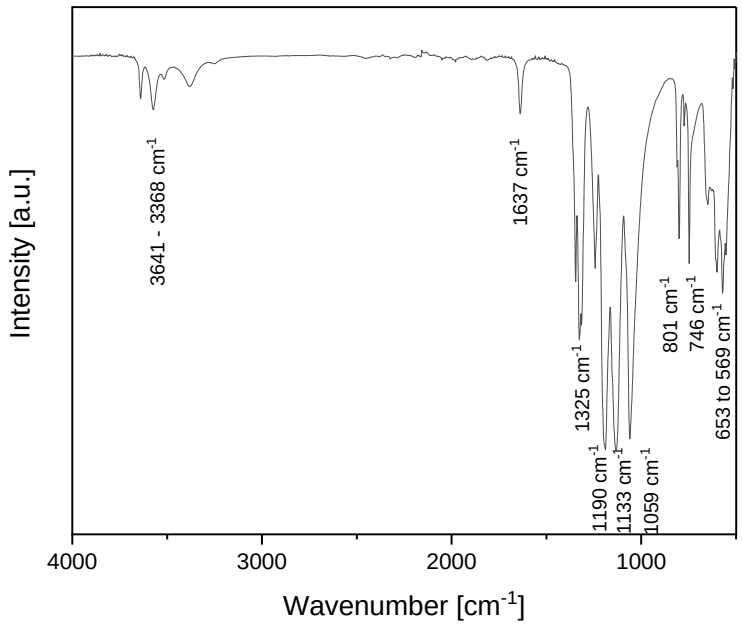

Figure 103: FT-IR spectra of LiTFSI between 4000 to 500 cm^{-1} under water-free argon atmosphere.

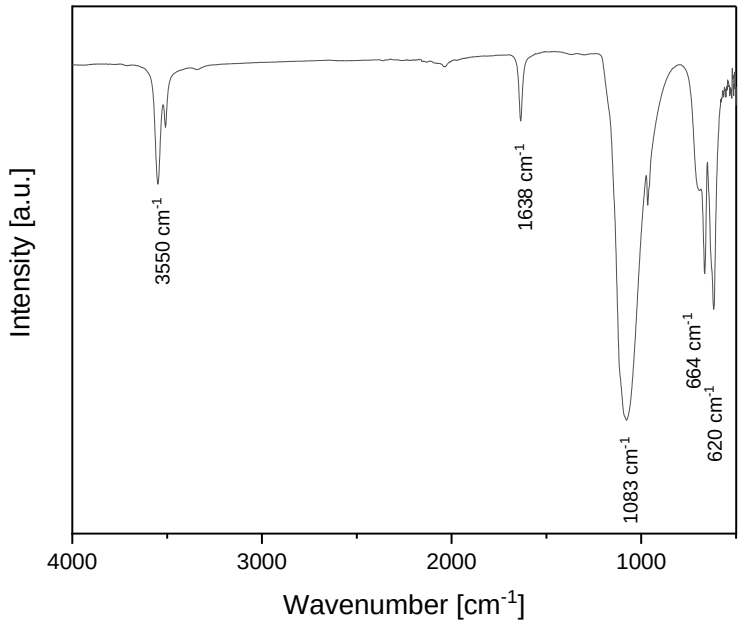

Figure 104: FT-IR spectra of $LiClO_4$ between 4000 to 500 cm^{-1} under water-free argon atmosphere.

Table 16: Initial/steady-state currents/resistances ($I_{0,cal}$/I_{SS}/R_0/R_{SS}), applied potential and calculated initial current ($I_{0,cal}$) by Ohmic´s law of the DC polarization experiments of **$EF_2$3b**, **$EF_2$3b Mg(ClO_4)$_2$**, **$EF_2$3b LiTFSI** and **$EF_2$3b LiClO$_4$** at 80 °C. [a] Resistances fitted for **$EF_2$3b** and **$EF_2$3b Mg(ClO_4)$_2$**, by equivalent circuit shown in Figure 105.

	$EF_2$3b	**$EF_2$3b Mg(ClO_4)$_2$**	**$EF_2$3b LiTFSI**	**$EF_2$3b LiClO$_4$**
$I_{0,pol}$ [mA]	$2.5\ 10^{-3}$	$0.83\ 10^{-3}$	$4.4\ 10^{-3}$	$1.83\ 10^{-3}$
R_0 [Ω] [a]	$2.25\ 10^{7}$	$7.79\ 10^{22}$	669.22	3259.42
$I_{0,cal}$ [mA]	$2.3\ 10^{-5}$	$1.97\ 10^{-3}$	$4.46\ 10^{-3}$	$1.86\ 10^{-3}$
I_{SS} [mA]	$2.69\ 10^{-6}$	$1.04\ 10^{-5}$	$1.35\ 10^{-3}$	$0.81\ 10^{-3}$
R_{SS} [Ω] [a]	$2.09\ 10^{8}$	$2.11\ 10^{25}$	669.18	3615.5
$I_{SS}/I_{0,pol}$	$1.1\ 10^{-4}$	$1.97\ 10^{-6}$	0.306	0.444
$I_{SS}/I_{0,cal}$	$2.5\ 10^{-6}$	$1.6\ 10^{15}$	0.302	0.437
ΔV [V]	0.527	0.494	0.010	0.010
t^+	-	-	0.24	0.26

Table 17: Initial/steady-state currents/resistances ($I_{0,cal}$/I_{SS}/R_0/R_{SS}), applied potential and calculated initial current ($I_{0,cal}$) by Ohmic´s law of the DC polarization experiments of **EF3b**, **EF3b Mg(ClO_4)$_2$**, **EF3b LiTFSI** and **EF3b LiClO$_4$** at 80 °C.

	EF3b	**EF3b Mg(ClO_4)$_2$**	**EF3b LiTFSI**	**EF3b LiClO$_4$**
$I_{0,pol}$ [mA]	$0.49\ 10^{-3}$	$4.4\ 10^{-3}$	$1.15\ 10^{-3}$	$2.11\ 10^{-3}$
R_0 [Ω] [a]	$5.29\ 10^{21}$	$9.65\ 10^{8}$	6127.07	623.09
$I_{0,cal}$ [mA]	$1.13\ 10^{-22}$	$4.64\ 10^{-10}$	$4.46\ 10^{-3}$	$1.87\ 10^{-3}$
I_{SS} [mA]	$1.41\ 10^{-6}$	$2.53\ 10^{-5}$	$0.52\ 10^{-3}$	$0.915\ 10^{-3}$
R_{SS} [Ω] [a]	$1.22\ 10^{22}$	$7.61\ 10^{7}$	5309.84	667.7
$I_{SS}/I_{0,pol}$	$2.86\ 10^{-3}$	$5.74\ 10^{-3}$	0.451	0.43
$I_{SS}/I_{0,cal}$	$1.25\ 10^{-13}$	54.43	0.410	0.49
ΔV [V]	0.597	0.448	0.011	0.009
t^+	-	-	0.22	0.40

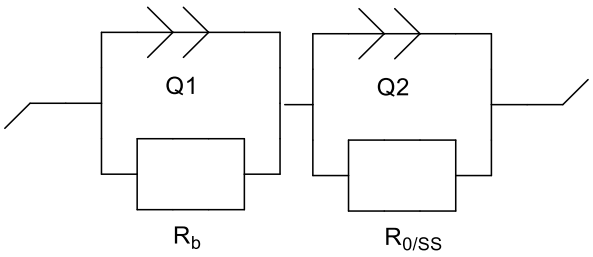

Figure 105: The equivalent circuit model of impedance spectroscopy employed for DC-polarization measurements of **$EF_2$3b**, **$EF_2$3b Mg(ClO_4)$_2$**, **EF3b** and **EF3b Mg(ClO_4)$_2$**.

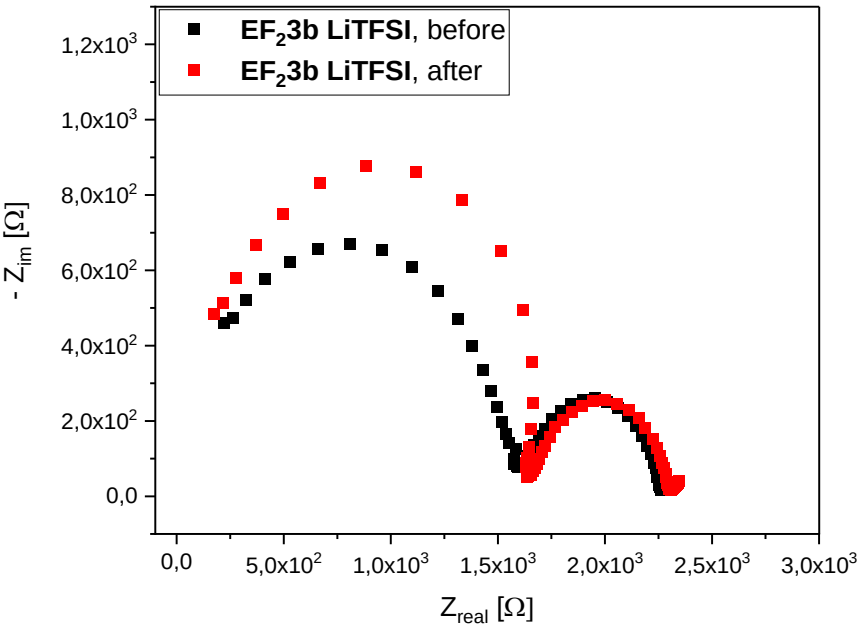

Figure 106: Impedance spectra before and after polarization of **$EF_2$3b LiTFSI** at 80 °C.

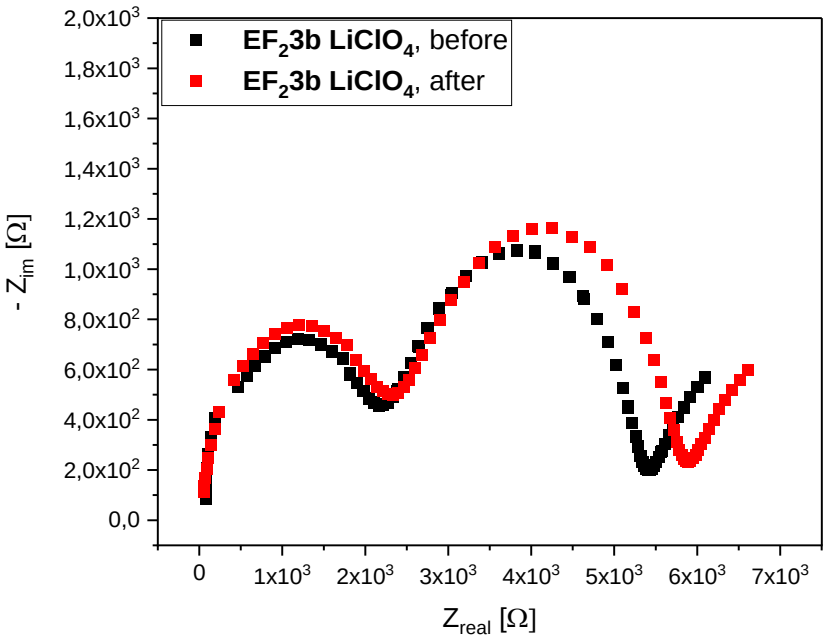

Figure 107: Impedance spectra before and after polarization of **$EF_2$3b $LiClO_4$** at 80 °C.

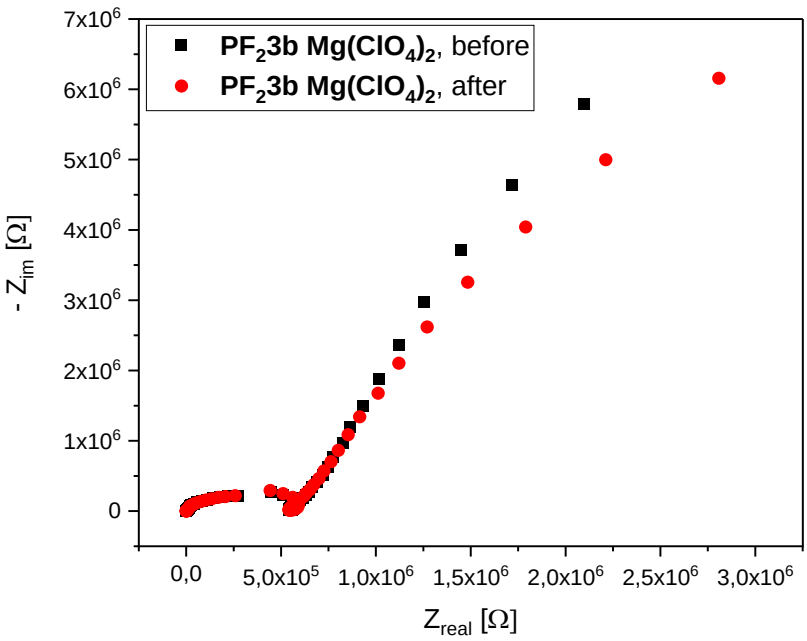

Figure 108: Impedance spectra before and after polarization of **$EF_2$3b $Mg(ClO_4)_2$** at 80 °C. Plots fitted by equivalent circuit shown in Figure 105.

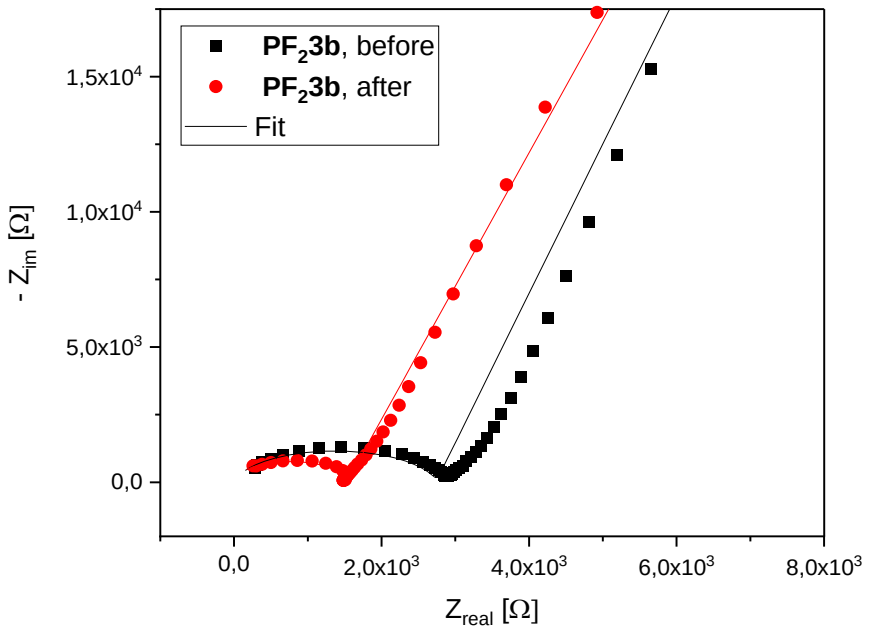

Figure 109: Impedance spectra before and after polarization of **EF₂3b** at 80 °C. Plots fitted by equivalent circuit shown in Figure 105.

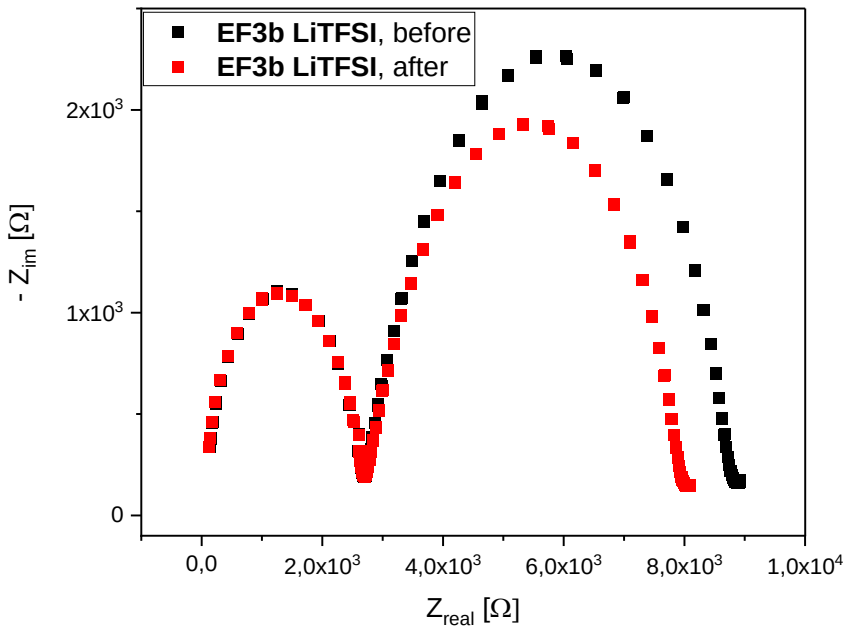

Figure 110: Impedance spectra before and after polarization of **EF3b LiTFSI** at 80 °C.

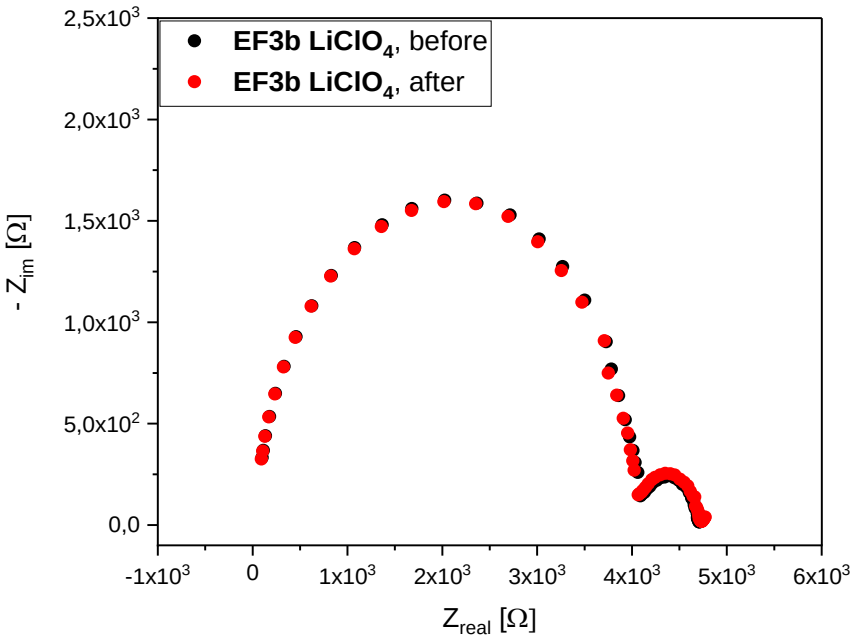

Figure 111: Impedance spectra before and after polarization of **EF3b $LiClO_4$** at 80 °C.

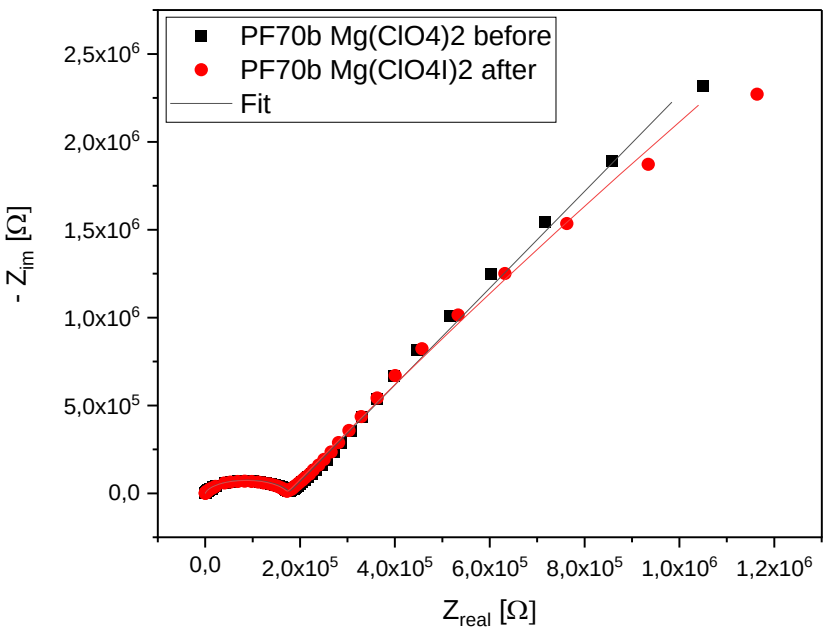

Figure 112: Impedance spectra before and after polarization of **$EF_2$3b $Mg(ClO_4)_2$** at 80 °C. Plots fitted by equivalent circuit shown in Figure 105.

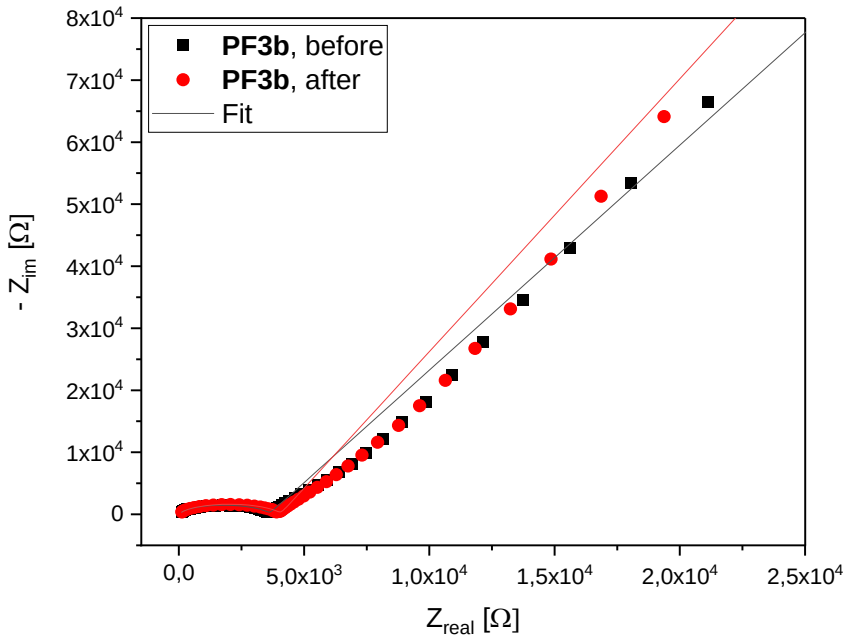

Figure 113: Impedance spectra before and after polarization of **EF$_2$3b** at 80 °C. Plots fitted by equivalent circuit shown in Figure 105.

1.18 Additional spectra and results for 'Magnesium polymer electrolytes based on polycarbonate poly(2-butyl-2-ethyltrimethylene-carbonate)'

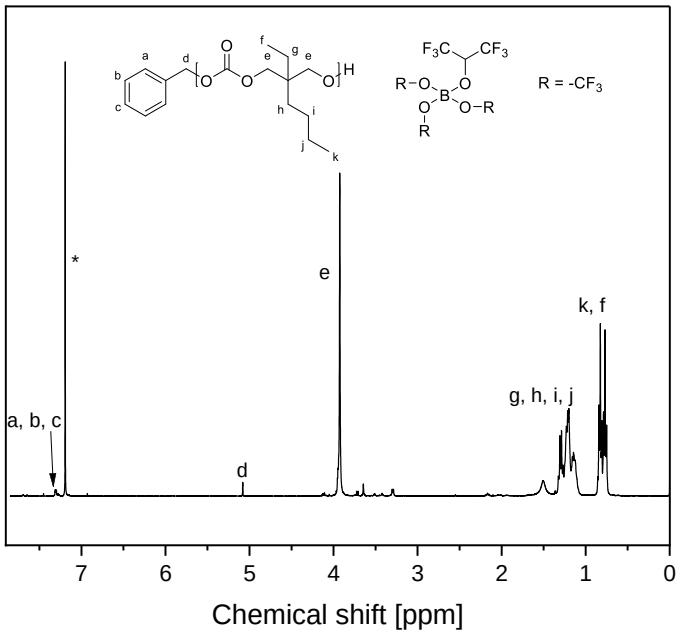

Figure 114: ^{1}H-NMR spectra of **HFIP40** in $CDCl_3$. Reproduced with permission from ACS Omega, in press. Unpublished work copyright 2023 American Chemical Society.

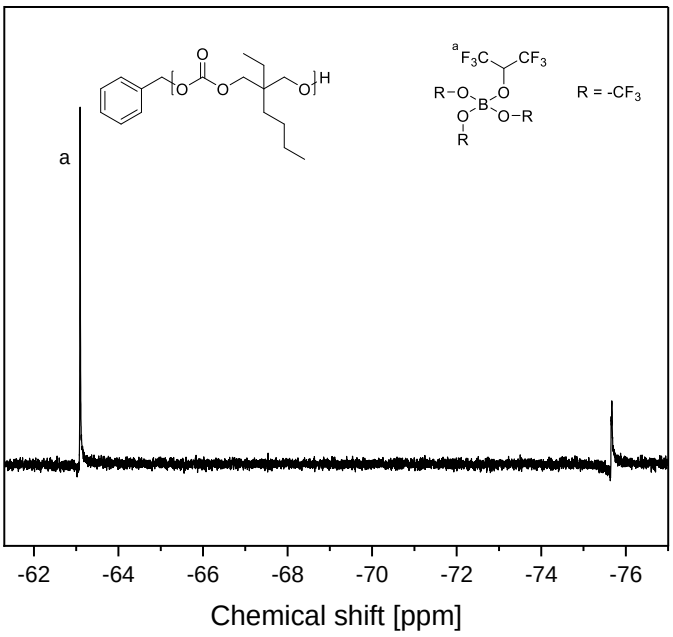

Figure 115: ^{19}F-NMR spectra of **HFIP40** in $CDCl_3$. Reproduced with permission from ACS Omega, in press. Unpublished work copyright 2023 American Chemical Society.

Table 18: Peak ratios of **TFSI40** to **TFSI5** of the peaks at 752 cm^{-1} (Peak 2) and 744 cm^{-1} (Peak 1) in %. Reproduced with permission from ACS Omega, in press. Unpublished work copyright 2023 American Chemical Society.

	Ratio of Peak 1:Peak 2 [%]
$Mg(TFSI)_2$	100:0
TFSI40	76.0:24.0
TFSI30	62.4:37.6
TFSI20	52.9:47.1
TFSI5	35.1:64.9

Table 19: Gradients of loss modulus G´ and storage modulus G´´ from DFS experiments, where G´´ > G´. Reproduced with permission from ACS Omega, in press. Unpublished work copyright 2023 American Chemical Society.

	Gradients of loss modulus *G´*	**Gradients of storage modulus *G´´***
P(BEC)	-1.498 ± 0.050	-0.988 ± 0.003
TFSI5	-1.415 ± 0.040	-0.981 ± 0.003
TFSI20	-1.334 ± 0.30	-0.972 ± 0.002
TFSI30	-1.425 ± 0.031	-0.983 ± 0.001
TFSI40	-1.075 ± 0.021	-0.824 ± 0.032
HFIP5	-1.388 ± 0.027	-1 ± 0
HFIP20	-0.669 ± 0.022	-0.717 ± 0.009
HFIP30	-0.691 ± 0.014	-0.669 ± 0.008
HFIP40	-0.985 ± 0.007	-0.772 ± 0.015

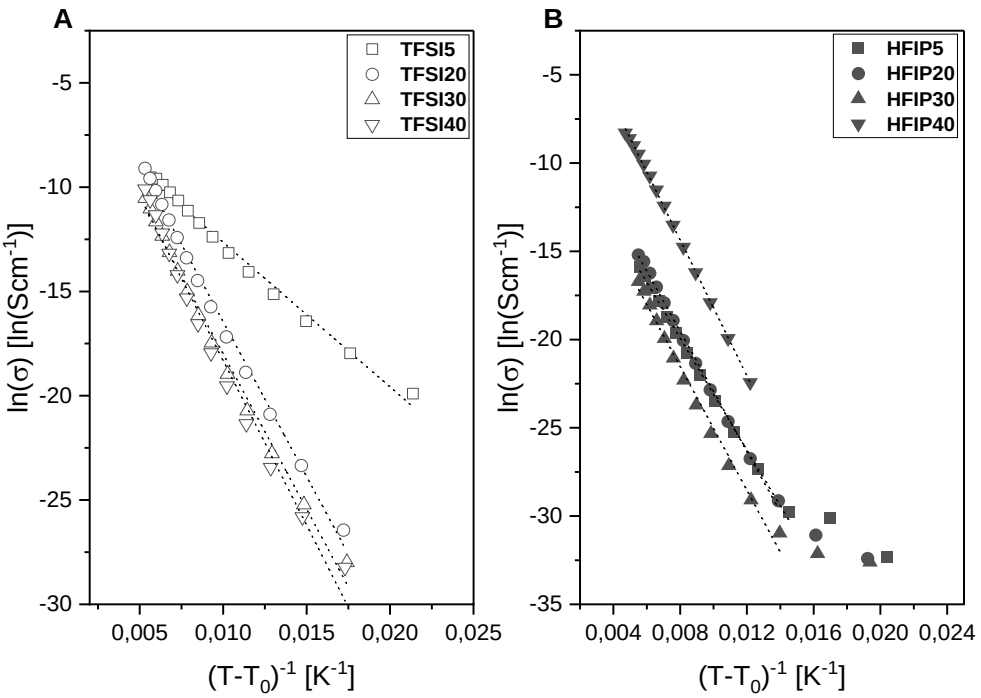

Figure 116: VFT plots (dotted line) of A) **TFSI5** to **TFSI40** and B) **HFIP5** to **HFIP40**. Reproduced with permission from ACS Omega, in press. Unpublished work copyright 2023 American Chemical Society.

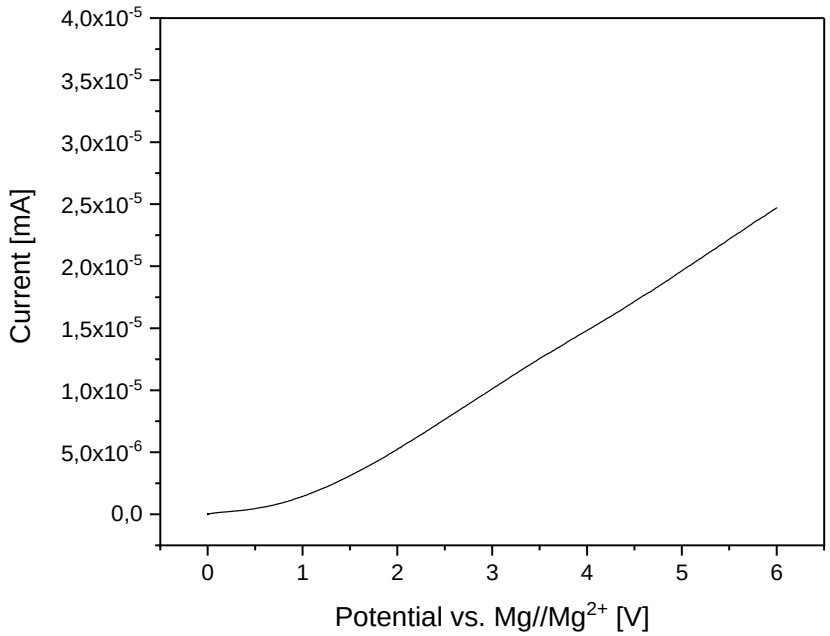

Figure 117: LSV measurement of **HFIP40** between 0 to 6 V vs. Mg/Mg^{2+} at 0.1 mVs^{-1}.

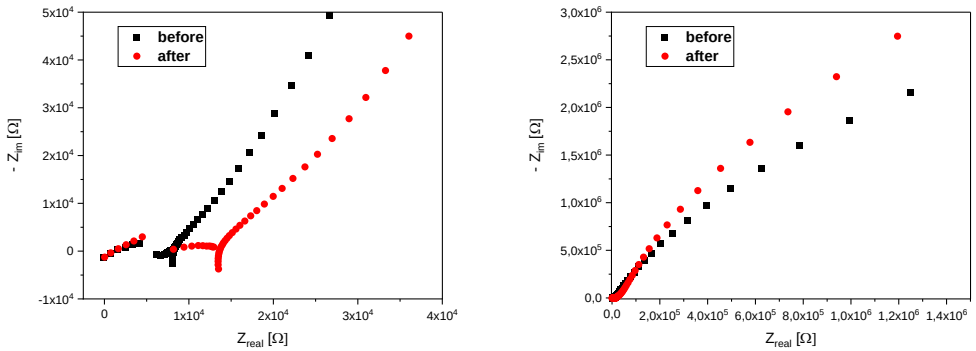

Figure 118: EIS results before and after cyclic voltammetry of **HFIP40**. Reproduced with permission from ACS Omega, in press. Unpublished work copyright 2023 American Chemical Society.